# Modulating the Single-Molecule Magnet, Magnetocaloric and Luminescent Behavior in Metallacrowns

by

Chun Y. Chow

A dissertation submitted in partial fulfillment
of the requirements for the degree of
Doctor of Philosophy
(Chemistry)
in The University of Michigan
2015

Doctoral Committee:

Professor Vincent L. Pecoraro, Chair
Associate Professor Bart M. Bartlett
Professor Talal Mallah, Université Paris Sud 11
Professor Stéphane Petoud, Université d'Orléans
Professor Melanie S. Sanford
Assistant Professor Donald J. Siegel

## Acknowledgments

I'm a big fan of brevity, so I'll keep this short and sweet. Firstly, I would like to thank Vince for giving me a chance at continuing my graduate career. He has given me the freedom to explore different areas of research and I am a better scientist for it. I am very grateful for his encouragement, guidance and constructive criticism. Vince gave me a great opportunity to work in France, where I met Talal Mallah, who has been tremendously helpful in learning magnetism. Stéphane Petoud has also been a great help with the luminescence portion of the work. I'd also like to thank the rest of my committee – Prof. Bart Bartlett, Prof. Melanie Sanford and Prof. Don Siegel for their insight and feedback all of these years.

Many thanks go to the great crystallographer, Jeff Kampf. I've learned a great deal about crystallography from him, a skill that has been very useful (and necessary) for this thesis. I'd also like to thank the rest of the Chemistry building staff (too many to name) for making things run so smoothly. I owe a debt of gratitude to the collaborators I've had the good fortune to work with including Dr. Svetlana Eliseeva, Dr. Victoria Campbell, Dr. Wolfgang Wernsdorfer, Dr. Cedric Tard (basketball buddy), Dr. Marco Evangelisti and Dr. Hélène Bolvin.

The Pecoraro group (past and present) has been great all these years. Ted and Joe, thanks for showing me the ropes early on. Evan, thanks for your sage advice on research and stuff. Tu and Jake, thanks for putting up with my thesis-writing craziness my last few months in lab. To the peptide side of the lab – Jeff, Fangting, Cathy, Alison, Casey, Ginny and Melissa – you guys have been great too, even though your research occasionally stunk up the lab. To the friends I've

made in grad school – Sam, Cam, Joe, Kayla, Adam, Tanya, Nomaan, Charles and everyone else – you guys have been awesome. Tailgating, golf, basketball, just hanging out and everything else has been a lot of fun.

Last but not least, I'd like to thank my family; my brother Bryan and my parents. Mom – thanks for all of your love and encouragement all of these years. Dad, thanks for teaching me the value of hard work and to always strive to be the best I can be. To my good friends back home – Jerry, Kyle, Mohammed and Seth – you've always been a source of support and encouragement.

# Table of Contents

# List of Figures

# List of Schemes

# List of Tables

# List of Appendices

# Abstract

## Modulating the Single-Molecule Magnet, Magnetocaloric and Luminescent Behavior in Metallacrowns

By

Chun Y. Chow

Chair: Vincent L. Pecoraro

The first part of this thesis focuses on the study of single-molecule magnets (SMMs), which have potential uses in high-density magnetic data storage. A new family of $[M_4Ln_2(shi^{3-})_4(Hshi^{2-})_2(H_2shi^{-})_2(C_5H_5N)_4(CH_3OH)_x(H_2O)_x]$ complexes (M = $Ga^{III}$, $Fe^{III}$; Ln = $Gd^{III}$, $Tb^{III}$, $Dy^{III}$, $Er^{III}$, $Y^{III}_{0.9}Dy^{III}_{0.1}$) were prepared in order to investigate the effect of *3d* and *4f* magnetic interactions on slow magnetic relaxation behavior. It was found the antiferromagnetic *3d-4f* coupling had adverse effects on slow magnetic relaxation. Furthermore, the dynamic magnetic behavior in the $Ga_4Dy_2$ analogue was elucidated, with two relaxation processes being attributed to the decoupled and excited ferromagnetic states.

The magnetocaloric effect (MCE) is a phenomenon which holds promise for low-temperature refrigeration applications. Iron(III), an inexpensive, isotropic $S = 5/2$ ion, was selected to develop efficient low-temperature magnetic refrigerants. An investigation of $Fe^{III}(X)_3[9\text{-}MC_{FeIIIN(shi)}\text{-}3]$ compounds (X = acetate or benzoate) revealed that inter- and intramolecular magnetic interactions could be tuned to achieve greater MCE behavior. The

acetate complex exhibited a $-\Delta S_m$ value of -15.4 J $kg^{-1}$ $K^{-1}$ ($T$ = 3 K, $\Delta H$ = 7 T), which is comparable to higher nuclearity $Fe^{III}$ clusters. Extensive antiferromagnetic intermolecular interactions resulted in a smaller MCE in the benzoate derivative and an analogous $Fe^{III}_2$(isopthalate)$_3$[9-$MC_{FeIIIN(shi)}$-3]$_2$ dimer compound. These studies show that rational design and control of magnetic interactions may be employed to develop high performance MCE materials.

$Ln^{III}$(benzoate)$_4$[12-$MC_{GaIIIN(shi)}$-4](pyridinium$^+$) complexes ($Ln^{III}$ = $Sm^{III}$, $Eu^{III}$, $Gd^{III}$, $Tb^{III}$, $Dy^{III}$, $Ho^{III}$, $Er^{III}$, $Tm^{III}$, $Yb^{III}$) were found to be capable of sensitizing both visible and NIR emitting $Ln^{III}$ ions. Efficient energy transfer from the ligand $T_1$ state to the emitting state on the $Ln^{III}$ led to the observation of remarkable luminescent behavior. In particular, solid state quantum yields for the $Yb^{III}$ and $Er^{III}$ analogues (5.88% and $4.4 \cdot 10^{-2}$%, respectively) are greater than any reported in the literature. This system presents a highly efficient and modular platform on which to develop practical bio-imaging agents.

The work presented in this thesis demonstrates that physical properties can be tuned through systematic ligand and metal substitution in metallacrown coordination complexes. These results have given new insight towards the understanding of single-molecule magnets, MCE materials and luminescent lanthanide complexes.

# Chapter I

# General Introduction

## 1.1 Metallacrowns: Design and Synthetic Considerations

The design and synthesis of multi-metallic coordination complexes poses a unique challenge in chemistry, as one must consider many variables including the size and reactivity of the chosen metal, geometric considerations for the organic ligand, as well as reaction conditions. Nevertheless, complex polymetallic structures may be designed through adherence to principles of coordination chemistry. As eloquently stated by Saalfrank, "the synergistic effect of serendipity and rational design" dictates the structural assembly of supramolecular complexes.[1] Inspired by organic crown ethers and rationalized by the tenets of coordination chemistry, metallacrowns (MCs) are a class of complexes which offer a high degree of geometric and structural control. Selection of the appropriate ligands lead to the MC topology which often affords the archetypal regular polygon shaped ringed structures, such as the 9-MC-3, 12-MC-4 and 15-MC-5. However, the inherent flexibility of these ligands also allows for unique structures to be synthesized by varying reaction conditions.

First recognized in 1989,[2] MCs rely on a multidentate ligand to coordinate more than one metal ion, thereby producing a macrocyclic structure. When using a hydroxamic acid as a ligand, an [M-N-O] repeat unit is formed where the O-atoms face toward the center of the ring and are capable of accommodating a central metal ion. MCs bear their name due to this similarity to the classical crown ether using the following nomenclature: $M_C X$[ring size-$MC_{M_R Z(L)}$-ring

oxygens]Y, where $M_C$ = central metal, X = bound anion, $M_R$ = ring metal, Z = third heteroatom of ring, L = organic ligand and Y = unbound anion. As an example, the homometallic MC in Figure 1.1 would be named $Mn^{II}(O_2CCH_3)_2$[12-$MC_{Mn^{III}N(shi)}$-4], where $Mn^{II}$ is the central metal, the ring is comprised of twelve total atoms with four repeating units, the ring metal is $Mn^{III}$, and the organic backbone is made up of the salicylhydroxamic acid ($H_3$shi) ligand. For the sake of simplicity, the nomenclature used in this thesis may omit bound and unbound anions or cations which are not critical in describing the structure. The basic MC structure type has been varied by substituting the oxygen atom for nitrogen (aza-MCs).[3-6] In addition, so called "inverse metallacrowns" occur when the ring metal faces the cavity allowing for anion recognition.[7] Thus, a wide variety of structures are possible depending on the chosen metal and ligand and this structural versatility has recently been reviewed.[8]

The two most common MCs are of the 12-MC-4 and 15-MC-5 type (Figure 1.2). However, under the right reaction conditions and using the correct choice of metal, a distorted 9-

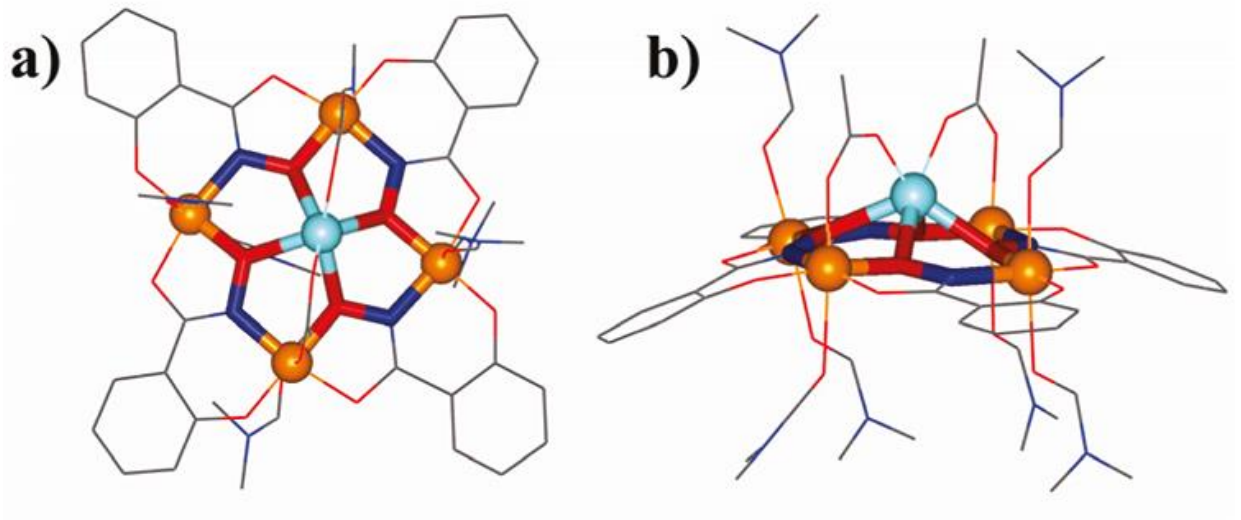


**Figure 1.1.** Crystal structure of $Mn^{II}(O_2CCH_3)_2$[12-$MC_{Mn^{III}N(shi)}$-4]. Color scheme: blue spheres – $Ho^{III}$, orange spheres – $Mn^{III}$, red tube – oxygen, and blue tubes - nitrogen. Reprinted with permission from reference 9. Copyright 2011 American Chemical Society.

-MC-3 structure can also be achieved. It should be noted that Figure 1.2 represents the idealized planar structures, X-ray crystallography reveals that actual structures may deviate in angles and planarity. By following the simple design principles, many hydroxamic acid-based ligands have been used to generate various MC complexes. For instance, the ligand $H_3$shi has the correct ligand geometry to prefer the 12-MC-4 topology (Figure 1.2). These ligands form a subunit with

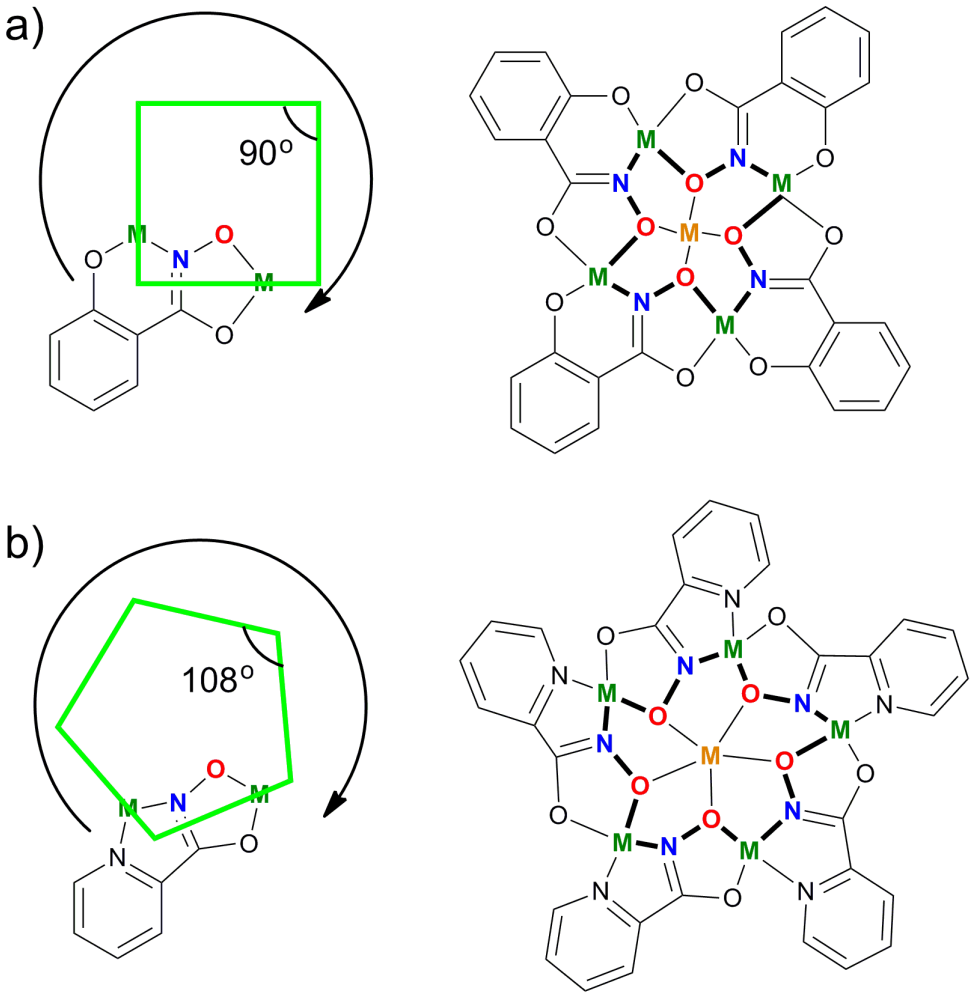


**Figure 1.2** Diagram of the metallacrown design strategy based on chelate ring geometry. a) The square shaped 12-MC-4 is generated from ligands which form a 90° internal angle between the lines bisecting the alternating 5- and 6- membered rings. The deprotonated form of salicylhydroxamic acid ($H_3$shi) is pictured. b) The pentagonal 15-MC-5 is generated from ligands which form a 108° internal angle between the lines bisecting the fused 5- membered rings. The deprotonated form of picoline hydroxamic acid ($H_2$picHA) is pictured. The metallacrown ring structure is highlighted in bold. Note that the 12-MC-4 structure can be synthesized with $H_2$picHA and $Zn^{II}$ ions, see references 10, 11 and 12 for details.

an idealized 90° internal angle between the lines bisecting the alternating 5- and 6- membered fused chelate rings, which repeat four times to form the square 12-MC-4 structure. Correspondingly, ligands such as $H_2$picHA prefer the 15-MC-5 structure type by forming subunits with idealized 108° internal angles that propagate five times to form the pentagonal structure (Figure 1.2). Due to the structural adaptability of these ligands and the capacity of lanthanides to serve as ring metals, other complex structure types can be achieved. For instance, with $H_3$shi, alternative motifs deviating from the 12-MC-4 structure type such as the 9-MC-3,[13,] 14-MC-5[14] and 15-MC-5[15] structures can also be synthesized depending on choice of metal and reaction conditions.

The synthesis of MCs requires considerations of several aspects including choice of ligand, metal, solvent, counter-ion, stoichiometry, and crystallization conditions. The discovery of new MC materials may often involve the 'shake and bake, mix and wait' strategy often employed in MOF research[16] to yield serendipitous and unpredictable structures; however, with careful attention to synthetic conditions, MC synthesis can attain a high degree of predictable geometric control over the molecular structure that is rarely achieved in self-assembly reactions.

It often is prudent to choose ring metals with the correct valency to match the protonation state of the chosen ligand. For triprotic ligands such as $H_3$shi, trivalent transition metal ions such as $Ga^{III}$, $Mn^{III}$ or $Fe^{III}$ are suitable to provide charge balance in the MC ring. On the other hand, the diprotic ligands like $H_2$picHA or $H_2$quinHA prefer divalent metals such as $Zn^{II}$, $Ni^{II}$ or $Cu^{II}$. Nevertheless, ligand/ring metal combinations with differing valencies may form MCs; several $Cu^{II}[12\text{-}MC_{Cu^{II}N(shi)}\text{-}4]^{2-}$ complexes have been synthesized where $Cu^{II}$ is a divalent ion and $H_3$shi is a triprotic ligand.[17] In these cases a suitable counteraction such as trimethylammonium must be used in the reaction. One must also consider the electronic structure of the ring metal. Metal

ions that are diamagnetic and have isotropic electron configurations such as $Zn^{II}$, $Ga^{III}$ and $Fe^{III}$ do not lead to a Jahn-Teller distortion, whereas $Mn^{III}$ and $Cu^{II}$ may show significant elongation along the *z*-axis. The presence (or lack thereof) of the distortion axis can lead to differences in the axially coordinated solvent/ligands, and may even generate different structures all together. In particular, much work has been done with $H_2$picHA and $H_2$quinHA with the divalent ring metal $Zn^{II}$, which has been shown to support numerous structure types. Perhaps the most interesting stoichiometric variations are mixed ligand/mixed metal metallacrowns as exemplified by the collapsed metallacrown, which includes 2 $pko^{-1}$ ligands (di-2-pyridyl ketone oximate) and two $shi^{3-}$ ligands while complexing two $Mn^{III}$ ions and two $Ni^{II}$ ions.[18]

Lanthanide choice can be an important factor in MC synthesis and design. In the 15-MC-5 motif, the central cavity coordinates lanthanide ions equatorially through five planar oxime oxygen atoms in a pentagonal arrangement. The larger crystal radius of the lanthanide ions is capable of accommodating five donor atoms in one plane. The apical positions can be coordinated by solvent or counter-anions such as nitrates or carboxylates to yield 8-coordinate lanthanide centers, though 9-coordinate geometries have been observed in lanthanides with larger ionic radii than $Pr^{III}$. Previously, in a detailed structural examination, it has been observed that the $Ln^{III}[15\text{-}MC_{Cu^{II}N(S\text{-}pheHA)}\text{-}5]^{3+}$ systems can support lanthanides with crystal radii ranging from 1.07 Å for $Tm^{III}$ to 1.24 Å for $La^{III}$.[19] A linear increase in the cavity radii commensurate with lanthanide crystal radii leads to an increase in $Cu^{II}$-$Cu^{II}$ distances. This expansion of the cavity results in a subsequent increase in the overall planarity of the MC complex.

Whereas the 15-MC-5 structure has large cavities which can bind central $Ln^{III}$ ions, the 12-MC-4 structure has a smaller cavity size, which forces the $Ln^{III}$ above the oxygen plane and may often require bridging carboxylate anions such as acetate.[20] For these types of complexes,

the four bridging carboxylates are required to satisfy the ligand field requirements of the $Ln^{III}$ ion. Thus, the metallacrown moiety has a charge of -1 and requires a counter-cation, which can be alkali metal ions such as $Na^+$ or $K^+$ that coordinate to the opposite face of the metallacrown. Sodium acetate is often utilized as a base and as a source for the bridging carboxylate and counter-cation. However, this is not always the case for all 12-MC-4 complexes; $Ln^{III}$[12-$MC_{Zn^{II}N(quinHA)}$-4](DMF)$_4$($NO_3$)$_3$ complexes have been synthesized where the central $Ln^{III}$ ion has been coordinated by four DMF molecules and is charge balanced by three lattice nitrates.[12]

Finally, solvent choice is another important factor in the formation of MCs. The most commonly used solvents are methanol, DMF, water and pyridine. In general, the reaction components of the metallacrown assembly are stirred in the selected solvent(s) and subsequent slow evaporation of the solvent leads to crystallization of the complex. Often, diffusion of a volatile nonpolar solvent such as diethyl ether may also lead to crystallization of the MC product. The choice of solvent must be able to dissolve the reaction components, yet must not too strongly solvate the formed metallacrown as to inhibit crystallization. Furthermore, the solubility of side products such as salts must be accounted for to ensure the crystallization of pure material.

The challenges involved in synthesizing crystalline metallacrowns suitable for single crystal X-ray diffraction have been briefly mentioned above. Although careful consideration of the factors influencing metallacrown formation may offer some degree of control of the molecular species formed, control of other design aspects such as crystal packing, which influence physical properties, and exact ligand field geometry still pose a considerable challenge. Nevertheless, metallacrown complexes with interesting structural features and physical properties have been synthesized using these design principles. The research discussed in this

thesis involves the synthesis and characterization of MCs to study their magnetic and luminescent properties.

### 1.2 A Brief History of Magnetism

According to legend, in the 6th century BCE, the Greek philosopher Thales of Miletus observed that lodestones (magnetite) were attracted to iron and other lodestones; the term *magnet* was later used to describe the iron ore found in the Greek city of Magnesia.[21] The remarkable physical properties of this material were soon put to use as the first compass was invented during the 3rd and 4th century BCE during the Han Dynasty in China.[22] Although the use of magnetic compasses were further refined during the following centuries, the physical origins of magnetism was not understood until the early 17th century, when English scientist William Gilbert noted in his work, *De Magnete*, that the earth behaved as a giant magnet.[22] Subsequent research in the 18th and 19th centuries by luminaries including Coulomb, Volta, Oersted, Biot, Faraday and Gauss further established fundamental physical laws of electricity and magnetism.[22]

In 1873, James Clerk Maxwell's unified theory of electromagnetism in his seminal work, *Treatise on Electricity and Magnetism* would provide a mathematical basis for the electromagnetic phenomena.[23] The Maxwell's equations would have a lasting impact on scientific research and has implications on the work presented in this thesis. The discovery of the electron in 1897 by J. J. Thomson[24] and the ensuing refinement of the theory through quantum mechanics would usher in a new era of scientific discovery in the 20th century. Key discoveries range from the advent of magnetic refrigeration[25] to superparamagnetism[26] to high temperature superconductors.[27]

With the improvement of structural and magnetic characterization techniques, coordination chemists began to study magnetic properties of compounds and gave rise to the

field of molecular magnetism. Indeed, Prussian blue, one of the very first synthetic pigments, behaves as a ferromagnet below 5.6 K.[28] Olivier Kahn is considered by many to be the father of molecular magnetism, and has been crucial in the understanding of inter- and intramolecular magnetic interactions in coordination complexes.[29]

Molecule-based materials have several advantages over their solid state counter-parts, including controllability of the structure, solubility, and in the case of single-molecule magnets, size. Molecular magnets, whose metal-metal interactions mediated through bridging ligands, are governed by the Goodenough-Kanamori rule of superexchange.[30-31] Thus, through careful consideration of molecular structure, it is possible to engineer materials to be suitable for various applications in magnetochemisty. In particular, the magnetism portion of my thesis research is focused on single-molecule magnets (SMMs) and paramagnetic refrigerants based on the magnetocaloric effect (MCE).

**1.3 Magnetic Interactions**

Before diving into molecule-based SMMs and MCE materials, it is essential to first discuss the fundamental theory behind magnetic interactions. For an in-depth examination of theory of molecular magnetism, the reader is referred to several books on the topic.[29, 32-33] Magnetic moments arising from atoms or molecules are derived from the spin and orbital angular momentum of unpaired electrons. The Hamiltonian describing the energy of a $d^n$ atom or ion due to various electronic and nuclear interactions is shown in Figure 1.3.[34] The magnitude of the energies of these interactions range from $10^4 - 10^5$ $cm^{-1}$ for the electronic and crystal field interactions[34] down to $10^{-7}$ $cm^{-1}$ for nuclear quadrupole resonances.[35] Thus, the study of these effects requires analytical techniques of varying sensitivity. In this thesis, we are primarily interested in magnetic and electronic interactions of intermediate magnitude, namely spin-orbit

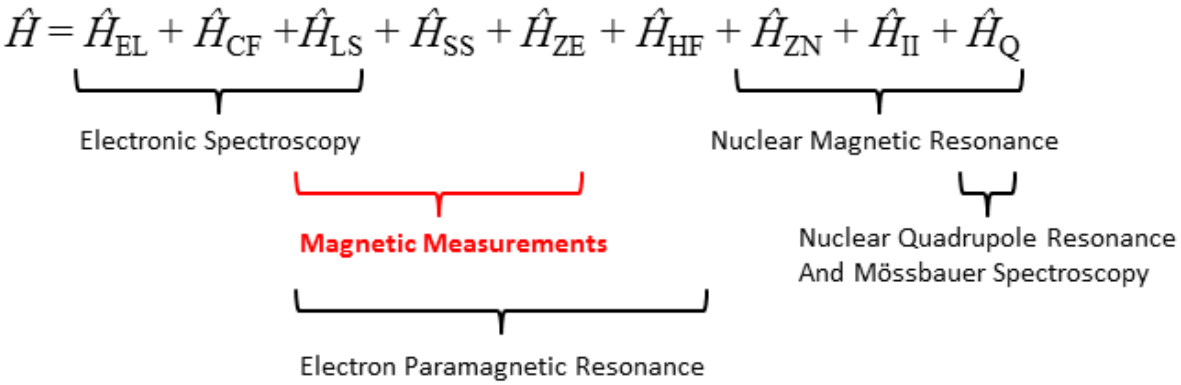


**Figure 1.3.** The Hamiltonian describing the energy of a $d^n$ transition metal. Brackets indicate the spectroscopic techniques used to characterize the various interactions. $\hat{H}_{EL}$ = electronic energy and electron repulsion energy; $\hat{H}_{CF}$ = crystal field; $\hat{H}_{LS}$ = spin-orbit coupling; $\hat{H}_{SS}$ = spin-spin interaction; $\hat{H}_{ZE}$ = electronic Zeeman effect; $\hat{H}_{HF}$ = hyperfine interaction; $\hat{H}_{ZN}$ = nuclear Zeeman effect; $\hat{H}_{II}$ = internuclear interaction; $\hat{H}_{Q}$ = nuclear quadrupole effect.

coupling ($0 – 10^2$ $cm^{-1}$ for transition metals/$10^3$ $cm^{-1}$ for lanthanides), spin-spin interactions ($0 – 10^2$ $cm^{-1}$) and the Zeeman effect ($0 – 1$ $cm^{-1}$). These three interactions will be discussed below to lay the foundation for the discussion of SMMs and MCE materials.

***Spin-Orbit Coupling: Zero-Field Splitting and Magnetic Anisotropy***

At the atomic level, the angular momentum of unpaired electrons, which is comprised of the spin and orbital angular momenta, creates a magnetic moment.[36] For lighter transition metals, especially those with isotropic electronic distributions (such as $Fe^{III}$ or $Mn^{II}$), the spin angular momentum is the dominant contribution to the magnetic moment, with the coupling between the spin and orbital components being weak. Under these conditions, the electronic structure can be described by the Russell-Saunders treatment. At high temperatures, *3d* based complexes may be adequately described by a *spin-only approximation*. However, in the heavier elements such as the *4f* lanthanides, there is significant spin-orbit coupling, which can be described by *j-j* coupling.[37-38] Spin-orbit coupling in both *3d* and *4f* ions leads to a splitting of the spin state

levels, known as zero-field splitting (ZFS), which causes magnetic anisotropy and has profound effects on the magnetic properties.

ZFS in transition metals contain an axial (*D*) and rhombic (*E*) component. For odd-electron ions, the spin microstates are split by the *D* component to form Kramer's doublets; the *E* component is manifested by shifting the energies of the various Kramer's doublets without further splitting. In even-electron systems, the *D* component also removes the microstate degeneracy by forming non-Kramer's doublets, however, in this case, the *E* component further splits the $+m_s$ and $-m_s$ components of the doublet. As the metallacrown structural analogy tends to form very axial ligand fields around the transition metals, the *E* component is negligible and will be disregarded for the remainder of the discussion.

In transition metals, spin-orbit coupling may be either first- or second-order depending on the symmetry of the ground state. For *3d* ions with orbital T states, a stronger first-order spin order coupling is operative, whereas those with E ground states are split by second-order spin-orbit coupling.[32] Isotropic ions (such as $Fe^{III}$) with A ground states have negligible spin-orbit coupling and zero-field splitting. The effect of the *D* parameter on ZFS is shown in Figure 1.4. When $D = 0$, the $m_s$ sublevels of the ground spin state are degenerate in energy. When $D < 0$, the largest $m_s$ state is lowest and energy; the opposite is true when $D > 0$.

For *4f* lanthanides, spin-orbit coupling is stronger than crystal field splitting. In atomic spectroscopy, the four models of coupling are Russell-Saunders coupling, *jj* coupling, Racah coupling and intermediate coupling.[39] For simplicity, the Russell-Saunders coupling approach is most commonly used to describe the energy levels of free lanthanide ions.[40] These energy levels are then further split by the crystal field. The cumulative effect of spin-orbit coupling and crystal-field splitting for a $Dy^{III}$ ion is shown in Figure 1.5.

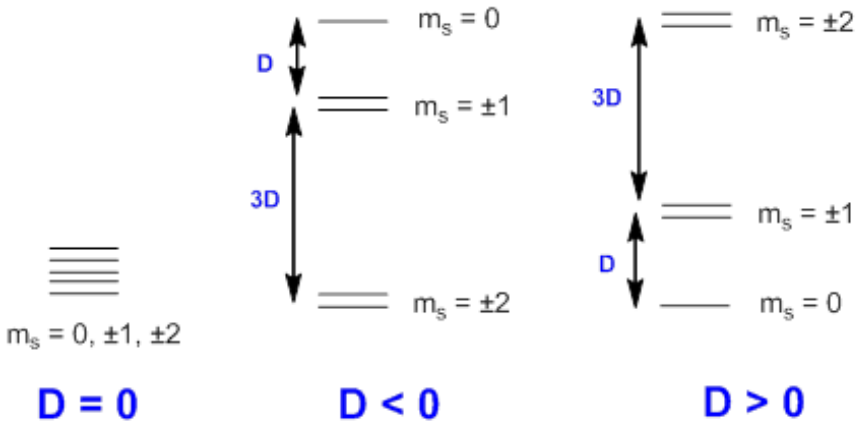


**Figure 1.4.** Depiction of the $m_s$ sublevels of the ground spin state of an S = 2 ion with $D = 0$ (paramagnetic), $D < 0$ and $D > 0$.

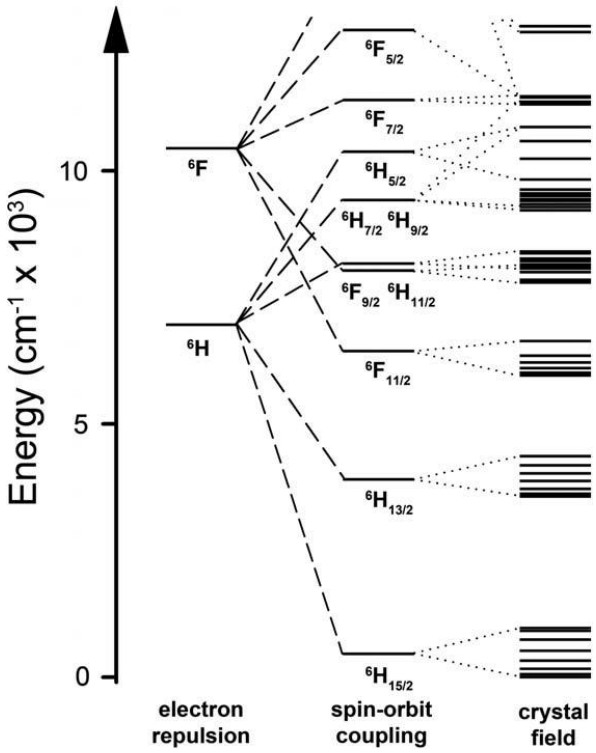


**Figure 1.5.** The low energy electronic structure for a $Dy^{III}$ ion. The nine *f*-electrons are first split by electron-electron repulsion, followed by spin-orbit coupling and finally, crystal field splitting. Reprinted with permission from reference 41. Copyright 2011 Royal Society of Chemistry.

***Magnetic Coupling***

In polynuclear systems, there is a magnetic interaction between neighboring metal atoms known as magnetic coupling, which is described as the parameter, *J*. The magnitude of *J* is usually on the order of 0-100 $cm^{-1}$, whereas covalent bond strengths are on the order of tens of thousands of wavenumbers. The coupling between two metal atoms can be ferromagnetic ($J > 0$), where the electron spins are aligned, or antiferromagnetic ($J < 0$), where the spins are oriented antiparallel. The sign and strength of the *J* coupling parameter is governed by the Goodenough-Kanamori rule of superexchange;[30-31] they are dependent on the overlap of the magnetic orbitals.[42] In the case of lanthanides, which have contracted *f*-orbitals,[43] magnetic coupling is generally very weak (< 1 $cm^{-1}$); these weak interactions play a role in both the properties of both SMM and MCE materials.

***Zeeman Effect***

The Zeeman effect describes the removal of the degeneracy of energies of electrons in an applied field.[44] For an $S = ½$ metal ion in an applied magnetic field, the energy of the $m_s = -½$ state is stabilized, whereas the energy of the $m_s = +½$ state is destabilized. The energy difference of the two $m_s$ states is

$$\Delta E = g\beta SH \tag{1.1}$$

Where *g* is the Landé factor, $\beta$ is the Bohr magneton, *S* is the spin state and *H* is the magnetic field. As will be described later, in magnetic susceptibility measurements, the applied field, *H* is small, and thus the Zeeman splitting will be weak (< 1 $cm^{-1}$). On the other hand, in magnetization experiments, *H* is large and Zeeman splitting will have a pronounced effect on the magnetic properties.

***Total Spin Hamiltonian***

The total spin Hamiltonian describing magnetic coupling ($J$), zero-field splitting ($D$ and $E$ terms) and the Zeeman effect of a dimer of spins, $S_1$ and $S_2$ is:

$$\hat{H} = -J_{12}\hat{S}_1\cdot\hat{S}_2 + D[\hat{S}_z^2 - S_T(S_T+1/3)] + E(\hat{S}_x^2-\hat{S}_y^2) + g\beta\hat{S}_uH_u \qquad (1.2)$$

where $J_{12}$ is the exchange parameter between $S_1$ and $S_2$; $\hat{S}_1$ and $\hat{S}_2$ are the spin operators corresponding to spins $S_1$ and $S_2$; $S_T$ is the total ground spin state; $\hat{S}_x$, $\hat{S}_y$, $\hat{S}_z$ and $\hat{S}_u$ are the spin operators corresponding to the directions $x$, $y$, $z$ and $u = x, y, z$; $H$ is the magnetic field along direction $u = x, y, z$. The splitting of the $m_s$ states in Equation 1.2 is visually depicted in Figure 1.6 for a $Cu^{II}$-$Cu^{II}$ dimer, where each $Cu^{II}$ has $S = ½$. The population of the $m_s$ states is temperature-dependent and follows Boltzmann statistics. Values for $J$, $D$ and $E$ and $g$ can be obtained by fitting the magnetic susceptibility data by incorporating the eigenvalues of Equation 1.2 into a modified van Vleck equation (Equation 1.8, described in the next section) or by use of programs such as *MAGPACK*,[45] which utilizes matrix-diagonalization routines.

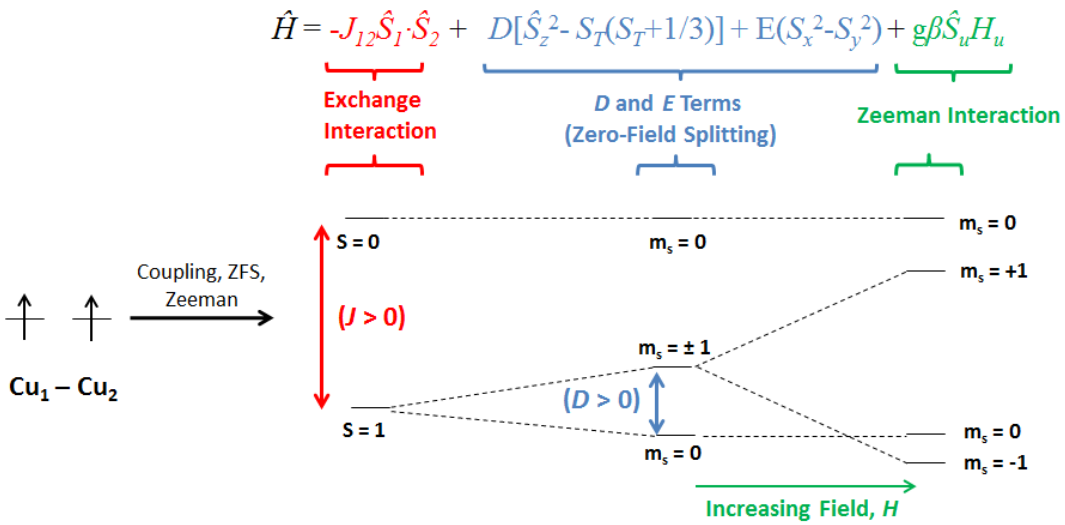


**Figure 1.6.** Heuristic depiction of the magnetic states of a $Cu^{II}$-$Cu^{II}$ dimer system, where $S_1 = S_2 = ½$. The two spins are first exchange coupled, with $J > 0$ (ferromagnetic). Zero-field splitting then splits the $S$ states, with $D > 0$ and $E = 0$. Finally the Zeeman effect in the presence of a magnetic field further splits the $m_s$ states.

It is easy to see that the complexity of the spin states will drastically increase for larger polynuclear systems with larger *S*. For certain symetric polynuclear systems, the energy levels of the spin states may be evaluated using the Kambe coupling scheme.[46] Furthermore, the fitting of the magnetic susceptibility data can be simplified by the use of isotropic metal ions such as $Fe^{III}$ and $Gd^{III}$, whose negligible anisotropy makes it possible to neglect the *D* and *E* terms.

***Magnetic Measurements and Data Analysis***

The current state-of-the-art in magnetometry is the Superconducting Quantum Interference Device (SQUID). This instrument can measure the magnetic moment of a powdered sample down to 2 K. By varying experimental parameters, one can obtain valuable information on the magnetic properties of a material.

Magnetization experiments are the isothermal application of an external field. The molar magnetization is the Boltzmann average of the magnetic moments:[42]

$$M = N_{\mathrm{A}} \frac{\sum_n (-\partial E_n/\partial H) e^{-E_n/k_B T}}{\sum_n e^{-E_n/k_B T}} \tag{1.3}$$

where $M$ is the magnetization, $N_{\mathrm{A}}$ is Avogadro's number, $E_n$ is the energy of quantum state $|n\rangle$, $H$ = magnetic field, $k_B$ is the Boltzmann constant ($1.380658 \times 10^{-23}$ J $K^{-1}$ or 0.69503877 $cm^{-1}$). Equation 1.3 is considered the fundamental equation of molecular magnetism, as it does not rely on any approximations.[29] Use of this expression requires knowledge of how $E_n$ changes with applied field, $H$ for all thermally populated states. To simplify the use of this equation, many of the equations described below are derived from Equation 1.3 based on various assumptions and approximations.[29]

For single-spin, paramagnetic compounds with no zero-field splitting, Equation 1.3 can be approximated as the Brillouin function:[29]

$$M = N_A g\beta S B_S(x) \tag{1.4}$$

$$B_S(x) = \frac{2S+1}{2S}\coth\left(\frac{2S+1}{2S}x\right) - \frac{1}{2S}\coth\left(\frac{x}{2}\right) \tag{1.5}$$

where $g$ is the Landé factor, $\beta$ is the Bohr magneton, $S$ is the spin state and $B_S(x)$ is the Brillouin function where $x = \frac{g\beta SH}{k_B T}$. Simple paramagnetic compounds can be fit with Equations 1.4 and 1.5 to determine the ground $S$ state. For molecules with complex and non-negligible coupling, these equations cannot be used. However, at high magnetic fields and low temperatures, the magnetization can be simplified to:[34]

$$M = N_A g\beta S \tag{1.6}$$

which corresponds to magnetic saturation (where the magnetization has flat lined). This equation can be used in magnetization experiments at low temperature and high fields, and can be used to determine the ground $S$ state for molecular complexes.

In dc susceptibility measurements, a small magnetic field is applied (usually 1000 or 2000 Oe) and the temperature is varied. At low magnetic field and high temperatures, the magnetic properties can be described by the simplified van Vleck equation:[34]

$$\chi_m = \frac{N_A g^2 \beta^2}{3k_B T} S(S+1) \tag{1.7}$$

In general, Equation 1.7 can be used to describe the dc susceptibility data for well isolated single-spin paramagnets or for polynuclear complexes at high temperatures.

Through the use of perturbation theory, van Vleck was able to derive a more precise approximation for the molar magnetic susceptibility:[29, 34]

$$\chi_m = \frac{N_A g^2 \beta^2}{3k_B T} \frac{\sum_S S(S+1)(2S+1)e^{-E_S/k_B T}}{\sum_S (2S+1)e^{-E_S/k_B T}} \tag{1.8}$$

where $E_S$ is the energy of spin state, $S$. For certain symmetrical compounds, $E_S$ can be obtained from the spin Hamiltonian (Equation 1.2) using the Kambe method[46] as a function of the coupling parameter(s), $J$; the ZFS parameters $D$ and $E$; and the Landé factor, $g$. It is important to note that the susceptibility is usually plotted as $\chi_m$T vs T, as it can visually give more information about the magnetic interactions.[42]

In general, magnetization measurements are at the low temperature, high field limit, which may allow for the evaluation of ground spin states for strongly coupled, low anisotropy polynuclear complexes. Susceptibility measurements are performed at low magnetic fields and can more accurately be used to determine the magnetic exchange parameter $J$.

**1.4 Superparamagnetism in Single-Molecule Magnets and Single-Ion Magnets**

Elemental iron and nickel are two metals which can display permanent ferromagnetic behavior.[47] In these metallic 3d network solids, magnetic domains are formed in order to minimize magnetic energy. Individual magnetic domains are separated by Bloch walls, whose thickness is dependent on the exchange coupling constants and magnetic anisotropy.[48] In the lowest energetic state, different magnetic domains are oriented in every direction, such that the material behaves as a paramagnet. When a large enough field is applied to magnetize the domains to point in the same direction, they remain locked in place even after the field is removed due to defects in the structure which causes domain wall pinning.[49]

It was found that when the particle size of Ni and Fe was shrunk to small enough sizes, single-domain magnetic behavior was observed.[26] These single-domain magnetic particles exhibit superparamagnetic behavior, where there is an energy barrier between the two lowest energy directions of magnetization, which leads to slow relaxation of the magnetization.[32] In 1993, a single-domain molecular compound, $Mn_{12}$(OAc), was reported by Sessoli and

coworkers.[50-51] This led to the emergence of the field of single-molecule magnets (SMMs). At low temperatures, these molecules retain their magnetization due to an energy barrier separating the two directions of their Ising type ground states. Due to their small size, SMMs are potentially useful in magnetic data storage, with storage densities up to 200,000 Gbits/in$^2$ for a molecule that is 1-2 nm in diameter.[52] Furthermore, due to the quantum effects that are prevalent in these molecules, another potential application is quantum computing.[53-54] The major issues regarding the use of SMMs are (1) increasing the energy barrier, (2) eliminating quantum tunneling which leads to demagnetization and (3) achieving large coercive fields at high temperatures in the magnetic hysteresis experiments.

$Mn^{III}_8Mn^{IV}_4O_{12}(O_2C_2H_3)_{16}(H_2O)_4$, commonly called $Mn_{12}$(OAc) was first synthesized by Lis in 1980 (Figure 1.7).[55] In this molecule, the eight $Mn^{III}$ were ferromagnetically coupled to each other and antiferromagnetically coupled to the four ferromagnetically coupled $Mn^{IV}$ ions to give a ground spin state of $S$ = 10.[56] The single-ion magnetic anisotropy of each $Mn^{III/IV}$ combines to give an axial zero-field splitting parameter, $D$ = -0.50 cm$^{-1}$, giving rise to the splitting in the ground spin state seen in Figure 1.7.[56] The barrier between the $+M_s$ and $-M_s$ ground sublevels is related to the ground spin state, $S$, and the parameter $D$:

$$U_{eff} = S^2|D| \text{ (integer spin)} \quad (1.9)$$

$$U_{eff} = (S^2\text{-}1/4)|D| \text{ (half-integer spin)} \quad (1.10)$$

For SMM behavior, $D$ must be negative in order for the largest $M_s$ sublevel to be the lowest energy. For $Mn_{12}$(OAc), the theoretical energy barrier is thus: $U_{eff} = 10^2|\text{-}0.5 \text{ cm}^{-1}| = 50 \text{ cm}^{-1}$. It is clear from Equations 1.9 and 1.10 that $S$ and $D$ must be large in order to get a large barrier height.

It was found that $Mn_{12}$(OAc) displayed maxima in the out-of-phase ac susceptibility

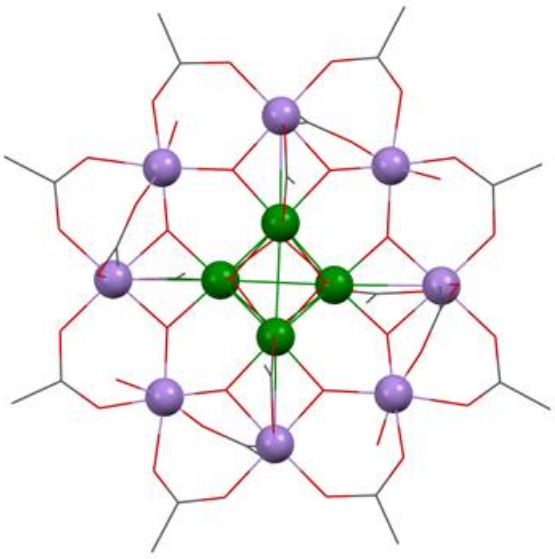

**Figure 1.7.** Crystal structure of $Mn^{III}_8Mn^{IV}_4O_{12}(O_2C_2H_3)_{16}(H_2O)_4$. Color scheme: purple spheres – $Mn^{III}$, green spheres – $Mn^{IV}$. This figure was reproduced from a crystal structure from reference 55.

(explained in the next section), to yield an experimental barrier of 42 $cm^{-1}$.[52] The experimentally determined energy barrier does not quite reach the theoretical limit (50 $cm^{-1}$) due to quantum tunneling of the magnetization (QTM). This phenomenon is a common occurrence in SMMs and is due to the superposition of the two $M_s$ states that are of degenerate energy (Figure 1.8).[57-58] QTM may be reduced upon application of a magnetic field, which removes the degeneracy of spin sublevels (Figure 1.9). For a more thorough mathematical description of tunneling, the reader is referred to several references.[32, 57-59] Common strategies to reduce quantum tunneling include limiting rhombic anisotropy[52] and increasing the strength of magnetic coupling.[60-62]

For *4f* lanthanide-based SMMs, the magnetic anisotropy comes from the crystal-field splitting of the ground *J* state. The spin-orbit coupling in lanthanides is very strong relative to the strength of their magnetic interactions, whereas the opposite is true for *3d* transition metals. Hence, lanthanides are at the *weak exchange* limit.[63] Nevertheless, the design principles involved in lanthanide-based SMMs are similar to transition metals. For all SMMs, strong ferromagnetic

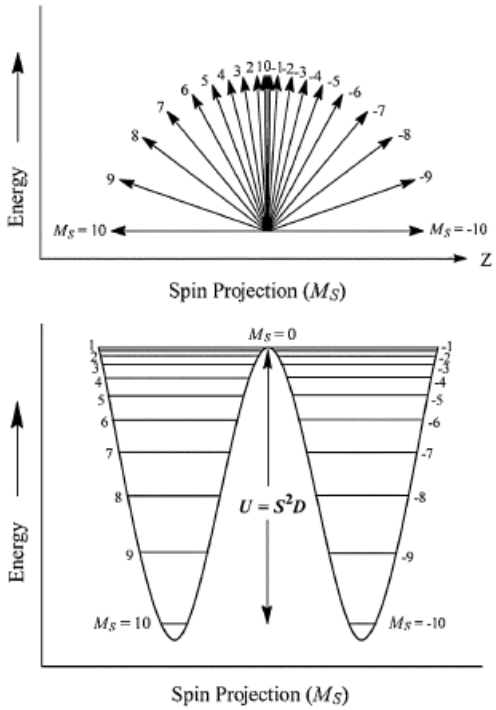


**Figure 1.8.** (top) The allowed quantized $M_s$ states of the spin vector of $Mn_{12}(OAc)$. (bottom) The 'spin double-well' for $Mn_{12}(OAc)$ depicting the relative energies of each $M_s$ sublevel of the ground $S$ =10 spin state as a function of the axial zero-field splitting parameter, $D$. Reprinted with permission from reference 64. Copyright 2009 Royal Society of Chemistry.

interactions are preferred and the ligand field around the metal ions should be very axial in order to limit QTM. Related to SMMs are single-ion magnets (SIMs), whose slow magnetic relaxation is derived from a single-magnetic center; and single-chain magnets (SCMs), where slow magnetic relaxation comes from strong magnetic coupling in a *1D* chain of magnetic centers.

***Characterization of SMMs***

Alternating Current (ac) magnetic susceptibility is the main characterization technique used to study the dynamic magnetic properties of SMMs. In this experiment, a small (~3 Oe) oscillating magnetic field is applied on the sample. In this experiment, the susceptibility, $\chi$, is related to the in-phase ("real") ac susceptibility, $\chi'$, and the out-of-phase ("imaginary") ac susceptibility, $\chi''$ by Equation 1.11.

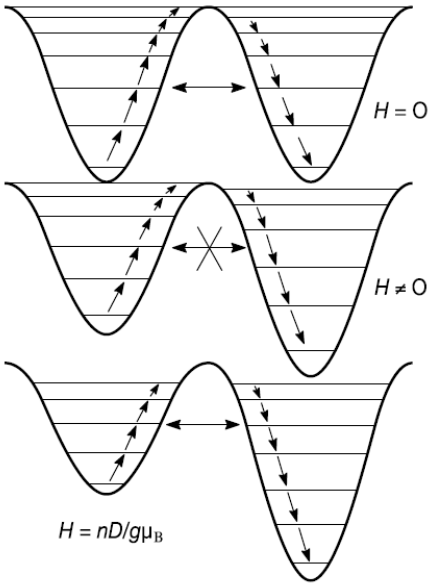


**Figure 1.9.** The 'spin double-well' under various applied fields. At $H = 0$, QTM occurs between $M_s$ levels of degenerate energy. At $H \neq 0$, QTM is quenched. Finally, at certain magnetic field strengths, resonant magnetization tunneling occurs when the $M_s$ levels are aligned. Reprinted with permission from reference 56. Copyright 2000 Materials Research Society.

$$\chi = \chi' + i\chi'' \tag{1.11}$$

For paramagnetic materials, the magnetic moment of sample follows the oscillating magnetic field. However, in superparamagnetic materials such as SMMs, at low enough temperatures and high enough frequencies, the magnetic moment of the sample lags behind the ac drive field, which is measured as the phase shift, φ. The in-phase and out-of-phase susceptibilities are related to the phase shift by the following:[65]

$$\chi' = \chi\cos\varphi \tag{1.12}$$

$$\chi'' = \chi\sin\varphi \tag{1.13}$$

A more detailed explanation of the theory can be read in references 66 and 67.

The presence of an out-of-phase, χ" signal is a strong indicator of superparamagnetic behavior. When the frequency of the ac drive field matches the frequency of the magnetic relaxation, a maximum occurs in the χ" vs T plot. The energy barrier, $U_{eff}$, of an SMM follows an

Arrhenius relationship:

$$\tau = \tau_0 e^{(U_{eff}/k_B T)} \tag{1.14}$$

where τ is the relaxation time (inverse frequency) and $\tau_0$ is a preexponential factor.[52] Thus, a plot of ln τ vs 1/T should be linear; fitting the slope and intercept would give values for $U_{eff}$ and $\tau_0$. It should be noted that for many SMMs, QTM is prevalent at low temperatures; therefore, the barrier is often extracted from the high temperature regime. Figure 1.10 shows the plot of χ" vs. T for $Mn_{12}$(OAc), by fitting the data to Equation 1.14, an experimental energy of 42 $cm^{-1}$ was observed.

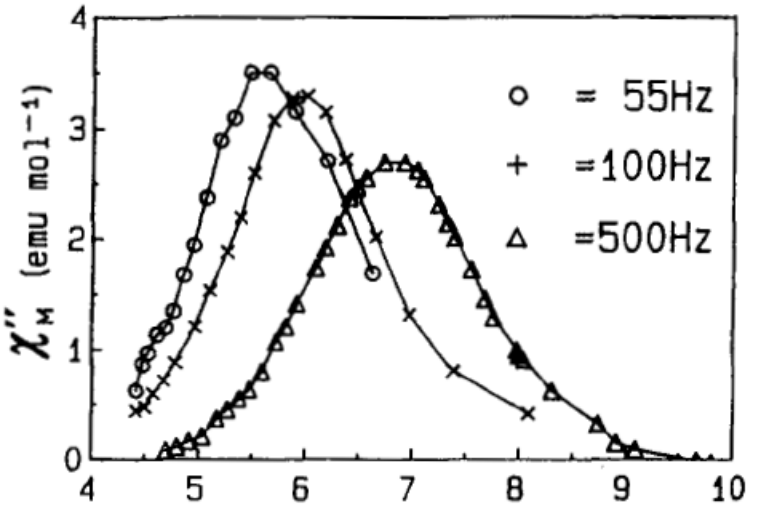


**Figure 1.10.** The out-of-phase ac magnetic susceptibility for $Mn^{III}_8Mn^{IV}_4O_{12}(O_2C_2H_3)_{16}(H_2O)_4$. Reprinted with permission from reference 52. Copyright 1993 American Chemical Society.

In 1941, Cole and Cole described a relaxation model for dielectrics;[68] later, Mydosh and coworkers applied this theory to the relaxation of magnetic complexes.[69] The in-phase and out-of-phase ac susceptibility can be fit simultaneously with a generalized Debye model:[70-71]

$$\chi'(\nu_{ac}) = \chi_S + \frac{(\chi_T - \chi_S)[1+(2\pi\nu_{ac}\tau)^{1-\alpha}\sin\left(\frac{\alpha\pi}{2}\right)]}{1+2(2\pi\nu_{ac}\tau)^{1-\alpha}\sin\left(\frac{\alpha\pi}{2}\right)+(2\pi\nu_{ac}\tau)^{2(1-\alpha)}} \tag{1.15}$$

and

$$\chi''(\nu_{ac}) = \frac{(\chi_T - \chi_S)[1+(2\pi\nu_{ac}\tau)^{1-\alpha}\cos\left(\frac{\alpha\pi}{2}\right)]}{1+2(2\pi\nu_{ac}\tau)^{1-\alpha}\sin\left(\frac{\alpha\pi}{2}\right)+(2\pi\nu_{ac}\tau)^{2(1-\alpha)}} \quad (1.16)$$

where $\chi_s$ is the adiabatic susceptibility, $\chi_T$ is the isothermal susceptibility, $\nu_{ac}$ is the ac frequency, $\tau$ is the magnetization relaxation time, and $\alpha$ is a value between 0 and 1 which is a measure of the distribution of relaxation processes. When $\alpha$ is zero, then there is a single relaxation process (Debye process).[72] When there are multiple relaxation processes, $\alpha$ becomes larger.

A plot of $\chi''$ vs $\chi'$ is known as a Cole-Cole or Argand plot and forms a semi-circular shape. Figure 1.11 shows a Cole-Cole plot for the molecule $(PPh_4)[Mn_{12}O_{12}(O_2CEt)_{16}(H_2O)_4]$, an analogue of $Mn_{12}(OAc)$.[71] When there is a distribution of single-relaxation processes ($\alpha > 0$), the semicircle becomes flattened. Furthermore, complex systems with more than one relaxation process with largely different relaxation times ($\tau$), multiple semi-circles may be present in the Argand plot.[72]

Another important characterization technique is measurement of magnetic hysteresis. In these experiments a magnetic field is applied in one direction to a magnetic sample. The field is increased along this direction and the magnetization of the sample will increase with the field

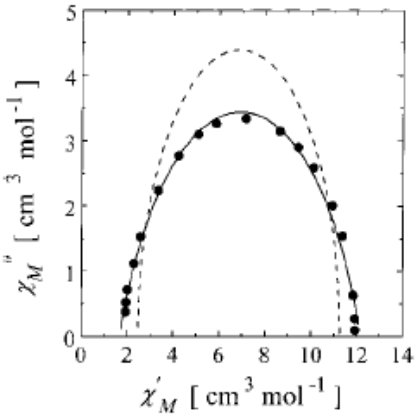


**Figure 1.11.** Cole-Cole plot for $(PPh_4)[Mn_{12}O_{12}(O_2CEt)_{16}(H_2O)_4]$. The solid line represents a least-squares fit of the data to the generalized Debye model. The dotted line represents a fit of the data to a single relaxation process. Reprinted with permission from reference 71. Copyright 1999 American Chemical Society.

until it reaches saturation. After it reaches this point, the magnetic field is reversed and swept in the opposite direction. At low enough temperatures, SMMs, which have large enough energy barriers will resist the change in magnetic field and an opening of the hysteresis loop will occur. Paramagnetic materials, however, will not display hysteretic behavior.

These hysteresis experiments may be performed on a powdered sample in a SQUID magnetometer, or more elegantly on a single crystal using a micro-SQUID.[73] Micro-SQUID analysis is useful because it allows for independent measurement of the magnetic properties along the easy-axis and hard plane of anisotropy. A molecule showing true SMM behavior would display hysteresis only along the easy-axis of magnetization.[32]

***Important SMMs***

Many SMMs have been investigated since the report of the first SMM, $Mn_{12}(OAc)$. For an extensive overview of the field, the reader is referred to several reviews.[74-79] Here, I discuss some recent advances in the SMM literature.

*$[[[(Me_3Si)_2N_2Ln(THF)]_2(\mu\text{-}\eta^2\text{:}\eta^2\text{-}N_2)]^-$*

In 2011, Long and coworkers reported a family of $N_2^{3-}$ radical bridged $[[[(Me_3Si)_2N_2Ln(THF)]_2(\mu\text{-}\eta^2\text{:}\eta^2\text{-}N_2)]^-$ complexes (Ln = Gd, Dy, Tb, Ho and Er) which exhibited high temperature magnetic hysteresis behavior (Figure 1.12).[60-61] The radical character of the $N_2^{3-}$ bridging ligand led to large Ln-Ln magnetic coupling. In the $[[[(Me_3Si)_2N_2Gd(THF)]_2(\mu\text{-}\eta^2\text{:}\eta^2\text{-}N_2)]^-$ complex, the Gd-Gd exchange coupling was determined to be -27 $cm^{-1}$, which is the largest found in lanthanide containing complexes.[61] Both the Dy and Tb derivatives were observed to display strong magnetic coupling. The Dy complex exhibited a barrier of 123 $cm^{-1}$ and displayed hysteresis behavior at temperatures up to 8 K. For the Tb derivative, the energy barrier was determined to be 227 $cm^{-1}$ and exhibited magnetic hysteresis at a record temperature

of 14 K (Figure 1.13). This remarkable behavior is thought to be the consequence of the quenching of quantum tunneling due to strong Ln-Ln magnetic interactions.

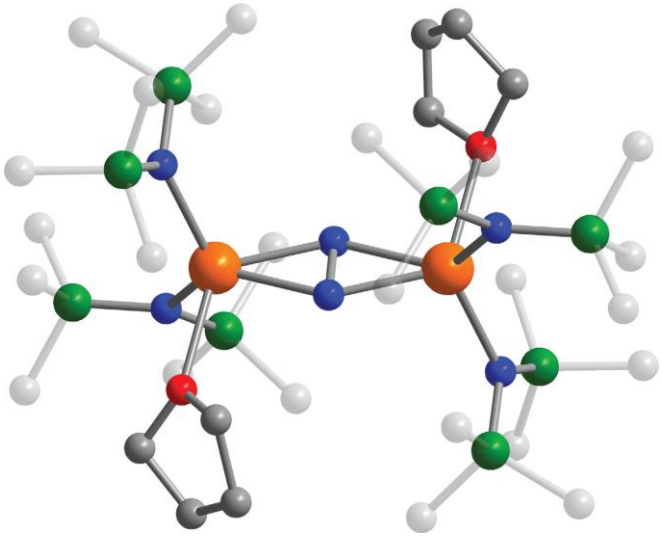

**Figure 1.12.** Structure of $[[[(Me_3Si)_2N_2Gd(THF)]_2(\mu\text{-}\eta^2\text{:}\eta^2\text{-}N_2)]^-$. Color scheme: orange spheres – Gd, green spheres – Si, blue spheres – N, red spheres – O, gray spheres – C. Reprinted with permission from reference 61. Copyright 2011 Nature Publishing Group.

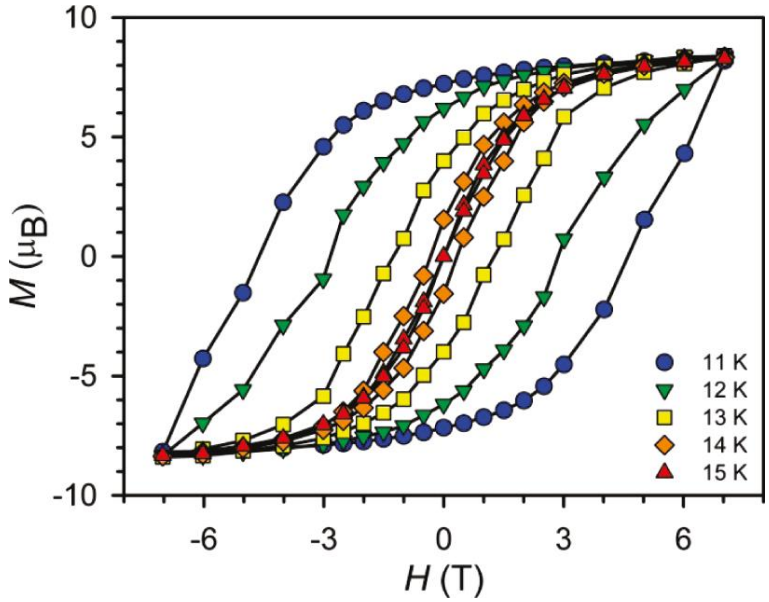


**Figure 1.13.** Magnetic hysteresis plot for $[[[(Me_3Si)_2N_2Tb(THF)]_2(\mu\text{-}\eta^2\text{:}\eta^2\text{-}N_2)]^-$ at a sweep rate of 0.9 T/s. Reprinted with permission from reference 60. Copyright 2011 American Chemical Society.

*$[Fe^{II}_2Dy^{III}(L)_2(H_2O)]ClO_4{\cdot}2H_2O$*

Recently, Liu and coworkers synthesized a $[Fe_2Dy(L)_2(H_2O)]ClO_4{\cdot}2H_2O$ [L = 2,2',2''-(((nitrilotris(ethane-2,1-diyl))tris(azanediyl))tris(methylene))tris(4-chlorophenol)] complex (Figure 1.14), which exhibits an energy barrier of 319 $cm^{-1}$ (Figure 1.15), which is the largest observed for a *3d-4f* complex.[80] It was found through magnetic measurements and DFT calculations that the $Fe^{II}$-$Dy^{III}$-$Fe^{II}$ system was ferromagnetically coupled. Analysis through Mössbauer spectroscopy showed that at low temperatures, the frozen magnetic moment of the $Dy^{III}$ ion slowed down the individual moments of the $Fe^{II}$ ions.

In comparison, an analogous $[Zn^{II}_2Dy^{III}_2(L)_2(MeOH)]NO_3{\cdot}3MeOH{\cdot}H_2O$ [(L = 2,2',2''-(((nitrilotris(ethane-2,1-diyl))tris(azanediyl))tris(methylene))tris-(4-bromophenol)] complex exhibited an energy barrier of 305 $cm^{-1}$.[81] The larger barrier for the $Fe^{II}$ derivative over the $Zn^{II}$ derivatives was attributed to a stronger axial ligand field around the $Dy^{III}$ for the former.[80]

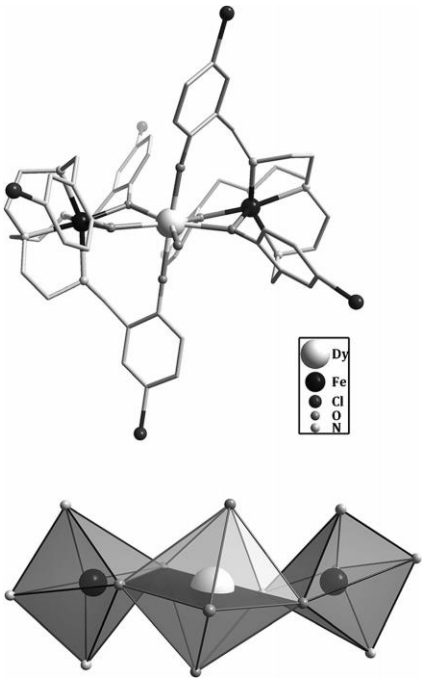


**Figure 1.14.** Structure of the $[Fe_2Dy(L)_2(H_2O)]ClO_4{\cdot}2H_2O$ complex (top) and the structural motif of the $Fe^{II}$-$Dy^{III}$-$Fe^{II}$ cores (bottom). Reprinted with permission from reference 80. Copyright 2014 Wiley-VCH Verlag GmbH & Co. KGaA.

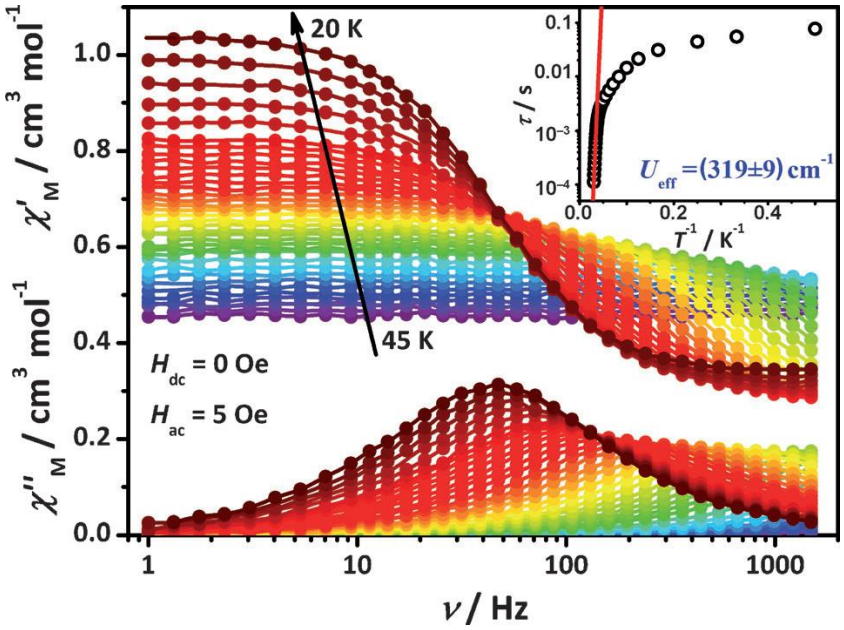


**Figure 1.15.** Plot of the ac magnetic susceptibility of $[Fe_2Dy(L)_2(H_2O)]ClO_4 \cdot 2H_2O$. Inset: Arrhenius plot of the ac data. The linear fit at the high temperature region corresponds to a barrier of 319 $cm^{-1}$. Reprinted with permission from reference 80. Copyright 2014 Wiley-VCH Verlag GmbH & Co. KGaA.

***Metallacrown SMMs***

*$Ln^{III}_6Mn^{III}_4Mn^{IV}_2$*

The field of SMMs was heavily influenced by manganese chemistry as the first SMM is a $Mn_{12}OAc$ complex described previously, and metallacrown chemistry has a long history of using manganese to form MCs.[8] The first MC-based SMM was reported by Zaleski and coworkers and had the formula $Dy^{III}_6Mn^{III}_4Mn^{IV}_2(H_2shi)_4(Hshi)_2(shi)_{10}(CH_3OH)_{10}(H_2O)_2$ (Figure 1.16).[82] This complex was the first *3d-4f* SMM with manganese, and just the second overall *3d-4f* SMM. Of the three different $Ln^{III}$ versions of this molecule reported, only the $Dy^{III}_6Mn^{III}_4Mn^{IV}_2(H_2shi)_4(Hshi)_2(shi)_{10}(CH_3OH)_{10}(H_2O)_2$ molecule possessed SMM behavior near 4 K; however, the blocking temperatures is below 2 K (Figure 1.17). Thus, the source of the SMM behavior is not totally reliant on the manganese ions, but the identity of the lanthanide ion is critical.

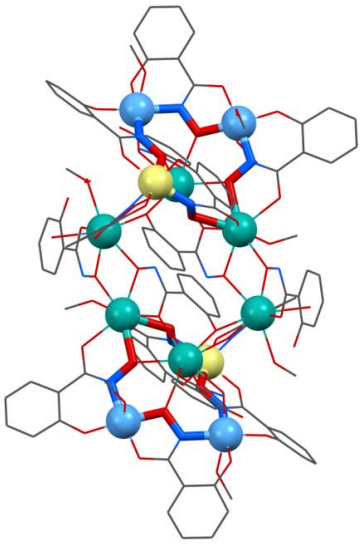

**Figure 1.16.** Single-crystal X-ray structure of $Dy^{III}_6Mn^{III}_4Mn^{IV}_2(H_2shi)_4(Hshi)_2(shi)_{10}(CH_3OH)_{10}(H_2O)_2$ with Dy(12-$MC_{Mn^{III}_2Mn^{IV}Dy^{III}}$-4) units highlighted in bold. Color scheme: green spheres – $Dy^{III}$, blue spheres – $Mn^{III}$, and gold spheres – $Mn^{IV}$. Reprinted with permission from reference 82. Copyright 2004 Wiley-VCH Verlag GmbH & Co. KGaA.

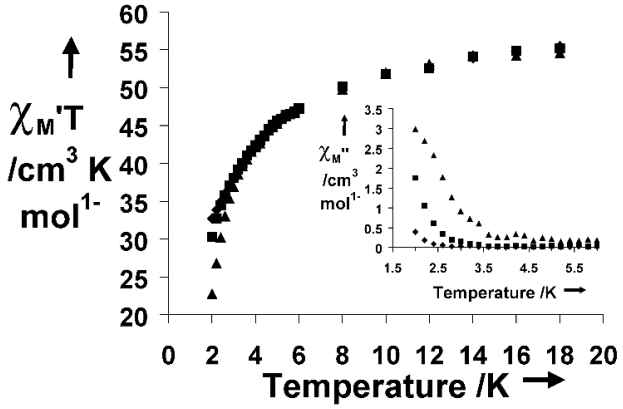


**Figure 1.17.** In-phase magnetic susceptibility of $Dy^{III}_6Mn^{III}_4Mn^{IV}_2(H_2shi)_4(Hshi)_2(shi)_{10}(CH_3OH)_{10}(H_2O)_2$. Inset: Out-of-phase magnetic susceptibility. (▲1000 Hz, ■100 Hz, ♦10 Hz). Reprinted with permission from reference 82. Copyright 2004 Wiley-VCH Verlag GmbH & Co. KGaA.

*$Ln^{III}_4Mn^{III}_6$*

Figure 1.18 shows $Ln^{III}_4Mn^{III}_6(H_2shi)_2(shi)_6(sal)_2(OAc)_4(OH)_2(CH_3OH)_8$ ($Ln^{III}$ = $Dy^{III}$ and $Ho^{III}$) molecules that were also observed to display SMM behavior.[83] In the solid phase, both the $Ho^{III}$ and $Dy^{III}$ analogues displayed a frequency-dependent out-of-phase magnetic

susceptibility signal near 4 K; however, the blocking temperatures are below 2 K and the signal of the $Ho^{III}$ version is much weaker than that of the $Dy^{III}$ version. To investigate the behavior of these molecules further, frozen solutions of both molecules were prepared in DMF. For the frozen solutions, the $Ho^{III}$ analogue no longer possessed a frequency-dependent out-of-phase signal, while for the frozen $Dy^{III}$ analogue, the frequency-dependent out-of-phase magnetic susceptibility signal remained and in fact the blocking temperature at 1000 Hz is above 2 K (Figure 1.19). In the solid state, the blocking temperature of the $Dy^{III}$ analogue could not be observed; however, by isolating the molecule in solution, the molecular magnetic behavior can be observed without complications from intermolecular interactions. For the $Ho^{III}$ analogue it is suspected that a hydrogen-bonding network may mediate short-range magnetic ordering or glassy behavior and give rise to the solid-state results. For the $Dy^{III}$ analogue a similar network likely complicates the magnetic measurements and partially masks the SMM behavior. For the $Dy^{III}$ analogue, the effective energy barrier for the reorientation of the magnetization is 11 $cm^{-1}$, and the magnetic relaxation time is estimated to be 26 s at 1 K.

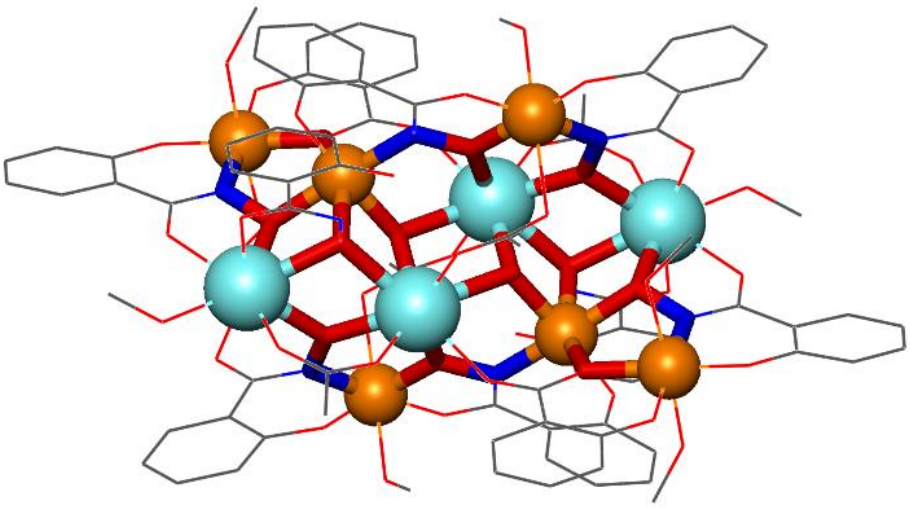

**Figure 1.18.** Single-crystal X-ray structure of $Ho^{III}_4Mn^{III}_6(H_2shi)_2(shi)_6(sal)_2(OAc)_4(OH)_2(CH_3OH)_8$. Color scheme: blue spheres – $Ho^{III}$, orange spheres – $Mn^{III}$, red tube – oxygen, and blue tubes - nitrogen. The figure is reproduced from a crystal structure in reference 83.

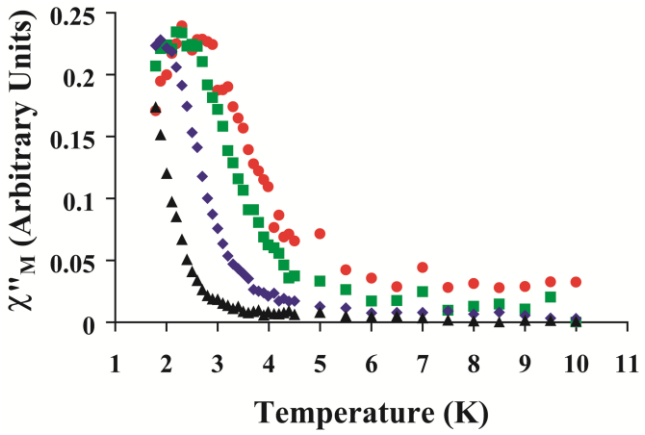


**Figure 1.19.** Out-of-phase magnetic susceptibility of a frozen DMF solution of $Dy^{III}_4Mn^{III}_6(H_2shi)_2(shi)_6(sal)_2(OAc)_4(OH)_2(CH_3OH)_8$. (●1000 Hz, ■500 Hz, ♦100 Hz, ▲10 Hz). Reprinted with permission from reference 83. Copyright 2007 American Chemical Society.

*$Ln^{III}(O_2CCH_3)(NO_3)_2[14\text{-}MC_{Mn^{III}Ln^{III}(\mu_3\text{-}O)(\mu\text{-}OH)N(shi)}\text{-}5]$*

Planar $Ln^{III}(O_2CCH_3)(NO_3)_2[14\text{-}MC_{Mn^{III}Ln^{III}(\mu_3\text{-}O)(\mu\text{-}OH)N(shi)}\text{-}5]$ complexes, where $Ln^{III}$= $Y^{III}$, $Gd^{III}$, $Tb^{III}$, $Dy^{III}$, and $Ho^{III}$) were reported in 2010 by Boron and coworkers (Figure 1.20).[14] This planar arrangement provides a pathway to potentially greater magnetoanisotropy. The $Tb^{III}$, $Dy^{III}$, and $Ho^{III}$ versions of this molecule displayed a frequency dependent out-of-phase magnetic susceptibility signal (Figure 1.21). For the $Dy^{III}$ analogue, a blocking temperature is observed above 2 K, and the effective energy barrier for the reorientation of the magnetization was determined to be 16.7 K. For the $Tb^{III}$ and $Ho^{III}$ versions the blocking temperature is below 2 K.

Magnetic Compton scattering (MCP) was used to investigate the $Y^{III}$, $Gd^{III}$, and $Dy^{III}$ analogues.[84] In the $Y^{III}$ derivative, the magnetic moment is mainly due to the spin angular momentum and there is only a small orbital angular momentum contribution, indicating that the total molecular anisotropy is small. This implies that even though the $Mn^{III}$ are in the same plane, the Ising-type anisotropy is not additive in this case. In the $Gd^{III}$ and $Dy^{III}$ complexes the spin of the central lanthanide ion was determined to be aligned parallel to the spin of the $Mn^{III}$

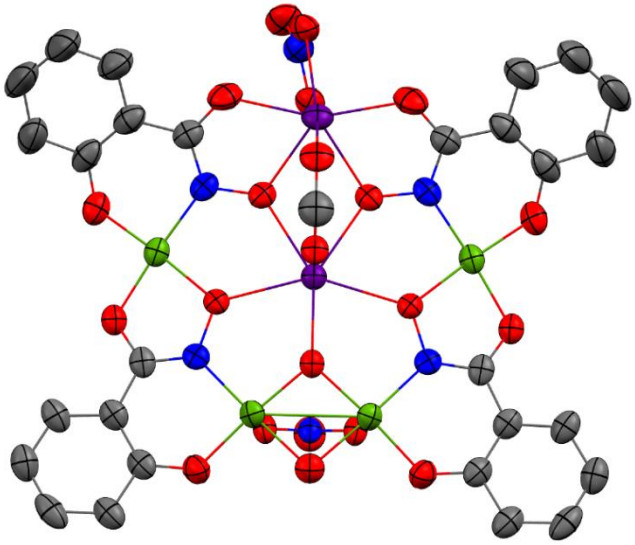

**Figure 1.20.** Single-crystal X-ray structure of $Dy^{III}(OAc)_2(NO_3)_2$[14-$MC_{Mn^{III}Ln^{III}(\mu_3\text{-}O)(\mu\text{-}OH)N(shi)}$-5] with the thermal ellipsoid plot at 50% probability. Color scheme: purple – $Dy^{III}$, green – $Mn^{III}$, red – oxygen, blue – nitrogen, gray – carbon. The figure was produced from a crystal structure in reference 14.

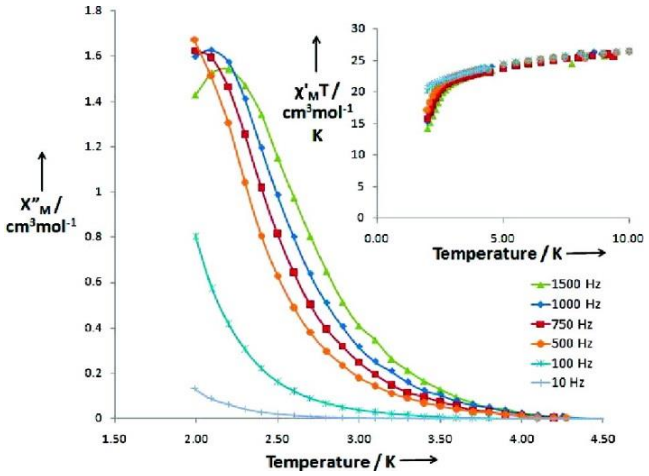


**Figure 1.21.** Out-of-phase magnetic susceptibility signal of $Dy^{III}(O_2CCH_3)(NO_3)_2$[14-$MC_{Mn^{III}Ln^{III}(\mu_3\text{-}O)(\mu\text{-}OH)N(shi)}$-5]. Inset: In-phase magnetic susceptibility signal. Reprinted with permission from reference 14. Copyright 2010 American Chemical Society.

ions. However, for the $Gd^{III}$ molecule again there is little to no orbital angular momentum contribution to the overall magnetic moment of the complex and a SMM is not produced. In the $Dy^{III}$ complex, the total magnetic moment is larger than the spin-only moment due to significant orbital angular momentum contributions by the $Dy^{III}$ ions to the total magnetic moment, which

likely gives rise to the SMM behavior in this complex. The MCP experiments again illustrate that the nature of the $Ln^{III}$ is crucial to the observed magnetic properties.

*$Ln^{III}(NO_3)_3$[15-$MC_{Cu^{II}N(S\text{-}pheHA)}$-5]*

In 2006, Zaleski and coworkers investigated the magnetic properties of a dimer and helical polymorph of $Ln^{III}(NO_3)_{3-x}(OH)_x$[15-$MC_{Cu^{II}N(S\text{-}pheHA)}$-5], where $Ln^{III}$ = $Dy^{III}$, $Ho^{III}$ amd $H_2S$-pheHA = phenylalanine hydroxamic acid (Figure 1.22).[85-86] The ground spin states for these molecules could not be determined, likely due to magnetic field-induced level crossing and/or population of low-lying excited states and the highly magnetoanisotropic $Ln^{III}$ ions. In the solid state, both the dimer and helical versions of the $Dy^{III}$ and $Ho^{III}$ MCs displayed a frequency-dependent out-of-phase magnetic susceptibility signal below 5 K. To understand the source of the out-of-phase magnetic behavior better, the compounds were dissolved in methanol and the out-of-phase magnetic susceptibility was recorded for the frozen solutions. In this case, the frequency dependent out-of-phase behavior only remained for the $Dy^{III}$ dimer and helical versions below 5 K; however, the blocking temperatures are below 2 K (Figure 1.23). This suggests that the $Dy^{III}$ analogues are SMMs in the solid state since glassy behavior and magnetic ordering cannot persist in the solution state where the molecules are isolated from each other.

It is not believed that the helical $Dy^{III}$ polymorph is an example of a SCM, but is better described as a chain of SMMs. The nature of the polymorph does not appear to affect the SMM properties of the molecules, as the ac magnetic susceptibility of both the dimer and helical polymorphs is similar down to 2 K. The onset temperature of the frequency-dependent behavior is nearly the same for the two polymorphs, and the magnitude of the out-of-phase signal is similar for all frequencies at 2 K. Thus, the helix may be described as a chain of SMMs, and the SMM behavior is a result of the identity of the lanthanide ion and not the polymorph. Lastly,

these $Dy^{III}(NO_3)_{3-x}(OH)_x$[15-$MC_{Cu^{II}N(S\text{-}pheHA)}$-5] molecules also serve as examples of chiral SMMs; however, the molecules do not display magnetochiral effects above 2 K, which is not surprising since the blocking temperatures of the molecules are below 2 K.

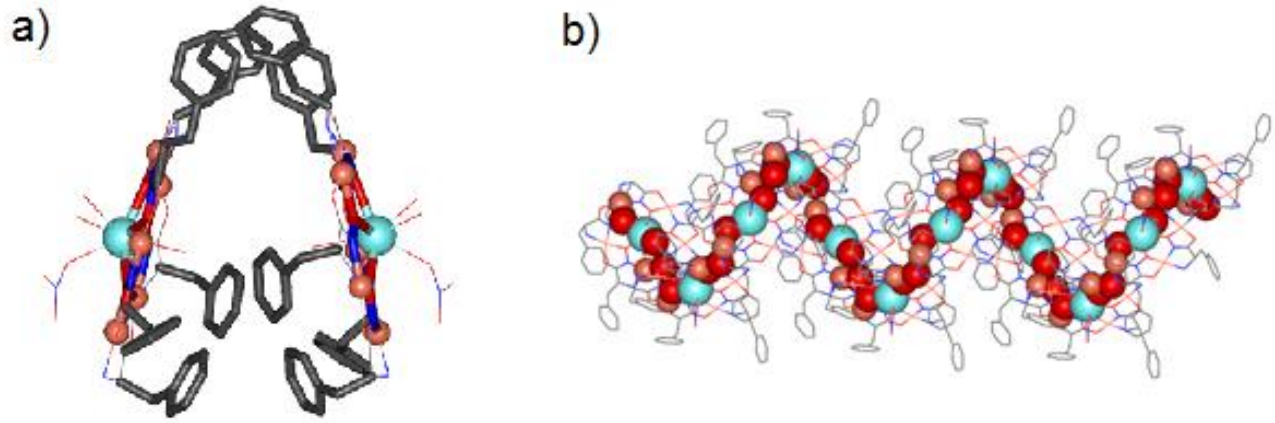


**Figure 1.22.** Crystal structures of a) the dimer and b) the helix polymorphs of $Ln^{III}(NO_3)_{3-x}(OH)_x$[15-$MC_{Cu^{II}N(S\text{-}pheHA)}$-5]. Reprinted with permission from reference 86. Copyright 2007 American Chemical Society.

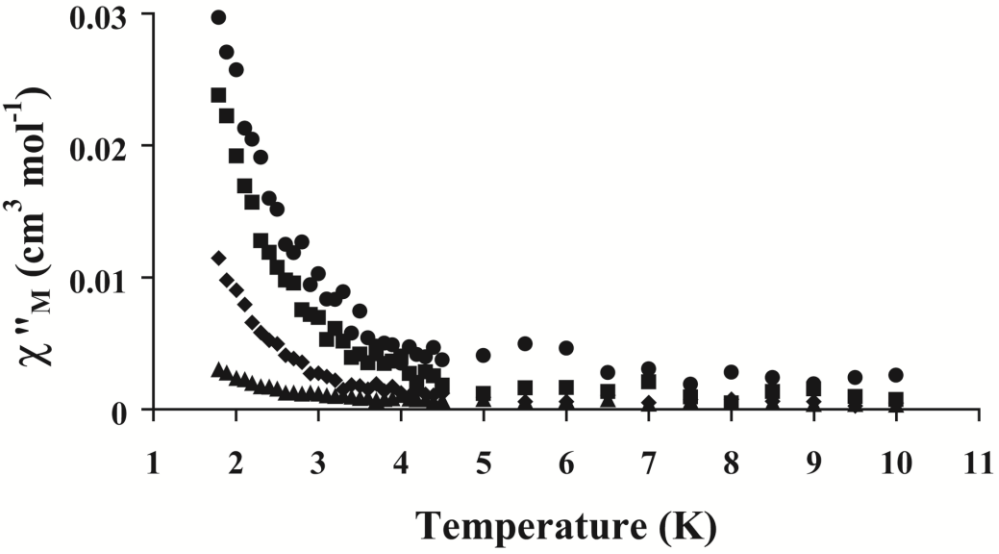


**Figure 1.23.** Out-of-phase magnetic susceptibility signal for a frozen methanol solution of $Dy(NO_3)_3$[15-$MC_{Cu^{II}N(S\text{-}pheHA)}$-5] (●1000 Hz, ■500 Hz, ♦100 Hz, ▲10 Hz). Reprinted with permission from reference 85. Copyright 2006 American Chemical Society.

## 1.5 Magnetocaloric Effect

Sub-Kelvin refrigeration is critical in many applications and experimental techniques in chemistry and condensed matter physics. Currently, $^3$He-$^4$He dilution refrigeration is the only method of continuous refrigeration below 0.3 K and can continuously cool to temperatures as low as 2 mK.[87] However, a drawback to this technique is the prohibitive cost of isotopic helium. Other refrigeration methods include adiabatic nuclear demagnetization[88] and adiabatic demagnetization of a paramagnetic salt,[89] the latter of which is the phenomenon that will be discussed in this section.

In the mid-1920s, Debye and Giauque proposed adiabatic demagnetization as a method of reaching sub-Kelvin temperatures.[25, 90] In the coming decade, Giauque successfully attained a temperature of 0.25 K through the demagnetization of $Gd_2(SO_4)_3 \cdot 8H_2O$.[91] Since then, magnetic refrigeration has been a standard technique in low-temperature refrigeration, relevant materials include $Ce_2Mg_3(NO_3)_{12} \cdot 24H_2O$ (CMN),[92-93] and gadolinium gallium garnet (GGG, $Gd_3Ga_5O_{12}$), which is the commercial standard in magnetic refrigerators and has been used in the liquefying helium.[94] Due to the "one-shot" nature of magnetic refrigeration (refrigerant warms up after the end of demagnetization), it has fallen out of favor to the aforementioned $^3$He-$^4$He dilution continuous refrigeration technique.[89]

Recently, new advances in adiabatic demagnetization refrigerators may allow for continuous cooling with paramagnetic materials, with potential implications in small-scale laboratory and space-borne applications.[95-97] Consequently, high performance molecule-based materials have become an area of focus in magnetochemistry.[89, 98-99]

Magnetic refrigeration with paramagnetic materials is based on the magnetocaloric effect (MCE).[99] This phenomenon relies on the field-temperature and entropy change of a

paramagnetic material. According to Equation 1.17, in a magnetorefrigerant, the total entropy of the system is the sum of the field- and temperature-dependent magnetic entropy, $S_M$, and the temperature-dependent lattice entropy, $S_{Latt}$ (electronic entropy is negligible):

$$S_{Total}(T, H) = S_M(T, H) + S_{Latt}(T, H) \quad (1.17)$$

It should be noted that $S_{Latt}$ dominates at high temperatures and $S_M$ at lower temperatures.

In the magnetic refrigeration process, the MCE material is first brought to the starting temperature ($T$) through a precooling bath. A magnetic field, $H$, is applied to isothermally magnetize the material; the heat of magnetization ($Q = T\Delta S$) is absorbed by the precooling bath. In this first step, the magnetic entropy during isothermal magnetization is lowered due to the ordering of the electronic spin. Since in an isothermal process $\Delta S_{Latt} = 0$, then according to Equation 1.17, $\Delta S_M = \Delta S_{Total} < 0$. This is represented by the process A → C in Figure 1.24. Conversely, during isothermal demagnetization $\Delta S_M > 0$.

In the second step of the magnetic refrigeration cycle, the material is isolated from the precooling bath and adiabatically demagnetized ($\Delta S_{Total} = 0$). Here, the spins becomes disordered and $\Delta S_M > 0$. To compensate for this, there must be a decrease in the lattice entropy ($\Delta S_{Latt} < 0$) which comes with a commensurate decrease in temperature of the material ($\Delta T_{ad} < 0$). The reverse process, adiabatic magnetization, where $\Delta S_M < 0$ and $\Delta T_{ad} > 0$, is represented by the process A → B in Figure 1.24. Finally, the refrigerant will warm up along the entropy curve of the final magnetic field, absorbing heat until it reaches the intial $T$ and $S_{Total}$, hence, the cooling power of the material is related to the entropy change during isothermal magnetization, $\Delta S_M$. Continuous cooling can be achieved through reversible magneto-thermal cycles.[89, 100]

Experimentally, the two most important parameters for MCE materials are the temperature during *adiabatic magnetization*, $\Delta T_{ad}$, and magnetic entropy change during

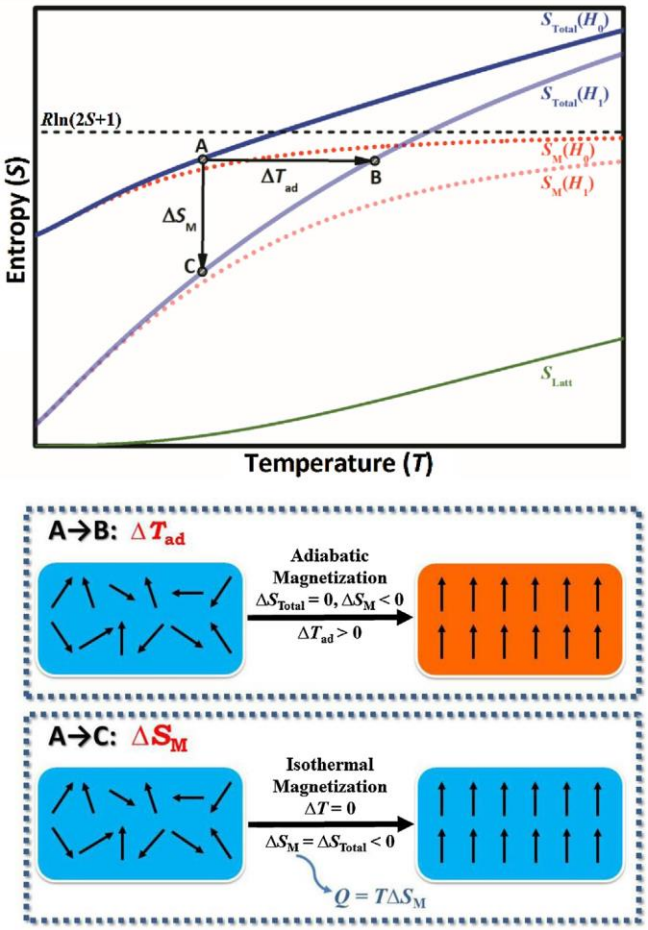


**Figure 1.24.** Entropy vs. temperature plot showing adiabatic magnetization (process A → B) and isothermal magnetization (process A → C). Reprinted with permission from reference 100. Copyright 2014 Elsevier.

*isothermal magnetization*, $\Delta S_M$. $\Delta T_{ad}$, which is related to the *total entropy*, $S_{Total}$ (Equation 1.17), must be measured by direct methods,[101] or more commonly, indirectly through heat capacity measurements through the thermodynamic expression,

$$\Delta T_{ad}(T, \Delta H) = -\int_{H_i}^{H_f} \left(\frac{T}{C(T,H)}\right)_H \left(\frac{\partial M(T,H)}{\partial T}\right)_H \mathrm{d}H \tag{1.18}$$

where $H$ = magnetic field ($f$ = final, $I$ = intial) and C = heat capacity.[99, 102] The magnetic entropy change, $\Delta S_M$, can also be determined through heat capacity measurements through application of

$$\Delta S_M(T, H) = \int_0^T \frac{C_M(T,H) - C_M(T,0)}{T} \mathrm{d}T \tag{1.19}$$

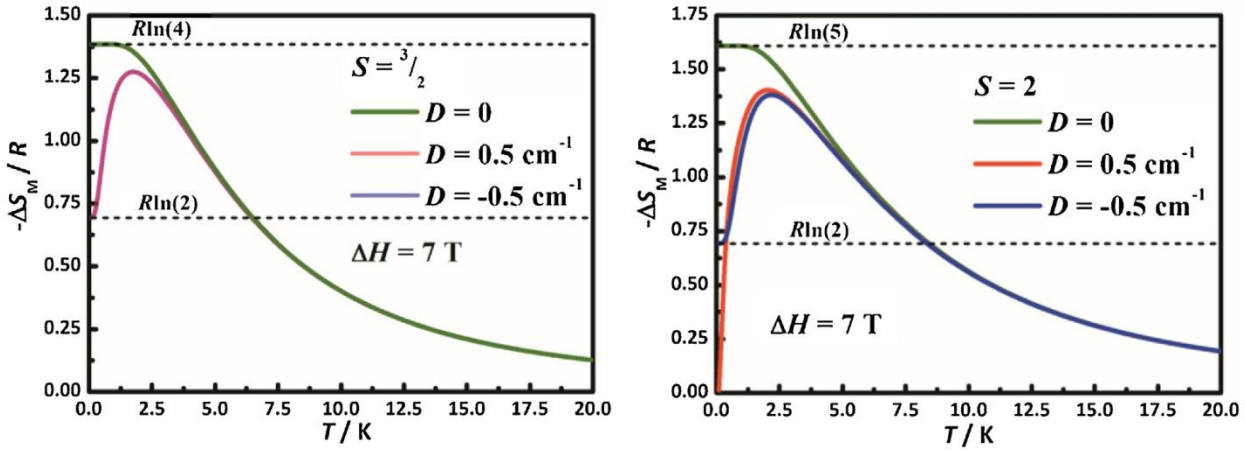


**Figure 1.25.** The influence on the axial ZFS parameter, $D$, on the $-\Delta S_M$ vs. $T$ plot for a Kramers ($S$ = 3/2) system (left) and a non-Kramers ($S$ = 2) system (right). Note that these values are for a powdered sample. Reprinted with permission from reference 100. Copyright 2014 Elsevier.

where $C_M(T, \mathrm{H})$ and $C_M(T, 0)$ are the magnetic heat capacities in a field $H$ and in zero field, respectively.[99, 103-104] Furthermore, $\Delta S_M$ may be evaluated through magnetization experiments using the Maxell equation for magnetic entropy,

$$\Delta S_M(T, \Delta H) = \int_{H_i}^{H_f} \left(\frac{\partial M(T,H)}{\partial T}\right)_H \mathrm{d}H \tag{1.20}$$

where $M$ = magnetization.[104] One of the goals of this thesis is to influence $\Delta S_M$ by modulating inter- and intramolecular magnetic interaction.

The total available magnetic entropy in a material is associated with the total magnetic degrees of freedom at $T = \infty$ and is equal to:

$$S_M = R\ln(2S+1) \tag{1.21}$$

where $R$ = the gas constant (8.3144621 J $K^{-1}$ $mol^{-1}$) and S = spin. When a magnetic field is applied to magnetically order a material, fewer spin states are populated and the magnetic entropy decreases. Unlike SMMs, MCE materials require isotropic metal ions with minimal zero-field splitting. It can be seen in Figure 1.25 that the presence of magnetic anisotropy (the zero-field splitting parameter, $D$) reduces the total available magnetic entropy regardless of the

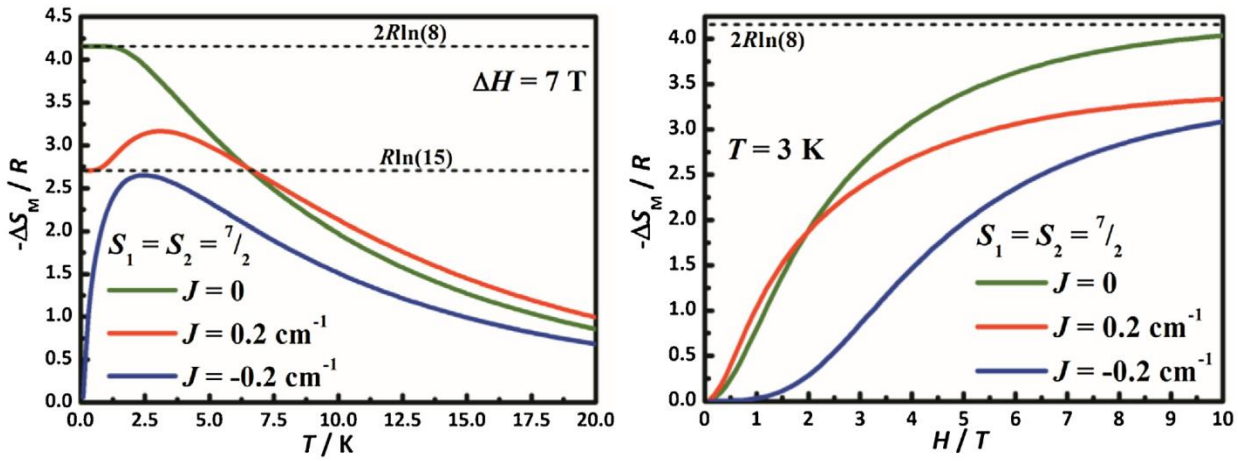


**Figure 1.26.** The influence of magnetic exchange coupling ($J$) of an $S_1 = S_2 = 7/2$ dimer on the (left) temperature-dependent and (right) field-dependent magnetic entropy change, $-\Delta S_M$. Reprinted with permission from reference 100. Copyright 2014 Elsevier.

sign of $D$. Therefore, isotropic metal ions such as $Fe^{III}$, $Mn^{II}$ and $Gd^{III}$ are best suited for use in MCE materials. Additionally, the presence of magnetic coupling may lower the total available magnetic entropy. As shown in Figure 1.26., for a simple dimer system where $S_1 = S_2 = 7/2$, both ferromagnetic and antiferromagnetic coupling reduces the temperature-dependent magnetic entropy change of the system.[104] However, weak ferromagnetic coupling may be necessary in order to achieve large $\Delta S_M$ values at lower fields.[103, 105] From Figure 1.26, for the same $S_1 = S_2 = 7/2$ system, $\Delta S_M$ is actually higher for weak ferromagnetic coupling than for the uncoupled dimer at lower fields. This is important because the use of cost effective electromagnets will limit the field to 2 T or less.[102]

In summary, the strategies to develop high performance MCE materials involve the use of isotropic, large spin metal ions to limit zero-field splitting. Weak ferromagnetic interactions are preferable as to develop materials for use in low magnetic fields. Finally, for potential space-based applications, weight is an issue as the cost of launching a payload into space is approximately $10,000/pound.[106] Consequently, the focus of MCE research is to improve the

magnetic entropy change per unit weight (J $kg^{-1}$ $K^{-1}$). Thus, it is prudent to maximize the metal : ligand weight ratio. This thesis will examine the first metallacrown-based MCE material based on $Fe^{III}$.

***Key Molecule-Based MCE Materials***

Interest in molecular MCE materials began in the early 2000s with the characterization of $Mn_{12}$ and $Fe_8$ complexes.[107] Since then, there have been numerous studies involving *3d*-, 4f- and mixed *3d*/*4f* MCE molecular clusters. Below, we will examine a few of the most important magnetic refrigerants.

*$[Fe^{III}{}_{14}O_6(L)_6(OMe)_{18}Cl_6]$ Complexes*

A large solvothermally synthesized $[Fe^{III}{}_{14}O_6(bta)_6(OMe)_{18}Cl_6]\cdot 2MeCO_2H\cdot 4H_2O$ (btaH = benzotriazole) cluster (Figure 1.27) was characterized to have a ground spin state of S = 23, which was among the largest at the time.[108] Later, more accurate measurements revealed that the actual ground state was S = 25 due to twelve ferromagnetically coupled $Fe^{III}$ ions, with the remaining two $Fe^{III}$ antiferromagnetically coupled.[109-110] This complex exhibited large MCE properties as determined through heat capacity and magnetic measurements, with $-\Delta S_M$ = 5.0 *R* = 17.3 J $kg^{-1}$ $K^{-1}$ and $\Delta T_{ad}$ = 5.8 K at *T* = 6 K and *H* = 7 T (Figure 1.28). The value of for the molar magnetic entropy change (5.0 *R*) is larger than the maximum allowed entropy for a *S* = 25 system ($R\ln(2S+1)$ = 3.9 *R*). This was attributed to the presence of excited states close in energy to the ground *S* = 25 state. Later, an isostructural complex $[Fe^{III}{}_{14}O_6(ta)_6(OMe)_{18}Cl_6]\cdot 4.5$ MeOH (taH = 1,2,3-triazole) shown in Figure 1.29, exhibited a similar *S* = 25 ground state, but had a larger $-\Delta S_M$ = 20.3 J $kg^{-1}$ $K^{-1}$ at *T* = 6 K and *H* = 7 T. This increase in $-\Delta S_M$ was ascribed to differences in intramolecular coupling, leading to a higher density of excited states, which is observed by the differences of the $\chi$'T maxima (Figure 1.30).[111]

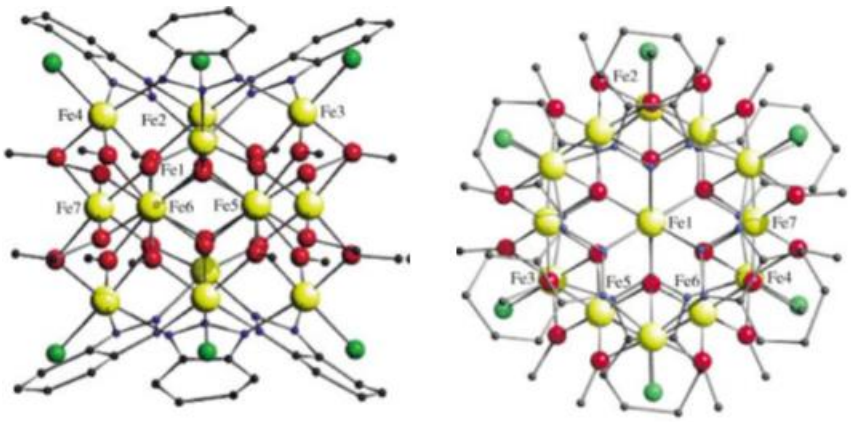


**Figure 1.27.** Crystal structure of $[Fe^{III}_{14}O_6(bta)_6(OMe)_{18}Cl_6]\cdot 2MeCO_2H\cdot 4H_2O$. Color scheme: yellow spheres – $Fe^{III}$; green – Cl; red – O; blue – N; gray – C. Reprinted with permission from reference 108. Copyright 2003 Wiley-VCH Verlag GmbH & Co. KGaA.

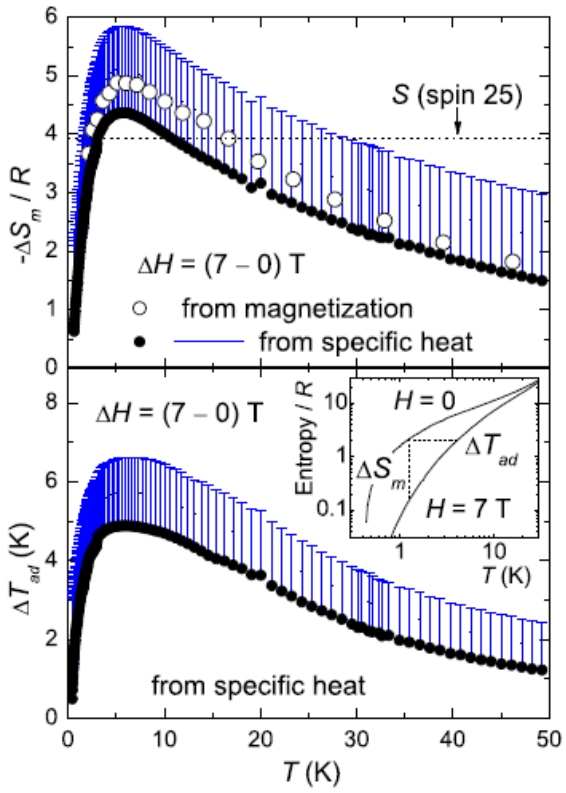


**Figure 1.28.** (Top) Temperature-dependence of $\Delta S_m$ of $[Fe^{III}_{14}O_6(bta)_6(OMe)_{18}Cl_6]$ obtained from specific heat measurements (filled dots and bars) and magnetization data (empty dots). (Bottom) Temperature dependence of the adiabatic temperature change, $\Delta T_{ad}$ obtained from specific heat measurements (filled dots and bars). Reprinted with permission from reference 110. Copyright 2005 Elsevier.

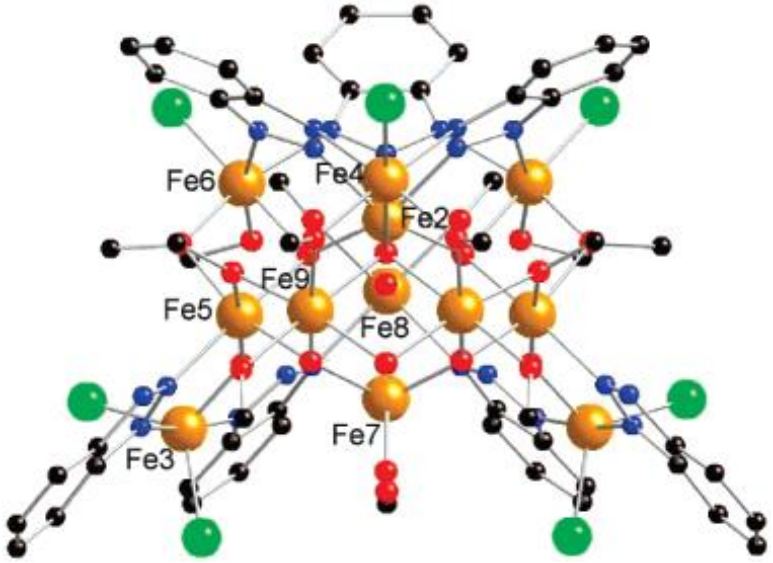


**Figure 1.29.** Structure of $[Fe^{III}_{14}O_6(ta)_6(OMe)_{18}Cl_6]\cdot 4.5$ MeOH. Color Scheme: orange spheres - $Fe^{III}$; green – Cl; red – O; blue – N; black – C. Reprinted with permission from reference 111. Copyright 2007 American Chemical Society.

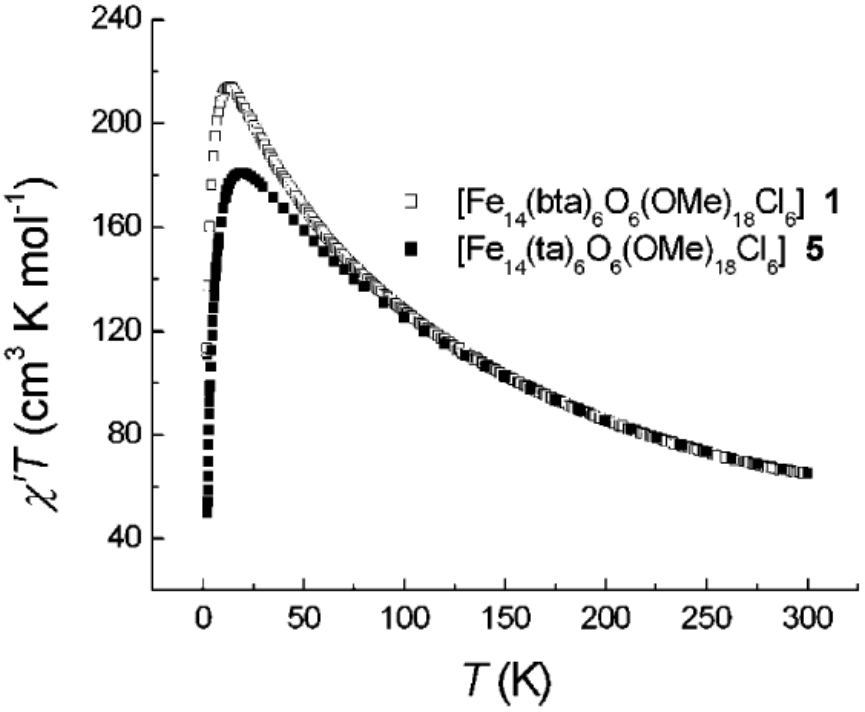


**Figure 1.30.** Temperature dependence of the χ'T vs T product for $[Fe^{III}_{14}O_6(bta)_6(OMe)_{18}Cl_6]$ and $[Fe^{III}_{14}O_6(ta)_6(OMe)_{18}Cl_6]$. Reprinted with permission from reference 111. Copyright 2007 American Chemical Society.

*$[Mn^{II}(glc)_2]_n$ vs. $[Mn^{II}(glc)_2(H_2O)_2]$*

Tong and coworkers reported the MCE behavior of a 3d coordination polymer $[Mn^{II}(glc)_2]_n$ (Figure 1.31) and its discrete monomer counterpart, $[Mn^{II}(glc)_2(H_2O)_2]$ (Figure 1.32), where Hglc = glycolic acid.[112] In the coordination polymer $[Mn^{II}(glc)_2]_n$ exhibited long-range antiferromagnetic coupling with a Néel temperature $T_N$ = 4.9 K and a small $-\Delta S_M$ = 6.9 J $kg^{-1}$ $K^{-1}$ at $T$ = 7 K and $H$ = 7 T. On the other hand, the molecular $[Mn^{II}(glc)_2(H_2O)_2]$ behaved as a well isolated paramagnet and exhibited a large $-\Delta S_M$ = 60.3 J $kg^{-1}$ $K^{-1}$ at $T$ = 1.8 K and $H$ = 7 T (Figure 1.33). The two complexes can be reversibly interconverted by the removal/addition of waters of hydration.[112]

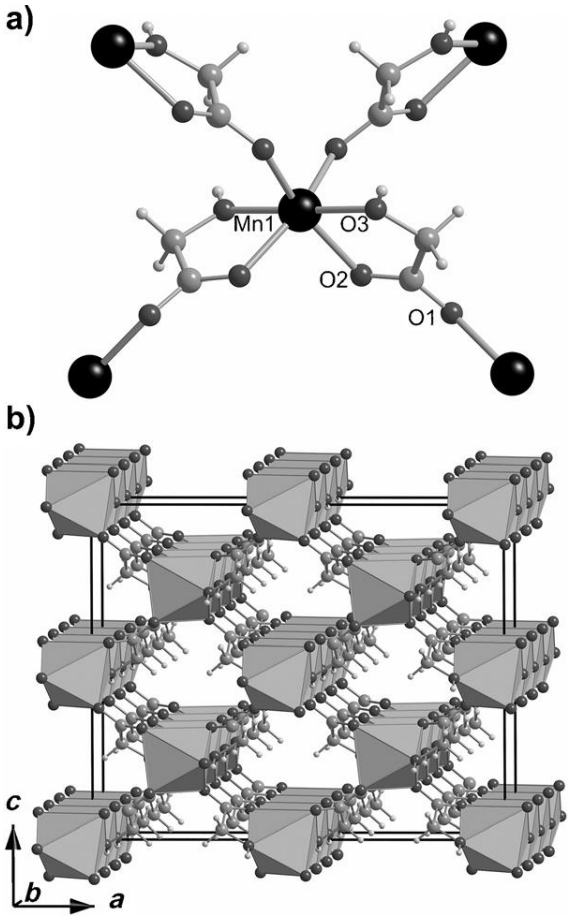


**Figure 1.31.** Structure of $[Mn^{II}(glc)_2]_n$. (a) the coordination environment of the $Mn^{II}$ ion. (b) polyhedral view of the 3d network. Color scheme: black – Mn; dark gray – O, light gray – C; white – H. Reprinted with permission from reference 112. Copyright 2014 Wiley-VCH Verlag GmbH & Co. KGaA.

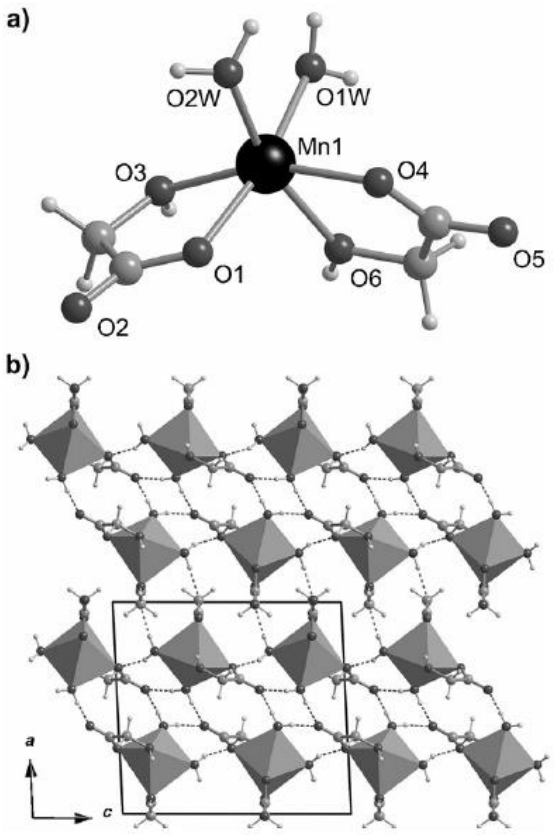


**Figure 1.32.** Structure of $[Mn^{II}(glc)_2(H_2O)_2$. (a) the coordination environment of the $Mn^{II}$ ion. (b) polyhedral view, including hydrogen bonds between adjacent molecules. Color scheme: black – Mn; dark gray – O, light gray – C; white – H. Reprinted with permission from reference 112. Copyright 2014 Wiley-VCH Verlag GmbH & Co. KGaA.

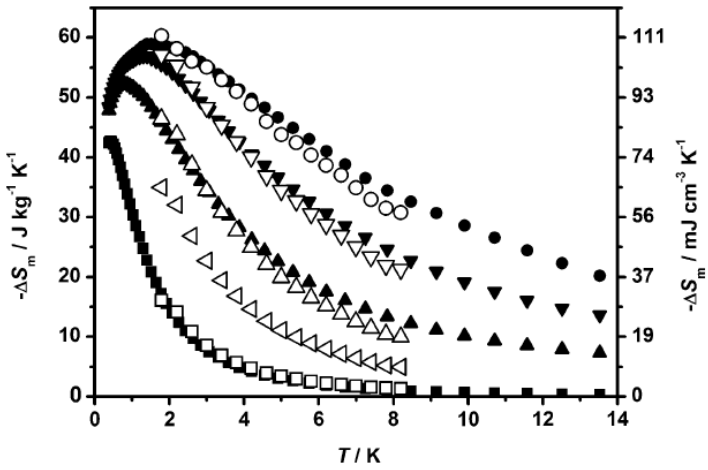


**Figure 1.33.** Temperature-dependence of $-\Delta S_m$ for $[Mn^{II}(glc)_2(H_2O)_2$ from heat capacity measurements (solid) and magnetic measurements (empty) at select $\Delta H$ (● – 7 T, ▼– 5 T; ▲ – 3 T; ◀ - 2 T; ■ – 1 T). Reprinted with permission from reference 112. Copyright 2014 Wiley-VCH Verlag GmbH & Co. KGaA.

*[Gd$^{III}$(OH)CO$_3$]$_n$*

Gd$^{III}$ is a promising metal ion for use in MCE materials due to its large $S$ = 7/2 spin and weak magnetic coupling due to contracted *f*-orbitals. Recently, a 3d network material with the formula [Gd$^{III}$(OH)CO$_3$]$_n$ (Figure 1.34) was characterized by heat capacity measurements to have impressive MCE properties, with a $-\Delta S_M$ = 66.4 J kg$^{-1}$ K$^{-1}$ and $T_{ad}$ > 20 K at $H$ = 7 T and $T$ = 1.8 K.[113] The maximum magnetic entropy change at low fields is also impressive, with $-\Delta S_M$ = 26.2 J kg$^{-1}$ K$^{-1}$ and 54.4 J kg$^{-1}$ K$^{-1}$ at $\Delta H$ = 1 K and $\Delta H$ = 3 T, respectively. Furthermore, both the *volumetric* and *gravimetric* magnetic entropy change exceeds all of the best performing MCE materials including gadolinium gallium garnet (Figure 1.35), making it one of the best performing MCE materials to date.[113]

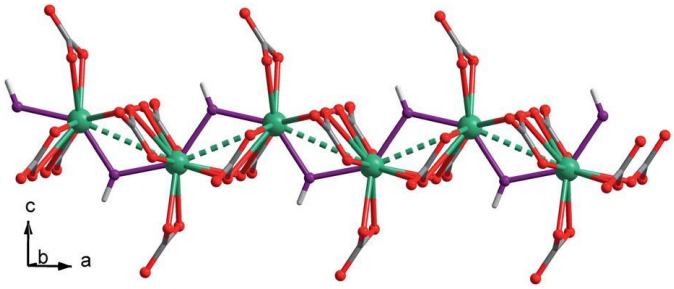


**Figure 1.34.** Structure of the [Gd$^{III}$(OH)CO$_3$]$_n$ along the *a* axis. Color scheme: green – gd; red and purple – O; gray – C; light gray – H. Reprinted with permission from reference 113. Copyright 2014 Royal Society of Chemistry.

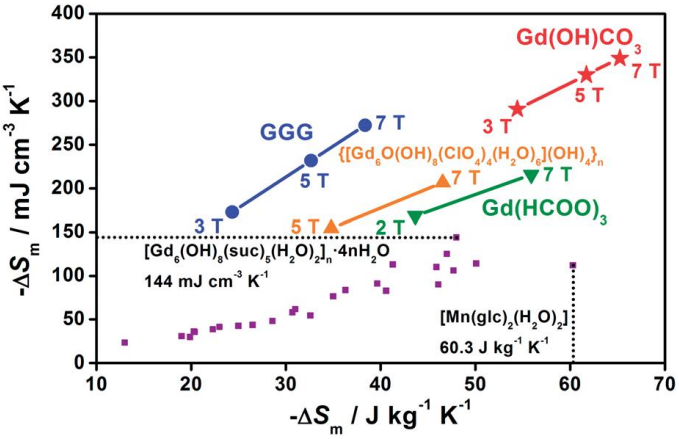


**Figure 1.35.** Comparison of the maximum -$\Delta S_m$ at selected $\Delta H$ for various MCE materials. Reproduced with permission from reference 113. Copyright 2014 Royal Society of Chemistry.

*[[$M^{III}F_3(Me_3tacn)]_2Gd^{III}{}_3F_2(NO_3)_7(H_2O)(CH_3CN)]\cdot 4CH_3CN$*

In 2014, Pedersen and coworkers reported the synthesis and characterization of a family of isostructural $[[M^{III}F_3(Me_3tacn)]_2Gd^{III}{}_3F_2(NO_3)_7(H_2O)(CH_3CN)]\cdot 4CH_3CN$ complexes where $M^{III}$ = $Cr^{III}$, $Fe^{III}$, $Ga^{III}$ and $Me_3tacn$ = N,N',N''-trimethyl-1,4,7-triazacyclononane (Figure 1.36).[114] Despite the larger spin of $Fe^{III}$ over $Cr^{III}$ (5/2 vs 3/2), the $Cr^{III}$ derivative displayed a greater magnetic entropy change than the $Fe^{III}$ complex, with $-\Delta S_M$ = 38.3 J $kg^{-1}$ $K^{-1}$ ($T$ = 2 K and $H$ = 7 T) for the former and $-\Delta S_M$ = 33.1 J $kg^{-1}$ $K^{-1}$ ($T$ = 4.2 K and $H$ = 7 T) for the latter. It was determined through a combination of magnetic measurements, DFT and heat capacity measurements that a magnetic phase transition for the $Fe^{III}$ complex below $T_c$ = 0.65 K due to strong $Fe^{III}$-$Gd^{III}$ coupling. The presence of stronger magnetic interactions consequently led to reduced MCE behavior.[114]

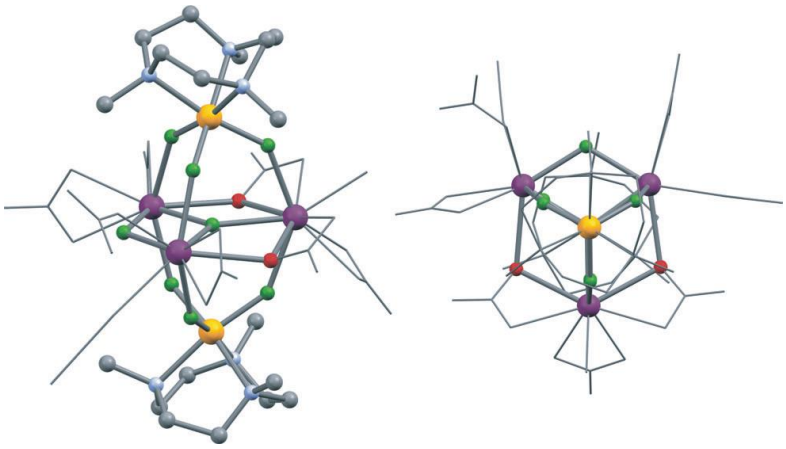

**Figure 1.36.** Crystal structure of $[[M^{III}F_3(Me_3tacn)]_2Gd^{III}{}_3F_2(NO_3)_7(H_2O)(CH_3CN)]\cdot 4CH_3CN$. Color scheme: purple – Gd; yellow – Fe; green – F; red – O; blue – N; gray – C. Reprinted with permission from reference 114. Copyright 2014 Wiley-VCH Verlag GmbH & Co. KGaA.

## 1.6 Lanthanide Luminescence

Many of the quantum mechanical properties of *4f* lanthanides which make them useful in SMMs also give rise to certain luminescence characteristics. The *f-f* transitions in the trivalent rare earth ions are characterized by narrow line widths and long luminescence lifetimes.[115] These

sharp transitions can range from the near-infrared (NIR) region for $Pr^{III}$, $Nd^{III}$, $Ho^{III}$, $Er^{III}$, $Tm^{III}$ and $Yb^{III}$, visible region for $Pr^{III}$, $Sm^{III}$, $Eu^{III}$, $Tb^{III}$, $Dy^{III}$ and $Ho^{III}$ and the ultraviolet (UV) region for $Gd^{III}$. Specifically, $Ln^{III}$ which luminesce in the NIR region are of interest for potential applications in OLEDs,[116] telecommunications,[117] solar energy conversion[118] and bio-imaging.[119-121] The longer wavelengths of the NIR emission allows for greater sensitivity of detection and tissue penetration depth in biological imaging applications.[122]

According to Judd-Ofelt theory because *f-f* transitions in free lanthanide ions are Laporte forbidden, they have a low probability of occurring.[40] However, the absorption coefficients due to this phenomenon is generally very weak, usually smaller than 1 $M^{-1}$ $cm^{-1}$ and excitation of these transitions can only occur with high powered laser source. *4f-5d* transitions, on the other hand, are parity allowed, although these transitions are at such high energy that they are usually not observed in coordination complexes.[115]

In order to circumvent the Laporte selections rules, another method of inducing lanthanide luminescence has been utilized: the "sensitization" of the lanthanide ions through an organic chromophore, also known as the antenna effect.[123] The Jablonsky diagram in Figure 1.37 shows several various energy transfer and radiative and non-radiative emission pathways.[115] Perhaps the most common mode of energy transfer is the $^1S^* \rightarrow {}^3T^* \rightarrow Ln^*$ pathway. In this mechanism, the ligand absorbs light to reach an excited single state, $^1S^*$, which then goes through intersystem crossing to reach the ligand $^3T^*$ state and finally transfers energy to the lanthanide accepting excited state, Ln*. Alternatively, the ligand may be excited to an intra-ligand charge transfer (ILCT) state which then transfers to the $^3T^*$ state, which sensitizes the $Ln^{III}$ excited accepting *J* state, Ln*.[122] The excited Ln* state is then relaxed back to the ground *J* state, emitting energy either through fluorescence, where there is no change in spin, as in Yb

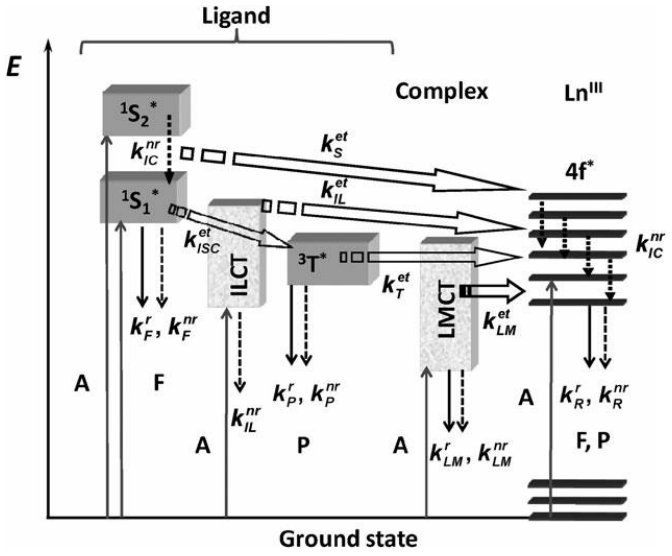


**Figure 1.37.** Jablonksy diagram representing the energy absorption, transfer and radiative emission (plain arrows) and non-radiative dissipation (dotted arrows) processes in lanthanide complexes. $^1S_1$* or $^1S_2$* = excited single state, $^3$T* = triplet state, A = absorption, F = fluorescence, P = phosphorescence, *k* = rate constant, *r* = radiative, *nr* = non-radiative, IC = internal conversion, ISC = intersystem crossing, ILCT = intra-ligand charge transfer, LMCT = ligand-to-metal charge transfer. Reprinted with permission from reference 124. Copyright 2010 Royal Society of Chemistry.

($^2F_{5/2} \rightarrow {}^2F_{7/2}$); or phosphorescence, where the transition involves a change in spin, as with Eu ($^5D_0 \rightarrow {}^7F_J$).[125] These intramolecular ligand-to-lanthanide energy migrations can occur via either a through-bond Dexter mechanism, or a through space Förster mechanism.[40] It can be seen in Figure 1.37 that multiple energy transfer pathways may occur, including competing radiative and non-radiative relaxation, which quenches lanthanide luminescence.

The two most important parameters obtained from the emission spectra of $Ln^{III}$ complexes are the quantum yield, *Q*, and the lifetime of the excited Ln* state, $\tau_{obs} = 1/k_{obs}$, where $k_{obs}$ is the rate constant ($s^{-1}$) of the depopulation of the excited state. In its most basic form, the quantum yield is

$$Q = \frac{\#\text{ emitted photons}}{\#\text{ absorbed photons}} \tag{1.22}$$

The *intrinsic quantum yield* reflects the direct excitation of a $Ln^{III}$ ion and is related to

$$Q_{\mathrm{Ln}}^{\mathrm{Ln}} = \frac{k^{rad}}{k_{obs}} = \frac{\tau_{obs}}{\tau^{rad}} \quad (1.23)$$

where $k^{rad}$ and $\tau^{rad}$ are the radiative rate constant and lifetime, respectively. $k_{obs}$ is the sum of the rates of various relaxation processes:

$$k_{obs} = k^{rad} + \sum_n k_n^{nr} \quad (1.24)$$

where $k_n^{nr}$ are the non-radiative rate constants.

Equation 1.23 is then related to the *overall quantum yield*, $Q_{\mathrm{Ln}}^{\mathrm{L}}$, by Equation 1.25:

$$Q_{\mathrm{Ln}}^{\mathrm{L}} = \eta_{sens} Q_{\mathrm{Ln}}^{\mathrm{Ln}} \quad (1.25)$$

where $\eta_{sens}$ is the sensitization efficiency – the efficiency of the energy transfer from the ligand to the $Ln^{III}$.[40]

Experimentally, the quantum yield may be measured by the absolute method with a fluorimeter with a integration sphere which determines the amount of light absorbed and emitted in all directions.[40] The absolute quantum yield is

$$Q_{\mathrm{abs}} = \frac{E_c}{[L_a(\lambda_{exc}) - L_c(\lambda_{exc})]F_{att}(\lambda_{exc})} \quad (1.26)$$

where $E_c$ is the integrated intensity of the entire emission spectrum, $L_a$ is the integrated intensity of the light exciting the empty sphere at wavelength $\lambda_{exc}$, $L_c$ is the integrated intensity of the light exiting the sphere containing sample and $F_{att}$ is a correction for the attenuators used.[40]

Since the sensitization of $Ln^{III}$ ions can occur through many mechanisms, the design of luminescent coordination compounds can be difficult. As a general rule, the ligand $^3T^*$ state should be approximately 2,500 to 3,000 $cm^{-1}$ higher in energy than the $Ln^{III}$ accepting state in order to limit back-energy transfer.[40] The main accepting and ground states for each $Ln^{III}$ ion can be seen in Figure 1.38. Additionally, energy difference between the $^1S_1^*$ and $^3T^*$ ligand states should be around 5,000 $cm^{-1}$ in order to allow the most efficient intersystem crossing to occur.

Finally, high energy vibrations such as C-H, N-H and O-H oscillators can quench lanthanide luminescence through vibronic coupling, therefore it is necessary to encapsulate the $Ln^{III}$ ion fully to preclude the X-H oscillators within its vicinity.[126] Finally, for use in *in vivo* and *in vitro* assays, water solubility and stability is important.

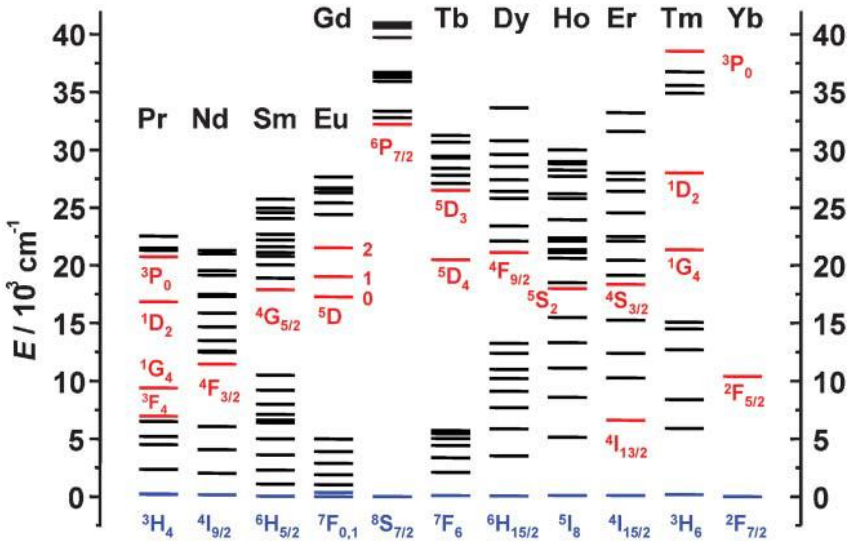


**Figure 1.38.** Partial energy diagrams for the lanthanide ions. The main accepting levels are in red and ground state is in blue. Reprinted with permission from reference 125. Copyright 2005 Royal Society of Chemistry.

### *Important Luminescent Complexes*

*$[Ln^{III}L]^-$*

In 2012, Raymond and coworkers reported the synthesis of isostructural $[Ln^{III}L]^-$ complexes ($Ln^{III}$ = Sm, Eu, Tb, Dy, Ho), with the ligand $H_4L$, which incorporated four TIAM chromophores attached to an H(2,2) backbone (Figure 1.39).[127] The complex $[Ho^{III}L]^-$ displayed NIR emission at 990/1010 nm, 1210 nm and 1450 nm which correspond to the $^5F_5 \rightarrow {}^5I_7$, $^5I_6 \rightarrow {}^5I_8$ and $^5F_5 \rightarrow {}^5I_8$ transitions, respectively (Figure 1.40). Additionally, there was visible emission at 645 nm corresponded to the $^5F_5 \rightarrow {}^5I_8$ transition. This was the first $Ho^{III}$ compound which exhibited the 1210 nm and 1450 nm emission in aqueous solution, as these transitions tend to be

very weak.[127] The $Sm^{III}$, $Eu^{III}$, $Tb^{III}$ and $Dy^{III}$ also displayed luminescence in aqueous solutions with very small values for the hydration number, *q*. This suggested that the $H_4L$ ligand effectively shielded the $Ln^{III}$ ions from external quenching.

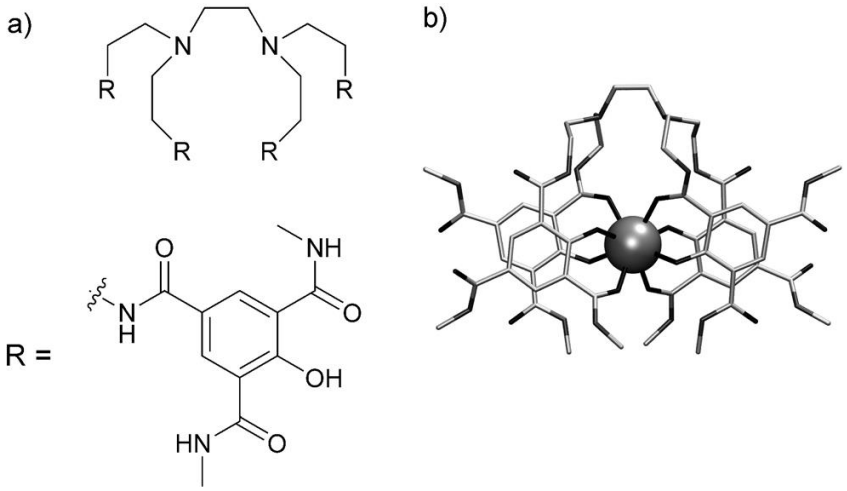


**Figure 1.39.** (a) Chemical structure of the H(2,2) scaffold and the TIAM chromophore. (b) Crystal structure of $[Ho^{III}L]^-$. Reprinted with permission from reference 127. Copyright 2012 Wiley-VCH Verlag GmbH & Co. KGaA.

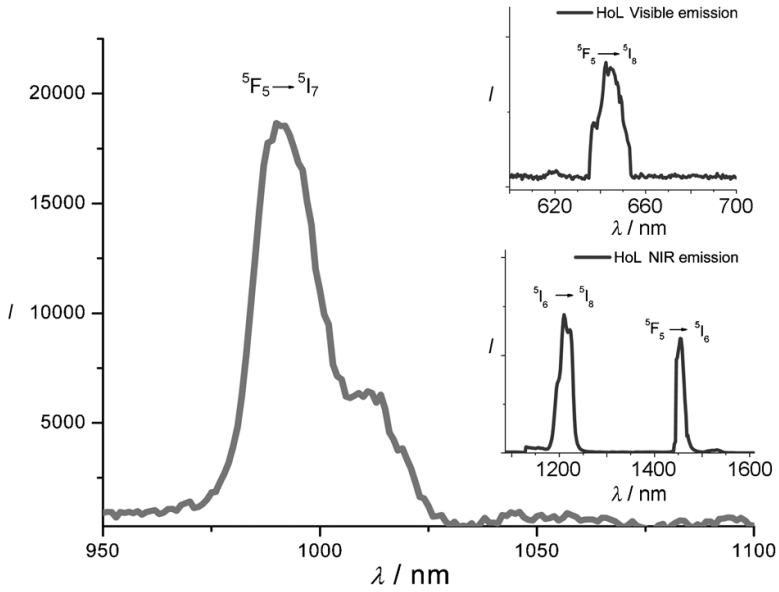


**Figure 1.40.** Emission spectra of $[Ho^{III}L]^-$ in water and less than 5% DMSO at $\lambda_{exc}$ = 330 nm. Reprinted with permission from reference 127. Copyright 2012 Wiley-VCH Verlag GmbH & Co. KGaA.

*Luminescent Ln[12-MC-4]$_2$[24-MC-8] Metallacrowns*

The $Zn^{II}$ ion is $d^{10}$ and, therefore, does not have visibly absorbing *d-d* transitions that would interfere with optical applications. A family of $Ln^{III}[12\text{-}MC_{Zn^{II}N(L)}\text{-}4]_2[24\text{-}MC_{Zn^{II}N(L)}\text{-}8]^{3+}$ (L = picHA or quinHA) MCs were examined for lanthanide luminescence since the "encapsulated sandwich" structure completely restricts solvent access to the lanthanide ion (Figure 1.41).

The first series of MCs to be examined were of the form $Ln^{III}[12\text{-}MC_{Zn^{II}N(picHA)}\text{-}4]_2[24\text{-}MC_{Zn^{II}N(picHA)}\text{-}8]^{3+}$.[126] In this system it was found that the absorption of the ligands was of insufficient energy to sensitize the visibly emitting lanthanides. However, for selected NIR emitting lanthanides ($Ln^{III}$ = $Yb^{III}$ and $Nd^{III}$) sensitization was achieved in both deuterated and protonated solvents. In addition to the low hydration number, this system excludes high energy oscillators (CH, NH, OH bonds) from the proximity of the $Ln^{III}$, preventing non-radiative deactivation. The synthetic achievements of this first generation of luminescent metallacrowns, including the determination of a delicate solvent dependence for the formation of the encapsulated sandwich structure, warranted further study.

In an effort to shift absorption into the near-visible region, the next generation of analogous MCs were synthesized using $H_2$quinHA as the ligand to form $Ln^{III}[12\text{-}MC_{Zn^{II}N(quinHA)}\text{-}4]_2[24\text{-}MC_{Zn^{II}N(quinHA)}\text{-}8]^{3+}$ complexes.[122] The typical $\pi$-$\pi^*$ absorption of the quinHA MCs remained similar to that of the picHA system; however, a new broad absorption band was observed at ca. 380 nm. This absorption was independent of choice in $Ln^{III}$, and it would not be expected for $Zn^{II}$ to participate in either metal-ligand charge transfer (MLCT) or ligand-metal charge transfer (LMCT) processes. It was, therefore, deduced that this new broad absorption is a ligand-based charge transfer, either an interligand CT through space between the 12-MC-4 and

24-MC-8 or an intraligand CT across one single ligand. This CT band was still of insufficient energy to sensitize visibly emitting lanthanides, but excitation through this CT state led to strong emission in the NIR. Strong emission from the $Yb^{III}$, $Nd^{III}$, and $Er^{III}$ derivatives allowed collection of high resolution spectra (Figure 1.42), and the photophysical data is summarized in Table 1.1. Of particular note is the extraordinarily high quantum yields of luminescence for $Nd^{III}$ and $Er^{III}$, in addition to the ability to sensitize this luminescence in the near-visible/visible region (380-400nm). While the distance between the $Ln^{III}$ and antennae is relatively long compared to other systems, the low hydration number and exclusion of ligand based high energy oscillators outweigh this long distance to give one of the best organic-$Ln^{III}$ sensitizing ligand systems.

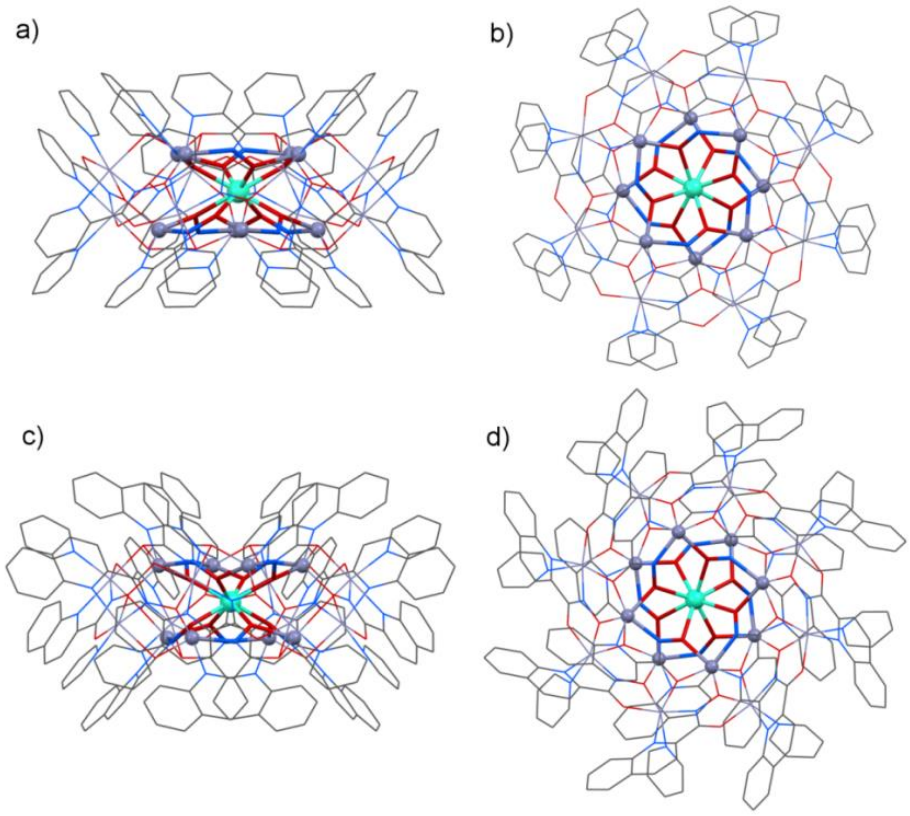


**Figure 1.41.** Single-crystal X-ray structures of $Tb^{III}[12\text{-}MC_{Zn^{II}N(\ picHA)}\text{-}4]_2[24\text{-}MC_{Zn^{II}N(picHA)}\text{-}8]^{3+}$ viewed along the (a) *a*-axis and (b) *c*-axis and $Dy^{III}[12\text{-}MC_{Zn^{II}N(\ quinHA)}\text{-}4]_2[24\text{-}MC_{Zn^{II}N(quinHA)}\text{-}8]^{3+}$ viewed along the (c) *a*-axis and (d) *c*-axis. The 12-MC-4 MC ring is highlighted in bold. Color Scheme: teal – $Ln^{III}$, gray-purple - $Zn^{II}$, red – oxygen, blue – nitrogen, gray – carbon. Reproduced from crystal structures from references 122 and 126.

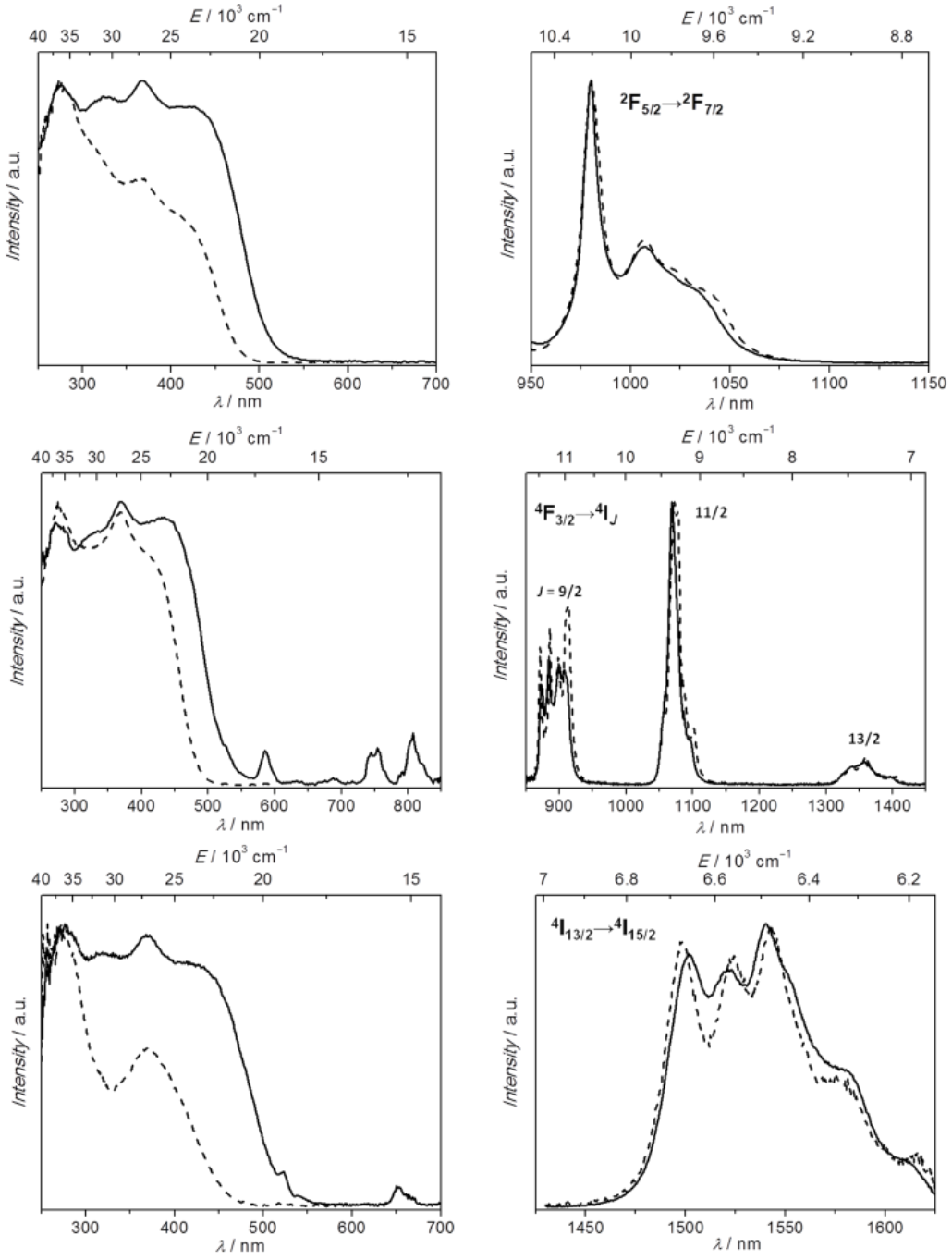


**Figure 1.42.** (Left) Corrected and normalized excitation and (right) emission spectra of $Ln^{III}[12\text{-}MC_{Zn^{II}N(quinHA)}\text{-}4]_2[24\text{-}MC_{Zn^{II}N(quinHA)}\text{-}8]^{3+}$ complexes in the solid state ($\lambda_{ex}$ = 420 nm, solid traces) and methanol solution (1 mg/mL, $\lambda_{ex}$ = 370 nm, dashed traces). (Top) $Yb^{III}$, $\lambda_{em}$ = 980 nm; (Middle) $Nd^{III}$, $\lambda_{em}$ = 1064 nm; (Bottom) $Er^{III}$, $\lambda_{em}$ = 1525 nm. Reprinted with permission from reference 122. Copyright 2014 American Chemical Society.

**Table 1.1.** Photophysical Parameters of $Ln^{III}[Zn^{II}MC_{quinHA}]$ and $Ln^{III}[Zn^{II}MC_{picHA}]$ Complexes ($Ln^{III}$ = Yb, Nd, Er) in Solid State and Methanol Solutions (1 mg/mL)[a]. Reprinted with permission from reference 122. Copyright 2014 American Chemical Society.

| Compound | state/solvent | $\tau_{obs}/\mu_s$ [b] | $q$ [c] | $\lambda_{ex}$/nm | $Q^L_{Ln}$/% |
|---|---|---|---|---|---|
| $Yb^{III}[Zn^{II}MC_{quinHA}]$ | Solid | 47.8(4) | 0 | 370 | 2.44(4) |
| | $CH_3OH$ | 14.88(1) | | | 0.25(1) |
| | $CH_3OD$ | 150.7(2) | | | 2.88(2) |
| $Yb^{III}[Zn^{II}MC_{picHA}]$ | Solid | 34.5(1) | 0 | 320 | 0.40(2) |
| | $CH_3OH$ | 12.1(1) | | | 0.13(1) |
| | $CH_3OD$ | 133(1) | | | 1.60(3) |
| $Nd^{III}[Zn^{II}MC_{quinHA}]$ | Solid | 1.79(2) | 0 | 370 | 1.13(4) |
| | $CH_3OH$ | 1.16(1) | | | 0.38(1) |
| | $CH_3OD$ | 4.11(3) | | | 1.35(1) |
| $Nd^{III}[Zn^{II}MC_{picHA}]$ | Solid | 1.18(2) | 0 | 320 | 0.40(1) |
| | $CH_3OH$ | 0.90(1) | | | 0.22(2) |
| | $CH_3OD$ | 3.53(2) | | | 0.98(1) |
| $Er^{III}[Zn^{II}MC_{quinHA}]$ | Solid | 5.73(2) | - | 370 | $4.2(1)\cdot10^{-2}$ |
| | $CH_3OH$ | 1.25(1) | | | $9.9(3)\cdot10^{-4}$ |
| | $CH_3OD$ | 11.40(3) | | | $3.6(1)\cdot10^{-2}$ |

[a]Data for 298 K. Standard deviation (2σ) between parentheses; estimated relative errors: $\tau_{obs}$, ±2%; $Q^L_{Ln}$, ±10%. [b]Under excitation at 355 nm. [c]The inner sphere hydration numbers were calculated according to the following equations: $q_{Yb} = 2\cdot(k_{CH_3OH} - k_{CD_3OD} - 0.1)$ (in μs) and $q_{Nd} = 290 \cdot (k_{CH_3OH} - k_{CD_3OD}) - 0.4$ (in ns).

## 1.7 Thesis Aims

The interplay between form (molecular structure) and function (physical properties) can be exploited using the metallacrown approach to molecular design. In particular, this thesis focuses on utilizing the tunable and predictable nature of metallacrowns in order to control the properties in magnetic (SMM and MCE) and luminescent phenomena. The flexibility of this strategy allows for the synthesis of *3d*, mixed *3d*/*4f* and pure *4f* (from a magnetic and spectroscopic point of view) complexes. Magnetic interactions, ligand field, second coordination sphere effects and even crystal packing can have drastic effects on the magnetic and luminescent properties of these molecules and will be examined in this thesis.

Chapter II will focus on a family of $Ln^{III}{}_2Ga^{III}{}_4$ compounds, in which the $Dy^{III}$ derivative displays SMM behavior. Since $Ga^{III}$ is diamagnetic, these complexes can be considered as pure *4f* based molecules. In Chapter III, we will investigate the superparamagnetic properties of

mixed $M^{III}/Ln^{III}$ ($M^{III}$ = $Mn^{III}$, $Fe^{III}$ and $Ga^{III}$) complexes in order to examine how *3d*/*4f* interactions affect slow magnetic relaxation. Magnetic refrigerants based on $Fe^{III}$ 9-MC-3 complexes will be studied in Chapter IV. Chapter V will diverge from the magnetic properties and instead examine the luminescent behavior of $Ln^{III}Ga^{III}_4$ complexes. Finally, the understanding gained from this thesis research, along with future research directions will be recapitulated in Chapter VI.

## References


1. Saalfrank, R. W.; Maid, H.; Scheurer, A. *Angew. Chem. Int. Ed.* **2008**, *47*, 8794-8824.
2. Lah, M. S.; Pecoraro, V. L. *J. Am. Chem. Soc.* **1989**, *111*, 7258-7259.
3. Hulsbergen, F. B.; Ten Hoedt, R. W. M.; Verschoor, G. C.; Reedijk, J.; Spek, A. L. *J. Chem. Soc. Dalton Trans.* **1983**, 539-545.
4. Raptis, R. G.; Fackler, J. P. *Inorg. Chem.* **1988**, *27*, 4179-4182.
5. Bovio, B.; Bonati, F.; Banditelli, G. *Inorg. Chim. Acta* **1984**, *87*, 25-33.
6. Fornies, J.; Martin, A.; Sicilia, V.; Martin, L. F. *Chem. Eur. J.* **2003**, *9*, 3427-3435.
7. Stemmler, A. J.; Kampf, J. W.; Pecoraro, V. L. *Inorg. Chem.* **1995**, *34*, 2271-2272.
8. Mezei, G.; Zaleski, C. M.; Pecoraro, V. L. *Chem. Rev.* **2007**, *107*, 4933-5003.
9. Zaleski, C. M.; Tricard, S.; Depperman, E. C.; Wernsdorfer, W.; Mallah, T.; Kirk, M. L.; Pecoraro, V. L. *Inorg. Chem.* **2011**, *50*, 11348-11352.
10. Jankolovits, J.; Kampf, J. W.; Pecoraro, V. L. *Inorg. Chem.* **2013**, *52*, 5063-5076.
11. Jankolovits, J.; Kampf, J. W.; Pecoraro, V. L. *Polyhedron* **2013**, *52*, 491-499.
12. Jankolovits, J.; Kampf, J. W.; Pecoraro, V. L. *Inorg. Chem.* **2014**, *53*, 7534–7546.
13. Lah, M. S.; Kirk, M. L.; Hatfield, W.; Pecoraro, V. L. *J. Chem. Soc., Chem. Commun.* **1989**, 1606-1608.
14. T. T. Boron, I.; Kampf, J. W.; Pecoraro, V. L. *Inorg. Chem.* **2010**, *49*, 9104-9106.
15. Kessissoglou, D. P.; Kampf, J. W.; Pecoraro, V. L. *Polyhedron* **1994**, *13*, 1379-1391.
16. Yaghi, O. M. O. K., M.; Ockwig, N. W.; Chae, H. K.; Eddaoudi, M.; Kim, J. *Nature* **2003**, *423*, 705-714.
17. Gibney, B. R.; Kessissoglou, D. P.; Kampf, J. W.; Pecoraro, V. L. *Inorg. Chem.* **1994**, *33*, 4840-4849.
18. Psomas, G.; Stemmler, A. J.; Dendrinou-Samara, C.; Bodwin, J. J.; Scheider, M.; Alexiou, M.; Kampf, J. W.; Kessissoglou, D. P.; Pecoraro, V. L. *Inorg. Chem.* **2001**, *40*, 1562-1570.
19. Zaleski, C. M.; Lim, C.-S.; Cutland-Van Noord, A. D.; Kampf, J. W.; Pecoraro, V. L. *Inorg. Chem.* **2011**, *50*, 7707-7717.
20. Azar, M. R.; Boron, T. T.; Lutter, J. C.; Daly, C. I.; Zegalia, K. A.; Nimthong, R.; Ferrence, G. M.; Zeller, M.; Kampf, J. W.; Pecoraro, V. L.; Zaleski, C. M. *Inorg. Chem.* **2014**, *53*, 1729-1742.
21. Keithley, J. F., *The Story of Electrical and Magnetic Measurements: From 500 BC to the 1940s*. IEEE Press: New York, 1999.
22. Lowrie, W., Fundamentals of Geophysics. Cambridge University Press: New York, 1997.
23. Hall, G. *Philos. Trans. R. Soc. London, Ser. A* **2008**, *366*, 1849-1860.
24. Kragh, H. *Phys. Teach.* **1997**, *35*, 328-332.
25. Giauque, W. F. *J. Am. Chem. Soc.* **1927**, *49*, 1864-1870.
26. Kittel, C.; Galt, J. K.; Campbell, W. E. *Phys. Rev.* **1950**, *77*, 725-725.
27. Bednorz, J. G.; Müller, K. A. *Z. Phys. B* **1986**, *64*, 189-193.
28. Verdaguer, M.; Girolami, G. S., Magnetic Prussian Blue Analogs. In *Magnetism: Molecules to Materials V*, Wiley-VCH Verlag GmbH & Co. KGaA: 2005; pp 283-346.
29. Kahn, O., *Molecular Magnetism*. VCH Publishers, Inc.: New York, 1993.
30. Goodenough, J. B. *J. Phys. Chem. Solids* **1958**, *6*, 287-297.
31. Kanamori, J. *J. Phys. Chem. Solids* **1959**, *10*, 87-98.
32. Gatteschi, D. S., R.; Villain, J., *Molecular Nanomagnets*. Oxford University Press: New York, 2006.
33. Carlin, R. L., *Magnetochemistry*. Springer-Verlag: Berlin, 1986.
34. Ribas Gispert, J., *Coordination Chemistry*. WILEY-VCH Verlag GmbH & Co. KGaA: Weinheim, 2008.
35. Smith, J. a. S. *J. Chem. Ed.* **1971**, *48*, 39.

36. Likhtenshtein, G. I.; Yamauchi, J.; Nakatsuji, S. I.; Smirnov, A. I.; Tamura, R., Fundamentals of Magnetism. In *Nitroxides*, Wiley-VCH Verlag GmbH & Co. KGaA: 2008; pp 1-45.
37. Rubio, J.; Perez, J. J. *J. Chem. Ed.* **1986**, *63*, 476.
38. Campbell, M. L. *J. Chem. Ed.* **1998**, *75*, 1339.
39. Chen, X. L., Y.; Tu, D., *Lanthanide-Doped Luminescent Nanomaterials: From Fundamentals to Bioapplications*. Springer Berlin Heidelberg: 2014.
40. Bünzli, J.-C.; Eliseeva, S., Basics of Lanthanide Photophysics. In *Lanthanide Luminescence*, Hänninen, P.; Härmä, H., Eds. Springer Berlin Heidelberg: 2011; Vol. 7, pp 1-45.
41. Rinehart, J. D.; Long, J. R. *Chem. Sci.* **2011**, *2*, 2078-2085.
42. Girerd, J.-J. J., Y., *Molecular Magnetism in Bioinorganic Chemistry*. University Science Books: Sausolito, 2000.
43. Cotton, S., *Lanthanide and Actinide Chemistry*. John Wiley & Sons Ltd.: West Sussex, 2006.
44. Palmer, G., *Electron Paramagnetic Resonance of Metalloproteins*. University Science Books: Sausolito, 2000.
45. Borras-Almenar, J. J.; Clemente-Juan, J. M.; Coronado, E.; Tsukerblat, B. S. *J. Comput. Chem.* **2001**, *22*, 985-991.
46. Kambe, K. *J. Phys. Soc. Jpn.* **1936**, *5*, 48-51.
47. Landrum, G. A.; Dronskowski, R. *Angew. Chem. Int. Ed.* **2000**, *39*, 1560-1585.
48. Cullity, B. D.; Graham, C. D., Domains and the Magnetization Process. In *Introduction to Magnetic Materials*, John Wiley & Sons, Inc.: 2008; pp 275-333.
49. Paul, D. I. *IEEE Trans. Magn.* **1980**, *16*, 1003-1005.
50. Sessoli, R.; Tsai, H.; Schake, A. R.; Wang, S.; Vincent, J. B.; Folting, K.; Gatteschi, D.; Christou, G.; Hendrickson, D. N. *J. Am. Chem. Soc.* **1993**, *115*, 1804-1816.
51. Sessoli, R.; Gatteschi, D.; Novak, M. A. *Nature* **1993**, *365*, 141-143.
52. Long, J., *Molecular Cluster Nanomagnets*. World Scientific Publishing: Hong Kong, 2003.
53. Winpenny, R. E. P. *Angew. Chem., Int. Ed.* **2008**, *47*, 7992-7994.
54. Leuenberger, M. N.; Loss, D. *Nature* **2001**, *410*, 789-793.
55. Lis, T. *Acta Crystallogr., Sect. B: Struct. Sci* **1980**, *36*, 2042-2046.
56. Christou, G.; Gatteschi, D.; Hendrickson, D. N.; Sessoli, R. *MRS Bull.* **2000**, *25*, 66-71.
57. Gatteschi, D.; Sessoli, R. *Angew. Chem. Int. Ed.* **2003**, *42*, 268-297.
58. Wernsdorfer, W.; Sessoli, R. *Science* **1999**, *284*, 133-135.
59. Ishikawa, N.; Sugita, M.; Wernsdorfer, W. *Angew. Chem. Int. Ed.* **2005**, *44*, 2931-2935.
60. Rinehart, J. D.; Fang, M.; Evans, W. J.; Long, J. R. *J. Am. Chem. Soc.* **2011**, *133*, 14236-14239.
61. Rinehart, J. D.; Fang, M.; Evans, W. J.; Long, J. R. *Nat. Chem.* **2011**, *3*, 538-542.
62. Wernsdorfer, W.; Aliaga-Alcalde, N.; Hendrickson, D. N.; Christou, G. *Nature* **2002**, *416*, 406-409.
63. Long, J. R. M.; Habib, F.; Lin, P.-H.; Korobkov, I.; Enright, G.; Ungur, L.; Wernsdorfer, W.; Chibotaru, L. F.; Murugesu, M. *J. Am. Chem. Soc.* **2011**, *133*, 5319-5328.
64. Bagai, R.; Christou, G. *Chem. Soc. Rev.* **2009**, *38*, 1011-1026.
65. Martien, D. Introduction to ac Susceptibility: AC Measurements. (accessed 9 November 2014).
66. Youssif, M. I. B., A. A.; Ali, I. A. *Egypt. J. Sol.* **2000**, *23*, 231-250.
67. White, R. M., *Quantum Theory of Magnetism*. Springer Berlin Heidelberg: New York, 2007.
68. Cole, K. S.; Cole, R. H. *J. Chem. Phys.* **1941**, *9*, 341-351.
69. Dekker, C.; Arts, A. F. M.; De Wijn, H. W.; Van Duyneveldt, A. J.; Mydosh, J. A. *Phys. Rev. B* **1989**, *40*, 11243-11251.
70. Baniodeh, A.; Lan, Y.; Novitchi, G.; Mereacre, V.; Sukhanov, A.; Ferbinteanu, M.; Voronkova, V.; Anson, C. E.; Powell, A. K. *Dalton Trans.* **2013**, *42*, 8926-8938.
71. Aubin, S. M. J.; Sun, Z.; Pardi, L.; Krzystek, J.; Folting, K.; Brunel, L.; Rheingold, A. L.; Christou, G.; Hendrickson, D. N. *Inorg. Chem.* **1999**, *38*, 5329-5340.

72. Guo, Y.-N.; Xu, G.-F.; Guo, Y.; Tang, J. *Dalton Trans.* **2011**, *40*, 9953-9963.
73. Wernsdorfer, W. *Supercond. Sci. Technol.* **2009**, *22*, 064013.
74. Woodruff, D. N.; Winpenny, R. E. P.; Layfield, R. A. *Chem. Rev.* **2013**, *113*, 5110-5148.
75. Habib, F.; Murugesu, M. *Chem. Soc. Rev.* **2013**, *42*, 3278-3288.
76. Zhang, P.; Guo, Y.-N.; Tang, J. *Coord. Chem. Rev.* **2013**, *257*, 1728-1763.
77. Feltham, H. L. C.; Brooker, S. *Coord. Chem. Rev.* **2014**, *276*, 1-33.
78. Sessoli, R.; Powell, A. K. *Coord. Chem. Rev.* **2009**, *253*, 2328-2341.
79. Glaser, T. *Chem. Commun.* **2011**, *47*, 116-130.
80. Liu, J.-L.; Wu, J.-Y.; Chen, Y.-C.; Mereacre, V.; Powell, A. K.; Ungur, L.; Chibotaru, L. F.; Chen, X.-M.; Tong, M.-L. *Angew. Chem. Int. Ed.* **2014**, n/a-n/a.
81. Liu, J.-L.; Chen, Y.-C.; Zheng, Y.-Z.; Lin, W.-Q.; Ungur, L.; Wernsdorfer, W.; Chibotaru, L. F.; Tong, M.-L. *Chem. Sci.* **2013**, *4*, 3310-3316.
82. Zaleski, C. M.; Depperman, E. C.; Kampf, J. W.; Kirk, M. L.; Pecoraro, V. L. *Angew. Chem., Int. Ed.* **2004**, *43*, 3912-3914.
83. Zaleski, C. M.; Kampf, J. W.; Mallah, T.; Kirk, M. L.; Pecoraro, V. L. *Inorg. Chem.* **2007**, *46*, 1954-1956.
84. Deb, A.; Boron, T. T.; Itou, M.; Sakurai, Y.; Mallah, T.; Pecoraro, V. L.; Penner-Hahn, J. E. *J. Am. Chem. Soc.* **2014**, *136*, 4889-4892.
85. Zaleski, C. M.; Depperman, E. C.; Kampf, J. W.; Kirk, M. L.; Pecoraro, V. L. *Inorg. Chem.* **2006**, *45*, 10022-10024.
86. Zaleski, C. M.; Cutland-Van Noord, A. D.; Kampf, J. W.; Pecoraro, V. L. *Cryst. Growth Des.* **2007**, *7*, 1098-1105.
87. Pobell, F., The 3He–4He Dilution Refrigerator. In *Matter and Methods at Low Temperatures*, Springer Berlin Heidelberg: 2007; pp 149-189.
88. Pobell, F., Refrigeration by Adiabatic Nuclear Demagnetization. In *Matter and Methods at Low Temperatures*, Springer Berlin Heidelberg: 2007; pp 215-258.
89. Pobell, F., Refrigeration by Adiabatic Demagnetization of a Paramagnetic Salt. In *Matter and Methods at Low Temperatures*, Springer Berlin Heidelberg: 2007; pp 203-213.
90. Debye, P. *Ann. Phys.* **1926**, *81*, 1154-1160.
91. Giauque, W. F.; Macdougall, D. P. *Phys. Rev.* **1933**, *43*, 768-768.
92. Fisher, R. A.; Hornung, E. W.; Brodale, G. E.; Giauque, W. F. *J. Chem. Phys.* **1973**, *58*, 5584-5604.
93. Vilches, O. E.; Wheatley, J. C. *Rev. Sci. Instrum.* **1966**, *37*, 819-831.
94. Mcmichael, R. D.; Ritter, J. J.; Shull, R. D. *J. Appl. Phys.* **1993**, *73*, 6946-6948.
95. Supanich, M.; Timbie, P. *AIP Conf. Proc.* **2002**, *605*, 387-390.
96. Duval, J.-M.; Cain, B. M.; Timbie, P. T. In *A miniature continuous adiabatic demagnetization refrigerator with compact shielded superconducting magnets*, 2004; pp 802-811.
97. Shirron, P.; Wegel, D.; Dipirro, M. *AIP Conf. Proc.* **2006**, *850*, 1573-1574.
98. Evangelisti, M.; Luis, F.; De Jongh, L. J.; Affronte, M. *J. Mater. Chem.* **2006**, *16*, 2534-2549.
99. Evangelisti, M., Molecule-Based Magnetic Coolers: Measurement, Design and Application. In *Molecular Magnets*, Bartolomé, J.; Luis, F.; Fernández, J. F., Eds. Springer Berlin Heidelberg: 2014; pp 365-387.
100. Liu, J.-L.; Chen, Y.-C.; Guo, F.-S.; Tong, M.-L. *Coord. Chem. Rev.* **2014**, *281*, 26-49.
101. Tocado, L.; Palacios, E.; Burriel, R. *J. Magn. Magn. Mater.* **2005**, *290–291, Part 1*, 719-722.
102. Pecharsky, V. K.; Gschneidner Jr, K. A. *J. Magn. Magn. Mater.* **1999**, *200*, 44-56.
103. Evangelisti, M.; Roubeau, O.; Palacios, E.; Camón, A.; Hooper, T. N.; Brechin, E. K.; Alonso, J. J. *Angew. Chem. Int. Ed.* **2011**, *50*, 6606-6609.
104. Phan, M.-H.; Yu, S.-C. *J. Magn. Magn. Mater.* **2007**, *308*, 325-340.

105. Hooper, T. N.; Schnack, J.; Piligkos, S.; Evangelisti, M.; Brechin, E. K. *Angew. Chem. Int. Ed.* **2012**, *51*, 4633-4636.
106. Nasa Advanced Space Transportation Program: Paving the Highway to Space. (accessed Oct 31).
107. Torres, F.; Hernández, J. M.; Bohigas, X.; Tejada, J. *Appl. Phys. Lett.* **2000**, *77*, 3248-3250.
108. Low, D. M.; Jones, L. F.; Bell, A.; Brechin, E. K.; Mallah, T.; Riviere, E.; Teat, S. J.; Mcinnes, E. J. L. *Angew. Chem. Int. Ed.* **2003**, *42*, 3781-3784.
109. Evangelisti, M.; Candini, A.; Ghirri, A.; Affronte, M.; Brechin, E. K.; Mcinnes, E. J. L. *Appl. Phys. Lett.* **2005**, *87*, -.
110. Evangelisti, M.; Candini, A.; Ghirri, A.; Affronte, M.; Piligkos, S.; Brechin, E. K.; Mcinnes, E. J. L. *Polyhedron* **2005**, *24*, 2573-2578.
111. Shaw, R.; Laye, R. H.; Jones, L. F.; Low, D. M.; Talbot-Eeckelaers, C.; Wei, Q.; Milios, C. J.; Teat, S.; Helliwell, M.; Raftery, J.; Evangelisti, M.; Affronte, M.; Collison, D.; Brechin, E. K.; Mcinnes, E. J. L. *Inorg. Chem.* **2007**, *46*, 4968-4978.
112. Chen, Y.-C.; Guo, F.-S.; Liu, J.-L.; Leng, J.-D.; Vrábel, P.; Orendáč, M.; Prokleška, J.; Sechovský, V.; Tong, M.-L. *Chem. Eur. J.* **2014**, *20*, 3029-3035.
113. Chen, Y.-C.; Qin, L.; Meng, Z.-S.; Yang, D.-F.; Wu, C.; Fu, Z.; Zheng, Y.-Z.; Liu, J.-L.; Tarasenko, R.; Orendac, M.; Prokleska, J.; Sechovsky, V.; Tong, M.-L. *J. Mater. Chem. A* **2014**, *2*, 9851-9858.
114. Pedersen, K. S.; Lorusso, G.; Morales, J. J.; Weyhermüller, T.; Piligkos, S.; Singh, S. K.; Larsen, D.; Schau-Magnussen, M.; Rajaraman, G.; Evangelisti, M.; Bendix, J. *Angew. Chem. Int. Ed.* **2014**, *53*, 2394-2397.
115. Eliseeva, S. V.; Bunzli, J.-C. G. *Chem. Soc. Rev.* **2010**, *39*, 189-227.
116. Kido, J.; Nagai, K.; Ohashi, Y. *Chem. Lett.* **1990**, *19*, 657-660.
117. Bünzli, J.-C. G.; Eliseeva, S. V. *J. Rare Earth* **2010**, *28*, 824-842.
118. Correia, S. F. H.; De Zea Bermudez, V.; Ribeiro, S. J. L.; Andre, P. S.; Ferreira, R. a. S.; Carlos, L. D. *J. Mater. Chem. A* **2014**, *2*, 5580-5596.
119. Moore, E. G.; Xu, J.; Dodani, S. C.; Jocher, C. J.; D'aléO, A.; Seitz, M.; Raymond, K. N. *Inorg. Chem.* **2010**, *49*, 4156-4166.
120. Comby, S.; Imbert, D.; Chauvin, A.-S.; Bünzli, J.-C. G. *Inorg. Chem.* **2005**, *45*, 732-743.
121. Verwilst, P.; Eliseeva, S. V.; Vander Elst, L.; Burtea, C.; Laurent, S.; Petoud, S.; Muller, R. N.; Parac-Vogt, T. N.; De Borggraeve, W. M. *Inorg. Chem.* **2012**, *51*, 6405-6411.
122. Trivedi, E. R.; Eliseeva, S. V.; Jankolovits, J.; Olmstead, M. M.; Petoud, S.; Pecoraro, V. L. *J. Am. Chem. Soc.* **2014**, *136*, 1526-1534.
123. Binnemans, K. *Chem. Rev.* **2009**, *109*, 4283-4374.
124. E., S. V.; Bunzli, J.-C. G. *Chem. Soc. Rev.* **2010**, *39*, 189-227.
125. Bunzli, J.-C. G.; Piguet, C. *Chem. Soc. Rev.* **2005**, *34*, 1048-1077.
126. Jankolovits, J.; Andolina, C. M.; Kampf, J. W.; Raymond, K. N.; Pecoraro, V. L. *Angew. Chem., Int. Ed.* **2011**, *50*, 9660-9664.
127. Law, G.-L.; Pham, T. A.; Xu, J.; Raymond, K. N. *Angew. Chem. Int. Ed.* **2012**, *51*, 2371-2374.

# Chapter II

# Assessing the Exchange Coupling and the Slow Relaxation of the Magnetization in Binuclear Lanthanide(III) Metallacrown Complexes

## 2.1 Introduction

In order to increase spin, magnetic anisotropy and subsequently, the energy barrier, much of the current SMM research has shifted from transition metal complexes such as $[Mn_{12}O_{12}(OCR)_{16}(H_2O)_4]$,[1-2] to lanthanide based complexes.[3] Due to strong unquenched orbital angular momentum and significant spin-orbit coupling, lanthanide ions possess large intrinsic anisotropy such that even mononuclear lanthanide complexes can exhibit slow magnetic relaxation.[4-10]

Unlike their transition-metal counterparts, lanthanide-based SMMs are at the weak-exchange limit,[11] and have dynamic magnetic behavior which cannot be adequately described within the framework of the zero-field splitting phenomenon,[12] which can be used to understand the origin of the energy barrier in transition-metal SMMs. Furthermore, lanthanide SMMs display dynamic magnetization behavior that can be complicated by the presence of multiple relaxation pathways.[13] Nonetheless, when it comes to designing SMMs with large energy barriers, more metal centers may be better, as it has been shown that metal-metal exchange coupling can aid in suppressing quantum tunneling phenomena that occur in transition metal complexes[14] and later for lanthanide-based SMMs.[15]

Correspondingly, SMMs with some of the largest energy barriers reported to date have been multinuclear lanthanide complexes.[16-18] Unfortunately, due to the radial contraction of 4*f* orbitals, lanthanide-lanthanide interactions tends to be weak and most polymetallic lanthanide SMMs have magnetic properties which are of single-ion origin;[3] for instance a tetranuclear $Dy^{III}_4$ exhibited barrier heights of 9.7 and 107 K corresponding to two crystallographically independent $Dy^{III}$ sites.[17] In these compounds, the variable temperature ac data show only one distinct relaxation peak indicative of the single-ion relaxation. In order to understand magnetic behavior in complex polynuclear SMMs, simpler model systems are essential in elucidating the underlying *4f-4f* interactions.[19-23]

Although the traditional MC design strategy only predicts mono-lanthanide compounds, poly-lanthanide metallacrowns can be synthesized by connecting MCs through carboxylate bridges[24-25] or by serendipity, as with various $Ln^{III}$-$Mn^{III}$ compounds synthesized by Boron.[26] The structural promiscuity of typical metallacrown ligands such as salicylhydroxamic acid ($H_3$shi) allows for crystallization of unpredictable structure types. This chapter will focus on the synthesis and characterization of an isotructural series of symmetric hexanuclear $Ga_4^{III}$-$Ln_2^{III}$ compounds with the general formula $[Ga_4Ln_2(shi^{3-})_4(Hshi^{2-})_2(H_2shi^{-})_2(C_5H_5N)_4(CH_3OH)(H_2O)] \cdot 3C_5H_5N \cdot 2CH_3OH \cdot 3H_2O$ ($Ln^{III}$ = $Gd^{III}$, $Tb^{III}$, $Dy^{III}$, $Er^{III}$, $Y^{III}$, $Y^{III}_{0.9}Dy^{III}_{0.1}$), and will be referred to as **$Ga_4Ln_2$**. To the best of our knowledge, compound **$Ga_4Dy_2$** is the first reported example of an antiferromagnetically coupled Ising-like lanthanide dimer with a diamagnetic ground state that shows a slow relaxation of the magnetization and an opening of the hysteresis loop at zero magnetic field, a behavior that was observed in the antiferromagnetically coupled $Dy_3$ complexes.[27]

## 2.2 Experimental

All reagents were purchased from commercial sources and were used without further purification. Elemental analysis was performed by Atlantic Microlabs Inc. All reactions were carried under aerobic conditions.

***Synthetic Methods***

**$Gd_2Ga_4$**: Salicylhydroxamic acid (153.1 mg, 1.000 mmol), $Gd(NO_3)_3{\cdot}6H_2O$ (112.8 mg, 0.2500 mmol), $Ga(NO_3)_3{\cdot}xH_2O$ (127.9 mg, 0.5000 mmol) were dissolved in 46 mL methanol. 13 mL pyridine was added drop wise to this solution, followed by 6.5 mL $H_2O$. The solution was stirred for 30 seconds and then filtered. Slow evaporation of half of the solution yielded crystalline compound after 2 weeks. Yield: 0.0850 g (26.9%), Anal. Calcd for $Gd_2Ga_4C_{94}H_{93.62}N_{15}O_{31.31}$: C, 44.66; H, 3.73; N, 8.31. Found: C, 43.94; H, 3.64; N, 8.37. Single-crystal unit cell: monoclinic, space group C2/c, $a$ = 25.2329 Å, $b$ = 22.0543 Å, $c$ = 17.9967 Å, α = 90.0000° $\beta$ =, 99.090°, γ = 90.0000°, V = 10043.9599 $Å^3$.

General Procedure for **$Tb_2Ga_4$, $Dy_2Ga_4$, $Er_2Ga_4$ and $Y_2Ga_4$**: Salicylhydroxamic acid (153.1 mg, 1.000 mmol), $Ln(NO_3)_3{\cdot}xH_2O$ (0.2500 mmol), $Ga(NO_3)_3{\cdot}xH_2O$ (127.9 mg, 0.5000 mmol) were dissolved in 21 mL methanol. 6 mL pyridine was added dropwise to this solution, followed by 3 mL $H_2O$. The solution was stirred for 30 seconds and then filtered. Slow evaporation of half of the solution yielded crystalline compound after 2 weeks.

[**$Ga_4Tb_2$**] Yield: 0.0892 g (28.3%), Anal. Calcd for $Tb_2Ga_4C_{94}H_{93}N_{15}O_{31}$: C, 44.70; H, 3.71; N, 8.32. Found: C, 44.45; H, 3.63; N, 8.38. Single-crystal unit cell: monoclinic, space group *C*2/*c*, $a$ = 25.1697 Å, $b$ = 22.1217 Å, $c$ = 17.9895 Å, $\beta$ = 99.302°, V = 9884.8 $Å^3$.

[**$Ga_4Dy_2$**] Yield: 0.1291 g (40.8%), Anal. Calcd for $Dy_2Ga_4C_{94}H_{93}N_{15}O_{31}$: C, 44.58; H, 3.70; N, 8.30. Found: C, 44.76; H, 3.41; N, 8.38. Single-crystal unit cell: monoclinic, space group *C*2/*c*, *a* = 25.1638 Å, *b* = 22.1781 Å, *c* = 18.0649 Å, $\beta$ = 99.353˚, V = 9947.72 $Å^3$.

[**$Ga_4Er_2$**] Yield: 0.0947 g (29.8%), Anal. Calcd for $Er_2Ga_4C_{93}H_{91}N_{15}O_{31}$: C, 44.41; H, 3.69; N, 8.26. Found: C, 44.28; H, 3.58; N, 8.49. Single-crystal unit cell: monoclinic, space group *C*2/*c*, *a* = 25.1476 Å, *b* = 22.1380 Å, *c* = 18.0285 Å, α = 90.0000˚ $\beta$ = 99.1768˚, γ = 90.0000 ˚, V = 9908.3211 $Å^3$.

[**$Ga_4Y_2$**] Yield: 0.1607 g (53.9%), Anal. Calcd for $Y_2Ga_4C_{94}H_{93}N_{15}O_{31}$: C, 47.328; H, 3.929; N, 8.807. Found: C, 47.54; H, 3.75; N, 8.86. Single-crystal unit cell: monoclinic, space group *C*2/*c*, *a* = 25.1043 Å, *b* = 22.1794 Å, *c* = 18.0733 Å, α = 90.000˚ $\beta$ = 99.377˚, γ = 90.000 ˚, V = 9908.3211 $Å^3$.

**$Y_{1.8}Dy_{0.2}Ga_4$**: Salicylhydroxamic acid (153.1 mg, 1.000 mmol), $Dy(NO_3)_3·5H_2O$ (11.0 mg, 0.0250 mmol), $Y(NO_3)_3·5H_2O$ (82.1 mg, 0.225 mmol), $Ga(NO_3)_3·xH_2O$ (127.9 mg, 0.5 mmol) were dissolved in 21 mL methanol. 6 mL pyridine was added drop wise to this solution, followed by 3 mL $H_2O$. The solution was stirred for 30 seconds and then filtered. Slow evaporation of half of the solution yielded crystalline compound after 2 weeks. Yield: 0.1363 g (45.4%), Anal. Calcd for $Y_{1.8}Dy_{0.2}Ga_4C_{94}H_{93}N_{15}O_{31}$: C, 47.04; H, 3.91; N, 8.75. Found: C, 46.82; H, 3.76; N, 8.94. Single-crystal unit cell: monoclinic, space group *C*2/*c*, *a* = 25.1476 Å, *b* = 22.1380 Å, *c* = 18.0285 Å, α = 90.0000˚ $\beta$ = 99.1768˚, γ = 90.0000 ˚, V = 9908.3211 $Å^3$.

***Physical Methods***

*X-ray Crystallography*. Single-crystal X-ray diffraction data for **$Ga_4Gd_2$**, **$Ga_4Dy_2$**, **$Ga_4Er_2$** and **$Ga_4Y_2$** were collected by Jeff W. Kampf at the University of Michigan. The crystal data for **$Ga_4Tb_2$** were collected by Régis Guillot at the Université de Paris Sud 11 in Orsay. I completed structural refinements on all the data sets.

Crystal data for compound **$Ga_4Gd_2$** were collected at 85(2) K on a Bruker SMART-APEX CCD-based X-ray diffractometer equipped with a low temperature device and fine-focus Mo-target X-ray tube (λ = 0.71073 Å), operated at 1500 W power (50 kV, 30 mA). The frames were integrated with the Bruker SAINT[28] software package with a narrow frame algorithm. The data were processed with SADABS[29] and corrected for absorption.

Crystal data for compound **$Ga_4Tb_2$** were collected on a Kappa X8 APPEX II Bruker diffractometer with graphite-monochromated Mo Ka radiation ( = 0.71073 Å). Crystals were mounted on a CryoLoop (Hampton Research) with Paratone-N (Hampton Research) as cryoprotectant and then flashfrozen in a nitrogen-gas stream at 100 K. The temperature of the crystal was maintained at the selected value (100K) by means of a 700 series Cryostream cooling device to within an accuracy of ±1 K. The data were corrected for Lorentz polarization, and absorption effects.

Crystal data for compounds **$Ga_4Dy_2$**, **$Ga_4Er_2$** and **$Ga_4Y_2$** were collected at 85(2) K on an AFC10K Saturn 944+ CCD-based X-ray diffractometer equipped with a Micromax007HF Cu-target microfocus rotating anode (λ = 1.54187 Å), operated at 1200 W power (40 kV, 30 mA). The data were processed with CrystalClear 2.0 and corrected for absorption.[30]

All structures were solved and refined with the SHELXTL (version 6.12) software package.[31] All non-hydrogen atoms were refined anisotropically. Hydrogen atoms are placed in their idealized positions. Additional details are provided in Table 2.1. Selected bond lengths are given in Table 2.2.

*Magnetic Measurements.* Variable-temperature susceptibility, variable-field magnetization and ac susceptibility measurements on polycrystalline samples mulled in eicosane were performed on a Quantum Design MPMS SQUID magnetometer. Variable-temperature dc susceptibility measurements were performed at 2000 Oe from 2-300 K. Isothermal magnetization measurements were performed at 2 K from 0-7 T. AC magnetic susceptibility measurements were done at both zero and applied fields (2000 Oe for **$Ga_4Dy_2$** and 750 Oe for **$Ga_4YDy$**) with an ac drive field of 3 Oe at frequencies ranging from 1 to 1488 Hz. Dc susceptibilities were corrected for the sample holder and eicosane and for diamagnetism of constituent atoms using Pascal's constants.

*Micro-SQUID Measurements*. Micro-SQUID measurements were performed by Wolfgang Wernsdorfer (Université J. Fourier, France). Magnetization measurements on oriented single crystals were carried out with an array of micro-SQUIDs.[32] The field aligned parallel to the easy-axis of magnetization by the transversal field method.[33] Measurements were performed at a temperature range from 0.03 to 5 K in fields up to 1.1 T with sweep rates between 0.008 and 0.280 T/s.

*Computational Details*. *Ab initio* calculations were performed by Hélène Bolvin (Université Toulouse III, France) with assistance from Jochen Autschbach and Frederic Gendron (University at Buffalo, State University of New York). The following computational methodologies were written by Hélène Bolvin. Calculations are performed using the crystallographic geometry.

**Table 2.1.** Crystallographic Details for the isostructural $\mathbf{Ga_4Ln_2}$ complexes.

| | $Ga_4Gd_2$ | $Ga_4Tb_2$ | $Ga_4Dy_2$ | $Ga_4Er_2$ | $Ga_4Y_2$ |
|---|---|---|---|---|---|
| mol formula | $Ga_4Gd_2C_{94}H_{93.62}N_{15}O_{31.31}$ | $Ga_4Tb_2C_{94}H_{93}N_{15}O_{31}$ | $Ga_4Dy_2C_{94}H_{93}N_{15}O_{31}$ | $Ga_4Er_2C_{93}H_{91}N_{15}O_{31}$ | $Ga_4Y_2C_{94}H_{93}N_{15}O_{31}$ |
| fw (g/mol) | 2527.80 | 2525.55 | 2532.71 | 2528.21 | 2385.53 |
| cryst syst/ space group | Monoclinic, *C*2/c | Monoclinic, *C*2/c | Monoclinic, *C*2/c | Monoclinic, *C*2/c | Monoclinic, *C*2/c |
| *T* (K) | 85(2) | 100(1) | 85(2) | 85(2) | 85(2) |
| wavelength (Å) | 0.71073 | 0.71073 | 1.54178 | 1.54178 | 1.54178 |
| *a* (Å) | 25.233(5) | 25.1697(6) | 25.1638(18) | 25.1476(5) | 25.1053(18) |
| *b* (Å) | 22.054(4) | 22.1217(6) | 22.1781(4) | 22.1380(4) | 22.1794(4) |
| *c* (Å) | 17.997(4) | 17.9895(5) | 18.0649(3) | 18.0285(13) | 18.0733(3) |
| α (deg) | 90 | 90 | 90 | 90 | 90 |
| β (deg) | 99.09(3) | 99.3020(10) | 99.353(7) | 99.177(7) | 99.377(7) |
| γ (deg) | 90 | 90 | 90 | 90 | 90 |
| *V* (Å$^3$) | 9889.3(3) | 9884.8(5) | 9947.7(8) | 9908.3 | 9929.1(8) |
| *Z* | 4 | 4 | 4 | 4 | 4 |
| density, ρ (g/cm$^3$) | 1.698 | 1.697 | 1.691 | 1.695 | 1.596 |
| abs coeff, μ (mm$^{-1}$) | 2.486 | 2.462 | 9.839 | 4.949 | 3.460 |
| *F*(000) | 5060 | 5056 | 5063 | 5048 | 4848 |
| θ range for data collection (deg) | 1.59 – 25.44 | 1.59 – 30.67 | 3.44 – 68.23 | 3.45 – 68.24 | 3.44 – 68.25 |
| limiting indices | $-30 \le h \le 30$, $-26 \le k \le 26$, $-21 \le l \le 21$ | $-30 \le h \le 36$, $-31 \le k \le 31$, $-25 \le l \le 25$ | $-27 \le h \le 29$ $-26 \le k \le 26$ $-21 \le l \le 21$ | $-30 \le h \le 30$, $-26 \le k \le 26$, $-21 \le l \le 21$ | $-30 \le h \le 30$, $-26 \le k \le 25$, $-21 \le l \le 21$ |
| reflns collected/ unique | 76042 / 9136 | 152738 / 15061 | 133023 / 9072 | 139170 / 9069 | 140855 / 9097 |
| completeness to θ (%) | 99.8 | 99.2 | 99.5 | 99.9 | 100.0 |
| no. of data/ restraints/ params | 9136 / 128 / 745 | 15061 / 70 / 750 | 9072 / 92 / 746 | 9069 / 76 / 741 | 9097 / 175 / 744 |
| goodness of fit on $F^2$ | 1.075 | 1.130 | 1.031 | 1.100 | 1.103 |
| final *R* indices [$I > 2\sigma(I)$] | R1[a] = 0.0422 wR2[b] = 0.1051 | R1[a] = 0.0372 wR2[b] = 0.0814 | R1[a] = 0.0572 wR2[b] = 0.1545 | R1[a] = 0.0868 wR2[b] = 0.2382 | R1[a] = 0.0437 wR2[b] = 0.1221 |
| *R* indices (all data) | R1[a] = 0.0616 wR2[b] = 0.1206 | R1[a] = 0.0657 wR2[b] = 0.0980 | R1[a] = 0.0627 wR2[b] = 0.1591 | R1[b] = 0.0957 wR2[a] = 0.2574 | R1[a] = 0.0459 wR2[b] = 0.1238 |
| largest diff peak and hole (e$^-$ Å$^{-3}$) | 1.657 and -0.742 | 1.467 and -0.899 | 1.792 and -1.514 | 2.175 and -0.899 | 0.942 and -0.745 |

[a]$R1 = \Sigma(||F_o| - |F_c||)/\Sigma|F_o|$. [b]$wR2 = [\Sigma[w(F_o^2 - F_c^2)^2]/\Sigma[w(F^\circ)^2]]^{1/2}$; $w = 1/[\sigma^2(F_o^2) + (mp)^2 + np]$; $p = [\max(F_o^2,0) + 2F_c^2]/3$ (*m* and *n* are constants); $\sigma = [\Sigma[w(F_o^2 - F_c^2)^2]/(n - p)]^{1/2}$.

**Table 2.2.** Selected bond lengths for **$Ga_4Ln_2$** complexes.

| Compound | Bond | Length (Å) | Compound | Bond | Length (Å) |
|---|---|---|---|---|---|
| **$Ga_4Gd_2$** | Gd(1)-O(1) | 2.301(4) | **$Ga_4Tb_2$** | Tb(1)-O(1) | 2.272(3) |
| | Gd(1)-O(9) | 2.326(3) | | Tb(1)-O(9) | 2.303(3) |
| | Gd(1)-O(2) | 2.329(3) | | Tb(1)-O(2) | 2.311(3) |
| | Gd(1)-O(2a) | 2.343(3) | | Tb(1)-O(2a) | 2.323(3) |
| | Gd(1)-O(5) | 2.349(3) | | Tb(1)-O(5) | 2.333(3) |
| | Gd(1)-O(510) | 2.381(12) | | Tb(1)-O(510) | 2.358(18) |
| | Gd(1)-O(7) | 2.427(3) | | Tb(1)-O(7) | 2.417(3) |
| | Gd(1)-O(11) | 2.550(3) | | Tb(1)-O(500) | 2.46(2) |
| | Gd(1)-O(500) | 2.56(4) | | Tb(1)-O(11) | 2.541(3) |
| **$Ga_4Dy_2$** | Dy(1)-O(1) | 2.268(3) | **$Ga_4Er_2$** | Er(1)-O(1) | 2.251(4) |
| | Dy(1)-O(9) | 2.309(3) | | Er(1)-O(9) | 2.282(5) |
| | Dy(1)-O(2) | 2.319(4) | | Er(1)-O(2) | 2.296(4) |
| | Dy(1)-O(2a) | 2.320(3) | | Er(1)-O(2a) | 2.298(4) |
| | Dy(1)-O(5) | 2.328(3) | | Er(1)-O(5) | 2.308(4) |
| | Dy(1)-O(510) | 2.365(11) | | Er(1)-O(510) | 2.23(2) |
| | Dy(1)-O(7) | 2.403(4) | | Er(1)-O(7) | 2.370(4) |
| | Dy(1)-O(500) | 2.48(2) | | Er(1)-O(500) | 2.48(2) |
| | Dy(1)-O(11) | 2.530(4) | | Er(1)-O(11) | 2.513(5) |
| **$Ga_4Y_2$** | Y(1)-O(1) | 2.258(2) | **Ln-Ln Distance (Å)** | | |
| | Y(1)-O(9) | 2.288(2) | | | |
| | Y(1)-O(2) | 2.292(2) | | $Ga_4Gd_2$ | 3.8558(9) |
| | Y(1)-O(2a) | 2.313(2) | | $Ga_4Tb_2$ | 3.8323(4) |
| | Y(1)-O(5) | 2.316(2) | | $Ga_4Dy_2$ | 3.8393(7) |
| | Y(1)-O(510) | 2.369(10) | | $Ga_4Er_2$ | 3.8252(8) |
| | Y(1)-O(7) | 2.393(2) | | $Ga_4Y_2$ | 3.8247(6) |
| | Y(1)-O(500) | 2.397(19) | | | |
| | Y(1)-O(11) | 2.524(2) | | | |

Magnetic properties were calculated using first principle methods on a monomeric species by replacing one of the lanthanide by a diamagnetic lutetium of configuration $4f^{14}$. Since the two lanthanide atoms are related by an inversion center, there is only one type of monomer. All atoms are described with all electron basis sets ANO-RCC,[34-35] Ln atoms with TZP quality, N and O atoms with DZP quality and other atoms with DZ quality. The excited states of the complexes have been calculated with the SO-CASSCF method using the MOLCAS78 suite of programs.[36] The active space consists of n electrons in the 7 4f orbitals for an atom of configuration $4f^n$. First, a CASSCF (Complete Active Space Self Consistent Field) calculation is

performed:[37] all the states with the maximal value of the spin are considered in the state average procedure. In the case of gadolinium, all the sextet states are considered in addition to the octuplet ground state. Spin-orbit coupling is evaluated as a state interaction between all CASSCF wave functions by the RASSI (Restricted Active Space State Interaction) method.[38] Spin-Orbit (SO) integrals are evaluated within the AMFI approximation.[39] The calculation of all the properties is implemented in a local program. g factors are calculated according to reference [40] even in the case of non-degenerate states (see Appendix A for details). The dipolar magnetic interaction is calculated as

$$\widehat{H}^{dip} = \frac{\mu_0}{4\pi R^3}\left\{\widehat{\vec{M}}^A . \widehat{\vec{M}}^B - 3\widehat{M}_z^A\ \widehat{M}_z^B\right\} \quad (2.1)$$

where $R$ is the intermetallic distance, $z$ the intermetallic direction and $\mu_0$ the magnetic constant. The exchange interactions are carried by the spin densities and are described by a Heisenberg-Dirac-Van Vleck (HDVV) Hamiltonian

$$\widehat{H}^{Heis} = -J\ \hat{\vec{S}}^A \cdot \hat{\vec{S}}^B \quad (2.2)$$

$\widehat{\vec{M}}^{A(B)}$ and $\hat{\vec{S}}^{A(B)}$ are the total and spin momentum operators for site A(B). This scheme has been first proposed by Lines in the 70s,[41] it has been applied to lanthanide complexes by Sutter *et al* in 2002[42] and since 2007, is applied in the group of Chibotaru[43] A local modification of MOLCAS was used to generate natural spin orbitals (NSOs) from SO-CASSCF calculations[44] (Appendix A).

**2.3 Results and Discussion**

**Synthesis and Characterization.** The multidentate ligand salicylhydroxamic acid ($H_3$shi) has been used in the synthesis of numerous metallacrown complexes,[45] including several single-molecule magnets.[46-48] Both predictable structure types (such as 9-MC-3, 12-MC-4) as well as compounds with unpredictable molecular geometry can be

synthesized with $H_3$shi by adjusting reaction and solvent conditions, allowing for isolation and study of a wide array of multinuclear metallacrown complexes. Pyridine (which acts as a base, a solvent and a ligand) has unique properties, which have resulted in several metallacrown complexes with both previously known and new structure types.[46, 49-50] This multipurpose solvent aids in crystallization by forming π-interactions and coordinates to metal sites, forming structures whose architectures are directed by π-interactions and steric effects.

The reaction of $H_3$shi, $Ga(NO_3)_3 \cdot xH_2O$ and $Ln(NO_3) \cdot xH_2O$ a 4:2:1 stoichiometric ratio in a solution of methanol, pyridine and water followed by slow evaporation of solvent afforded neutral macrocyclic complexes (Scheme 2.1) with the general formula $[Ga_4Ln_2(shi^{3-})_4(Hshi^{2-})_2(H_2shi^{-})_2(C_5H_5N)_4(CH_3OH)(H_2O)] \cdot 3C_5H_5N \cdot 2CH_3OH \cdot 3H_2O$. The structures of **$Ga_4Ln_2$** compounds were determined by X-ray crystallography to be isostructural and crystallize in the monoclinic space group *C*2/c (Table 2.1). Slight differences in the composition of bound and lattice solvents were observed across the series of complexes. Compound **$Ga_4YDy$** was determined to have the same unit cell parameters and is isostructural to **$Ga_4Dy_2$** and **$Ga_4Y_2$**. It was synthesized with 10% $Dy^{III}$ and 90% $Y^{III}$ in solution. Statistically speaking, such a reaction would form crystals composed of 81% **$Ga_4Y_2$** (diamagnetic), 18% **$Ga_4YDy$** and 1% **$Ga_4Dy_2$**.

As a representative example, the structure of compound **$Ga_4Dy_2$** (Figure 2.1) can be described as a centrosymmetric $\mu_2$-oxo bridged di-lanthanide core surrounded by four peripheral $Ga^{III}$ ions. In the core moiety of the asymmetric unit, one $Dy^{III}$ and two $Ga^{III}$ ions are chelated by four fully and partially deprotonated ligands and coordinated by pyridine and methanol or water solvent molecules. In Figure 2.1, Dy1 is chelated by the carbonyl (O1) and hydroximate oxygens

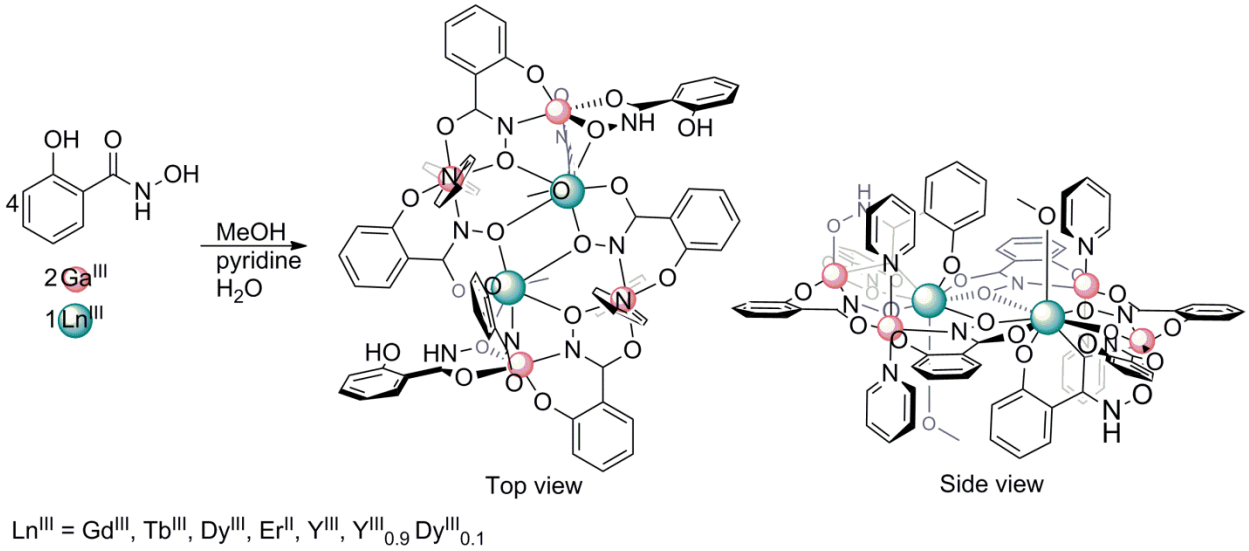


**Scheme 2.1.** Synthesis of **$Ga_4Ln_2$** complexes.

(O2) carbonyl (O1) and hydroximate oxygens (O2) of an in-plane $shi^{3-}$ and by the carbonyl (O7) and phenoxide oxygens of an out-of-plane $Hshi^{2-}$. The symmetry-generated hydroximate oxygen O2a also coordinates to Dy1, to form a $Dy_2(\mu_2\text{-}O)_2$ core. Hydroximate oxygens from an in-plane $shi^{3-}$ (O5) and $Hshi^{2-}$ (O11) also coordinate, bridging Dy1 to Ga2a and Ga1 respectively. Dy1 is capped by a disordered water (O510) or methanol (O500, C500) with shared occupancy, to complete the coordination sphere around Dy1 which can be described as having distorted 8-coordinate trigonal dodecahedral geometry as determined by the SHAPE software (Appendix A, Table A1).[51] The four outer $Ga^{III}$ cations, with roughly octahedral geometry, surround the two central $Dy^{III}$ ions and are ligated by fully and partially deprotonated $H_3shi$. Four fully deprotonated $shi^{3-}$ and two $H_2shi^-$ coordinate the four $Ga^{III}$ and two $Dy^{III}$ ions to form the molecular plane, with two doubly deprotonated $Hshi^{2-}$ pointing above and below the plane. (Figure 2.1).

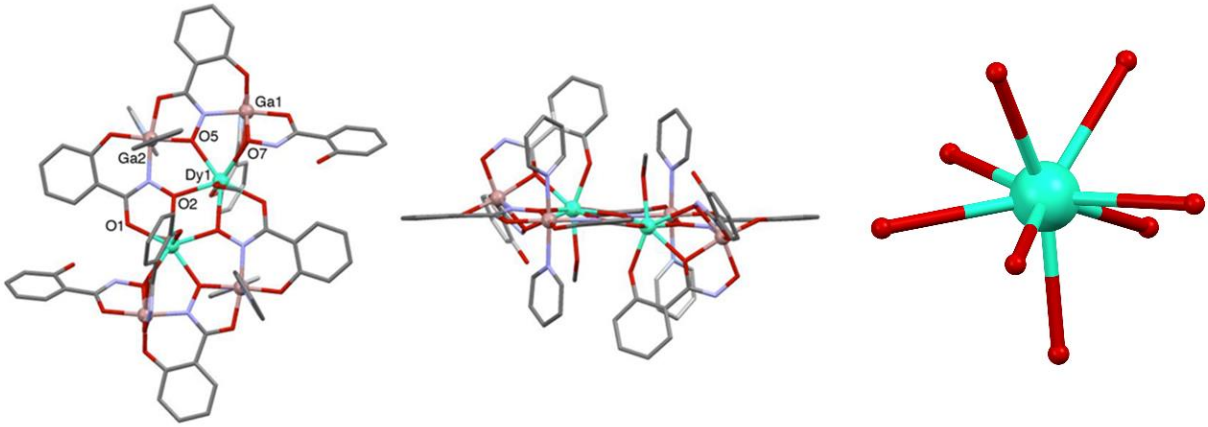


**Figure 2.1.** X-ray crystal structure of complex **$Ga_4Dy_2$**. Top view (left) and Side view (middle). The first coordination sphere around the $Dy^{III}$ is in distorted trigonal dodecahedral geometry (right). Color code: teal spheres = $Dy^{III}$; salmon spheres = $Ga^{III}$; gray = C; red = O; blue = N. Hydrogen atoms and lattice solvents are omitted for clarity.

**DC Magnetic Studies and Theoretical Calculations.** For complexes **$Ga_4Gd_2$**, **$Ga_4Tb_2$**, **$Ga_4Dy_2$**, **$Ga_4Er_2$** and **$Ga_4YDy$**, the variable-temperature dc susceptibility measurements were performed at an applied field of 2000 Oe from 2 to 300 K (Figure 2.2).; the variable-field magnetization measurements were performed at 2 K from 0 to 7 T (Figure 2.3). The general behavior of all compounds is consistent with other lanthanide complexes reported in the literature.[21, 27, 52]

**(i) $Ga_4Gd_2$.** The room temperature $\chi_m T$ value for **$Ga_4Gd_2$** ($Gd^{III}$: $^8S_{7/2}$, 15.9 $cm^3$ K $mol^{-1}$) is in good agreement with the expected value for two non-interacting $Gd^{III}$ ions. Upon cooling, $\chi_m T$ is almost constant down to T = 10 K and then slightly decreases to reach a value of 7.8 $cm^3$ K $mol^{-1}$ at 2 K. This decrease is probably due to an intramolecular antiferromagnetic exchange coupling between the two $Gd^{III}$ ions. The magnetization curve increases with the applied magnetic field and reaches saturation (13.8 Bohr Magneton) at 7 T. It is possible to fit the susceptibility and the magnetization data using a model based of the spin Hamiltonian

$$H = -JS_{Gd1} \cdot S_{Gd2} + g\beta H_z S_z \qquad (2.3)$$

with $g$ = 1.98 and $J$ = – 0.16 $cm^{-1}$ where $g$ is the Lande factor and $J$ the interaction parameter between the local S = 7/2 spins of the $Gd^{III}$ ions (Figures 2.2 and 2.3, top left). This value is in agreement with those reported in the literature for dinuclear $\mu$-oxo $Gd^{III}$ with a similar geometry.[53] The $Gd^{III}$ ion has no first order angular momentum and negligible zero field splitting. In such a case, the dipolar interaction is expected to be very weak. Thus, the antiferromagnetic interaction found experimentally is mainly due to superexchange and splits the S = 0 and S = 7 states by an energy equal to 4.48 $cm^{-1}$ ($JS(S+1)/2$, with $|J|$ = 0.16 $cm^{-1}$ and S = 7) (Appendix A, Tables A2 and A3).

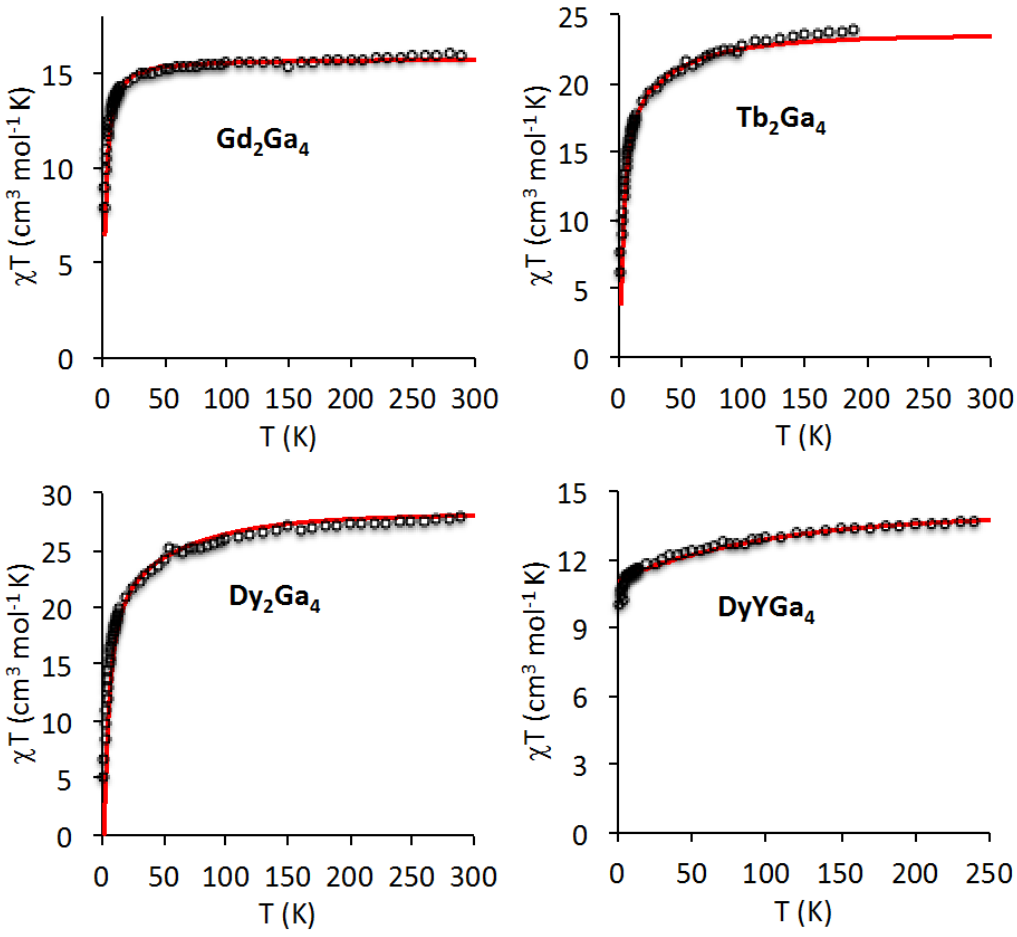


**Figure 2.2.** Temperature dependence of the χT product at 2000 Oe for **$Ga_4Gd_2$** (top left), **$Ga_4Tb_2$** (top right)**,** **$Ga_4Dy_2$** (bottom left)**,** **$Ga_4YDy$** (bottom right). The solid lines correspond to the best fit (see text).

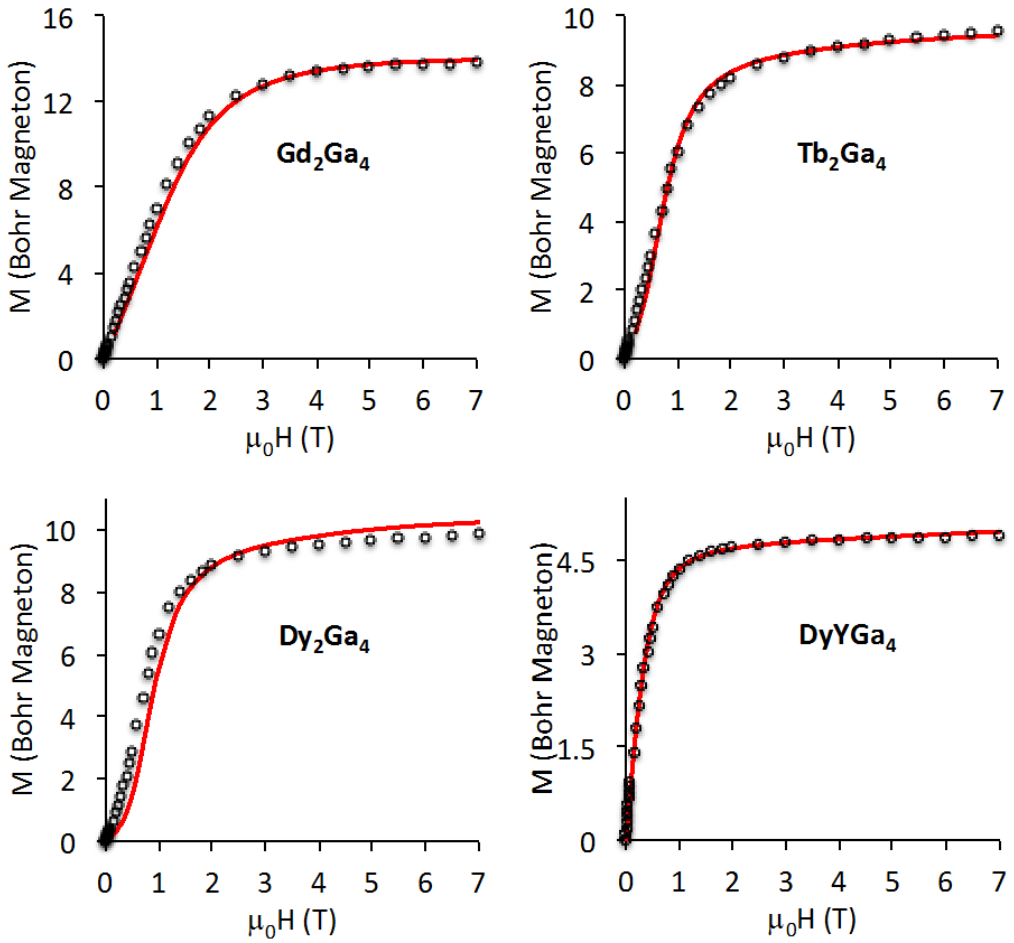


**Figure 2.3.** Magnetization vs. applied field at 2 K for **$Ga_4Gd_2$** (top left), **$Ga_4Tb_2$** (top right)**,** **$Ga_4Dy_2$** (bottom left)**,** **$Ga_4YDy$** (bottom right). The solid lines correspond to the best fit (see text).

**(ii) $Ga_4Tb_2$, $Ga_4Dy_2$ and $Ga_4YDy$.** The $\chi_mT$ product and the field dependent magnetization at 2 K for **$Ga_4YDy$** (Figure 2.2 and 2.3) show magnetic behavior expected for a mononuclear $Dy^{III}$ complex ($^6H_{15/2}$, $C$ = 14.17 $cm^3$ K $mol^{-1}$). *Ab initio* calculations allows for the determination of the spectrum of the energy levels and the associated $g_i$ values where i = 1, 2 and 3 are the directions of the g anisotropy tensor with 1 corresponding to the largest value (Appendix A, Table A4). The ground state corresponds to $M_J$ = ±15/2 with a very large $g_1$ = 19.85 ($g_2$ = 0.08, $g_3$ = 0.04) value, indicating an easy axis of the magnetization as depicted in Figure 2.4. The magnetization axis forms an

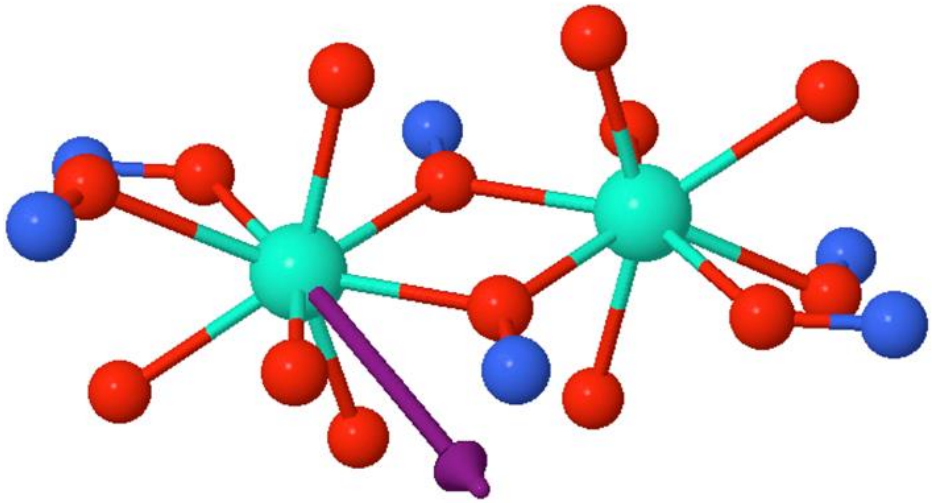

**Figure 2.4.** Orientation of the magnetization axis of the ground Kramer doublet $M_J = \pm 15/2$ of the $Dy^{III}$ ion in **$Ga_4YDy$**.

angle of 79° with the Dy–Dy axis and is very close to the plane containing the $Dy^{III}$ ions and the bridging oxygen atoms. The experimental magnetic data can be reproduced using the $M_J$ energy spectrum determined from *ab initio* calculations (Figure 2.2 and 2.3, bottom right), which confirm the nature of the ground level ($M_J = \pm 15/2$) and the fact that the diluted compound contains mainly the paramagnetic $Ga_4YDy$ species.

The $\chi_m T$ product for **$Ga_4Tb_2$** and **$Ga_4Dy_2$** have the usual behavior expected for $Tb^{III}$ and $Dy^{III}$ ions ($^7F_6$ ground state $C = 11.82$ cm$^3$ mol$^{-1}$ K for an isolated $Tb^{III}$). For both complexes, it slowly decreases from 300 K to around 50 K and then more abruptly (Figure 2.2). This behavior is due to the thermal depopulation of excited $M_J$ sublevels and may be also to the presence of an antiferromagnetic interaction between the lanthanide ions. The magnetization measured at 2 K presents a sigmoidal shape at low applied magnetic fields with an inflection point around 0.5 T, which is the signature of the presence of an antiferromagnetic coupling within the two compounds (Figure 2.3). It is worth noting that the magnetization *vs.* field curve of **$Ga_4YDy$** does not possess an

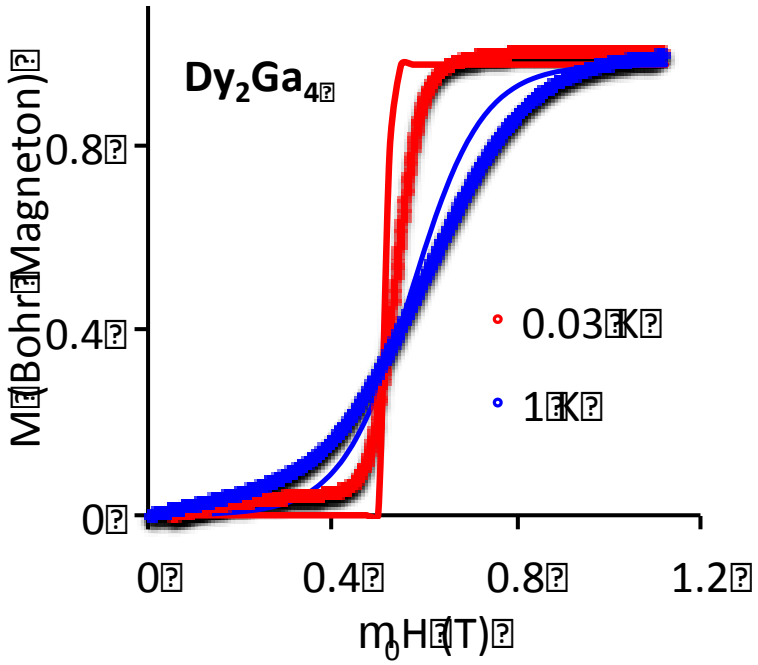


**Figure 2.5.** Magnetization *vs.* applied field at T = 1 and 0.03 K for **$Ga_4Dy_2$**, with the crystal anisotropy axis oriented parallel to the magnetic field. The thin solid lines are the experimental data; thick solid lines correspond to the best fit (see text).

inflection point and its $\chi_m$T product value at 2 K (10.8 $cm^3\ mol^{-1}$ K) is larger than that of **$Ga_4Dy_2$** (2.6 $cm^3\ mol^{-1}$ K per 1 $Dy^{III}$), which confirm that the inflection point in **$Ga_4Dy_2$** is due to *intra*- and not to *inter*molecular antiferromagnetic interactions. In order to more accurately determine the value of the inflection point in the M = f($\mu_0 H$) curve, the magnetization of a single crystal of **$Ga_4Dy_2$** was measured at very low temperatures using an array of micro-squids, with the magnetic field parallel to the anisotropy axis of the crystal. The curves at T = 1 and 0.03 K show sharp steps and a crossing point at $\mu_0 H$ = 0.51 T (Figure 2.5).

These sharp steps are the result of the crossover from an antiparallel (antiferromagnetic: AF) to a parallel (ferromagnetic: F) alignment of the anisotropic moment of the two $Dy^{III}$ ions. The value of the magnetic field at the crossing point allows

for the determination of the energy gap, ΔE, between the AF and the F states using Equation 1.1, where $\Delta E = g_1 * \beta * \mu_0 H = 19.47 * 0.496 * 0.51 = 4.9$ cm$^{-1}$. The *ab initio* calculations for an isolated $Dy^{III}$ ion (Figure 2.4) confirm that the magnetic dipole interaction between the two $Dy^{III}$ ions in **$Ga_4Dy_2$** is antiferromagnetic, which is expected since the easy magnetization axis is almost perpendicular to the Dy–Dy axis. These calculations lead to an AF-F energy gap of 1.26 cm$^{-1}$, which is well below the experimental one extracted from the micro-SQUID magnetization data (4.9 cm$^{-1}$). In order to account for the experimental energy gap, an additional interaction due to the exchange coupling between the two $Dy^{III}$ ions was introduced (Equation 2.2). A good fit of the susceptibility, magnetization and micro-SQUID data of **$Ga_4Dy_2$** is obtained using a $J_{exc}$ value of – 0.29 cm$^{-1}$ (Figures 2.3 and 2.5; Appendix A, Table A5). The difference between the calculated and the experimental micro-SQUID data at low temperature (Figure 2.5) is due to the presence of intermolecular dipolar interaction within the crystal which are dominant at low temperatures.

For **$Ga_4Tb_2$**, the situation is similar to that of the Dy analogue. An easy axis of magnetization is present: $g_1$ = 17.85 and $g_2 = g_3 = 0$ for the $M_J = \pm 6$ ground levels (Appendix A, Table A6). The axis of anisotropy forms an angle of 79° with the Tb – Tb intermetallic axis (Figure 2.6). The computed dipolar interaction leads to a splitting between the AF (ground level) and the F states of 0.5 cm$^{-1}$, which is not sufficient to reproduce the experimental data (Appendix A, Table A7). As is the case with **$Ga_4Dy_2$**, introducing an additional antiferromagnetic exchange interaction (J = – 0.12 cm$^{-1}$) increases this energy by 2.7 cm$^{-1}$ and allows for a reasonable fitting of the magnetic data (Figure 2.3, top right; Appendix A, Table A7).

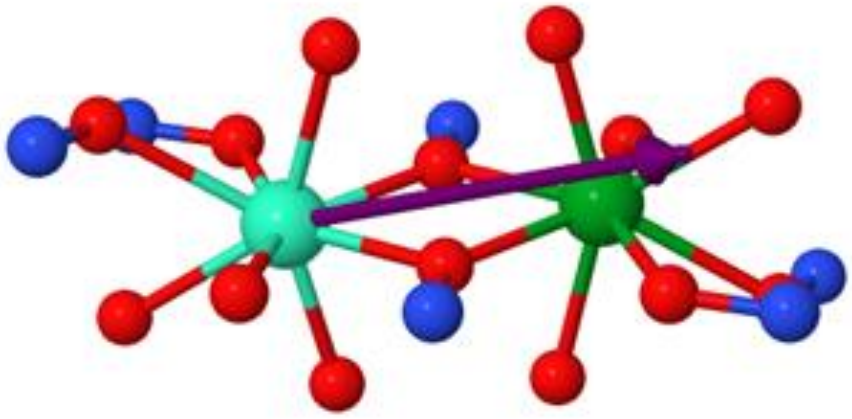

**Figure 2.6.** Orientation of the magnetization axis of the ground Kramer doublet $M_J = \pm 15/2$ of the $Tb^{III}$ ion in **$Ga_4Tb_2$**, where one $Tb^{III}$ has been replaced by a $Lu^{III}$ ion.

**(iii) $Ga_4Er_2$.** The $\chi_m T$ value at room temperature (22.7 $cm^3\,mol^{-1}\,K$) corresponds to two isolated $Er^{III}$ ions ($Er^{III}$: $^4I_{15/2}$, $C$ = 11.5 $cm^3\,K\,mol^{-1}$) (Figure 2.7). Upon cooling, $\chi_m T$ slightly decreases and reaches a value of 12.9 $cm^3\,K\,mol^{-1}$ at 2 K, as expected for anisotropic ions. The magnetization curve increases sharply between 0 and 1 T and then continuously up to 7 T without reaching saturation (Figure 2.7).

No inflection point is present at low magnetic field, which excludes the presence of an antiferromagnetic coupling as for the other compounds. For the ground state, the *ab initio* calculations give three different g values: $g_1$ = 9.94, $g_2$ = 5.25 and $g_3$ = 0.25 (Appendix A, Table A8). The magnetic anisotropy is planar, with two non-equivalent directions. The largest magnetization direction (along $g_1$) is found in a direction forming an angle of 32° with the intermetallic axis and lies almost in the $Er_2O_2$ plane (Figure 2.8).

The magnetization curve computed from *ab initio* calculations, does not fit the experimental data for **$Ga_4Er_2$**. A scaling factor of 1.8 increases the energy of the first excited state and reduces the effect of second order Zeeman interaction (see Appendix A

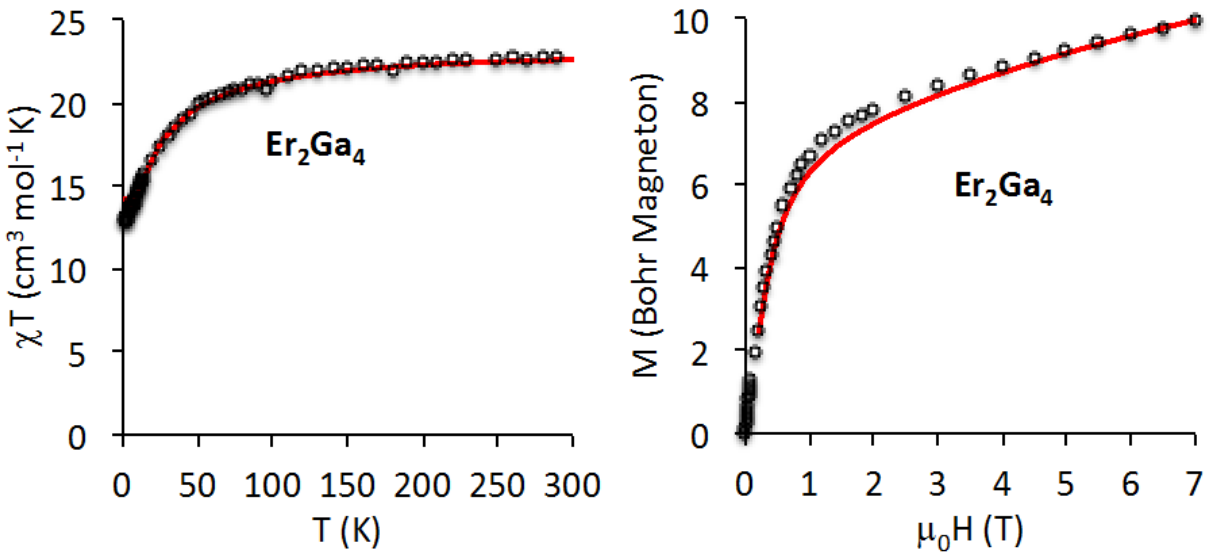


**Figure 2.7.** Temperature dependence of the χT product at 2000 Oe (left) and magnetization vs. applied field at 2 K for **$Ga_4Er_2$**. The solid lines correspond to the best fit (see text).

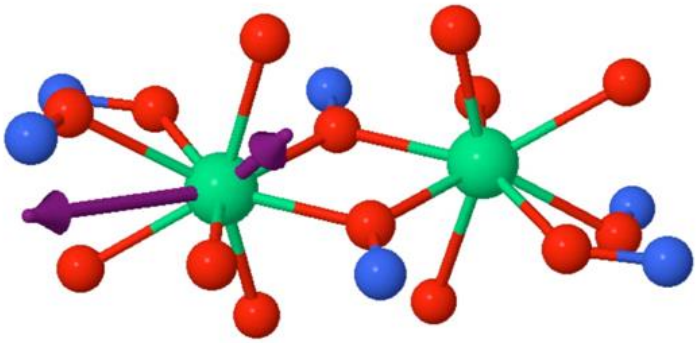

**Figure 2.8.** Orientation of the two components of the easy plane of magnetization for the ground Kramer's doublet of $Er^{III}$ ion in **$Ga_4Er_2$** where one $Er^{III}$ has been replaced by a $Lu^{III}$ ion.

for details of the calculations) and improves the agreement of theoretical and experimental curves, particularly above 1 T. Since the planes of magnetization form a small angle with the intermetallic axis, the dipolar interaction is ferromagnetic. The magnetic behavior in the weak field region can be reproduced by considering the presence of a ferromagnetic coupling between the two ions due to exchange ($J_{exch}$ = +2.4 $cm^{-1}$) (Figure 2.7; Appendix A, Table A9). It is worth noting that when the ground state has a weak $M_J$ value and the excited states are close to the ground one as in the present case, a

very weak error on the energy values and on the $g_i$ values may have a dramatic effect on the shape of the magnetization curve. This is why a reduction factor that changes the ground-excited state gap was necessary to better reproduce the magnetic data. In addition, if the ratio between $g_1$ and $g_2$ is different, the slope of the magnetization curve in the low field region is changed. For instance, if $g_1$ is close to $g_2$ (close to 10, which defines an anisotropic easy plane of magnetization), the experimental curve can be reproduced without considering an additional ferromagnetic exchange interaction between the two $Er^{III}$ ions.

In summary, the magnetic studies together with theoretical calculations show that there is an easy axis of magnetization for the $Dy^{III}$ and the $Tb^{III}$ complexes with an intra-molecular dipolar antiferromagnetic interaction, whereas for $Er^{III}$, there is an easy plane of magnetization that leads to a ferromagnetic dipolar interaction between the two ions. Furthermore, an additional exchange interaction due to exchange between the metal ions is necessary to reproduce the experimental data that was found to be antiferromagnetic for the Dy and the Tb complexes and ferromagnetic (or absent) for the Er analogue. The analysis of the g values of the ground doublets allow us to extract the spin and the orbital contributions to the overall magnetization (Appendix A, Table A10).

In order to get a qualitative insight into the nature of the exchange interaction between the metal ions and particularly, the difference between AF coupled Gd, Tb and Dy complexes and F coupled Er compound, calculations were performed to determine the shape of the Natural Spin Orbitals (NSOs)[54] on one lanthanide site (Figure 2.9, 2.10 and 2.11 for $\mathbf{Ga_4Dy_2}$, $\mathbf{Ga_4Tb_2}$, $\mathbf{Ga_4Er_2}$, respectively, see Appendix A for details). The comparison of the overlap integrals between the NSOs within the binuclear complexes for

the Dy and the Er cases show that they are about ten times larger for the $Dy_2Ga_4$ then for the $Er_2Ga_4$ (Appendix A, Tables A11, A12 and A13). Since the overlap integral between NSOs is directly related to the magnitude of the antiferromagnetic contribution to the exchange interaction,[55-57] one can conclude that such interaction is expected to be much larger for the **$Ga_4Dy_2$** than for **$Ga_4Er_2$,** as found experimentally. The origin of the difference in behavior between the two complexes may be related to the weaker the magnetization density on the bridging oxo ligands for $Er^{III}$ than for $Dy^{III}$ (Figures 2.9, 2.10 and 2.11). It is difficult to draw any conclusion from such qualitative analysis on the ferromagnetic exchange contribution.

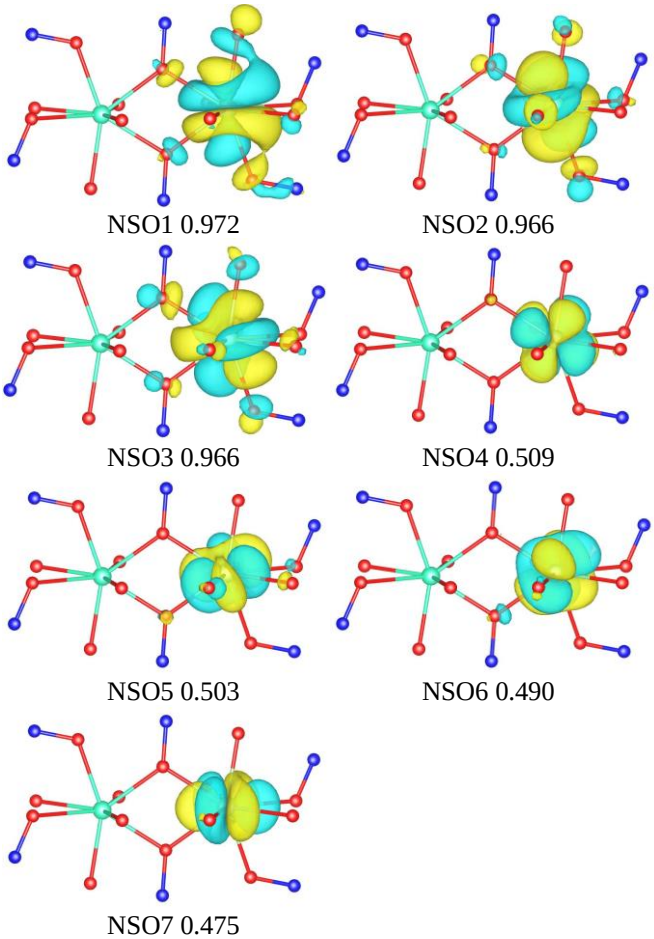


**Figure 2.9.** NSO for a $Dy^{III}$ site of **$Ga_4Dy_2$** determined along the direction 1**,** corresponding to the orientation of the magnetization axis. Each NSO is drawn taking into account its weight.

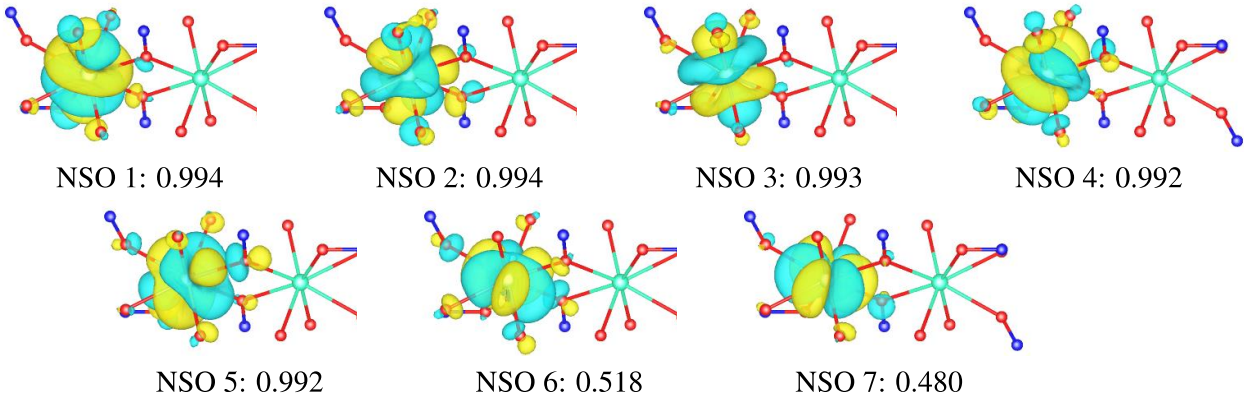


**Figure 2.10.** NSO for a $Tb^{III}$ site of compound $\mathbf{Ga_4Tb_2}$ determined along the direction **1** corresponding to the orientation of the magnetization axis. Here, the weight of each NSO is not taken into account in the drawing.

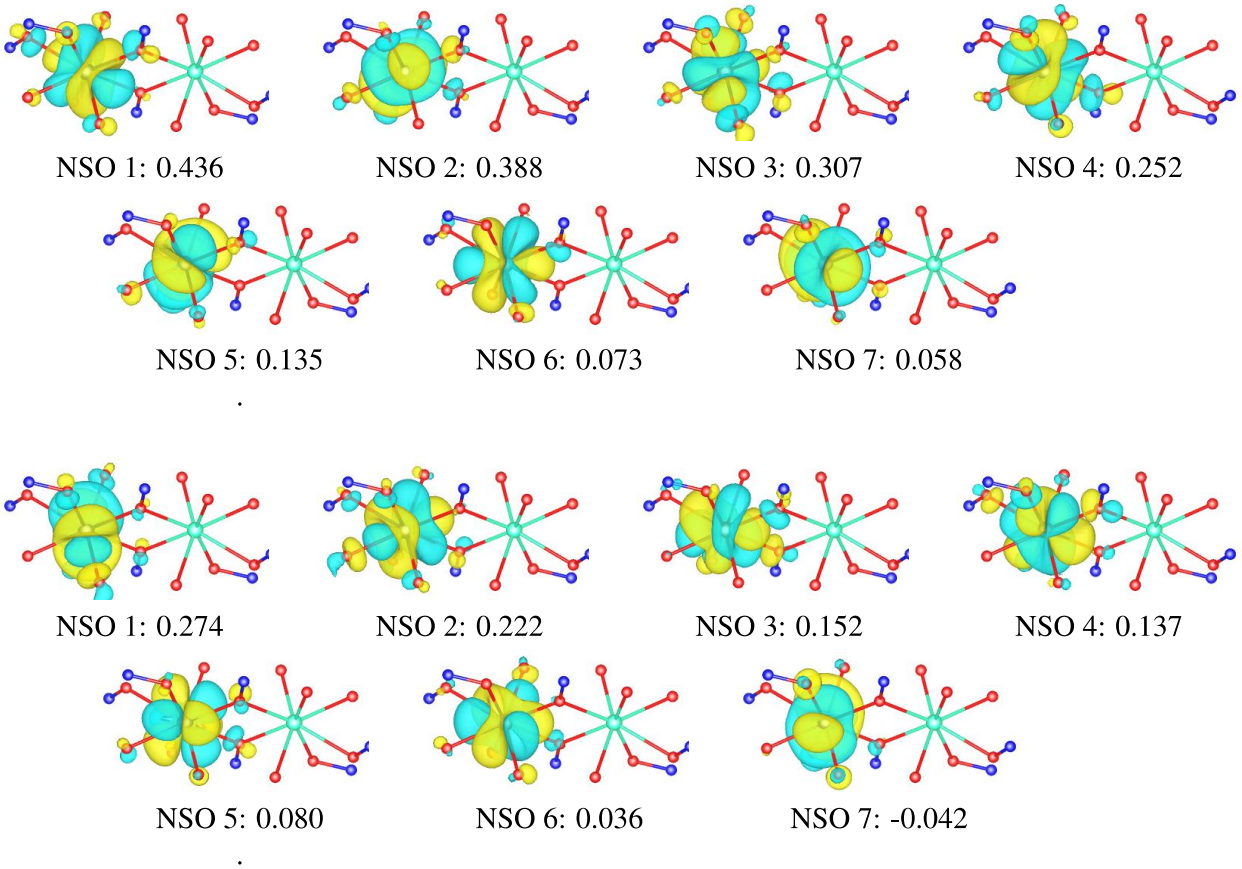


**Figure 2.11.** NSO for an $Er^{III}$ site for $\mathbf{Ga_4Er_2}$ determined along the direction **1** (top) and **2** (bottom) corresponding to the orientation of the magnetization plane. Here, the weight of each NSO is not taken into account in the drawing.

**Low temperature micro-squid studies.** The micro-SQUID data of compound **$Ga_4Dy_2$** shows that the magnetic moment is saturated at $\mu_0 H$ = 1 T and T = 0.03 K (Figure 2.12). Upon decreasing the field with a sweep rate of 0.035 T/s, the magnetization undergoes a sharp decrease to ca. 5% of saturation (Figure 2.12). The micro-SQUID magnetization curves at different temperatures cross at 0.51 T. An opening of the hysteresis was observed at zero field with a coercive field $\mu_0 H_C$ = 540 Oe (Figure 2.13). Upon decreasing the magnetic field sweep rate from 0.28 to 0.008 T/s, the coercive field decreases from 678 to 421 Oe indicating the occurrence of quantum tunneling of the magnetization because the width of the hysteresis loop depends on the field sweep rate (Figure 2.13). The sharp step at 0.51 T is the result of crossover from the F to the AF states as explained previously.

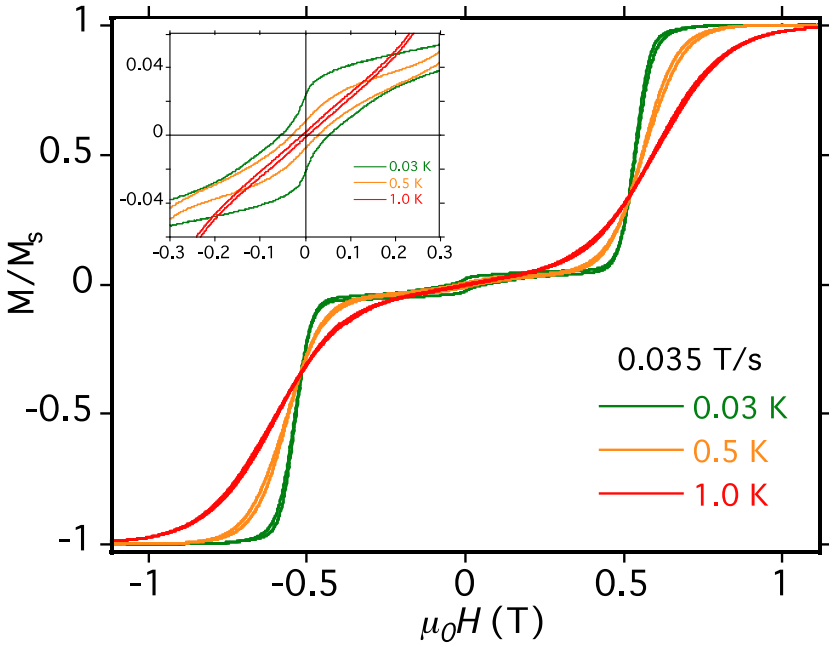


**Figure 2.12.** Micro-SQUID hysteresis plot for **$Ga_4Dy_2$**. $M/M_S = f(\mu_0 H)$ at 0.03, 0.5 and 1 K for dc field sweep rate of 0.035 T/s.

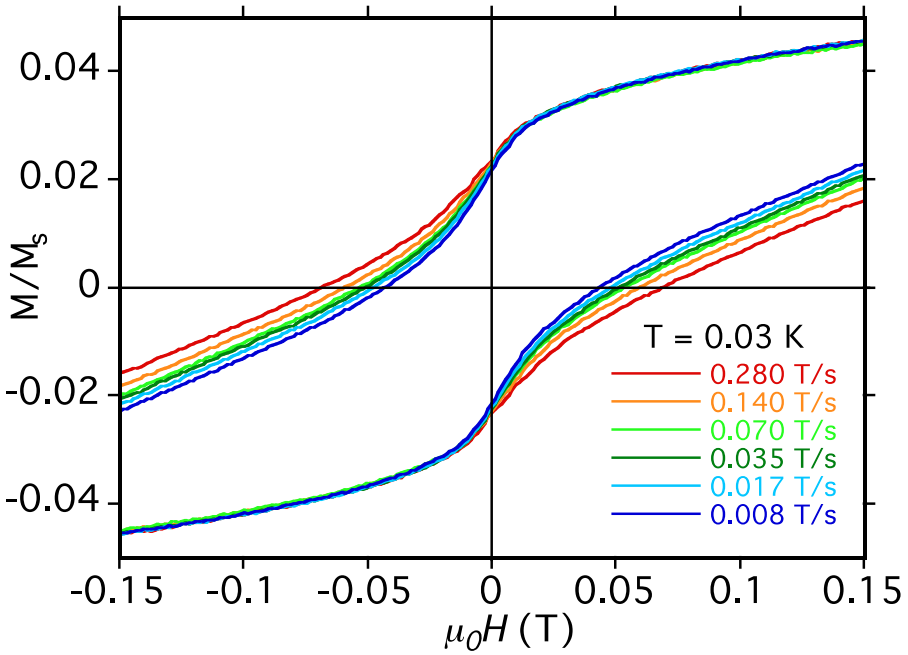


**Figure 2.13.** Micro-SQUID hysteresis plot for **$Ga_4Dy_2$**. $M/M_S = f(\mu_0 H)$ at T = 0.03 K measured at different sweep rates showing the dependence of the width of the loop with the sweep rate.

To the best of our knowledge, an opening of the hysteresis loop has never been observed in a binuclear $Dy_2$ complex but was seen in the antiferromagnetic trinuclear $Dy_3$ complex reported by Powell and Sessoli.[27, 52] Since no hysteresis loop can occur when all the molecules are in the antiferromagnetic state (diamagnetic state) and since the excited ferromagnetic state cannot be populated at T = 0.03 K, the presence of the residual 5% magnetization below the step at 0.51 T can only be due to the presence of residual molecules in the ferromagnetic state. Actually, at large positive magnetic field, the moments are in the |– –> configuration of the ferromagnetic state. Upon decreasing the field *at a given sweep rate*, the majority of the molecules undergo a crossover from the ferro- |– –> to the antiferromagnetic (|+ –>; |– +>) state, but a small amount remains in the ferro- |– –> configuration (see Scheme 2).

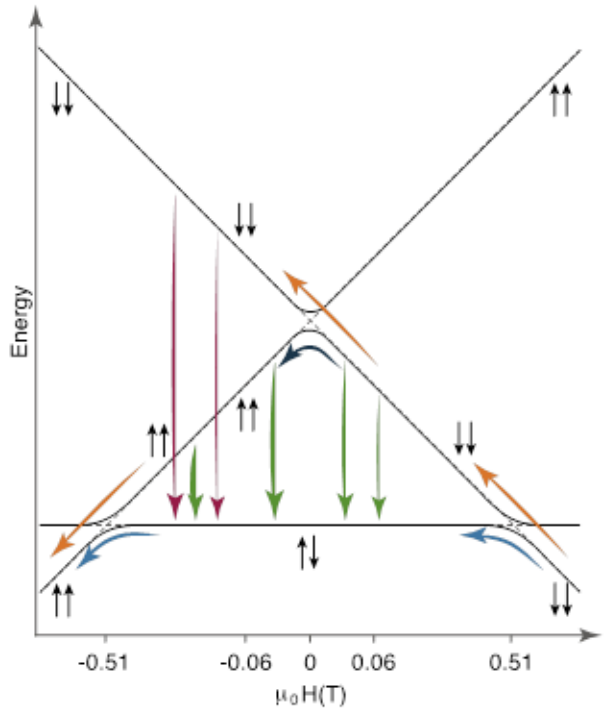


**Scheme 2.2.** Field-dependent energy diagram showing the different relaxation processes for the **$Ga_4Dy_2$**.

**Dynamic ac susceptibility studies.** Ac susceptibility measurements may bring complementary information on the dynamics of the magnetization reversal at higher temperatures. A frequency dependence of the out-of-phase component of the susceptibility was observed only for **$Ga_4Dy_2$** and the diluted **$Ga_4YDy$** complex, with all other compounds showing no out-of-phase behavior. For compound **$Ga_4Dy_2$**, ac susceptibility measurements were first performed under zero dc applied external field, in the temperature range between 2 and 22 K and frequency range from 1 to 1488 Hz with an ac drive field of 3 Oe, with the temperature-dependent and frequency-dependent ac susceptibilities shown in Figures 2.14 and 2.15, respectively.

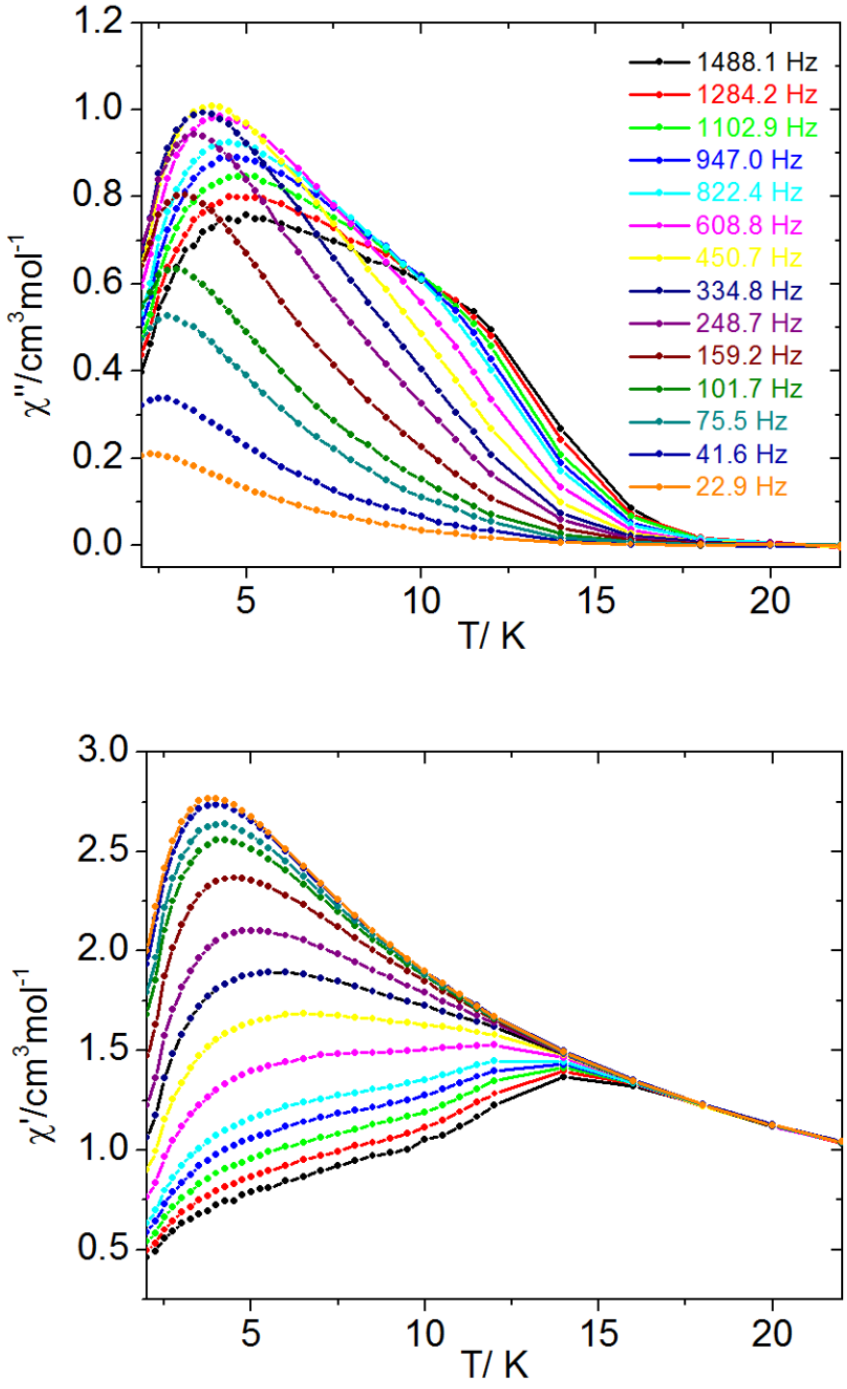


**Figure 2.14.** Temperature-dependence of the out-of-phase (top) and in-phase (bottom) ac magnetic susceptibility for **$Ga_4Dy_2$** under zero applied dc field.

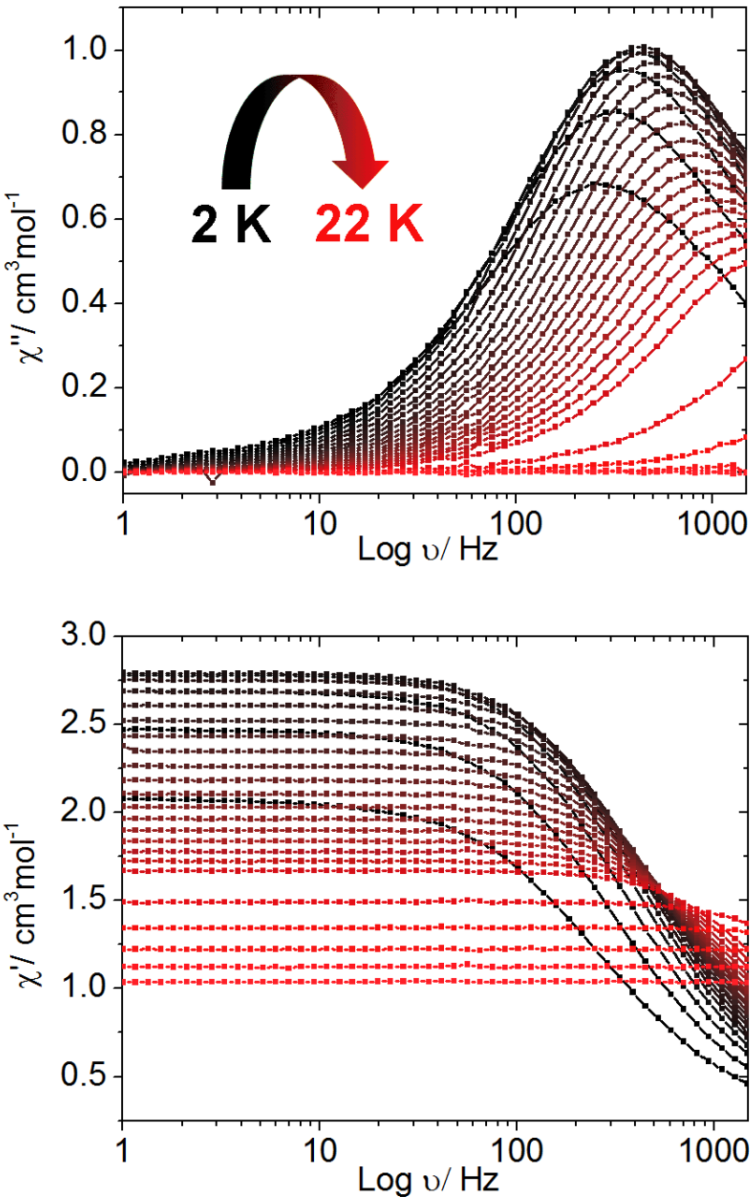


**Figure 2.15.** Frequency dependent out-of-phase (a) and in-phase (b) ac magnetic susceptibility for **$Ga_4Dy_2$** under zero applied dc field.

The temperature-dependent out- of-phase susceptibility of **$Ga_4Dy_2$** (Figure 2.14) shows that upon increasing the frequency of the oscillating field, the temperature of the maxima ($T_{Bf}$) shifts toward high temperatures as expected. On the other hand, the intensity ($cm^3\ mol^{-1}$) of the χ" signals increases with increasing frequency until it reaches

a maximum at 450 Hz ($T_{B450}$ = 4.00 K), after which the intensity decreases (Figure 2.14). This behavior is consistent with the fact that the slow relaxation corresponds to an excited state that becomes more and more populated when the temperature of the maximum is shifted upward and is evidence that the relaxation process observed is due to the excited ferromagnetic state that lies at 4.9 $cm^{-1}$ above antiferromagnetic ground state. Assuming an activated relaxation process in the 2-5 K region, fitting the ln$\tau$ *vs*. $1/T_B$ plot from the temperature-dependent out-of phase data using Equation 1.14 reveals that $\tau_0 = 3.6x10^{-6}$ s and $U_{eff}$ = 18 K (Figure 2.16). The temperature-dependent out-of-phase susceptibility curves display shoulders at higher temperatures in the 10-14 K region that appear only for frequencies above 500 Hz. This second relaxation process can be assigned to the isolated $Dy^{III}$ ions because in this temperature range the two magnetic states are almost equally populated and the magnetic moments behave as if they were uncoupled. The analysis of the data leads to a thermal activated behavior relaxation process with $\tau_0 = 6.8x10^{-6}$ s and $U_{eff}$ = 26 K (Figure 2.16).

The frequency-dependent out-of-phase susceptibility curves for different temperatures (Figure 2.15) show only one maximum that shifts to high frequency upon heating. The intensity of the curves follow the behavior observed in the temperature-dependent plot in Figure 2.14, where the magnitude of $\chi$" increases from 2 to 4.25 K and then decreases. This shows that the relaxation process is due to the excited ferromagnetic state.

The Cole-Cole plots for compound **$Ga_4Dy_2$** at zero applied dc field were obtained for temperatures between 2 and 11 K (Figure 2.17). The plots have close to an ideal semicircular shape indicating that only a few relaxation processes are present. The

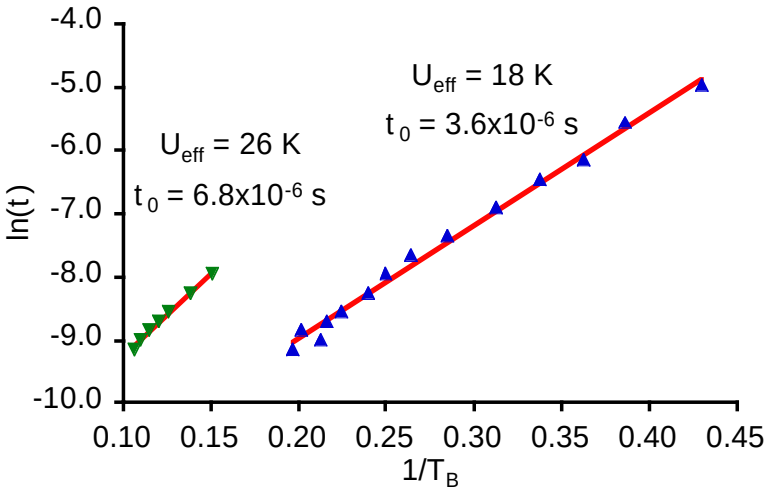


**Figure 2.16.** Arrhenius plot for **$Ga_4Dy_2$** with data extracted from the frequency-dependent data at zero applied dc field for the low (▼) and the high (▲) temperature processes. The solid lines are the best linear fit.

semicircles were fitted using a generalized Debye model (Equations 1.15 and 1.16). The fits provided values for the α parameter, which decreased with increasing temperature, from 0.18 at 2 K to 0.032 at 11 K (Figure 2.17, right). The low α value at high temperatures indicates that only one relaxation process is present. As the temperature is decreased, the α parameter increases because other relaxation processes come into play, which is consistent with the above analysis.

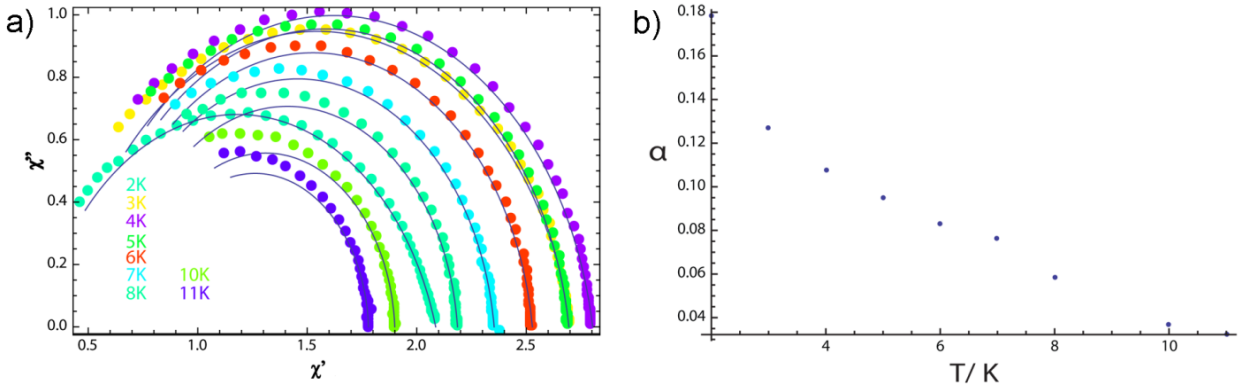


**Figure 2.17.** Cole-Cole plots for compound **$Ga_4Dy_2$** under zero applied dc field. (a) Data from 2 to 11 K with fits (blue lines) obtained from the Debye equation. (b) Plot of α parameter vs. temperature.

The ac data for compound **$Ga_4Dy_2$** were also recorded in the presence of an applied 2000 Oe dc field. The same general behavior with two relaxation processes is observed, but with some differences in the temperature-dependent (Figure 2.18) and frequency-dependent (Figure 2.19) ac susceptibility. Upon increasing the frequency, the intensity of $\chi$" increases and reaches a maximum at 36 Hz ($T_{B36}$ = 3.0 K), instead of 450 Hz under zero dc field. The high temperature process starts to be observable at 88 Hz instead of 450 Hz when a dc field of 2000 Oe is applied, which is compatible with a process due to the uncoupled $Dy^{III}$ ions.

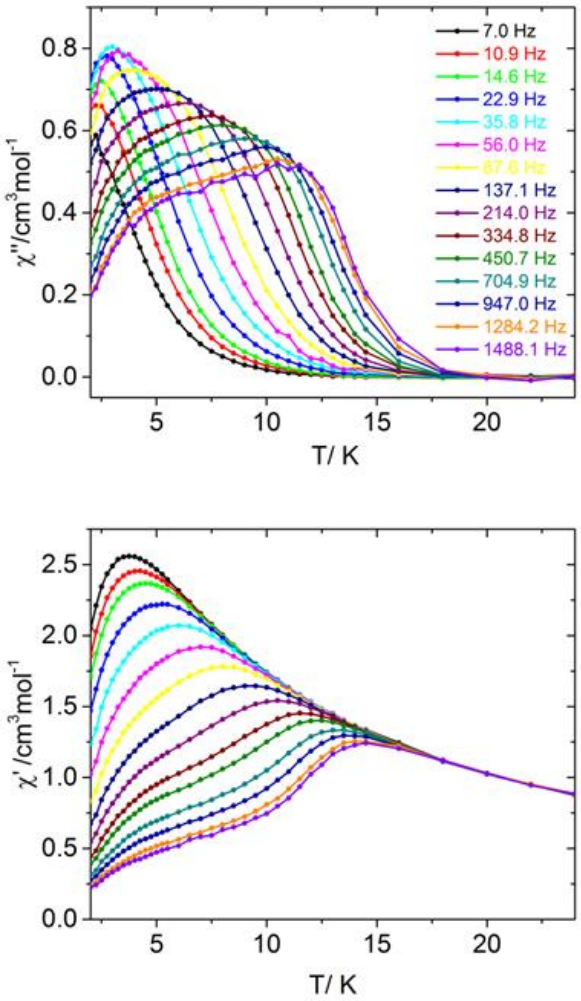


**Figure 2.18.** Temperature-dependence of the out-of-phase (top) and in-phase (bottom) ac magnetic susceptibility for **$Ga_4Dy_2$** under an applied dc field of 2000 Oe, at indicated frequencies.

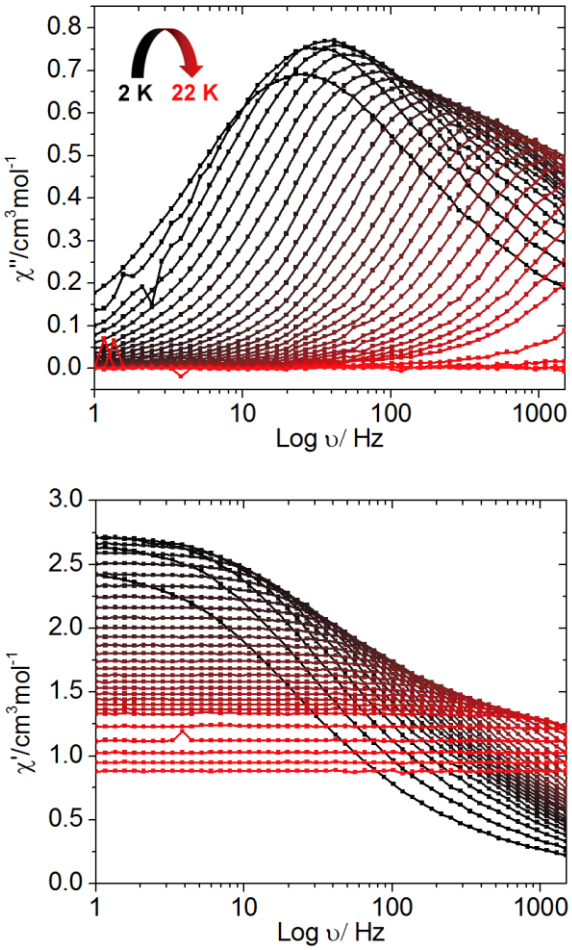


**Figure 2.19.** Frequency dependent out-of-phase (top) and in-phase (bottom) ac magnetic susceptibility for **$Ga_4Dy_2$** under an applied dc field of 2000 Oe.

The temperature-dependent out-of-phase ac susceptibility for **$Ga_4YDy$** under zero dc applied field (Figure 2.20) revealed a frequency dependent maxima higher temperature with a tail at low temperature due to quantum tunneling of the magnetization, as it is generally observed for $Dy^{III}$ ions.[58] This last process can also be observed in the low temperature regime in the frequency-dependent data (Figure 2.21), where the maxima positions are relatively temperature independent. The barrier extracted from the frequency-dependent data for **6** at zero applied dc field is $U_{eff}$ = 31 K, with $\tau_0 = 7.0\times10^{-6}$ s (Figure 2.22), close to that of the binuclear compound **$Ga_4Dy_2$** ($U_{eff}$ = 26 K). This is

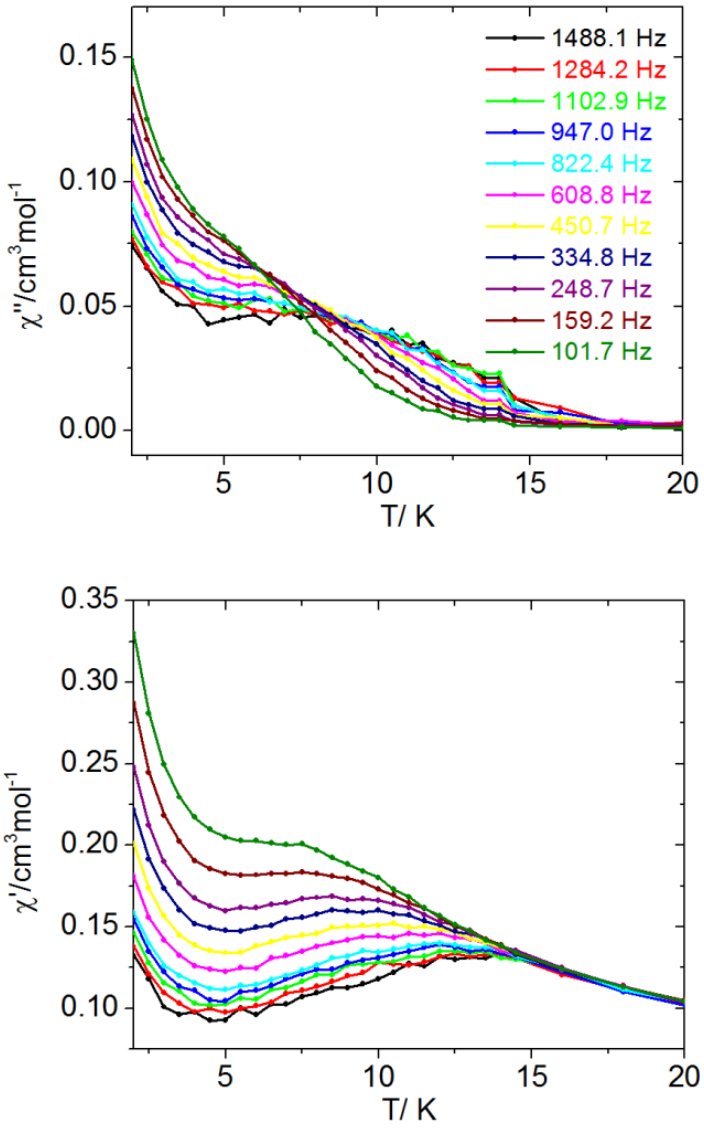


**Figure 2.20.** Temperature-dependence of the out-of-phase (top) and in-phase (bottom) out-of-phase ac magnetic susceptibility for **$Ga_4YDy$** under zero applied dc field.

consistent with a process due to the uncoupled $Dy^{III}$ ions in **$Ga_4Dy_2$**. At lower temperatures, the relaxation tends to be temperature independent (Figure 2.21) as expected when the quantum tunneling process dominates.

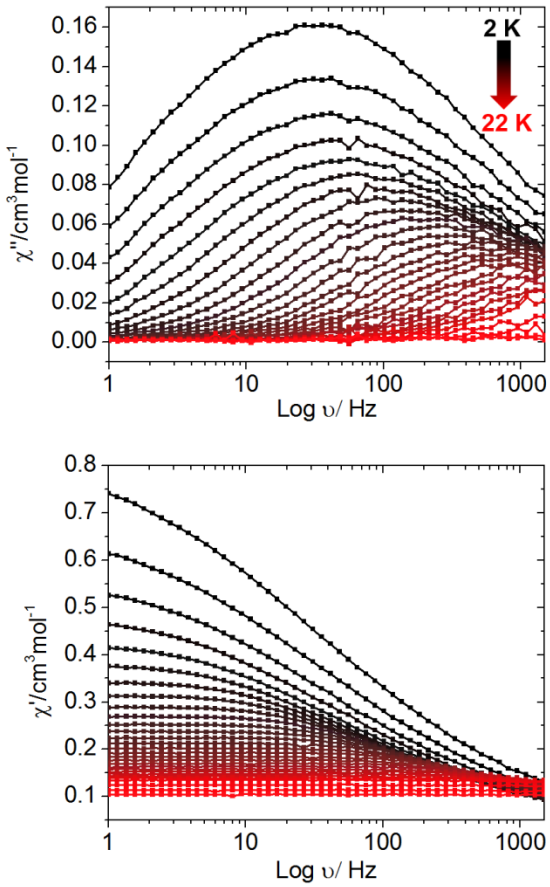


**Figure 2.21.** Frequency-dependent out-of-phase (a) and in-phase (b) ac magnetic susceptibility for **$Ga_4$YDy** under zero applied dc field.

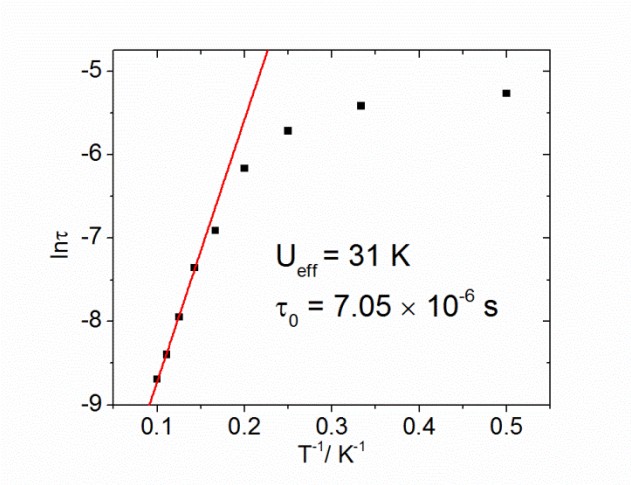


**Figure 2.22.** Arrhenius plot for the ac out-of-phase data for **$Ga_4$YDy** under zero applied dc field, with data extracted from the frequency-dependent scans.

Applying a dc magnetic field may slow down the tunneling and make other processes more visible. Field optimization experiments at 2 K (Figure 2.23) reveal that the optimal applied dc field is between 600 and 800 Oe. In the presence of a 750 Oe dc field, maxima in the temperature-dependent ac susceptibility plot for **$Ga_4YDy$** can be observed (Figure 2.24). Quantum tunneling of the magnetization has been mostly quenched as evidenced by the absence of overlapping peaks in the frequency-dependent data (Figure 2.25) and disappearance of the low temperature tail in the temperature dependent data (Figure 2.24). A linear fit of the high temperature data gives an energy barrier $U_{eff}$ = 107 K, with $\tau_0$ = $1.01 \times 10^{-7}$ s (Figure 2.26), the behavior at low temperature shows that tunneling has not been completely quenched. As expected, the barrier is much higher than the zero-field barrier of 31 K. It is about half the value of the computed energy difference between the ground and the first excited states (153 $cm^{-1}$ = 220 K; Appendix A, Table A4), which is consistent with the persistence of a relaxation by quantum tunneling via the ground state and via the first excited one. The persistence of quantum tunneling is due to the lack of a perfect axial g-tensor ($g_1$ = 19.47, $g_2$ = 0.08 and $g_3$ = 0.04) and thus to a small mixing between the ground and the excited $M_J$ states.

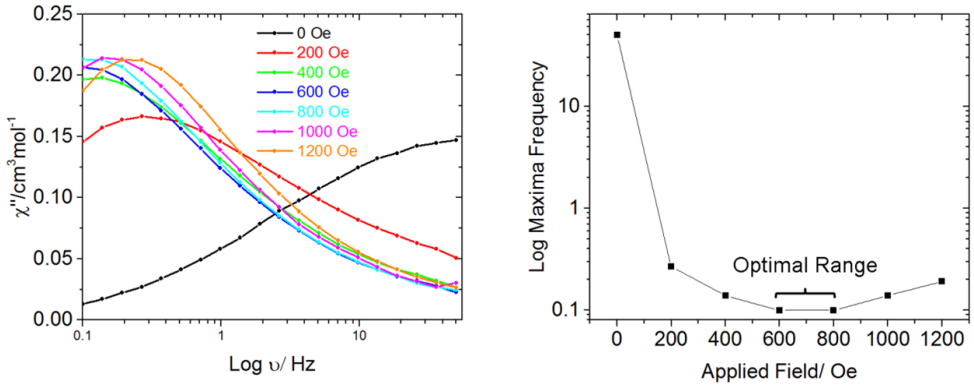


**Figure 2.23.** Field optimization of compound **$Ga_4YDy$**. (left) Out-of-phase susceptibility measurements at 2 K at a frequency range from 1 Hz to 500 Hz at various applied fields. (right) Plot of frequency maxima vs applied field.

The comparison of the χ" curves at 1284 Hz measured at zero and 2000 Oe for **$Ga_4Dy_2$** and at 750 Oe for **$Ga_4YDy$** (Figure 2.27) shows that the maximum of the temperature-dependent out-of-phase susceptibility for **$Ga_4Dy_2$** and **$Ga_4YDy$** are at the same temperature, which confirms that the high temperature process in **$Ga_4Dy_2$** is actually due to the isolated $Dy^{III}$ ions.

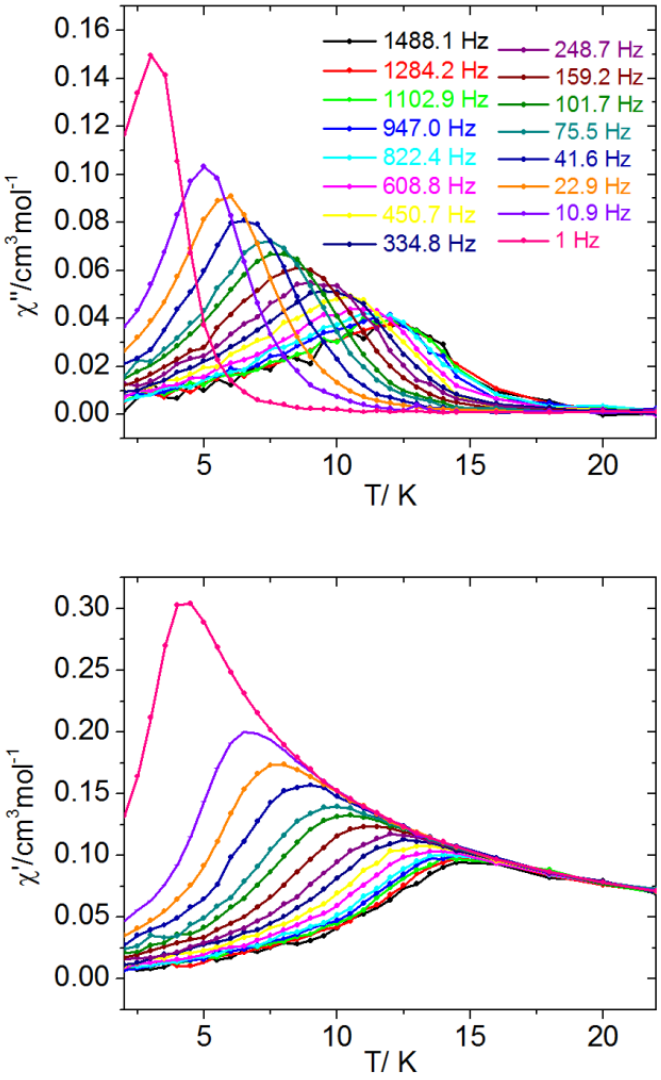


**Figure 2.24.** Temperature-dependence of the out-of-phase (a) and in-phase (b) out-of-phase ac magnetic susceptibility for **$Ga_4YDy$** under an applied dc field of 750 Oe

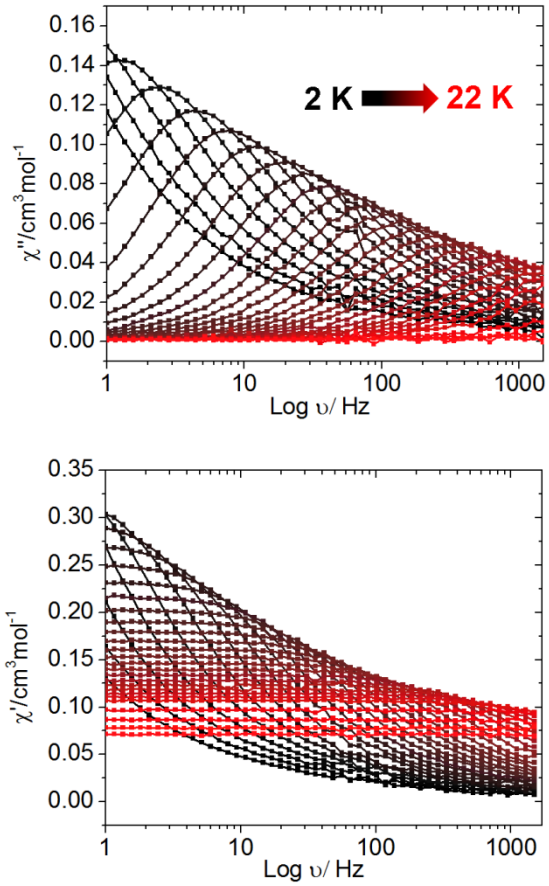


**Figure 2.25.** Frequency dependent out-of-phase (a) and in-phase (b) ac magnetic susceptibility for **$Ga_4YDy$** under an applied dc field of 750 Oe.

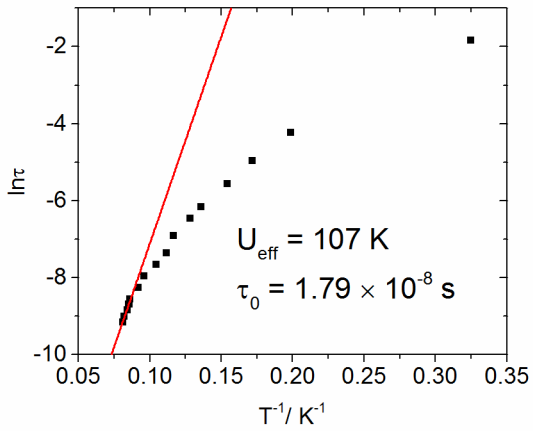


**Figure 2.26.** Arrhenius plot for the ac out-of-phase data for **$Ga_4YDy$** under an applied dc field of 750 Oe, with data extracted from the temperature-dependent scans.

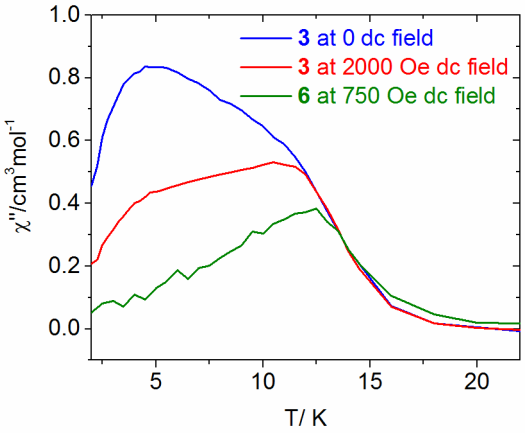


**Figure 2.27.** Temperature-dependence of the out-of-phase ac susceptibility for **$Ga_4Dy_2$** in zero dc field (—), in 2000 Oe dc field (—) and for **$Ga_4YDy$** in 750 Oe dc field (—) at 1284 Hz.

**Structure-property relationship.** The $Dy_2(\mu_2\text{-}O)_2$ core of **$Ga_4Dy_2$**, has a Dy-Dy distance of 3.839 Å and a Dy-O-Dy angle of 111.70˚. This $\mu_2$-O bridging motif in this complex contributes to the antiferromagnetic interactions between the two $Dy^{III}$ centers. The first coordination sphere of the $Dy^{III}$ ions could be analyzed with the SHAPE software.[51, 59] The best match ideal geometry around the $Dy^{III}$ site was determined to be trigonal dodecahedron ($D_{2d}$) (Appendix A, Table A1).

The $Dy_2(\mu_2\text{-}O)_2$ motif of the **$Ga_4Dy_2$** complexes is not uncommon and has been shown to produce SMM behavior in several examples in the literature.[52, 60-62] The most comparable example is the complex $[Dy^{III}_2(valdien)_2(NO_3)_2]$.[52] This centrosymmetric complex also has distorted trigonal dodecahedral geometry around the $Dy^{III}$ ions which are connected by a $(\mu_2\text{-}O)_2$ bridged. As with **$Ga_4Dy_2$**, the $Dy^{III}$ ions in this complex are antiferromagnetically coupled and has an energy barrier in zero applied dc field of 76 K. However, a closer inspection of the temperature-dependent ac out-of-phase behavior in $[Dy^{III}_2(valdien)_2(NO_3)_2]$ reveals that only one peak (of single-ion origin) is observed. The

energy barrier for this complex at zero applied dc field is 76 K, which is comparable to the 107 K barrier height of complex **$Ga_4YDy$** (at an applied field of 750 Oe).

To the best of our knowledge, compound **$Ga_4Dy_2$** is the first antiferromagnetically coupled $Dy^{III}$ dimer to exhibit a coupled relaxation process in addition to a single-ion process under zero applied dc field. We reasoned that significant antiferromagnetic coupling between the $Dy^{III}$ ions in **$Ga_4Dy_2$** may lead to a *J* ground state with excited $m_J$ states which contribute to magnetic blocking. Previously, a $Dy^{III}_3$ dimer complex[11, 27] with antiferromagnetically coupled $Dy^{III}$ ions has been reported to display SMM behavior. However, this compound was shown to display ac out-of-phase behavior originating from toroidal magnetic moment.[11] Due to the symmetry elements in **$Ga_4Dy_2$**, it is likely that the $Dy^{III}$ ions have more Ising-type magnetic moments. These results are unprecedented, since it would be expected that ferromagnetically coupled $Dy^{III}$ ions would be expected to exhibit a higher energy barrier than individual, decoupled ions. Such a finding may have implications in the design of future SMMs.

**2.4 Conclusions**

Utilizing the metallacrown synthetic approach, we have structurally and magnetically characterized a family of isostructural **$Ga_4Ln_2$** complexes. Significant antiferromagnetic coupling in the $Dy^{III}$ derivative **$Ga_4Dy_2$**, has led to slow magnetic relaxation behavior attributed to both coupled and single-ion processes. It can be seen that diluted sample **$Ga_4YDy_2$**, comprising mainly of single $Dy^{III}$ ions, exhibits significant quantum tunneling at zero-field ($U_{eff}$ = 31 K), but tunneling can be quenched at an optimized field of 750 Oe and results in an energy barrier height of 107 K for the single-ion relaxation process. These findings may provide insight to the design and

understanding of intramolecular magnetic coupling in lanthanide complexes in order to obtain materials with a higher energy barrier to the reorientation of magnetization.

## References


1. Sessoli, R.; Tsai, H.; Schake, A. R.; Wang, S.; Vincent, J. B.; Folting, K.; Gatteschi, D.; Christou, G.; Hendrickson, D. N. *J. Am. Chem. Soc.* **1993**, *115*, 1804-1816.
2. Christou, G.; Gatteschi, D.; Hendrickson, D. N.; Sessoli, R. *MRS Bull.* **2000**, *25*, 66-71.
3. Woodruff, D. N.; Winpenny, R. E. P.; Layfield, R. A. *Chem. Rev.* **2013**, *113*, 5110-5148.
4. Ishikawa, N.; Sugita, M.; Ishikawa, T.; Koshihara, S.; Kaizu, Y. *J. Am. Chem. Soc.* **2003**, *125*, 8694-8695.
5. Campbell, V. E.; Guillot, R.; Riviere, E.; Brun, P.-T.; Wernsdorfer, W.; Mallah, T. *Inorg. Chem.* **2013**, *52*, 5194-5200.
6. Li, D.-P.; Wang, T.-W.; Li, C.-H.; Liu, D.-S.; Li, Y.-Z.; You, X.-Z. *Chem. Commun.* **2010**, *46*, 2929-2931.
7. Yamashita, A.; Watanabe, A.; Akine, S.; Nabeshima, T.; Nakano, M.; Yamamura, T.; Kajiwara, T. *Angew. Chem., Int. Ed.* **2011**, *50*, 4016-4019.
8. Watanabe, A.; Yamashita, A.; Nakano, M.; Yamamura, T.; Kajiwara, T. *Chem.-Eur. J.* **2011**, *17*, 7428-7432.
9. Zhou, N.; Ma, Y.; Wang, C.; Feng Xu, G.; Tang, J.-K.; Xu, J.-X.; Yan, S.-P.; Cheng, P.; Li, L.-C.; Liao, D.-Z. *Dalton Trans.* **2009**, 8489-8492.
10. Aldamen, M. A.; Clemente-Juan, J. M.; Coronado, E.; Martí-Gastaldo, C.; Gaita-Ariño, A. *J. Am. Chem. Soc.* **2008**, *130*, 8874-8875.
11. Chibotaru, L. F.; Ungur, L.; Soncini, A. *Angew. Chem., Int. Ed.* **2008**, *47*, 4126-4129.
12. Boča, R. *Coord. Chem. Rev.* **2004**, *248*, 757-815.
13. Blagg, R. J. U., L.; Tuna, F.; Speak, J.; Comar, P.; Collison, D.; Wernsdorfer, W.; Mcinnes, E. J. L.; Chibotaru, L. F.; Winpenny, R. E. P. *Nat. Chem.* **2013**, *5*, 673-678.
14. Wernsdorfer, W.; Aliaga-Alcalde, N.; Hendrickson, D. N.; Christou, G. *Nature* **2002**, *416*, 406-409.
15. Rinehart, J. D.; Fang, M.; Evans, W. J.; Long, J. R. *J. Am. Chem. Soc.* **2011**, *133*, 14236-14239.
16. Blagg, R. J.; Muryn, C. A.; Mcinnes, E. J. L.; Tuna, F.; Winpenny, R. E. P. *Angew. Chem., Int. Ed.* **2011**, *50*, 6530-6533.
17. Lin, P.-H.; Burchell, T. J.; Ungur, L.; Chibotaru, L. F.; Wernsdorfer, W.; Murugesu, M. *Angew. Chem., Int. Ed.* **2009**, *48*, 9489-9492.
18. Guo, Y.-N.; Xu, G.-F.; Gamez, P.; Zhao, L.; Lin, S.-Y.; Deng, R.; Tang, J.; Zhang, H.-J. *J. Am. Chem. Soc.* **2010**, *132*, 8538-8539.
19. Habib, F.; Murugesu, M. *Chem. Soc. Rev.* **2013**, *42*, 3278-3288.
20. Tuna, F.; Smith, C. A.; Bodensteiner, M.; Ungur, L.; Chibotaru, L. F.; Mcinnes, E. J. L.; Winpenny, R. E. P.; Collison, D.; Layfield, R. A. *Angew. Chem., Int. Ed.* **2012**, *51*, 6976-6980.
21. Sulway, S. A.; Layfield, R. A.; Tuna, F.; Wernsdorfer, W.; Winpenny, R. E. P. *Chem. Commun.* **2012**, *48*, 1508-1510.
22. Nematirad, M.; Gee, W. J.; Langley, S. K.; Chilton, N. F.; Moubaraki, B.; Murray, K. S.; Batten, S. R. *Dalton Trans.* **2012**, *41*, 13711-13715.
23. Katoh, K.; Horii, Y.; Yasuda, N.; Wernsdorfer, W.; Toriumi, K.; Breedlove, B. K.; Yamashita, M. *Dalton Trans.* **2012**, *41*, 13582-13600.
24. Jankolovits, J.; Lim, C.-S.; Mezei, G.; Kampf, J. W.; Pecoraro, V. L. *Inorg. Chem.* **2012**, *51*, 4527-4538.
25. G. Mezei; Kampf, J. W.; Pan, S.; Poeppelmeier, K. R.; Watkins, B.; Pecoraro, V. L. *Chem. Commun.* **2007**, *11*, 1148-1150.
26. Boron, T. T. Control of Single-Molecule Magnetic Properties Using Metallacrowns. University of Michigan, Ann Arbor, 2012.

27. Tang, J.; Hewitt, I.; Madhu, N. T.; Chastanet, G.; Wernsdorfer, W.; Anson, C. E.; Benelli, C.; Sessoli, R.; Powell, A. K. *Angew. Chem., Int. Ed.* **2006**, *45*, 1729-1733.
28. *Saint Plus v. 7.60A*, Bruker Analytical X-ray: Madison, WI, 2008.
29. Sheldrick, G. M. *SADABS, v. 2008/1*, Program for Empirical Absorbtion Correction of Area Detector Data: Gottingen, Germany, 2008.
30. Corporation, R. *Crystalclear 2.0*, Tokyo, Japan.
31. Sheldrick, G. M. *Acta. Cryst.* **2008**, *A64*, 112-122.
32. Wernsdorfer, W. *Supercond. Sci. Technol.* **2009**, *22*, 064013.
33. Wernsdorfer, W.; Chakov, N. E.; Christou, G. *Phys. Rev. B* **2004**, *70*, 132413.
34. Roos, B. O.; Lindh, R.; Malmqvist, P.-Å.; Veryazov, V.; Widmark, P.-O.; Borin, A. C. *The Journal of Physical Chemistry A* **2008**, *112*, 11431-11435.
35. Roos, B. O.; Lindh, R.; Malmqvist, P.-Å.; Veryazov, V.; Widmark, P.-O. *The Journal of Physical Chemistry A* **2003**, *108*, 2851-2858.
36. Aquilante, F.; De Vico, L.; Ferré, N.; Ghigo, G.; Malmqvist, P.-Å.; Neogrády, P.; Pedersen, T. B.; Pitoňák, M.; Reiher, M.; Roos, B. O.; Serrano-Andrés, L.; Urban, M.; Veryazov, V.; Lindh, R. *J. Comput. Chem.* **2010**, *31*, 224-247.
37. Roos, B. O.; Taylor, P. R.; Si�doteGbahn, P. E. M. *Chemical Physics* **1980**, *48*, 157-173.
38. Malmqvist, P. Å.; Roos, B. O.; Schimmelpfennig, B. *Chem. Phys. Lett.* **2002**, *357*, 230-240.
39. Heß, B. A.; Marian, C. M.; Wahlgren, U.; Gropen, O. *Chem. Phys. Lett.* **1996**, *251*, 365-371.
40. Bolvin, H. *ChemPhysChem* **2006**, *7*, 1575-1589.
41. Lines, M. E. *J. Chem. Phys.* **1971**, *55*, 2977-2984.
42. Kahn, M. L.; Ballou, R.; Porcher, P.; Kahn†, O.; Sutter, J.-P. *Chem. Eur. J.* **2002**, *8*, 525-531.
43. Petit, S.; Pilet, G.; Luneau, D.; Chibotaru, L. F.; Ungur, L. *Dalton Trans.* **2007**, 4582-4588.
44. Gendron, F.; Páez-Hernández, D.; Notter, F.-P.; Pritchard, B.; Bolvin, H.; Autschbach, J. *Chem. Eur. J.* **2014**, *20*, 7994-8011.
45. Mezei, G.; Zaleski, C. M.; Pecoraro, V. L. *Chem. Rev.* **2007**, *107*, 4933-5003.
46. T. T. Boron, I.; Kampf, J. W.; Pecoraro, V. L. *Inorg. Chem.* **2010**, *49*, 9104-9106.
47. Zaleski, C. M.; Tricard, S.; Depperman, E. C.; Wernsdorfer, W.; Mallah, T.; Kirk, M. L.; Pecoraro, V. L. *Inorg. Chem.* **2011**, *50*, 11348-11352.
48. Zaleski, C. M.; Kampf, J. W.; Mallah, T.; Kirk, M. L.; Pecoraro, V. L. *Inorg. Chem.* **2007**, *46*, 1954-1956.
49. Jankolovits, J.; Andolina, C. M.; Kampf, J. W.; Raymond, K. N.; Pecoraro, V. L. *Angew. Chem., Int. Ed.* **2011**, *50*, 9660-9664.
50. Seda, S. H.; Janczak, J.; Lisowski, J. *Inorg. Chem. Commun.* **2006**, *9*, 792-796.
51. Casanova, D.; Llunell, M.; Alemany, P.; Alvarez, S. *Chem.-Eur. J.* **2005**, *11*, 1479-1494.
52. Long, J. R. M.; Habib, F.; Lin, P.-H.; Korobkov, I.; Enright, G.; Ungur, L.; Wernsdorfer, W.; Chibotaru, L. F.; Murugesu, M. *J. Am. Chem. Soc.* **2011**, *133*, 5319-5328.
53. Roy, L. E.; Hughbanks, T. *J. Am. Chem. Soc.* **2006**, *128*, 568-575.
54. NSOs represent the unpaired electron occupancy of the seven *f*-orbitals.
55. Anderson, P. W., 2 - Exchange in Insulators: Superexchange, Direct Exchange, and Double Exchange. In *Magnetism*, Suhl, G. T. R., Ed. Academic Press: 1963; pp 25-83.
56. Girerd, J.-J.; Charlot, M.-F.; Kahn, O. *Mol. Phys.* **1977**, *34*, 1063-1076.
57. Kahn, O., *Molecular Magnetism*. VCH Publishers, Inc.: New York, 1993.
58. Le Roy, J. J.; Jeletic, M.; Gorelsky, S. I.; Korobkov, I.; Ungur, L.; Chibotaru, L. F.; Murugesu, M. *J. Am. Chem. Soc.* **2013**, *135*, 3502-3510.
59. Ruiz-Martinez, A.; Casanova, D.; Alvarez, S. *Dalton Trans.* **2008**, 2583-2591.
60. Zou, L.; Zhao, L.; Chen, P.; Guo, Y.-N.; Guo, Y.; Li, Y.-H.; Tang, J. *Dalton Trans.* **2012**, *41*, 2966-2971.

61. Lin, P.-H.; Burchell, T. J.; Clérac, R.; Murugesu, M. *Angew. Chem., Int. Ed.* **2008**, *47*, 8848-8851.
62. Guo, Y.-N.; Chen, X.-H.; Xue, S.; Tang, J. *Inorg. Chem.* **2011**, *50*, 9705-9713.

# Chapter III

# A Systematic Investigation of the Magnetic Interactions in Mixed *3d*/*4f* Complexes

## 3.1 Introduction

Aside from pure $3d^{1\text{-}2}$ and pure $4f^{3}$ SMMs, the rationale behind the synthesis of heterometallic mixed *3d*/*4f* coordination clusters[4-5] is based on a basic premise: can the large anisotropy of lanthanides be combined with the spin and strong coupling behavior of transition metals to generate complexes exhibiting large energy barriers and magnetic hysteresis at high temperatures? The metallacrown approach had previously led to the synthesis of several mixed *3d*/*4f* SMMs, including the first mixed Mn/Ln SMM complex described in Chapter I.

Recently, the Powell group has investigated numerous mixed $Ln^{III}/Fe^{II}$ and $Ln^{III}/Fe^{III}$ complexes in order to investigate the interactions between the *3d* and *4f* ions.[6-16] In the case of a $Fe^{II}_2Dy^{III}$ complex,[16] the anisotropic barrier was determined to be 319 $cm^{-1}$, whereas it was 305 $cm^{-1}$ for the $Zn^{II}_2Dy^{III}$ analogue.[17] *Ab initio* calculations showed that enhancement of the axial crystal field due to the paramagnetic $Fe^{II}$ ions (vs. diamagnetic $Zn^{II}$) led to a higher energy first excited Kramers' doublet for the $Dy^{III}$ ion.[16] Furthermore, Mössbauer measurements showed that the interaction between the $Fe^{II}$ and $Dy^{III}$ ions effectively slow down the nuclear magnetic relaxation of the $Fe^{II}$ ions.[16] For isotropic $Fe^{III}$ ions, the Powell group has investigated various $Fe^{III}_2Ln^{III}_2$ complexes which exhibit both ferromagnetic[12] and antiferromagnetic[8, 10] exchange

between the $Fe^{III}$ and $Ln^{III}$ ions. In both cases, it was found that the magnetic dipole originating from the anisotropic lanthanide centers affects the Larmor precession time of the $Fe^{III}$ ions, as observed by Mössbauer spectroscopy.[8, 12]

In this Chapter, we will look into how peripheral *3d* metal ions influence the magnetic relaxation of $Dy^{III}$ ions. Two distinct cases will be investigated, where (i) two closely interacting $Ln^{III}$ are surrounded by four paramagnetic ions and (ii) a single, central $Ln^{III}$ is enclosed be four paramagnetic metals. In case (i), the system that is studied has the molecular formula $[Fe^{III}_4Dy^{II}_2(shi^{3-})_4(Hshi^{2-})_2(H_2shi^{-})_2(C_5H_5N)_4(CH_3OH)(H_2O)]$. Herein referenced as **$Fe_4Ln_2$**, these compounds are isostructural to the **$Ga_4Ln_2$** complexes described in Chapter II. In case (ii), a comparison of **$M_4Dy$** complexes with the general formula $Dy^{III}(benzoate)_3[12\text{-}MC_{M^{III}N(shi)}\text{-}4](pyridinium^{+})$ (where $M^{III}$ = $Ga^{III}$ and $Mn^{III}$) will be discussed. In the case of the $Ga^{III}$ (diamagnetic) analogues, the magnetic moment will originate solely from the central $Dy^{III}$ ion. On the other hand, $Mn^{III}$ ($S$ = 2) ions will contribute to the molecular magnet moment. In general, $Mn^{III}$ ions exhibit significant magnetic anisotropy ($D \approx \pm 3$ $cm^{-1}$). Examination of the magnetic properties of the **$Fe_4Ln_2$** and **$M_4Dy$** compounds will give insight into how *3d – 4f* exchange interactions affect SMM behavior.

### 3.2 Experimental

All reagents were purchased from commercial sources and were used without further purification. Elemental analysis was performed by Atlantic Microlabs Inc. All reactions were carried under aerobic conditions.

#### *Synthetic Methods*

**$Fe_4Dy_2$**: Salicylhydroxamic acid (153.1 mg, 1.000 mmol), $Gd(NO_3)_3{\cdot}6H_2O$ (112.8 mg, 0.2500 mmol), $Fe(NO_3)_3{\cdot}9H_2O$ (127.9 mg, 0.5000 mmol) were dissolved in 46 mL

methanol. 13 mL pyridine was added drop wise to this solution, followed by 6.5 mL $H_2O$. The solution was stirred for 30 seconds and then filtered. Slow evaporation of half of the solution yielded crystalline compound after 2 weeks. Yield: 0.0892 g (28.3%), Anal. Calcd for $Tb_2Ga_4C_{94}H_{93}N_{15}O_{31}$: C, 44.70; H, 3.71; N, 8.32. Found: C, 44.45; H, 3.63; N, 8.38. Single-crystal unit cell: monoclinic, space group *C*2/*c*, *a* = 25.1697 Å, *b* = 22.1217 Å, *c* = 17.9895 Å, $\beta = 99.302^{\circ}$, V = 9884.8 $Å^3$.

$[DyGa_4(shi^{3-})_4(C_6H_5CO_2)_4(C_5H_5N)(CH_3OH)] \cdot C_5H_6N \cdot C_5H_5N \cdot CH_3OH$ (**$Ga_4Dy$**): $H_3$shi (153.1 mg, 1.0 mmol), $Dy(NO_3)_3 \cdot 5H_2O$ (0.25 mmol), $Ga(NO_3)_3 \cdot xH_2O$ (225.7 mg, 1.0 mmol) was dissolved in 40 mL methanol. Sodium benzoate (432.3 mg, 3.0 mmol) was added to the solution and stirred overnight. The solution was filtered, followed by addition of 2 mL pyridine. The solution was stirred for 15 minutes and then filtered. Slow evaporation of the half of the solution yielded crystalline compound after 2 weeks. Yield: 106.6 mg (23.3%). Anal. Calcd for $DyGa_4C_{73}H_{60}N_7O_{22}$: C, 47.95; H, 3.31; N, 5.36. Found: C, 48.08; H, 3.10; N, 5.54.

$[DyMn_4(shi^{3-})_4(C_6H_5CO_2)_4(C_5H_5N)(CH_3OH)] \cdot C_5H_6N \cdot C_5H_5N \cdot CH_3OH$ (**$Mn_4Dy$**): $H_3$shi (153.1 mg, 1.0 mmol), $DyCl_3 \cdot 6H_2O$ (94.2 mg, 0.25 mmol), $MnCl_2 \cdot 6H_2O$ (197.9 mg, 1.0 mmol) was dissolved in 40 mL methanol. Sodium benzoate (576.4 mg, 4.0 mmol) was added to the solution and stirred overnight. The solution was filtered, followed by addition of 2 mL pyridine. The solution was stirred for 3 hours and then filtered. Slow evaporation of the half of the solution yielded crystalline compound after 2 weeks. Yield: 128.1 mg (%). Anal. Calcd for $DyMn_4C_{73}H_{60}N_7O_{22}$: C, 47.95; H, 3.31; N, 5.36. Found: C, 48.08; H, 3.10; N, 5.54.

***Physical Methods***

*X-ray Crystallography.* Single-crystal X-ray diffraction data for **$Fe_4Dy_2$**, **$Ga_4Dy$** and **$Mn_4Dy$** were collected by Jeff W. Kampf at the University of Michigan. I completed all structural refinements.

Crystal data for compounds **$Fe_4Dy_2$** and **$Ga_4Dy$** were collected at 85(2) K on an AFC10K Saturn 944+ CCD-based X-ray diffractometer equipped with a Micromax007HF Cu-target microfocus rotating anode ($\lambda$ = 1.54187 Å), operated at 1200 W power (40 kV, 30 mA). The data were processed with CrystalClear 2.0 and corrected for absorption.[18]

Crystal data for compound **$Mn_4Dy$** were collected at 85(2) K on a Bruker SMART-APEX CCD-based X-ray diffractometer equipped with a low temperature device and fine-focus Mo-target X-ray tube ($\lambda$ = 0.71073 Å), operated at 1500 W power (50 kV, 30 mA). The frames were integrated with the Bruker SAINT[19] software package with a narrow frame algorithm. The data were processed with SADABS[20] and corrected for absorption.

All structures were solved and refined with the SHELXTL (version 6.12) software package.[21] All non-hydrogen atoms were refined anisotropically. Hydrogen atoms are placed in their idealized positions. Additional details are provided in Table 3.1. Selected bond lengths are given in Table 3.2.

**Table 3.1.** Crystallographic Details for **$Fe_4Dy_2$**, **$Ga_4Dy$** and **$Mn_4Dy$**.

| | **$Fe_4Dy_2$** | **$Ga_4Dy$** | **$Mn_4Dy$** |
|---|---|---|---|
| mol formula | $C_{93}H_{94}N_{15}O_{31}Fe_4Dy_2$ | $C_{73}H_{60}N_7O_{22}Ga_4Dy$ | $C_{76}H_{50}N_8O_{20}DyMn_4$ |
| fw (g/mol) | 2394.14 | 1828.66 | 1777.50 |
| cryst syst/ space group | Monoclinic, C2/c | Monoclinic, P21/c | Monoclinic, P2(1)/n |
| *T* (K) | 85(2) | 85(2) | 85(2) |
| wavelength (Å) | 1.54178 | 1.54178 | 0.71073 A |
| *a* (Å) | 25.0993(5) | 17.1202(3) | 17.1601(13) |
| *b* (Å) | 22.2455(4) | 17.1515(3) | 17.1033(12) |
| *c* (Å) | 18.2761(13) | 28.505(2) | 24.4861(18) |
| α (deg) | 90 | 90 | 90 |
| β (deg) | 99.732(7) | 122.170(5) | 98.6070(10) |
| γ (deg) | 90 | 90 | 90 |
| *V* (Å$^3$) | 10057.5(8) | 7085.1(5) | 7105.6(9) |
| *Z* | 4 | 4 | 4 |
| density, ρ (g/cm$^3$) | 1.581 | 1.714 | 1.662 |
| abs coeff, μ (mm$^{-1}$) | 13.009 | 7.958 | 1.812 |
| *F*(000) | 4808 | 3651 | 3552 |
| θ range for data collection (deg) | 3.42 to 68.24 | 3.05 to 68.25 | 1.69 to 27.29 |
| limiting indices | $-30 \le h \le 26$<br>$-26 \le k \le 12$<br>$-22 \le l \le 22$ | $-20 \le h \le 20$<br>$-20 \le k \le 20$<br>$-34 \le l \le 34$ | $-22 \le h \le 22$<br>$-22 \le k \le 22$<br>$-31 \le l \le 31$ |
| reflns collected/ unique | 32508 / 9178 | 191116 / 12987 | 147223 / 15972 |
| completeness to θ (%) | 99.6 | 100.0 | 100.0 |
| no. of data/ restraints/ params | 9178 / 321 / 745 | 12987 / 55 / 1021 | 15972 / 4 / 1014 |
| goodness of fit on $F^2$ | 1.104 | 1.068 | 0.964 |
| final *R* indices [$I > 2\sigma(I)$] | R1[a] = 0.0936<br>wR2[b] = 0.2414 | R1[a] = 0.0346<br>wR2[b] = 0.0868 | R1[a] = 0.0529<br>wR2[b] = 0.1343 |
| *R* indices (all data) | R1[a] = 0.1051<br>wR2[b] = 0.2624 | R1[a] = 0.0347<br>wR2[b] = 0.0869 | R1[a] = 0.0866<br>wR2[b] = 0.1548 |
| largest diff peak and hole (e$^-$ Å$^{-3}$) | 2.706 and -0.823 | 2.569 and -0.719 | 2.086 and -0.787 |

[a] $R1 = \Sigma(||F_o| - |F_c||)/\Sigma|F_o|$. [b] $wR2 = [\Sigma[w(F_o^2 - F_c^2)^2]/\Sigma[w(F^\circ)^2]]^{1/2}$; $w = 1/[\sigma^2(F_o^2) + (mp)^2 + np]$; $p = [\max(F_o^2,0) + 2F_c^2]/3$ (*m* and *n* are constants); $\sigma = [\Sigma[w(F_o^2 - F_c^2)^2]/(n-p)]^{1/2}$.

**Table 3.2.** Selected bond lengths for **$Fe_4Dy_2$**, **$Ga_4Dy$**, and **$Mn_4Dy$**.

| Compound | Bond | Length (Å) | Compound | Bond | Length (Å) |
|---|---|---|---|---|---|
| **$Fe_4Dy_2$** | Dy(1)-O(1a) | 2.254(5) | **$Ga_4Dy$** | Dy(1)-O(121) | 2.293(2) |
| | Dy(1)-O(2) | 2.317(5) | | Dy(1)-O(8) | 2.315(2) |
| | Dy(1)-O(9) | 2.320(5) | | Dy(1)-O(131) | 2.319(2) |
| | Dy(1)-O(2a) | 2.329(5) | | Dy(1)-O(5) | 2.325(2) |
| | Dy(1)-O(5) | 2.343(5) | | Dy(1)-O(11) | 2.330(2) |
| | Dy(1)-O(510) | 2.377(15) | | Dy(1)-O(2) | 2.340(2) |
| | Dy(1)-O(7) | 2.387(5) | | Dy(1)-O(111) | 2.368(2) |
| | Dy(1)-O(500) | 2.43(3) | | Dy(1)-O(101) | 2.368(2) |
| | Dy(1)-O(11) | 2.526(5) | | | |
| **$Mn_4Dy$** | Dy(1)-O(111) | 2.284(4) | | | |
| | Dy(1)-O(121) | 2.290(4) | | | |
| | Dy(1)-O(131) | 2.294(4) | | | |
| | Dy(1)-O(101) | 2.297(4) | | | |
| | Dy(1)-O(2) | 2.375(3) | | | |
| | Dy(1)-O(11) | 2.392(4) | | | |
| | Dy(1)-O(5) | 2.404(4) | | | |
| | Dy(1)-O(8) | 2.409(4) | | | |

*Magnetic Measurements*. Variable-temperature susceptibility, variable-field magnetization and ac susceptibility measurements on polycrystalline samples mulled in eicosane were performed on a Quantum Design MPMS SQUID magnetometer. Variable-temperature dc susceptibility measurements were performed at 2000 Oe from 2-300 K. Isothermal magnetization measurements were performed at 2 K from 0-7 T. AC magnetic susceptibility measurements were done at both zero and applied fields with an ac drive field of 3 Oe at frequencies ranging from 1 to 1488 Hz. Dc susceptibilities were corrected for the sample holder and eicosane and for diamagnetism of constituent atoms using Pascal's constants.

### 3.3 Results and Discussion

**Synthesis and Characterization.** The **$Fe_4Ln_2$** complexes were synthesized in a similar fashion as the **$Ga_4Ln_2$** compounds discussed in Chapter II (Figure 3.1). Due to the immediate precipitation of dark, insoluble material, the reaction solution was diluted (with respect to the **$Ga_4Ln_2$** complexes) in order to slow down crystal growth. **$Fe_4Dy_2$** and **$Fe_4Gd_2$** crystallized in the same space group (C2/c) as the gallium derivatives. The crystal structure of **$Fe_4Dy_2$** shows the same general molecular morphology as the **$Ga_4Ln_2$**.

Both **$Ga_4Dy$** (Figure 3.2) and **$Mn_4Dy$** (Figure 3.3) exhibit a 12-MC-4 topology similar to structures described by Azar et al.[22] In both compounds, benzoate was employed as a bridging ligand between the central lanthanide and ring metals. Due to the addition of pyridine in the reaction solution, in both complexes, pyridine coordinates to the ring metals and a charged pyridinium$^+$ counter-cation is present in the lattice to provide charge balance.

In **$Ga_4Dy$** and **$Mn_4Dy$**, the central $Dy^{III}$ ion has a pseudo square pyramidal ligand field which may be suitable to generate an easy-axis type anisotropy. First introduced by Coronado[23] and later revisited by Boron,[24] single-ion lanthanide complexes which have square antiprism geometry may be evaluated by certain geometric parameters. Unlike the symmetric $LnZn_{16}$ complexes and polyoxometalate complexes studied by Boron[24] and Coronado,[23] respectively, the "top" (benzoate) and "bottom" (metallacrown ring) oxygen planes of the **$M_4Dy$** complexes are not equivalent, and the compounds may be described as having pseudo $C_{4v}$ symmetry. However, their analysis may still be a useful qualitative tool to understand the geometry around the $Dy^{III}$ ion.

Following the same analyses used by Boron,[24] the distance between the oxygen mean planes ($O_{mp} - O_{mp}$), average oxygen to oxygen distance in the metallacrown ring (avg. $O_{edge}$) and

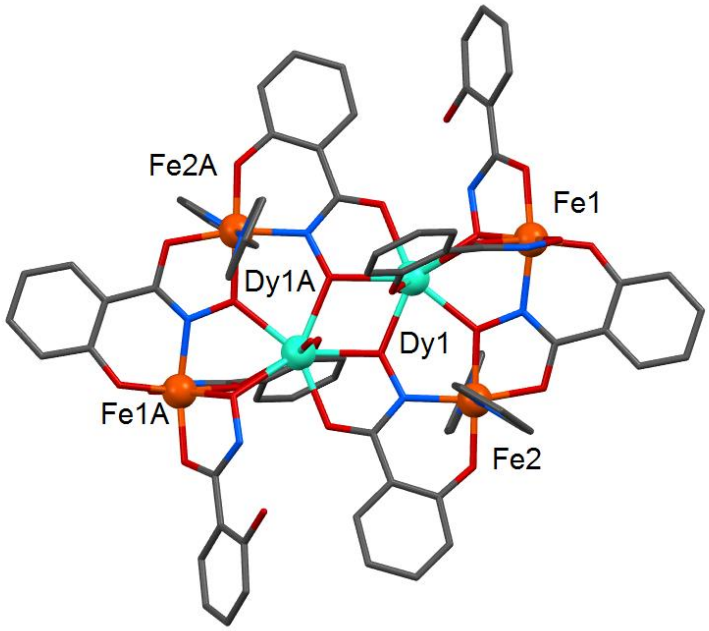


**Figure 3.1.** Crystal structure of **$Fe_4Dy_2$**. Color scheme: orange spheres – $Fe^{III}$, teal spheres – $Dy^{III}$, red tubes – O, blue tubes – N, gray tubes – C. Hydrogens and lattice solvents were omitted.

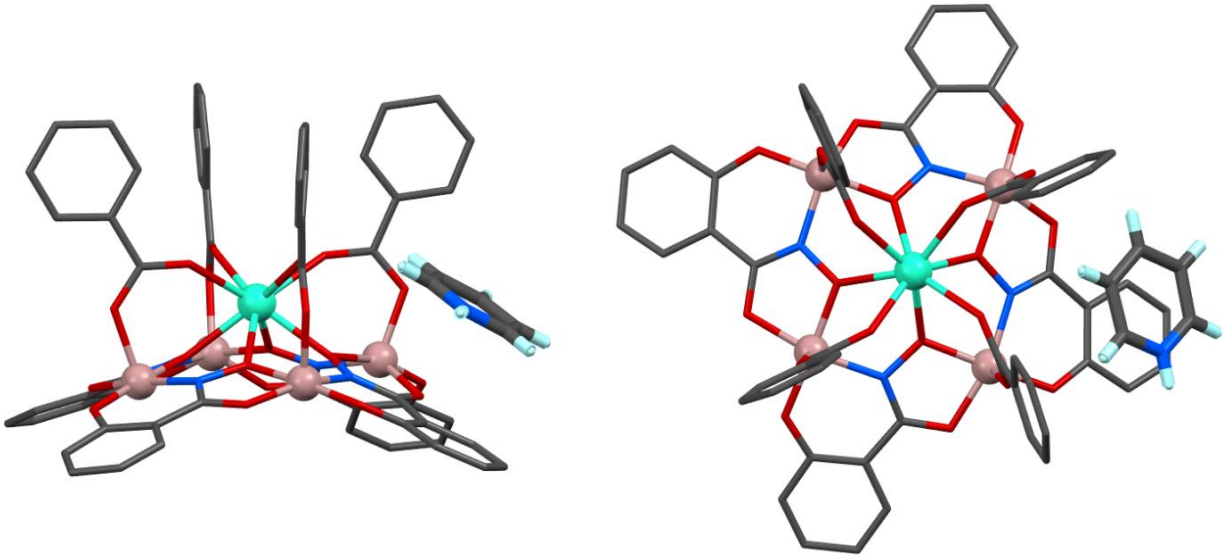

**Figure 3.2.** Crystal structure of **$Ga_4Dy$**. (left) Side-view. (right) Top-down view. Color scheme: lilac spheres – $Ga^{III}$, teal spheres – $Dy^{III}$, red tubes – O, blue tubes – N, gray tubes – C. The $pyridinium^+$ counter-ion is in bold. Hydrogens, coordinating and lattice solvents were omitted for clarity.

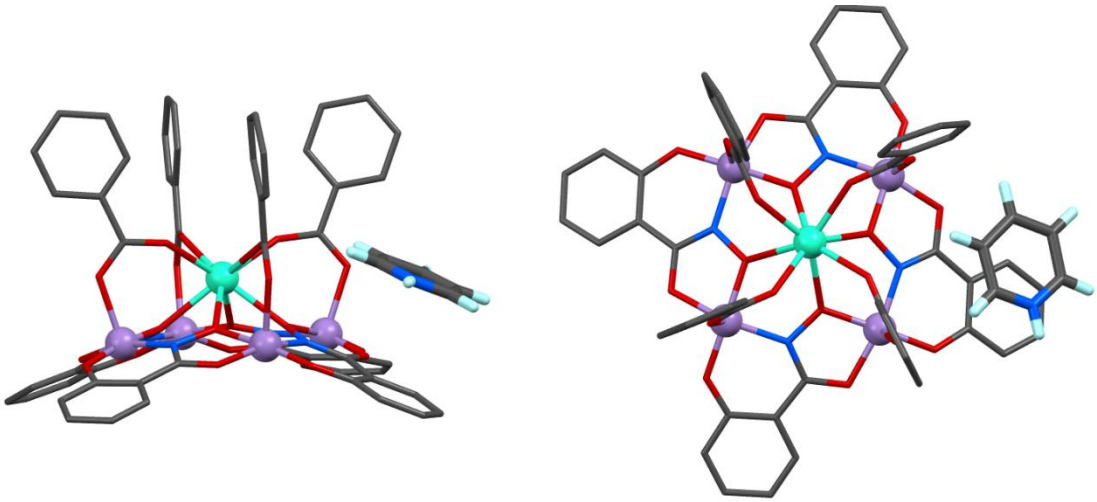

**Figure 3.3.** Crystal structure of **$Mn_4Dy$**. (left) Side-view. (right) Top-down view. Color scheme: purple spheres – $Mn^{III}$, teal spheres – $Dy^{III}$, red tubes – O, blue tubes – N, gray tubes – C. The pyridinium$^+$ counter-ion is in bold. Hydrogens, coordinating and lattice solvents were omitted for clarity.

skew angles are reported in Table 3.3 and Table 3.4. For **$Ga_4Dy$** and **$Mn_4Dy$**, the ratio between the $O_{mp}$ – $O_{mp}$ and $O_{edge}$ distances are less than one (Table 3.3). This suggests an axial compression around the $Dy^{III}$, which, according to Rinehart and Long, is necessary for easy-axis anisotropy in oblate shaped lanthanide ions.[25] According to Coronado,[23] lanthanides with square antiprism geometry should have an ideal skew angle of 45° in order to optimize SMM behavior. The skew angles in **$Mn_4Dy$** are closer to this ideal value than they are in **$Ga_4Dy$** (Table 3.4).

**Magnetic Properties. (i) $Fe_4Dy_2$.** The variable-temperature dc magnetic susceptibility for **$Fe_4Dy_2$** were measured at an applied field of 2000 Oe and in a temperature range of 300 to 2 K (Figure 3.4). The room temperature $\chi_mT$ product (43.32 $cm^3$ K $mol^{-1}$) is slightly below the

**Table 3.3.** $O_{mp}$ – $O_{mp}$ and average $O_{edge}$ distances for **$Ga_4Dy$** and **$Mn_4Dy$**.

| Compound | $O_{mp}$ - $O_{mp}$ (Å) | Avg. $O_{edge}$ | Ratio |
|---|---|---|---|
| **$Ga_4Dy$** | 2.53 | 2.64 | 0.958 |
| **$Mn_4Dy$** | 2.57 | 2.68 | 0.958 |

**Table 3.4.** Skew angles for **$Ga_4Dy$** and **$Mn_4Dy$**.

| Compound | Bond | Skew Angle (°) |
|---|---|---|
| **$Ga_4Ln$** | O2-Dy1-O101 | 48.23 |
| | O2-Dy1-O111 | 41.41 |
| | O5-Dy1-O111 | 47.68 |
| | O5-Dy1-O121 | 42.13 |
| | O8-Dy1-O121 | 48.77 |
| | O8-Dy1-O131 | 41.24 |
| | O11-Dy1-O131 | 48.45 |
| | O11-Dy1-O101 | 42.09 |
| **$Mn_4Dy$** | O2-Dy1-O101 | 47.59 |
| | O2-Dy1-O111 | 43.03 |
| | O5-Dy1-O111 | 47.60 |
| | O5-Dy1-O121 | 42.57 |
| | O8-Dy1-O121 | 47.23 |
| | O8-Dy1-O131 | 42.43 |
| | O11-Dy1-O131 | 46.82 |
| | O11-Dy1-O101 | 42.73 |

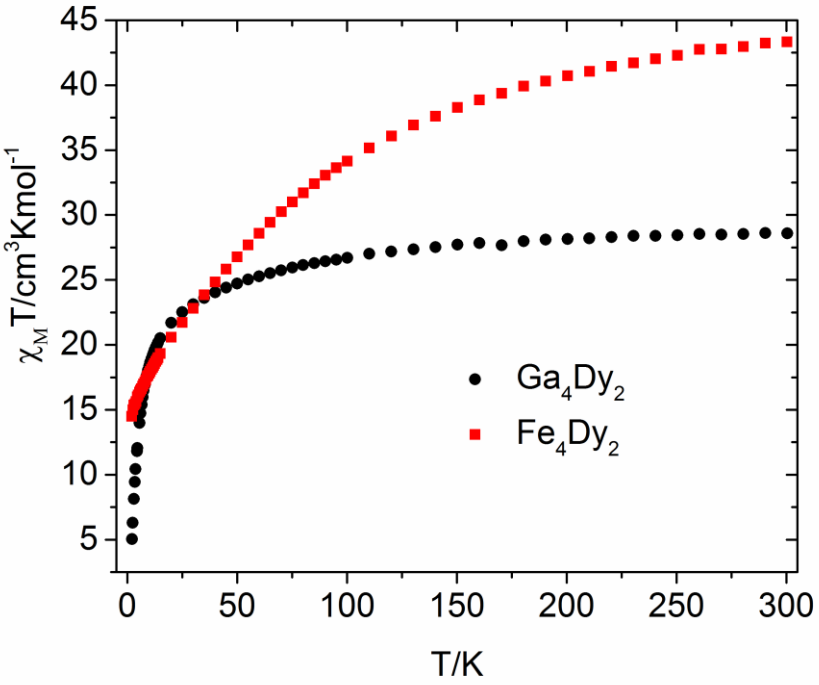


**Figure 3.4.** $\chi_m$T vs. T for **$Fe_4Dy_2$** and **$Ga_4Dy_2$** (described in Chapter I).

expected value (45.84 $cm^3$ K $mol^{-1}$) for two $Dy^{III}$ and four $Fe^{III}$ non-interacting ions ($Fe^{III}$: $^6A_{1g}$, $S$ = 5/2, g = 2, $C$ = 4.375 $cm^3$ K $mol^{-1}$; $Dy^{III}$: $^6H_{15/2}$, $C$ = 14.17 $cm^3$ K $mol^{-1}$). The $\chi_m T$ product is still increasing at 300 K, suggesting a significant and complex coupling scheme. Upon cooling, $\chi_m T$ decreases until it reaches a value of 13.84 $cm^3$ K $mol^{-1}$ at 2 K. This value is much higher than the 2 K value for the **$Ga_4Dy_2$** complex in Chapter II (5.04 $cm^3$ K $mol^{-1}$). This indicates that the $Fe^{III}$-$Dy^{III}$ interactions are significant at low temperatures. If they were negligible, the antiferromagnetic Fe1-Fe2 and Fe1A-Fe2A interactions (see Figure 3.1) should lead to no contribution to the magnetic moment and the $\chi_m T$ product should be similar to that of **$Ga_4Dy_2$**.

The magnetization curve of **$Fe_4Dy_2$** at 2 K reaches a maximum of 9.87 $N\mu_B$ at a field of 7 T, which is lower than the 10.36 $N\mu_B$ value for **$Ga_4Dy_2$** (Figure 3.5). Whereas the magnetization curve for **$Ga_4Dy_2$** is close to saturation at 7 T, it still steadily increasing for **$Fe_4Dy_2$**. Below 1 T, the magnetization for **$Fe_4Dy_2$** increases much more sharply than for **$Ga_4Dy_2$**. However, above 1 T, the magnetization value for **$Ga_4Dy_2$** overtakes that of **$Fe_4Dy_2$** (Figure 3.5). If the $Dy^{III}$ ions were completely decoupled from the $Fe^{III}$ in compound **$Fe_4Dy_2$**, it would be expected that the magnetization at 7 T would be greater than for the $Ga^{III}$ derivative. This is another indication that significant $Fe^{III}$-$Dy^{III}$ interaction is present at low temperatures.

The ac susceptibility for **$Fe_4Dy_2$** at zero applied dc field shows an out-of-phase signal, but without maxima above 2 K, suggesting a small energy barrier (Figure 3.6). In contrast, **$Ga_4Dy_2$** exhibits maxima in the $\chi$" vs. T plot, with barrier heights of 18 K and 26 K for the ferromagnetic and decoupled relaxation processes (Figure 2.16). A possible explanation for this is that the $Fe^{III}$-$Dy^{III}$ magnetic interactions leads to low-lying excited states which speeds up relaxation through mixing and/or quantum tunneling. Attempts to quench possible quantum

tunneling were unsuccessful, as no maxima was observed in the temperature-dependent χ" plot at fields up to 6000 Oe (Figure 3.7).

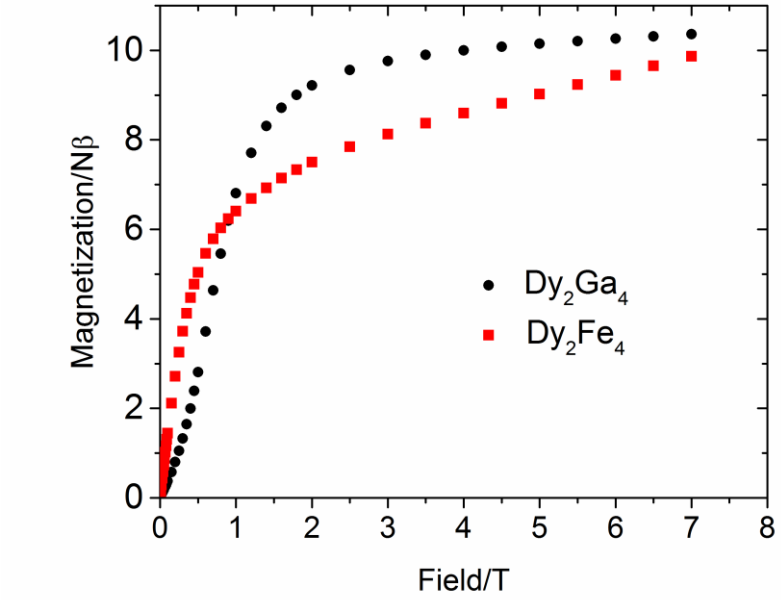


**Figure 3.5.** M/N$\mu_B$ (per $Fe_4$) vs. Field for **$Fe_4Dy_2$** and **$Ga_4Dy_2$**.

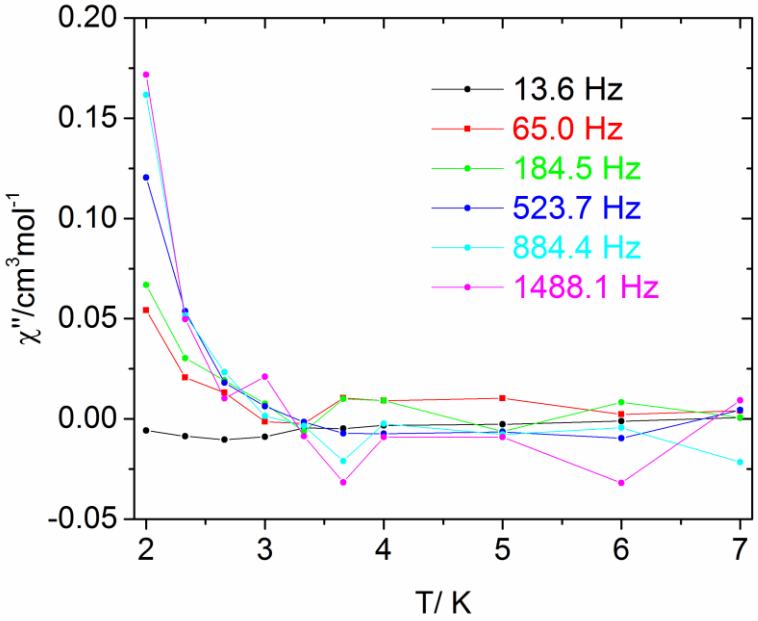


**Figure 3.6.** Temperature-dependent out-of-phase ac susceptibility under zero applied dc field for **$Fe_4Dy_2$**.

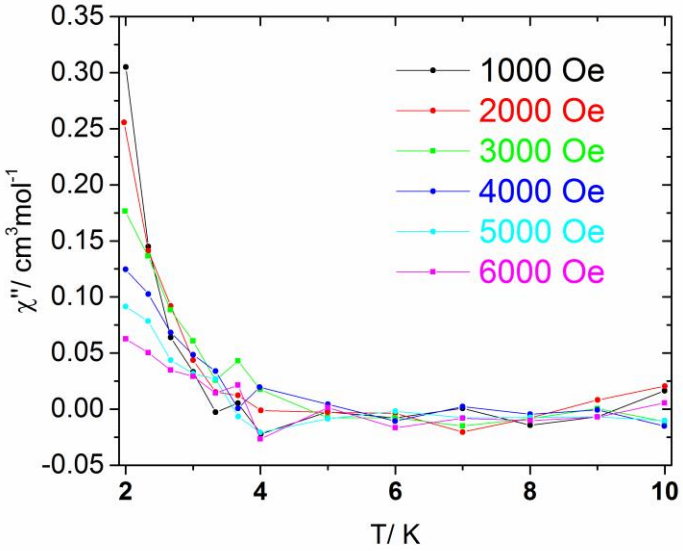


**Figure 3.7.** Temperature-dependent out-of-phase ac susceptibility for **$Fe_4Dy_2$** under applied fields ranging from 1000 Oe to 6000 Oe.

**(ii) $Ga_4Dy$** and **$Mn_4Dy$.** The variable-temperature dc magnetic susceptibility for **$Fe_4Dy_2$** were measured at an applied field of 2000 Oe and in a temperature range of 300 to 2 K (Figure 3.8). The room temperature $\chi_m T$ product for **$Ga_4Dy$** and **$Mn_4Dy$** are 14.90 $cm^3$ K $mol^{-1}$ and 26.21 $cm^3$ K $mol^{-1}$, respectively, which is in good agreement with the expected value of 5 non-interacting ions (Table 3.5). Upon cooling to 2 K, the $\chi_m T$ product decreases to reaches a value of 10.30 $cm^3$ K $mol^{-1}$ and 10.69 $cm^3$ K $mol^{-1}$ for **$Ga_4Dy$** and **$Mn_4Dy$**, respectively. For **$Ga_4Dy$**, this decrease can be attributed to the depopulation of the Stark sublevels of the $Dy^{III}$ ion. For **$Mn_4Dy$**, the decrease in $\chi_m T$ may be due to a combination of antiferromagnetic coupling, zero-field splitting in the $Mn^{III}$ ions, and depopulation of the Stark sublevels of the $Dy^{III}$ ion.

The $\chi_m T$ product at 2 K for both compounds are relatively similar (Table 3.5). This suggests that at low temperatures **$Mn_4Dy$**, dominant antiferromagnetic interactions between $Mn^{III}$ ions leads to an $S = 0$ ground state for the ring system. Thus, the $\chi_m T$ product at 2 K is

**Table 3.5.** Summarized dc susceptibility data for **$Ga_4Dy$** and **$Mn_4Dy$**.

| Compound | Curie constant for $Dy^{III}$ ($cm^3$ K $mol^{-1}$) | Calc. $\chi_mT$ for four non-interacting $M^{III}$ ring ions ($cm^3$ K $mol^{-1}$) | Calc. $\chi_mT$ for four non-interacting $M^{III}$ ring ions and $Dy^{III}$ ($cm^3$ K $mol^{-1}$) | $\chi_mT$ at 300 K ($cm^3$ K $mol^{-1}$) | $\chi_mT$ at 2 K ($cm^3$ K $mol^{-1}$) |
|---|---|---|---|---|---|
| **$Ga_4Dy$** | 14.17 | 0.00 | 14.17 | 14.90 | 10.30 |
| **$Mn_4Dy$** | 14.17 | 12.00 | 26.17 | 26.21 | 10.69 |

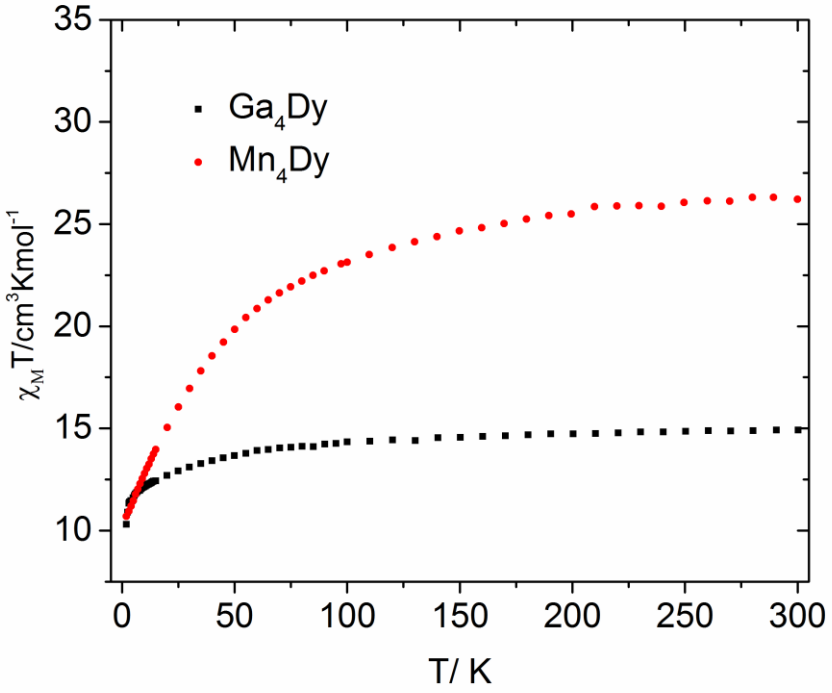


**Figure 3.8.** $\chi_m$T vs. T for **$Ga_4Dy$** and **$Mn_4Dy$**.

mainly due to a weakly coupled $Dy^{III}$ ion. This is consistent with a previously reported $Li(Cl)_2$[12- $MC_{Mn^{III}N(shi)}$-4] complex that is structurally similar to **$Mn_4Dy$**, where the central metal is a diamagnetic $Li^+$ ion.[26] In this complex, the $Mn^{III}$ – $Mn^{III}$ exchange was determined to be -4.0 $cm^{-1}$, which yields an $S$ = 0 ground state.

As seen in Figure 3.9, the magnetization data were collected at 2 K at fields from 0 to 7 T (5.5 T for **$Mn_4Dy$**). Below ca. 0.4 T, the magnetization curves for **$Ga_4Dy$** and **$Mn_4Dy$** follow a similar

trend and are roughly super imposable (Figure 3.9). This is evidence which corroborates the above postulation that the ring $Mn^{III}$ ions are antiferromagnetically coupled and leads to an $S = 0$ state. At low temperatures and fields, the magnetic moment of each of the three compounds corresponds to that of an uncoupled or weakly coupled $Dy^{III}$ ion. When the field is increased above 0.4 T, the magnetic excited states of the ring system in **$Mn_4Dy$** become populated and begin to deviate from the magnetization of the **$Ga_4Dy$** complex.

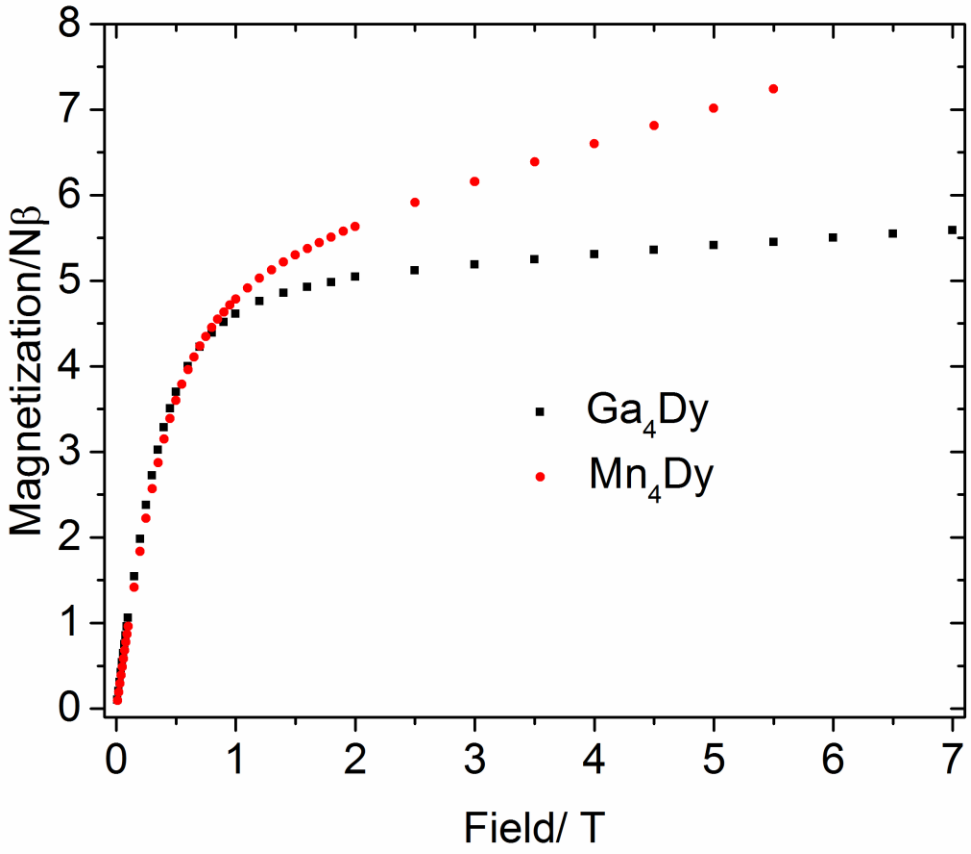


**Figure 3.9.** M/N$\mu_B$ vs. Field for **$Ga_4Dy$** and **$Mn_4Dy_2$**.

The zero-field ac susceptibility plots for **$Ga_4Dy$**, **$Mn_4Dy$** show out-of-phase behavior at low temperatures, but does not exhibit a maxima above 2 K (Figure 3.10 and 3.11, respectively). As described above, the ligand field around the $Dy^{III}$ ion of **$Ga_4Dy$** and **$Mn_4Dy$** has a pseudo square antiprism geometry, with an axial compression, which is manifested in the out-of-phase behavior at zero-field.

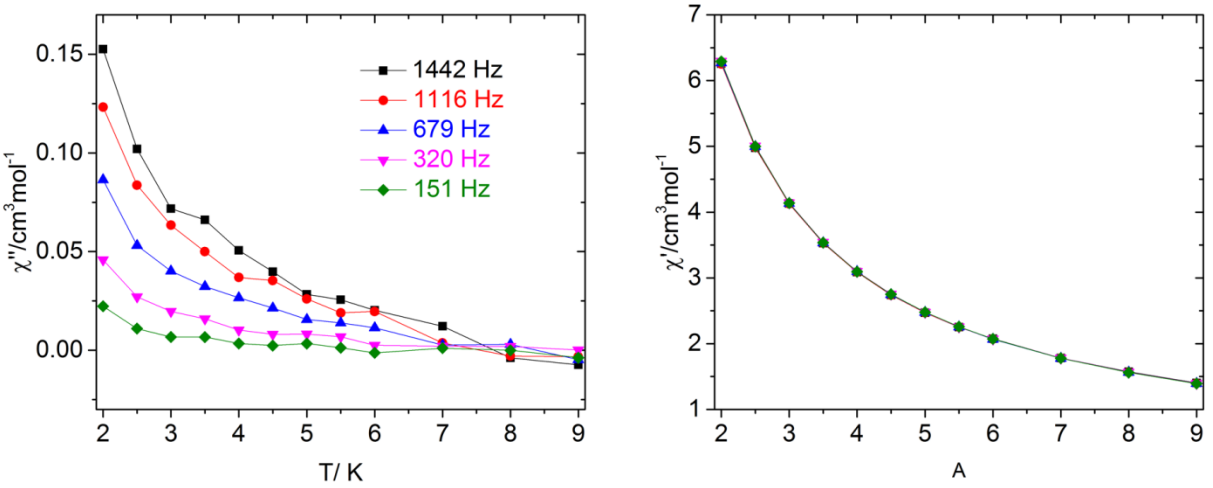


**Figure 3.10.** Temperature-dependent out-of-phase (left) and in-phase (right) ac susceptibility for **$Ga_4Dy$** under zero applied dc field.

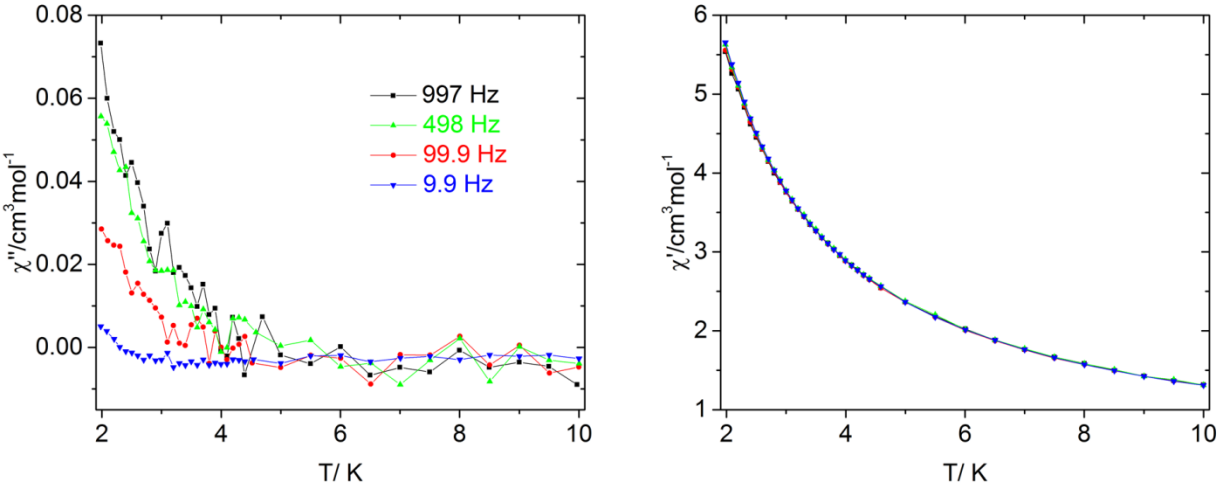


**Figure 3.11.** Temperature-dependent out-of-phase (left) and in-phase (right) ac susceptibility for **$Mn_4Dy$** under zero applied dc field.

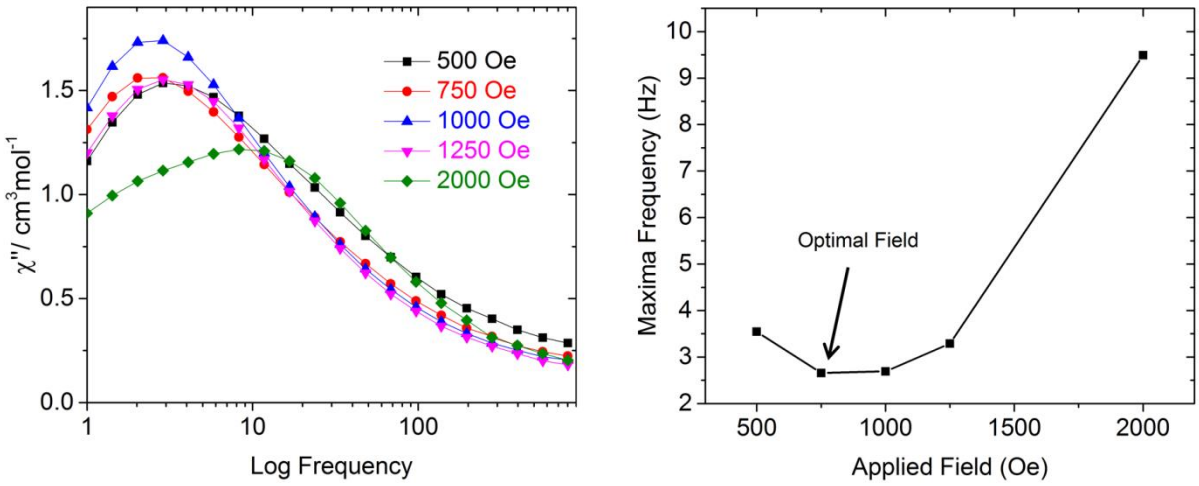


**Figure 3.12.** Field optimization of compound **$Ga_4Dy$**. (left) Out-of-phase susceptibility measurements at 2 K at a frequency range from 1 Hz to 500 Hz at various applied fields. (right) Plot of frequency maxima vs applied field.

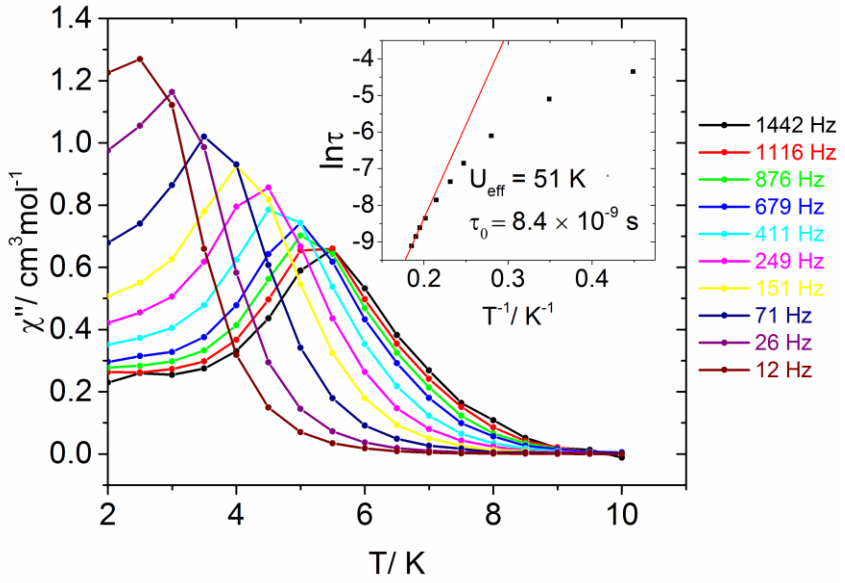


**Figure 3.13.** Temperature-dependent out-of-phase ac susceptibility **$Ga_4Dy$** under an applied dc field of 750 Oe. Inset: Energy barrier calculated from the Arrhenius plot.

In order to quench the quantum tunneling in **$Ga_4Dy$**, a static dc field can be applied to give a Zeeman splitting of the Stark sublevels; the removal of the degeneracy of the $m_J$ has been known to reduce through-barrier relaxation processes.[27] The optimal static dc field was

determined to be 750 Oe (see figure 3.12). A full ac susceptibility scan was performed under the optimal field from 2 to 10 K at frequencies between 1 and 1442 Hz (Figure 3.13). The presence of maxima in the χ" vs. T plot shows that quantum *tunneling* of the magnetization has been mostly quenched. The thermally activated relaxation follows an Arrhenius relationship (Equation 1.14). A linear fit of the high temperature region reveals an energy barrier of $U_{eff}$ = 51 K, with $\tau_0 = 8.4 \cdot 10^{-9}$ s (Figure 3.13). It is apparent that the non-ideal skew-angle (41.21° - 48.77°) in **$Ga_4Ln$** leads to significant quantum tunneling in an applied field. In a 2012 report by Hailong and coworkers, the ac properties of three (phthalocyaninato)(porphyrinato) dysprosium(III) complexes showed that the complex with a skew angle closest to 45° showed the highest energy barrier.[28]

Attempts to find an optimal field to quench quantum tunneling in **$Mn_4Dy$** was unsuccessful (Figure 3.14). At different applied fields and at a temperature of 2 K, a weak χ" signal increased with decreasing frequency (Figure 3.14), with no maxima observed. When the same experiment was performed at 5 K, the χ" signal became very noisy and undecipherable (Figure 3.17). It appears that multiple relaxation processes may be present.

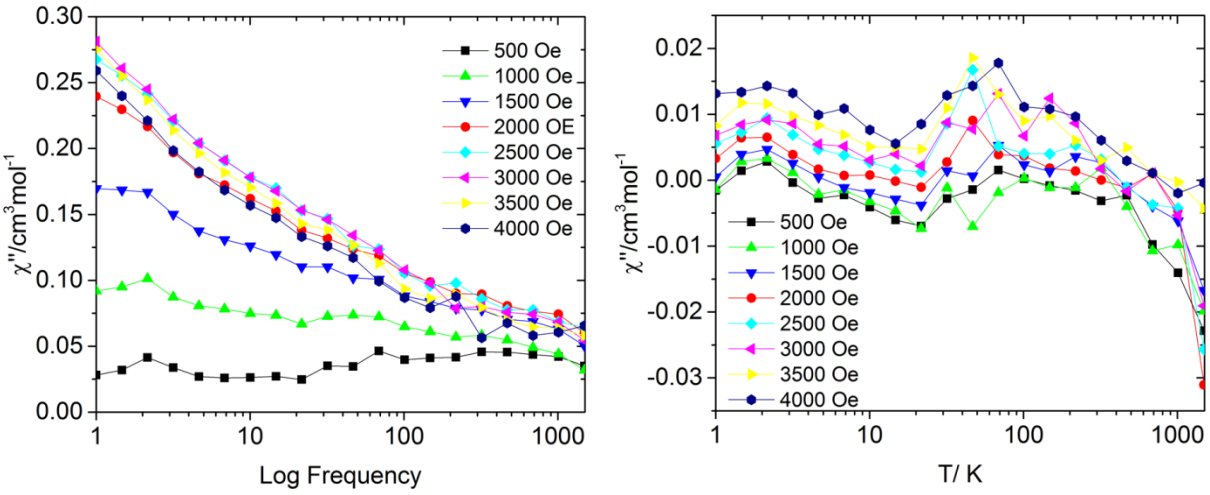


**Figure 3.14.** Frequency-dependent out-of-phase ac susceptibility plot for **$Mn_4Dy$** under applied fields ranging from 500 Oe to 4000 Oe at 2 K (left) and 5 K (right)

## 3.4 Conclusions

The systematic examination of heterometallic *3d*/*4f* metallacrown complexes reveal that antiferromagnetic interactions between lanthanides and transition metals effectively quench SMM behavior. This result is surprising, since magnetic interactions in *4f* lanthanides are generally weak. In case (i), the anisotropic barrier in **$Fe_4Dy_2$** is much reduced in comparison to the **$Ga_4Dy_2$** analogue. This finding was attributed to non-negligible $Fe^{III}$-$Dy^{III}$ interactions, which were observed in the dc magnetic data. In case (ii), the presence of a paramagnetic transition metal ($Mn^{III}$) in the 12-MC-4 ring system complicated the dynamic relaxation behavior. Both **$Ga_4Dy$** and **$Mn_4Dy$** did not exhibit a maxima in the temperature-dependent out-of-phase ac susceptibility above 2 K. Under an optimal field of 750 Oe, quantum tunneling could be effectively quenched in **$Ga_4Dy$**. On the other hand, an applied static dc field caused the ac behavior of **$Mn_4Dy$** to become noisy and unreliable.

The results of the work described in this Chapter suggest that for antiferromagnetically coupled *3d*/*4f* metallacrowns, the presence of an *antiferromagnetically* coupled paramagnetic transition metal decreases the anisotropic barrier. In comparison, in Powell's $Fe^{II}_2Dy^{III}$ complex, it was found that *ferromagnetic 3d-4f* coupling to anisotropic $Fe^{II}$ ions led to a larger barrier height than for the $Zn^{II}_2Dy^{III}$ analogue.[16-17] These results are not surprising, as ferromagnetic interactions should lead to a larger spin state. However, the *design* of ferromagnetic coupling remains a difficult prospect in coordination chemistry.

## References


1. Glaser, T. *Chem. Commun.* **2011**, *47*, 116-130.
2. Atanasov, M.; Aravena, D.; Suturina, E.; Bill, E.; Maganas, D.; Neese, F. *Coord. Chem. Rev.*
3. Woodruff, D. N.; Winpenny, R. E. P.; Layfield, R. A. *Chem. Rev.* **2013**, *113*, 5110-5148.
4. Feltham, H. L. C.; Brooker, S. *Coord. Chem. Rev.* **2014**, *276*, 1-33.
5. Polyzou, C. D.; Efthymiou, C. G.; Escuer, A.; Cunha-Silva, L.; Papatriantafyllopoulou, C.; Perlepes, S. P. *Pure Appl. Chem.* **2013**, *85*, 315+.
6. Schmidt, S.; Prodius, D.; Novitchi, G.; Mereacre, V.; Kostakis, G. E.; Powell, A. K. *Chem. Commun.* **2012**, *48*, 9825-9827.
7. Mereacre, V.; Klöwer, F.; Lan, Y.; Clérac, R.; Wolny, J. A.; Schünemann, V.; Anson, C. E.; Powell, A. K. *Beilstein J. Nanotechnol.* **2013**, *4*, 807-814.
8. Baniodeh, A.; Lan, Y.; Novitchi, G.; Mereacre, V.; Sukhanov, A.; Ferbinteanu, M.; Voronkova, V.; Anson, C. E.; Powell, A. K. *Dalton Trans.* **2013**, *42*, 8926-8938.
9. Xiang, H.; Mereacre, V.; Lan, Y.; Lu, T.-B.; Anson, C. E.; Powell, A. K. *Chem. Commun.* **2013**, *49*, 7385-7387.
10. Peng, G.; Mereacre, V.; Kostakis, G. E.; Wolny, J. A.; Schünemann, V.; Powell, A. K. *Chem. Eur. J.* **2014**, *20*, 12381-12384.
11. Peng, G.; Kostakis, G. E.; Lan, Y.; Powell, A. K. *Dalton Trans.* **2013**, *42*, 46-49.
12. Bag, P.; Goura, J.; Mereacre, V.; Novitchi, G.; Powell, A. K.; Chandrasekhar, V. *Dalton Trans.* **2014**, *43*, 16366-16376.
13. Abbas, G.; Lan, Y.; Mereacre, V.; Buth, G.; Sougrati, M. T.; Grandjean, F.; Long, G. J.; Anson, C. E.; Powell, A. K. *Inorg. Chem.* **2013**, *52*, 11767-11777.
14. Polyzou, C. D.; Baniodeh, A.; Magnani, N.; Mereacre, V.; Zill, N.; Anson, C. E.; Perlepes, S. P.; Powell, A. K. *R. Soc. Chem. Adv.* **2015**, *5*, 10763-10767.
15. Goura, J.; Mereacre, V.; Novitchi, G.; Powell, A. K.; Chandrasekhar, V. *Eur. J. Inorg. Chem.* **2015**, *2015*, 156-165.
16. Liu, J.-L.; Wu, J.-Y.; Chen, Y.-C.; Mereacre, V.; Powell, A. K.; Ungur, L.; Chibotaru, L. F.; Chen, X.-M.; Tong, M.-L. *Angew. Chem. Int. Ed.* **2014**, n/a-n/a.
17. Liu, J.-L.; Chen, Y.-C.; Zheng, Y.-Z.; Lin, W.-Q.; Ungur, L.; Wernsdorfer, W.; Chibotaru, L. F.; Tong, M.-L. *Chem. Sci.* **2013**, *4*, 3310-3316.
18. Corporation, R. *Crystalclear 2.0*, Tokyo, Japan.
19. *Saint Plus v. 7.60A*, Bruker Analytical X-ray: Madison, WI, 2008.
20. Sheldrick, G. M. *SADABS, v. 2008/1*, Program for Empirical Absorbtion Correction of Area Detector Data: Gottingen, Germany, 2008.
21. Sheldrick, G. M. *Acta. Cryst.* **2008**, *A64*, 112-122.
22. Azar, M. R.; Boron, T. T.; Lutter, J. C.; Daly, C. I.; Zegalia, K. A.; Nimthong, R.; Ferrence, G. M.; Zeller, M.; Kampf, J. W.; Pecoraro, V. L.; Zaleski, C. M. *Inorg. Chem.* **2014**, *53*, 1729-1742.
23. Aldamen, M. A.; Clemente-Juan, J. M.; Coronado, E.; Martí-Gastaldo, C.; Gaita-Ariño, A. *J. Am. Chem. Soc.* **2008**, *130*, 8874-8875.
24. Boron, T. T. Control of Single-Molecule Magnetic Properties Using Metallacrowns. University of Michigan, Ann Arbor, 2012.
25. Rinehart, J. D.; Long, J. R. *Chem. Sci.* **2011**, *2*, 2078-2085.
26. Zaleski, C. M.; Tricard, S.; Depperman, E. C.; Wernsdorfer, W.; Mallah, T.; Kirk, M. L.; Pecoraro, V. L. *Inorg. Chem.* **2011**, *50*, 11348-11352.
27. Palacios, M. A.; Titos-Padilla, S.; Ruiz, J.; Herrera, J. M.; Pope, S. J. A.; Brechin, E. K.; Colacio, E. *Inorg. Chem.* **2014**, *53*, 1465-1474.
28. Wang, H.; Wang, K.; Tao, J.; Jiang, J. *Chem. Commun.* **2012**, *48*, 2973-2975.

# Chapter IV

# The Magnetocaloric Effect in Iron Based Metallacrowns

## 4.1 Introduction

Molecular nanomagnets are attractive candidates for use as low-temperature MCE refrigerants based on the magnetocaloric effect (MCE), due to relatively weak metal-metal magnetic coupling. As discussed in Chapter I, the ideal system would be molecules which have a large ground spin state, low magnetic anisotropy and weak (preferably ferromagnetic) magnetic exchange. Therefore, the three most suitable metal ions for MCE materials are the $Mn^{II}$, $Fe^{III}$ and $Gd^{III}$ ions.[1] The $Mn^{II}$ ion has an isotropic $S$ = 5/2 configuration and has been used to develop materials with large MCE;[2] however, its tendency to oxidize to $Mn^{III}$, a highly anisotropic ion, often causes problems with synthesis and stability. Due to an $S$ = 7/2 spin state and intrinsically weak magnetic coupling, $Gd^{III}$ has been the most common metal ion used to synthesize high-performance MCE materials.[1] However, prohibitive costs may preclude mass production and difficulties in the design of lanthanide coordination complexes[3] make $Gd^{III}$ a less attractive option for industrial MCE applications. The $Fe^{III}$ ion has an advantage in cost compared to $Gd^{III}$, and furthermore, its lower atomic mass allows for a larger theoretical limit to the value of $-\Delta S_m$ (893.3 J $kg^{-1}$ $K^{-1}$ vs 421.3 J $kg^{-1}$ $K^{-1}$ for $Gd^{III}$). With these factors in consideration, the focus of this chapter is the synthesis and magnetic characterization of three new $Fe^{III}$-based MCE materials.

Several $Fe^{III}$-based molecules have been reported in the literature to exhibit MCE behavior. The cluster $[Fe^{III}_8O_2(OH)_{12}(tacn)_6]Br_6$ (tacn = trizacyclononane) which has been

extensively studied,[4-7] was shown to possess an $S$ = 10 ground state and displays a direction-dependent MCE, where $-\Delta S_m$ varies with the orientation of sample with an applied magnetic field.[8] Later efforts to improve the performance of $Fe^{III}$-based MCE materials have led to high nuclearity clusters such as the $Fe_{14}$ complexes described previously in Chapter I. More recently, an $Fe_{17}$ cluster with an $S$ = 35/2 ground state was reported to exhibit a modest $-\Delta S_m$ = 8.9 J $kg^{-1}$ $K^{-1}$ at 2.7 K and 7 T. It is worth noting that the spin multiplicity in an $M_n$ cluster (M = metal ion, n = number of ions) is equal to $(2S + 1)^n$, which potentially allows for higher total spin; however, the larger the cluster is, the more difficult it is to understand in detail its magnetic properties. For example, a molecule having eight $Fe^{III}$ ions possesses $(2\cdot5/2+1)^8$ = 1679616 spin states, which is too large for conventional matrix diagonalization methods.[4] Such large clusters require time-consuming computational studies to elucidate the exchange pathways.[9] The impetus for the work described in this chapter was the synthesis and characterization of three simple $Fe^{III}$-based MCs. The structure-property relationships as related to the MCE will be discussed.

The first iron-based MC was an $Fe^{III}(acetate)_3[9\text{-}MC_{Fe^{III}N(shi)}\text{-}3](MeOH)_3 \cdot 3MeOH$ complex, herein referenced as **$Fe_4$OAc**, reported by Lah and coworkers in 1989.[10] The coupling of this system could be described by a 2-$J$ model; this simplicity made the complex a viable candidate to study how its magnetic interactions related to the MCE. To expand on this model, modulation of the magnetic coupling was achieved through substitution of the carboxylate bridging ligand. The acetate bridge in **$Fe_4$OAc** was replaced with benzoate to form an $Fe^{III}(benzoate)_3[9\text{-}MC_{Fe^{III}N(shi)}\text{-}3](MeOH)_3\cdot 2MeOH\cdot 3H_2O$ compound referenced herein as **$Fe_4$OBz**. To further examine intramolecular coupling, two $Fe^{III}[9\text{-}MC_{Fe^{III}N(shi)}\text{-}3]$ subunits were connected by three isopthalate bridging ligands to form an $Fe^{III}{}_2(isopthalate)_3[9\text{-}MC_{Fe^{III}N(shi)}\text{-}3]_2$

dimer complex (**$Fe_8$**). The intra- and intermolecular interactions of these MCs were investigated through structural and magnetic analysis.

## 4.2 Experimental

All reagents were purchased from commercial sources and were used without further purification. Elemental analysis was performed by Atlantic Microlabs Inc. All reactions were carried under aerobic conditions.

### *Synthetic Methods*

$Fe^{III}$(acetate)$_3$[9-$MC_{Fe^{III}N(shi)}$-3](MeOH)$_3$·xMeOH (**$Fe_4$OAc**): Synthesis follows a modified literature procedure.[10] $H_3$shi (153.1 mg, 1.0 mmol) was dissolved in 10 mL methanol. To this, a solution of Fe(acetate)$_2$ (260.9 mg, 1.5 mg) in 10 mL methanol was added drop wise and the mixture was stirred for 1 hr. The solution was filtered and allowed to slowly evaporate for ~3 weeks, which yielded dark cube shaped crystals. The sample was filtered, washed with 20 mL methanol and air dried. Yield: 134.1 mg (36.4%), Anal. Calcd for $Fe_4C_{31}H_{51}N_3O_{26}$: C, 33.69; H, 4.65; N, 3.80. Found: C, 33.47; H, 4.60; N, 3.78. Single-crystal unit cell: monoclinic, space group C2/c, a = 21.55 Å, b = 21.55 Å, c = 21.55 Å, α = 90˚ β =, 90˚, γ = 90˚, V = 10014.4 $Å^3$ (matches literature values).

$Fe^{III}$(benzoate)$_3$[9-$MC_{Fe^{III}N(shi)}$-3](MeOH)$_3$·2MeOH·3$H_2O$ (**$Fe_4$OBz**): $H_3$shi (153.1 mg, 1.0 mmol), $FeCl_3 \cdot 6H_2O$ (360.4 mg, 1.33 mmol) was dissolved in 20 mL methanol. Sodium benzoate (432.3 mg, 3.0 mmol) was added to the solution and the mixture was stirred for 1.5 hrs. The solution was filtered and allowed to slowly evaporate for ~3 weeks, which yielded dark crystals. The sample was filtered, washed with 20 mL methanol and air dried. Yield: 191.8 mg (45.9%),Anal. Calcd for $Fe_4C_{46}H_{51}N_3O_{23}$: C, 44.65; H, 4.15; N, 3.40. Found: C, 44.86; H, 4.12;

N, 3.40. Single-crystal unit cell: monoclinic, space group C2/c, a = 18.4496 Å, b = 18.4496 Å, c = 31.7599 Å, α = 90˚ β =, 90˚, γ = 120˚, V = 9362.32 $Å^3$.

General Procedure for $Fe^{III}_2$(isopthalate)$_3$[9-$MC_{Fe^{III}N(shi)}$-3]$_2$(EtOH)$_6$·x$H_2O$ (**$Fe_8$**): $H_3$shi (229.7 mg, 1.5 mmol), $FeCl_3 \cdot 6H_2O$ (540.6 mg, 2.0 mmol) and isopthalic acid (124.6 mg, 0.75 mmol) was dissolved in 120 mL ethanol and 8 mL $H_2O$. Ammonium bicarbonate (474.5 mg, 6 mmol) was added to the solution and the mixture was stirred for 1.5 hrs. Dark precipitate formed and was filtered off. The solution was allowed to slowly evaporate over 3 to 4 weeks to yield small dark crystals. The sample was filtered and washed with a 60 mL of a 1:1 solution of ethanol and $H_2O$ and allowed to air dry. Single-crystal unit cell: a = 33.2164(9) Å, b = 33.2164(9) Å, c = 61.4234(16) Å, α = 90˚ β =, 90˚, γ = 120˚, V = 58691(3) $Å^3$.

**$Fe_8$-A**: Yield: mg (214.4 mg, 35.5% %), Anal. Calcd for $Fe_8C_{66}H_{96}N_6O_{60}$: C, 33.30; H, 4.07; N, 3.57. Found: C, 33.59; H, 4.06; N, 3.54.

**$Fe_8$-B**: Yield: mg (147.5, 27.7%), Anal. Calcd for $Fe_8C_{70}H_{70}N_6O_{42}$: C, 39.77; H, 3.34; N, 3.98. Found: C, 39.47; H, 3.25; N, 3.91.

**$Fe_8$-C**: Yield: mg (149.2, 28.6%), Anal. Calcd for $Fe_8C_{68}H_{62}N_6O_{41}$: C, 39.53; H, 3.02; N, 4.07. Found: C, 39.53; H, 2.81; N, 4.10.

**$Fe_8$-A-Dry**: Anal. Calcd for $Fe_8C_{66}H_{50}N_6O_{37}$: C, 40.32; H, 2.56; N, 4.27. Found: C, 40.81; H, 2.59; N, 4.30.

***Physical Methods***

*X-ray Crystallography*. Single-crystal X-ray diffraction data for **$Fe_4$OBz** were collected by Jeff W. Kampf at the University of Michigan. The structural refinement was performed by myself. The crystal data for the **$Fe_8$** compound were collected and refined by Régis Guillot at the Université de Paris Sud 11 in Orsay, France.

Crystal data for the compound **$Fe_4$Obz** were collected at 85(2) K on an AFC10K Saturn 944+ CCD-based X-ray diffractometer equipped with a Micromax007HF Cu-target microfocus rotating anode (λ = 1.54187 Å), operated at 1200 W power (40 kV, 30 mA). The data were processed with CrystalClear 2.0[11] and corrected for absorption.

Crystal data for the compound **$Fe_8$** were collected on a Kappa X8 APPEX II Bruker diffractometer with graphite-monochromated Mo-Kα radiation ( = 0.71073 Å). Crystals were mounted on a CryoLoop (Hampton Research) with Paratone-N (Hampton Research) as cryoprotectant and then flashfrozen in a nitrogen-gas stream at 100 K. The temperature of the crystal was maintained at the selected value (100K) by means of a 700 series Cryostream cooling device to within an accuracy of ±1 K. The data were corrected for Lorentz polarization, and absorption effects.

All structures were solved and refined with the SHELXTL (version 6.12) software package[12] All non-hydrogen atoms were refined anisotropically. Hydrogen atoms were placed in their idealized positions. Experimental parameters and crystallographic data are provided in Table 4.1.

*Powder X-ray Diffraction (PXRD).* Powder X-ray diffraction data for air-dried samples of **$Fe_4$OAc**, **$Fe_4$OBz** and **$Fe_8$** were collected at room temperature using a Bruker D8 Advance Diffractometer with Cu-Kα raciation (1.5406 Å, 40 kV, 40 mA). Powder diffraction patterns were collected at room temperature from 3° to 50° (2θ) using a step size of 0.05° and a scan time of 0.5 second/step.

In order to obtain PXRD data of fresh (solvated) samples of **$Fe_8$**, of crystals were collected from the mother liquor and quickly submerged in mineral oil to minimize solvent loss. The samples were then mounted on a CryoLoop™ and PXRD data were collected using a

**Table 4.1.** Crystallographic Details for **$Fe_4$OBz** and **$Fe_8$**.

| | **$Fe_4$OBz** | **$Fe_8$** |
|---|---|---|
| mol formula | $Fe_4C_{50}H_{3-}N_3O_{10}$ | $Fe_8C_{66}H_{48}N_6O_{56}$ |
| fw (g/mol) | 1056.17 | 2267.90 |
| cryst syst/ space group | R-3 | R-3 |
| *T* (K) | 473(2) | 296(2) |
| wavelength (Å) | 1.54178 | 0.71073 |
| *a* (Å) | R-3 | 33.2164(9) |
| *b* (Å) | 18.4496(2) | 33.2164(9) |
| *c* (Å) | 18.4496(2) | 61.4234(16) |
| α (deg) | 31.760(2) | 90 |
| β (deg) | 90 | 90 |
| γ (deg) | 90 | 120 |
| *V* (Å$^3$) | 120 | 58691(3) |
| *Z* | 3 | 24 |
| density, ρ (g/cm$^3$) | 1.686 | 1.540 |
| abs coeff, μ (mm$^{-1}$) | 11.543 | 1.202 |
| *F*(000) | 4815 | 27408 |
| θ range for data collection (deg) | 3.10 to 68.22 | 1.50 to 26.49 |
| limiting indices | $-22 \le h \le 2$<br>$-22 \le k \le 22$<br>$-38 \le l \le 38$ | $-41 \le h \le 31$<br>$-41 \le k \le 41$<br>$-76 \le l \le 76$ |
| reflns collected/ unique | 76364/3818 | 199732/13499 |
| completeness to θ (%) | 100 | 99.8 |
| no. of data/ restraints/ params | 3818/44/266 | 13499/26/578 |
| goodness of fit on $F^2$ | 1.120 | 1.558 |
| final *R* indices [$I > 2\sigma(I)$] | R1[a] = 0.0754<br>WR2[b] = 0.2176 | R1[a] = 0.1214<br>WR2[b] = 0.3482 |
| *R* indices (all data) | R1[a] = 0.0784<br>WR2[b] = 0.2232 | R1[a] = 0.1928<br>WR2[b] = 0.3906 |
| largest diff peak and hole (e$^-$ Å$^{-3}$) | 1.362 and -0.574 | 3.128 and -0.681 |

[a]$R1 = \Sigma(||F_o| - |F_c||)/\Sigma|F_o|$. [b]$wR2 = [\Sigma[w(F_o^2 - F_c^2)^2]/\Sigma[w(F^\circ)^2]]^{1/2}$; $w = 1/[\sigma^2(F_o^2) + (mp)^2 + np]$; $p = [\max(F_o^2,0) + 2F_c^2]/3$ (*m* and *n* are constants); $\sigma = [\Sigma[w(F_o^2 - F_c^2)^2]/(n - p)]^{1/2}$.

Rigaku R-Axis Spider diffractometer with an image plate detector and a graphite monochromated Cu-Kα radiation (1.5406 Å, 50 kV, 40 mA) source. Images were collected for 7 min while rotating the sample about the φ-axis and oscillated in ω to reduce preferred orientation. Images were integrated from 3° to 50° with a 0.02° step size.

*Thermogravimetric Analysis.* Thermogravimetric analyses were performed on a TA Instruments Q50 TGA. The temperature was ramped from 25 °C to 600 °C at a rate of 20 °C/min under a flow of 40% $O_2$/ 60% $N_2$ gas.

*Magnetic Measurements.* Variable-temperature susceptibility and variable-field magnetization measurements on polycrystalline samples mulled in eicosane were performed on a Quantum Design MPMS SQUID magnetometer. Variable-temperature dc susceptibility measurements were performed at 2000 Oe from 300-2 K. Isothermal magnetization measurements were performed at 2-30 K from 0-7 T. Dc susceptibilities were corrected for the sample holder and eicosane and for diamagnetism of constituent atoms using Pascal's constants.

*Acknowledgements.* Dr. Marco Evangelisti assisted in fitting the magnetization data to the Maxwell equation (Equation 1.20) to obtain values of magnetic entropy change.

**4.3 Results and Discussion**

**Synthesis and Structural Characterization. (i) $Fe_4$OAc.** The synthesis and structural description of **$Fe_4$OAc** (Figure 4.1) have previously been reported in literature.[10] A modified synthetic procedure was employed, where Fe(acetate)$_2$ was reacted with $H_3$shi in methanol (in air) to yield dark block crystals which have the same unit cell dimensions as the reported structure. Furthermore, the experimental PXRD pattern of the sample matched well with the calculated pattern (Figure 4.2), suggesting that even after being air dried, the sample retained crystallinity. The crystal packing suggests that the individual molecules are well isolated (Figure 4.3). The closest intermolecular Fe-Fe distance is 7.595 Å with negligible π-π interactions.

**(ii) $Fe_4$OBz**. The reaction of $FeCl_3 \cdot 6H_2O$, $H_3$shi and sodium benzoate in methanol yielded dark black crystals of **$Fe_4$OBz** (Figure 4.4). The sodium benzoate was employed as both a base and a source of carboxylate bridging anions. The PXRD pattern showed that the sample

retained crystallinity upon exposure to air (Figure 4.5), and as such, the crystal structure can be reliably used to explain its magnetic properties. The resulting structure is analogous to **$Fe_4$OAc**, with the more bulky benzoate groups replacing the acetate bridges. As shown in Figure 4.6, the overlaid structures of **$Fe_4$OBz** and **$Fe_4$OAc** reveal similar overall molecular geometry. The

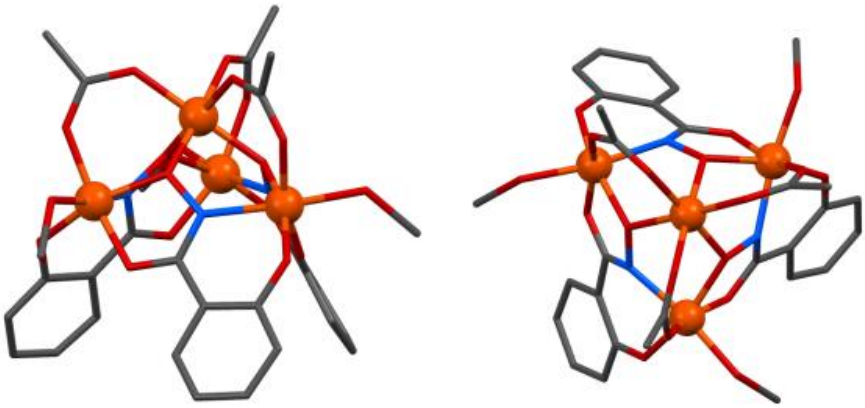

**Figure 4.1.** Crystal structure of **$Fe_4$OAc**. Side (left) and top-down (right) views. Color scheme: orange spheres – $Fe^{III}$, red tubes – O, blue tubes – N, gray tubes – C. Hydrogens and lattice solvents were omitted.

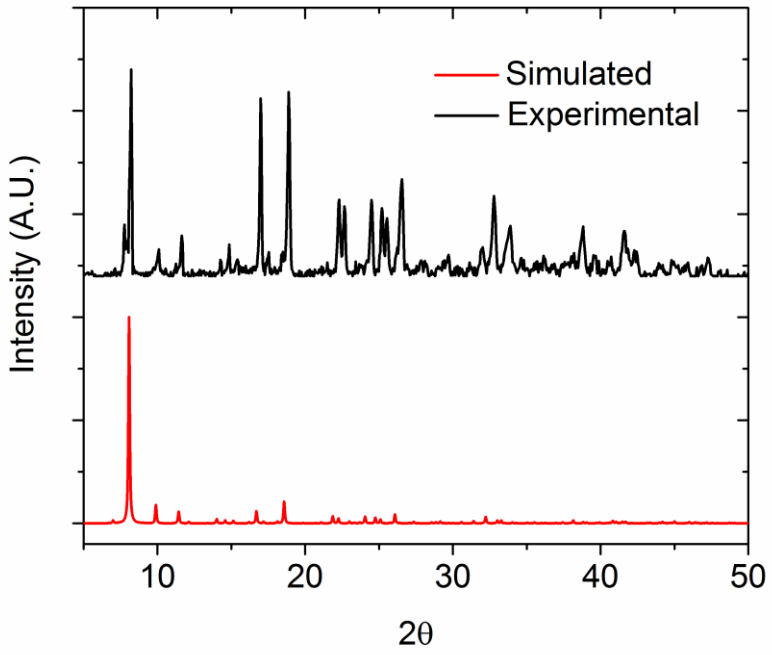


**Figure 4.2.** Experimental PXRD pattern of **$Fe_4$OAc** (black) and simulated pattern (red).

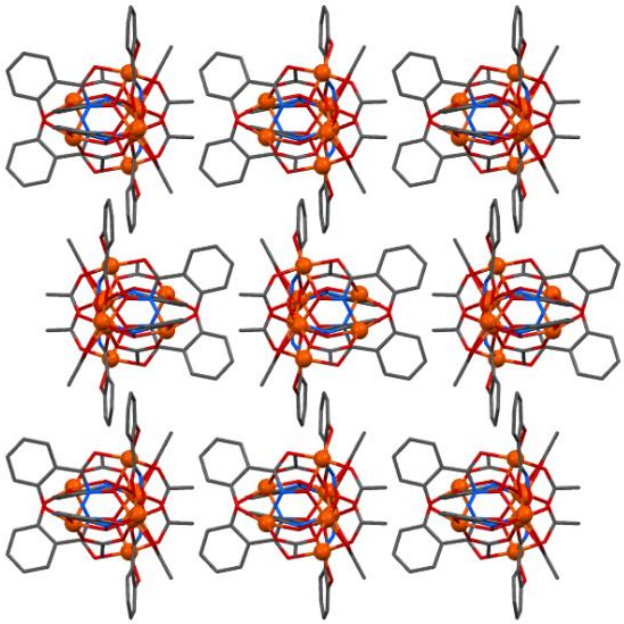

**Figure 4.3.** Packing diagram of **$Fe_4$OAc**. For clarity hydrogens, coordinating and lattice solvents have been omitted.

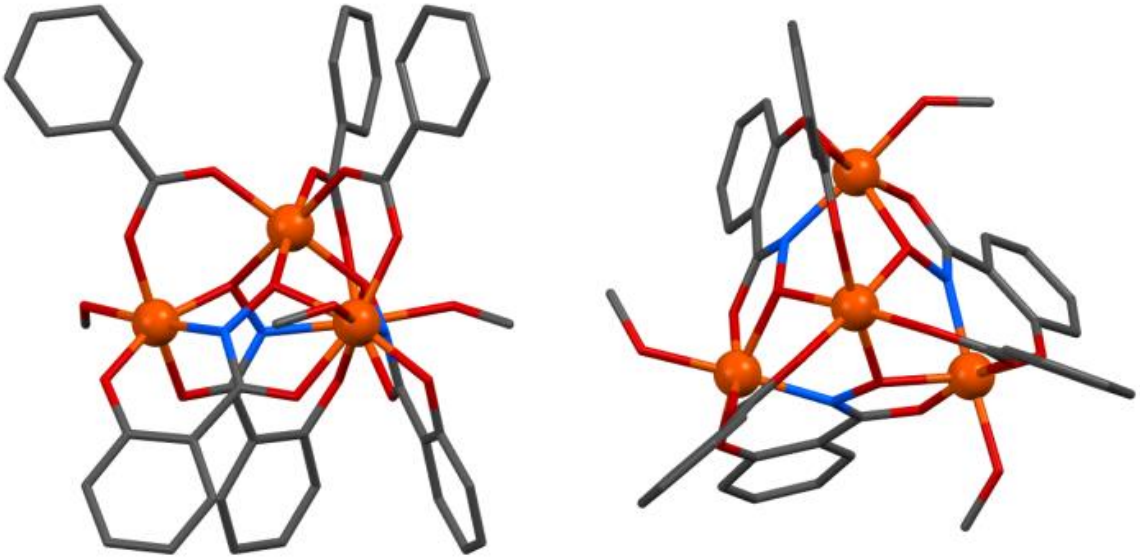

**Figure 4.4.** Crystal structure of **$Fe_4$OBz**. Side (left) and top-down (right) views. Color scheme: orange spheres – $Fe^{III}$, red tubes – O, blue tubes – N, gray tubes – C. Hydrogens and lattice solvents have been omitted.

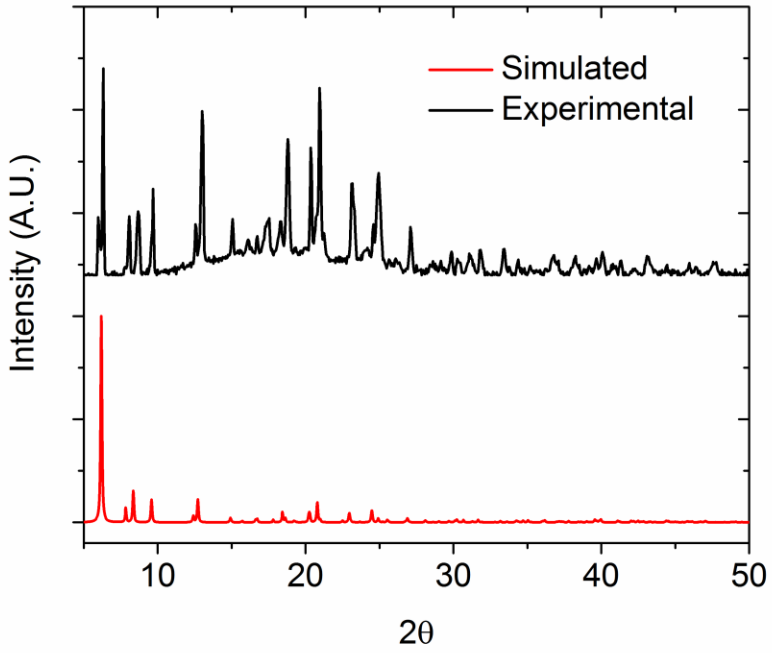


**Figure 4.5.** PXRD pattern of **$Fe_4$OBz** (black) and simulated pattern (red).

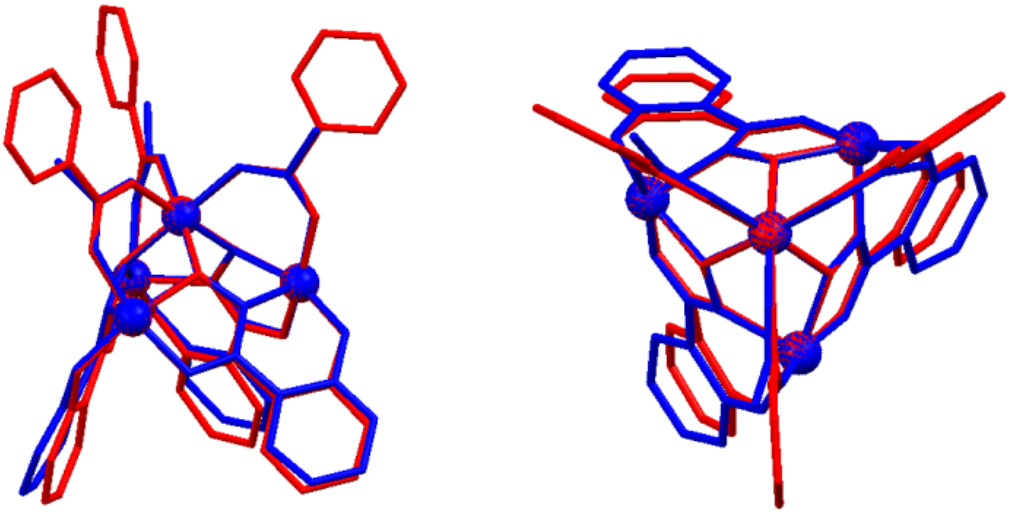

**Figure 4.6.** Overlaid crystal structures of **$Fe_4$OAc** (blue) and **$Fe_4$OBz** (red). Molecules were tethered at the $Fe^{III}$ sites.

structure of **$Fe_4$OBz** displays a more puckered arrangement of the $shi^{3-}$ ligands. The more electron-withdrawing nature of the benzoate group leads to a larger central Fe to carboxylate

**Table 4.2.** Selected Bond Distances

| | $Fe_c$-$Fe_r$ Distance (Å) | $Fe_r$-$Fe_r$ Distance (Å) | Avg. $Fe_c$ Bond Length (Å) | Avg. $Fe_r$ Bond Length (Å) | Avg. $Fe_c$ – $O_{carb}$ Distance (Å) | Avg. $Fe_c$ – $O_{ox}$ Distance (Å) |
|---|---|---|---|---|---|---|
| **$Fe_4$OBz** | 3.416 | 4.834 | 2.019 | 2.016 | 2.015 | 2.023 |
| **$Fe_4$OAc** | 3.415 | 4.850 | 2.002 | 2.020 | 2.005 | 1.999 |
| **$Fe_8$ Dimer** | 3.386 | 4.839 | 1.983 | 1.976 | 1.971 | 1.993 |

$Fe_c$ = central Fe; $Fe_r$ = ring Fe; $O_{carb}$ = carboxylate oxygen; $O_{ox}$ = oxime oxygen

oxygen distance in **$Fe_4$OBz** compared **$Fe_4$OAc** with value of 2.015 Å and 2.005 Å, respectively (Table 4.2). The larger average central Fe-$O_{carb}$ bond length in $Fe_4$OBz is accompanied by a concomitant decrease in average $Fe_r$ bond length (Table 4.2).

The crystal packing of the **$Fe_4$OBz** molecules appear to be dictated by π-π interactions between adjacent benzoate groups on neighboring molecules. Most notably, two **$Fe_4$OBz** molecules facing tail-to-head are arranged such that the benzoate bridges are clasped together to form an intermolecular dimer, resulting in a short central $Fe^{III}$ – central $Fe^{III}$ intermolecular distance of 6.389 Å (Figure 4.7). Here, the interacting benzoates are situated 4.623 Å apart at a 60° angle; according to the Hunter-Sanders model,[13] this interaction can be classified as a repulsive face-to-face π-stacking. The **$Fe_4$OBz** intermolecular dimers subsequently assemble in a hexagonal packing arrangement (Figure 4.7) which leads to further intermolecular interactions. As shown in Figure 4.8, the phenyl moiety of a $shi^{3-}$ ligand is involved in edge-to-face π-interactions with two benzoate groups on an adjacent **$Fe_4$OBz** dimer. The distance of the $shi^{3-}$ hydrogens to the centroids of the benzoates range from 3.225 – 3.970 Å, which are close enough to be considered edge-to-face interactions.[13] The cumulative effect of many interactions has a large effect on the low-temperature magnetic properties (*infra vide*).

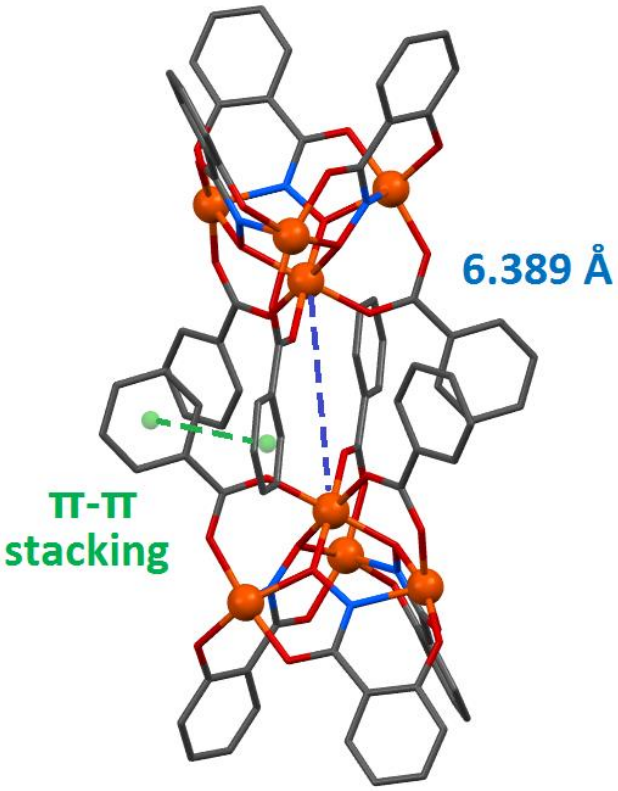


**Figure 4.7.** Crystal packing of **$Fe_4$OBz**. A pair of adjacent intermolecular dimers. Blue dashed line is the central $Fe^{III}$ – central $Fe^{III}$ distance. Green dashed line represents face-to-face π-π stacking.

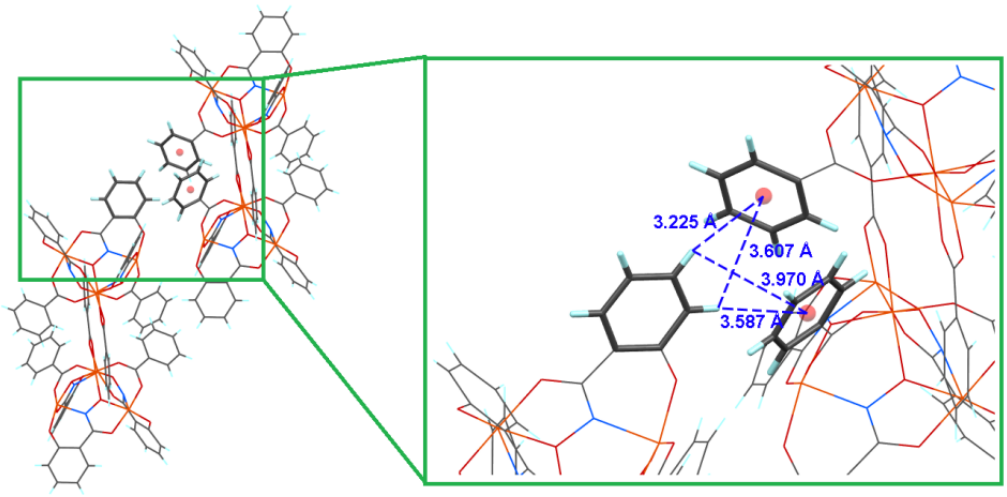


**Figure 4.8.** π-π interactions between adjacent intermolecular dimers of **$Fe_4$OBz**. For clarity the phenyl groups engaging in π-interactions are in bold.

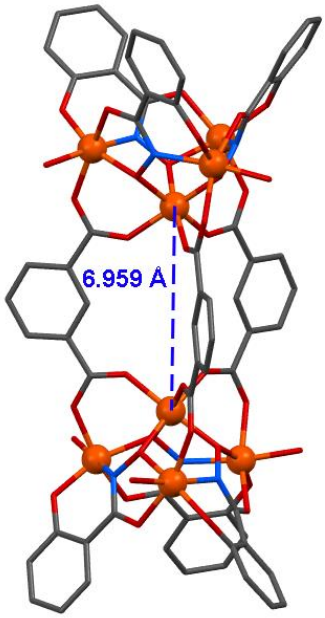


**Figure 4.9.** Crystal structure of the **$Fe_8$** dimer. Color scheme: orange spheres – $Fe^{III}$, red tubes – O, blue tubes – N, gray tubes – C. Hydrogens and lattic solvents were omitted.

**(iii) $Fe_8$.** The **$Fe_8$** compound is synthesized through the reaction of $H_3$shi, $FeCl_3 \cdot 6H_2O$ and isopthalic acid in an ethanol/water solution, with ammonium bicarbonate as a base. It was found that $H_2O$ was a necessary additional solvent that facilitated crystallization and solubilized ammonium salt impurities. This molecule can be simply described as two 9-MC-3 units connected through bifunctional isophthalate bridging ligands forming an intramolecular dimer (Figure 4.9). The central $Fe^{III}$ of each 9-MC-3 unit is 6.959 Å apart, which is actually longer than central Fe – central Fe distance in the **$Fe_4$OBz** intermolecular dimer (6.389 Å). An overlay of **$Fe_8$** with **$Fe_4$OBz** shows similar geometry, although the monomer complex has a more puckered 9-MC-3 ring (Figure 4.10).

Each dimeric **$Fe_8$** is involved in extensive π-interactions with neighboring molecules which are oriented in parallel (Figure 4.11). In addition, the $Fe^{III}$ – $Fe^{III}$ distances between the

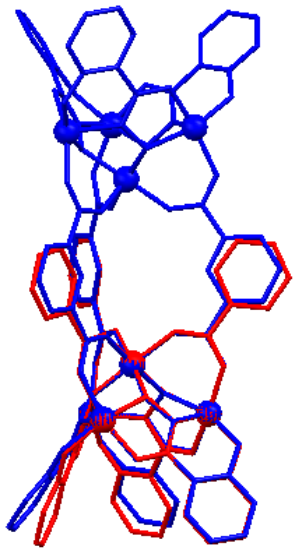

**Figure 4.10.** Overlaid crystal structures of **$Fe_8$** dimer (blue) and **$Fe_4$OBz** monomer (red). Molecules were tethered at the $Fe^{III}$ sites.

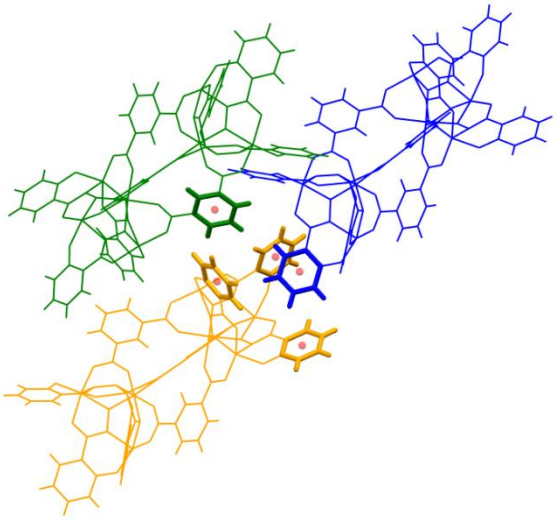

**Figure 4.11.** Possible intermolecular π-π interactions in **$Fe_8$**. For each molecule, there exists several potential edge-to-face and face-to-face interactions with neighboring molecules between the aromatic groups from the $shi^{3-}$ and isopthalate bridging ligands (bolded).

ring $Fe^{III}$ of adjacent molecules are a relatively short 4.800 Å. The dimer molecules pack in a honeycomb arrangement, with large ~15 Å solvent channels (Figure 4.12). Due to this large size, the lattice electron density was too diffuse and required the use of the SQUEEZE routine of

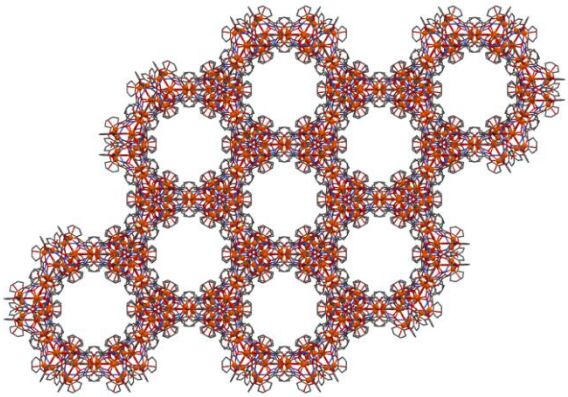

**Figure 4.12.** Packing diagram of **Fe$_8$** along the *c*-axis. Solvent channels are ca. 15 Å in diameter.

PLATON[14] to remove the diffraction contribution from these solvents. Also, there is significant solvent loss upon exposure to air, which can be observed by comparing the PXRD patterns of a fresh sample extracted from the mother liquor and immersed in mineral oil with an air dried sample (Figure 4.13). The PXRD pattern of the fresh sample retains crystallinity and matches the simulated powder pattern from the crystal structure. However, exposure to air will lead to loss of solvent and crystallinity, with the dried product having a large diffraction peak at an angle (2θ) of ~ 8°. All air dried samples of **Fe$_8$** show this peak at approximately the same angle, regardless of lattice solvent composition.

The solvent content in the dimeric $Fe_8$ complex was found to be quite sensitive to crystallization conditions such as temperature, humidity and crystallization time. Three separate batches of **Fe$_8$** was synthesized and yielded different levels of solvation and will be referred to

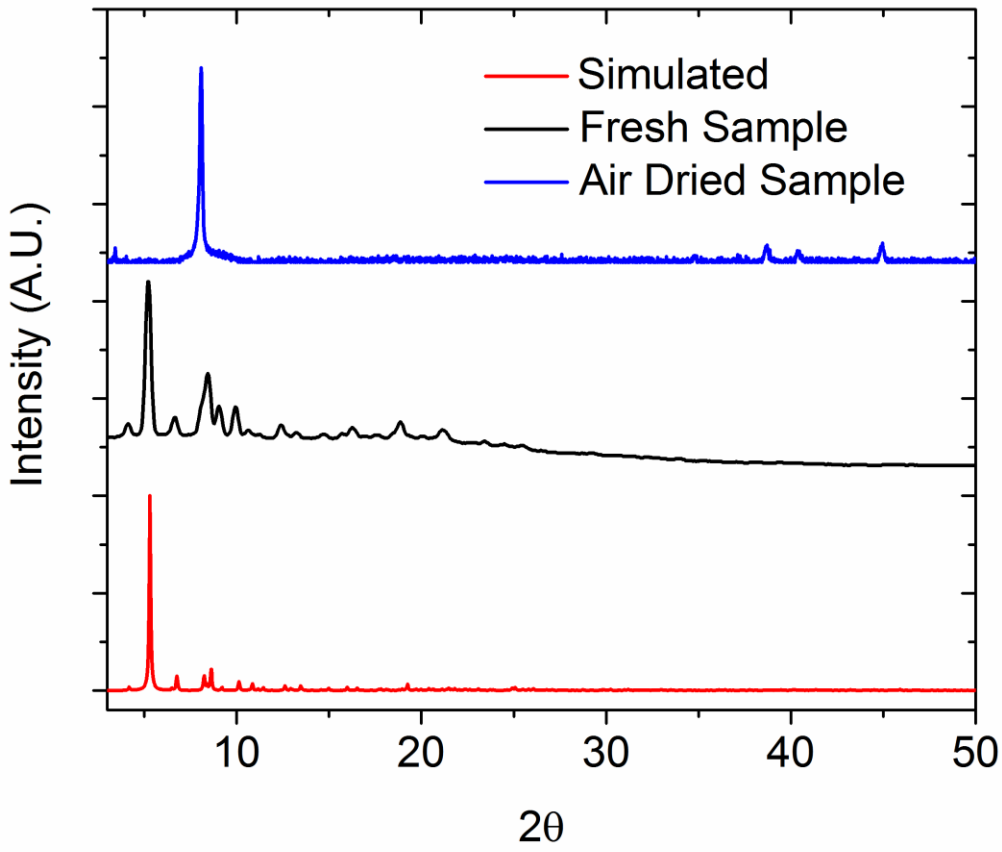


**Figure 4.13.** PXRD patterns of **$Fe_8$** dimer. Simulated pattern (red), pattern of a fresh sample immersed in mineral oil (black) and an air dried sample (blue).

as **$Fe_8$-A**, **$Fe_8$-B** and **$Fe_8$-C** (ordered in decreasing levels of solvation). An aliquot of **$Fe_8$-A** was crushed and dried in vacuo at 50 °C for 3 days to remove solvent retained in the lattice and will be referred to as **$Fe_8$-A-Dry**. The molecular formula and molecular weight (MW) of these samples were determined through elemental analysis, TGA and PXRD data (described in detail in Appendix B). For consistency, the MW of **$Fe_4$OAc** and **$Fe_4$OBz** were also determined by the same method. A summary of the MW for all compounds is presented in Table 4.3 and will be the values used to treat the magnetic data.

**Table 4.3.** Summary of molecular weights obtained by analysis of CHN and TGA data.

| Compound | MW (g/mol) |
|---|---|
| **$Fe_4$OAc** | 1111.55 |
| **$Fe_4$OBz** | 1250.92 |
| **$Fe_8$-A** | 2413.88 |
| **$Fe_8$-B** | 2126.37 |
| **$Fe_8$-C** | 2089.32 |
| **$Fe_8$-A-dry** | 1964.75 |

**Magnetic Properties.** The variable-temperature dc magnetic susceptibility for all samples were measured at an applied field of 2000 Oe and in a temperature range of 300 to 2 K. The room temperature $\chi_m T$ product for both **$Fe_4$OAc** and **$Fe_4$OBz** is around 10 $cm^3$ K $mol^{-1}$, much smaller than the expected value of 17.5 $cm^3 K mol^{-1}$ for four non-interacting $Fe^{III}$ ($S$ = 5/2, g = 2), suggesting that significant antiferromagnetic exchange is present. For **$Fe_4$OAc**, the $\chi_m T$ product gradually decreases from 9.67 $cm^3$ K $mol^{-1}$ at 300 K down to 8.29 $cm^3$ K $mol^{-1}$ at 150 K (Figure 4.14), which is followed by an upswing to a maximum value of 14.35 $cm^3$ K $mol^{-1}$ at 5.5 K, and then a decrease to 13.96 $cm^3$ K $mol^{-1}$ at 2 K. For **$Fe_4$OBz,** $\chi_m T$ slowly decreases with decreasing temperature from 300 K to 130 K and rises to a maxima of 10.01 $cm^3$ K $mol^{-1}$ at 30 K, followed by a decrease to 1.19 $cm^3$ K $mol^{-1}$ at 2 K (Figure 4.14).

As shown in Figure 4.14, below ca. 50 K, the $\chi_m T$ profile of **$Fe_4$OAc** and **$Fe_4$OAc** deviate significantly. The much steeper decrease $\chi_m T$ values at temperatures below 30 K for **$Fe_4$OBz** in comparison to **$Fe_4$OAc** suggests that predominant antiferromagnetic intermolecular interactions are present in the former. Also, the $\chi_m T$ product at 2 K for **$Fe_4$OBz** (1.19 $cm^3$ K $mol^{-1}$) is much lower than it is for **$Fe_4$OAc** (13.96 $cm^3$ K $mol^{-1}$). As a qualitative estimation, the low temperature $\chi_m T$ data can be extrapolated down to 0 K, where only the lowest energy spin state(s) is populated. The extrapolated $\chi_m T$ value at 0 K for **$Fe_4$OBz** is -0.22 $cm^3$ K $mol^{-1}$, which essentially suggests a diamagnetic ground state. On the other hand, for **$Fe_4$OAc**, the extrapolated 0 K value

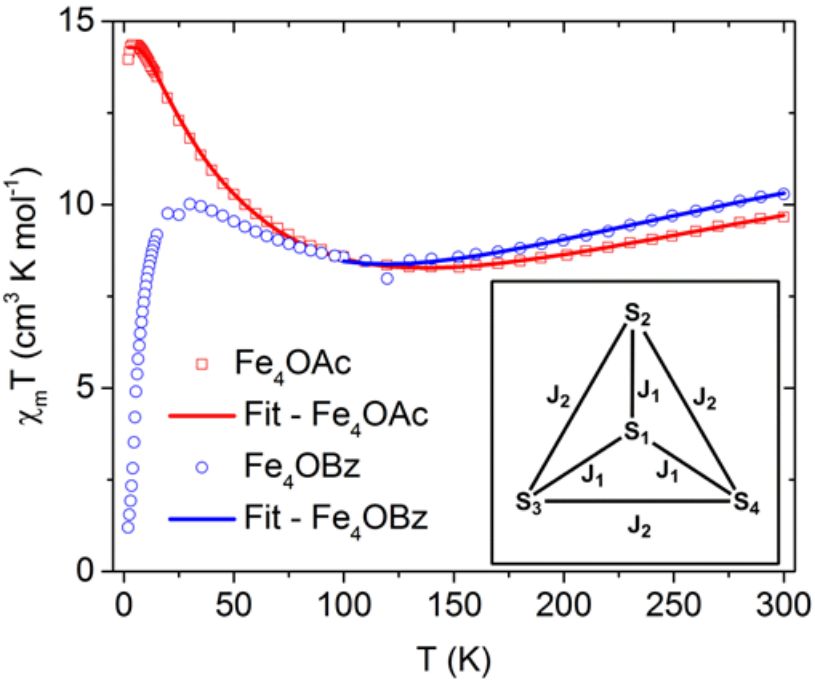


**Figure 4.14.** $\chi_m T$ vs. T for **$Fe_4$OAc** and **$Fe_4$OBz**. Experimental data are open symbols, the fits (see text) are solid lines. Inset: coupling scheme for the $Fe_4$ systems.

is 13.35 $cm^{-1}$ K $mol^{-1}$. Assuming g = 2.00, the theoretical $\chi_m T$ values for $S$ = 4 and $S$ = 5 are 10 and 15 $cm^3$ K $mol^{-1}$, respectively, indicating that **$Fe_4$OAc** has an $S$ = 5 ground state with a g value slightly smaller than 2.00 (calculated to be 1.89, using Equation 1.7)

In order to obtain exchange coupling parameters for the analogous $Fe_4$ clusters, the $\chi_m T$ data were fit to an appropriate theoretical expression. Since both **$Fe_4$OAc** and **$Fe_4$OBz** molecules have 3-fold rotational symmetry, a 2-$J$ coupling scheme (inset in Figure 4.14) was employed. The corresponding HDVV spin Hamiltonian:

$$H = -J_1(\hat{S}_1 \cdot \hat{S}_2 + \hat{S}_1 \cdot \hat{S}_3 + \hat{S}_1 \cdot \hat{S}_4) - J_2(\hat{S}_2 \cdot \hat{S}_3 + \hat{S}_3 \cdot \hat{S}_4 + \hat{S}_2 \cdot \hat{S}_4) \quad (4.1)$$

where $J_1$ is the ring Fe – central Fe exchange, $J_2$ is the ring Fe – ring Fe exchange and $\hat{S}_x$ are the spin operators of the $Fe^{III}$ ions. The eigenvalues of Equation 4.1 can be determined through the Kambe method[15] and are given by Equation 4.2.

$$E(S_{123}, S_T) = -\frac{J_1}{2}\left[S_T(S_T+1) - S_{234}(S_{234}+1) - \frac{35}{4}\right] - \frac{J_2}{2}\left[S_{234}(S_{234}+1) - \frac{105}{4}\right] \quad (4.2)$$

where $S_{234} = S_2 + S_3 + S_4$ and $S_T = S_1 + S_{234}$. A theoretical expression for $\chi_{mT}$ vs. T was derived from the van Vleck equation and eigenvalues from Equation 4.2, along with a molecular field model,[16] which takes into account intermolecular interactions, *zJ*.

A fit for the entire temperature range of the $\chi_m$T data for **$Fe_4$OAc**, gave values of $J_1$ = -27.27 $cm^{-1}$, $J_2$ = -5.95 $cm^{-1}$, $g$ = 1.99 and $zJ$ = -0.09 $cm^{-1}$ (Figure 4.14). The larger absolute value for $J_1$ as opposed to $J_2$ is not surprising, since ring Fe – central Fe exchange interactions may go through the oxime bridge (single atom) as well as the carboxylate and oximate bridge, whereas the ring Fe – ring Fe interactions are mediated only through a 2 atom oximate connection. The small intermolecular interaction, *zJ*, can be explained by the lack of apparent intermolecular contacts, as described in the structural section and visualized in Figure 4.3. As such, the negligible *zJ* term may be ignored and the energy diagram of the spin states as a function of $J_2/J_1$ can be obtained using the eigenvalues obtained from Equation 4.2 (Figure 4.15). The experimentally determined value of $J_2/J_1$ is 0.218, indicating that the ground state is $S$ = 5, with a doubly degenerate $S$ = 4 excited state that is 23.2 $cm^{-1}$ higher in energy (vertical green dashed line, Figure 4.15), and is in good agreement with $S$ states obtained from extrapolation described previously. In principle, good MCE materials have the largest possible spin state and low lying excited states.[17] Assuming antiferromagnetic coupling, MCE materials based on the $Fe_4$ 9-MC-3 metallacrown topology can theoretically be optimized by having a $J_2/J_1$ ratio of 0.333 (vertical black dashed-dotted line, Figure 4.15), at the spin-frustrated state where the $S$ = 5 state and doubly degenerate $S$ = 4 state are of equal energy (*vide infra*). It must be stated that the absolute value of the energy between the spin states is dependent on the strength of the coupling, thus ideally, $J_1$ and $J_2$ should be small.

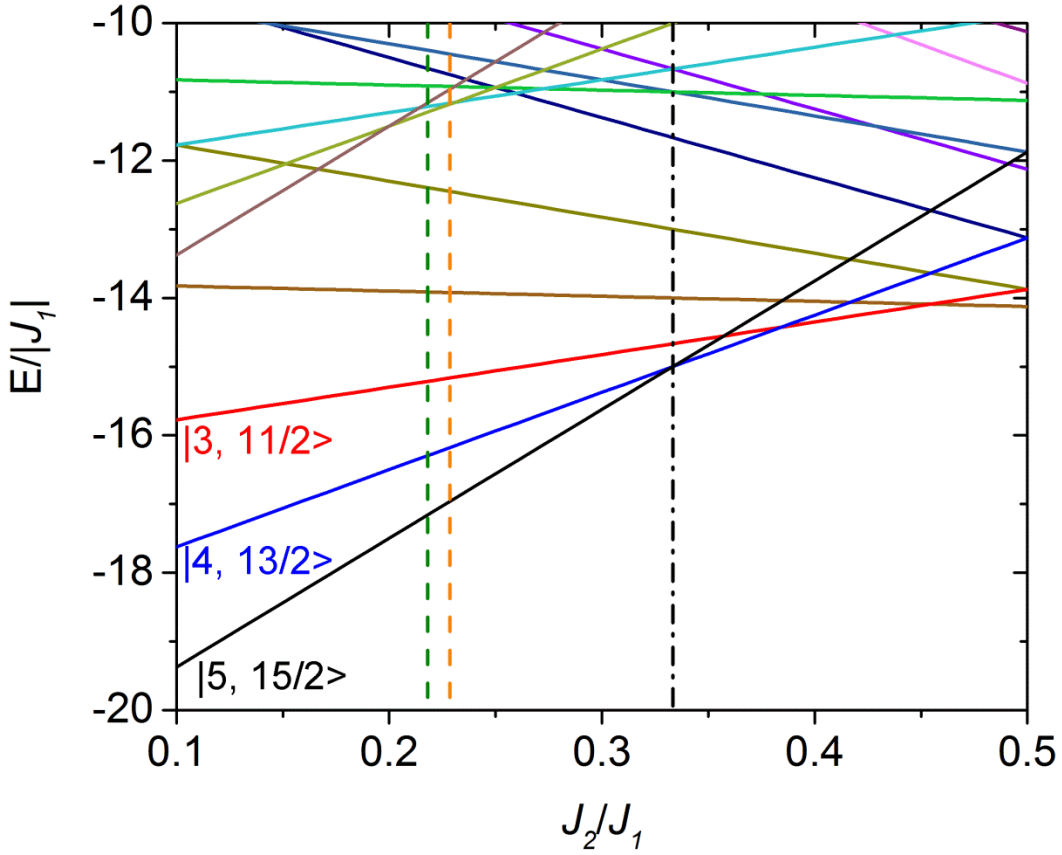


**Figure 4.15.** Energy Diagram for the spin states of the $Fe_4$ 9-MC-3 system plotted as $E/|J_1|$ vs. $J_2/J_1$. More negative $E/|J_1|$ values are lower in energy. The vertical green dashed line represents the $J_2/J_1$ ratio for **$Fe_4$OAc** and the vertical orange dashed line represent the $J_2/J_1$ ratio for **$Fe_4$OBz**. The ideal $J_2/J_1$ ratio of 0.333 is represented by the vertical black dashed-dotted line.

For **$Fe_4$OBz**, the intermolecular face-to-face and edge-to-face π-interactions appear to have led to significant antiferromagnetic exchange since the $\chi_m T$ product extrapolated to 0 K suggests a diamagnetic ground state. It has been previously reported that π-interactions can effectively mediate magnetic exchange. A 2007 study found that organic biphenylalenyl biradicaloid molecules have a large -0.29 eV (-2339 $cm^{-1}$) intermolecular exchange interactions facilitated by π-π stacking.[18] Although this extremely large magnetic exchange was due to the spin-delocalization of organic radicals, there have also been recent reports of π-interactions

affecting magnetic properties in superparamagnetic[19] and photomagnetic coordination complexes.[20]

As a result of significant cluster-cluster interactions, attempts to fit the full range of the susceptibility data for **$Fe_4$OBz** were unsuccessful. To circumvent this, only the high temperature data truncated at 100 K was included and with the intermolecular term, *zJ*, set to 0. The best fit parameters obtained were $J_1$ = -24.23 $cm^{-1}$, $J_2$ = -5.54 $cm^{-1}$ and $g$ = 1.97 (Figure 4.14). The comparable $J_2$ values for **$Fe_4$OBz** and **$Fe_4$OAc** can be attributed to the structural similarities seen in Figure 4.5. However, the difference in $J_1$ values between the analogues may be ascribed to the change in electron withdrawing effects of the benzoate and acetate bridges. The phenyl group in benzoate is a more electron withdrawing substituent than the methyl substituent in acetate. It is reasonable that the weaker electron density in the carboxylate bridge for **$Fe_4$OBz** is manifested in its smaller $J_1$ exchange interaction.

It should be noted that the coupling parameters obtained for **$Fe_4$OBz** may only be (approximately) representative of non-interacting $Fe_4$ clusters at high temperature, since the full temperature range could not be fit. At lower temperatures, the cumulative effect of numerous intermolecular exchange pathways via π-interactions makes it difficult to assess the true ground spin state. Nonetheless, it is worthwhile to examine the spin states obtained from the coupling parameters. From the fit of the susceptibility data, $J_2/J_1$ for **$Fe_4$OBz** is 0.228, quite similar to the value of 0.218 for **$Fe_4$OAc**. While the $J_2/J_1$ ratio has moved closer to the ideal value (0.333) in the energy diagram in Figure 4.15, the MCE of **$Fe_4$OBz** will be complicated by intermolecular interactions.

Magnetization data for **$Fe_4$OAc** and **$Fe_4$OBz** were collected at 2 K and in fields from 0 – 7 T and plotted as $M/N\mu_B$ vs H in Figure 4.16, where $N$ is Avagadro's number and $\mu_B$ is the Bohr

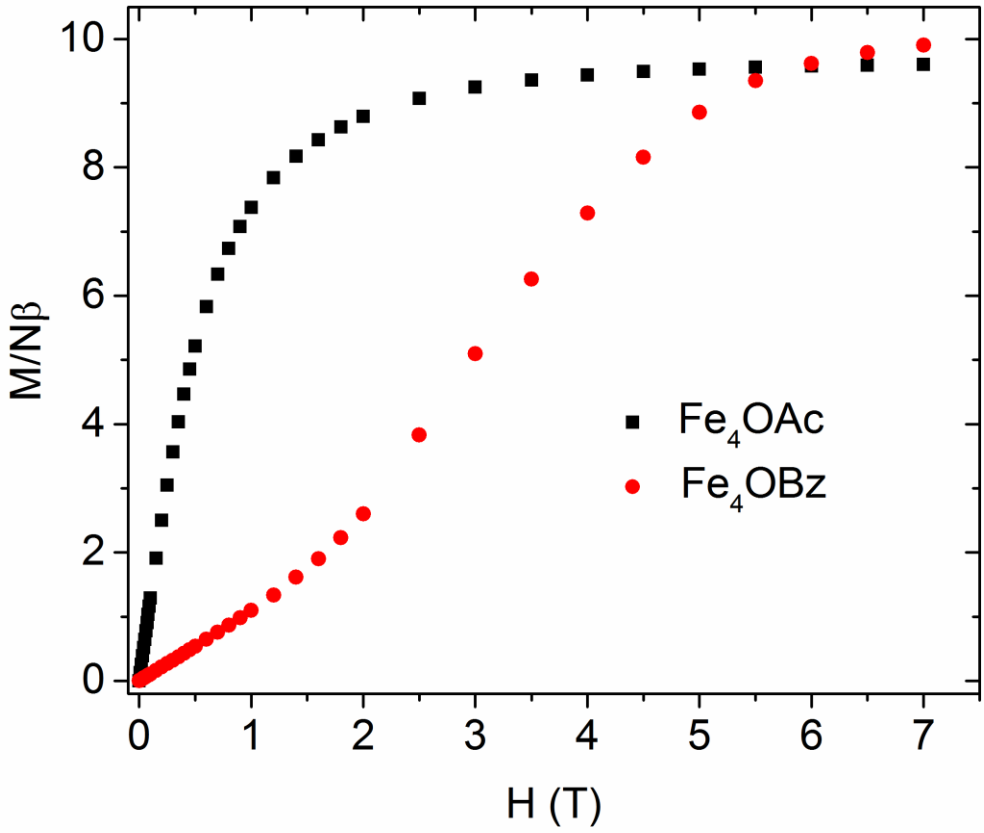


**Figure 4.16.** M/N$\mu_B$ (per $Fe_4$) vs. Field for **$Fe_4$OAc** and **$Fe_4$OBz**.

magneton. For **$Fe_4$OAc**, the magnetization sharply rises at low fields and nearly saturates to a value of 9.61, which is consistent with 10 electrons in an $S$ = 5 system. The magnetization data rises much more slowly for **$Fe_4$OBz**, with an inflection at ~3 T that likely represents the 'decoupling field' at which the long-range antiferromagnetic interactions are broken. The magnetization increases until it reaches a value of 9.90 at 7 T; which again, is consistent with an $S$ = 5 ground state.

The temperature-dependent susceptibility for **$Fe_8$-A**, **$Fe_8$-B**, **$Fe_8$-C**, and **$Fe_8$-A-Dry** presented in Figure 4.17 shows similar $\chi_m$T data at temperatures above 200 K. For the most solvated sample, **$Fe_8$-A**, the general profile of the susceptibility is similar to that of the $Fe_4$

monomer complexes and reaches a maximum value of 18.81 $cm^3$ K $mol^{-1}$ at 15 K. The second most solvated sample, **$Fe_8$-B**, has a maximum at 20 K, but at a much lower value of 14.63 $cm^3$ K $mol^{-1}$. **$Fe_8$-C** and **$Fe_8$-A-Dry** do not exhibit maxima and the $\chi_m T$ product decreases with decreasing temperature. One possible explanation for this data is that with decreasing solvation, antiferromagnetic intermolecular interactions become increasingly dominant at lower temperatures.

The magnetization data at 2 K for the dimer compounds steadily increase with increasing field, reaching values of 17.30 (8.65 per monomer subunit), 13.81 (6.91 per monomer subunit), 11.24 (5.62 per monomer subunit) and 8.35 (4.18 per monomer subunit) at 7 T for **$Fe_8$-A**, **$Fe_8$-B**, **$Fe_8$-C**, and **$Fe_8$-A-Dry**, respectively (Figure 4.18). The lower magnetization values per

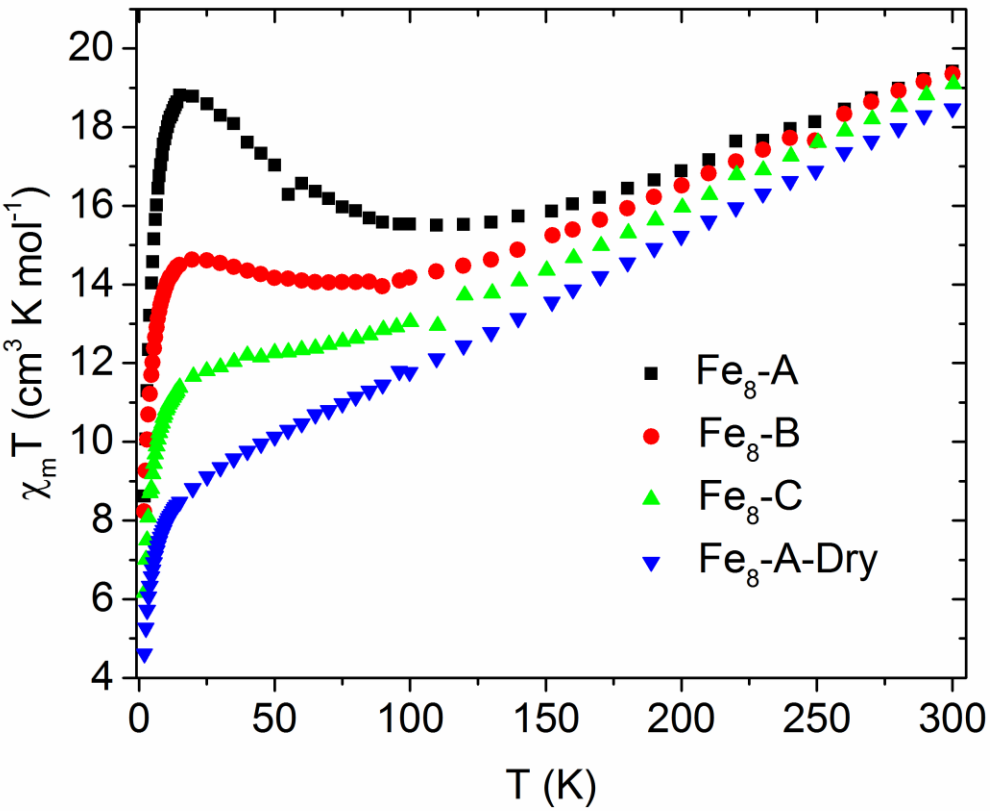


**Figure 4.17.** $\chi_m T$ vs. T for **$Fe_8$-A**, **$Fe_8$-B**, **$Fe_8$-C** and **$Fe_8$-A-Dry**.

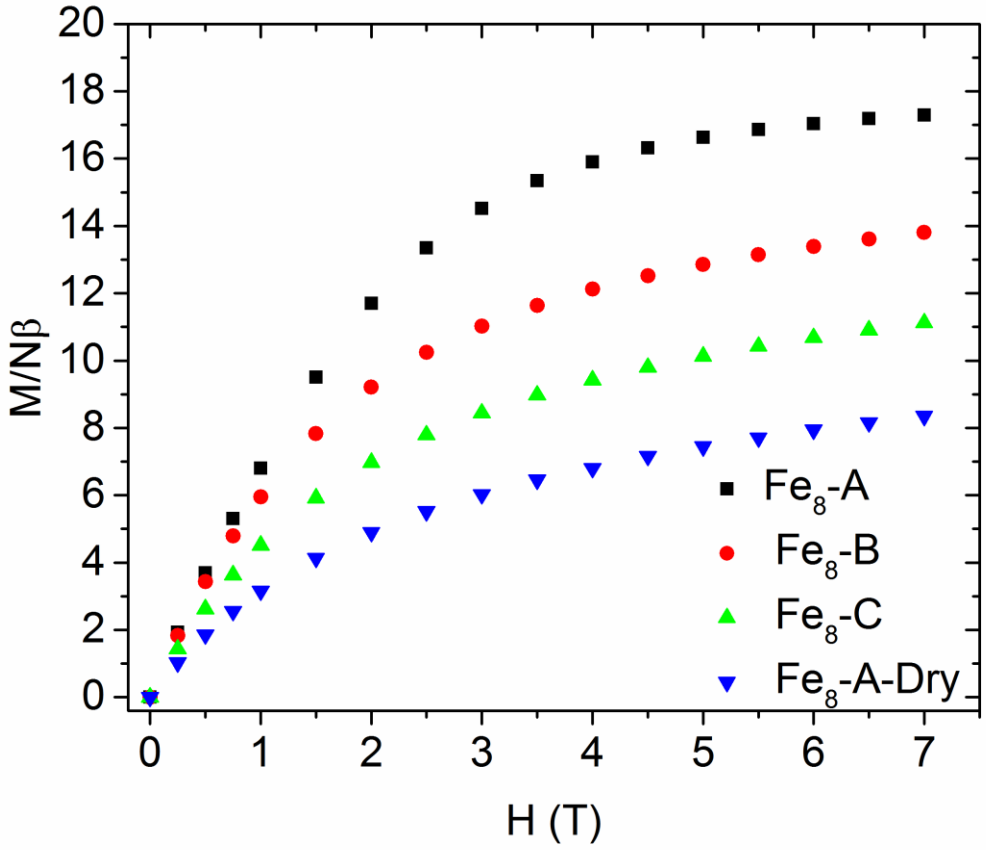


**Figure 4.18.** M/N$\mu_B$ (per $Fe_8$) vs. field for **$Fe_8$-A**, **$Fe_8$-B**, **$Fe_8$-C** and **$Fe_8$-A-Dry**.

monomer subunit is smaller than the values for **$Fe_4$OAc** and **$Fe_4$OBz**, which means either intra-cluster interactions through the isopthalate, intermolecular interactions or both are prevalent even at high fields and low temperatures.

**Magnetocaloric Effect.** In order to determine the magnetocaloric effect, magnetization experiments at fields between 0 and 7 T were performed at from 2 K to 20 K (2 K to 32 K for **$Fe_4$OBz**). The Maxwell relationship (Equation 1.20) was applied to the data to obtain estimates for the magnetic entropy change, $-\Delta S_m$. The magnetization curves and magnetic entropy change as a function of temperature for **$Fe_4$OAc** and **$Fe_4$OBz** are plotted in Figures 4.19 and 4.20.

For **$Fe_4$OAc**, at all magnetic fields, $-\Delta S_m$ increases with decreasing temperature and reaches a maximum of 14.7 J $kg^{-1}$ $K^{-1}$ at 3 K and $\Delta H$ = 7 T (Figure 4.19). This entropy change is higher than all reported iron compounds except for the previously described $Fe_{14}$ structures.[21-23] However, it should be noted that for those compounds, the maximum $-\Delta S_m$ occurs at a higher temperature of 6 K. At the lowest temperatures, (< 3 K), **$Fe_4$OAc** has the largest $-\Delta S_m$ for all reported Fe-based MCE materials. Additionally, there is a significant MCE at lower applied fields, with $-\Delta S_m$ = 11.2 J $kg^{-1}$ $K^{-1}$ at 3 K and $\Delta H$ = 3 T. Practically, this may be significant as having large $-\Delta S_m$ values at low working temperatures and $\Delta H$ values would be advantageous in cooling to the sub-Kelvin regime and allow for the use of standard electromagnets (which operate at low field strengths) in magnetic refrigerators.

The MCE of **$Fe_4$OBz** is significantly reduced in comparison to **$Fe_4$OAc**, with a maximum $-\Delta S_m$ = 7.4 J $kg^{-1}$ $K^{-1}$ at $T$ = 7 K and $H$ = 7 T (Figure 4.20). This behavior can be explained by the stronger antiferromagnetic interactions for **$Fe_4$OBz** described above. Interestingly, at lower temperatures and fields, **$Fe_4$OBz** exhibits an *inverse* MCE, where $-\Delta S_m$ assumes a negative value. This can be interpreted as a *decrease* in temperature upon magnetization of the sample. Although the inverse MCE has been observed in various solid state materials,[24-27] to our knowledge, this is the first time this phenomenon has been observed in molecular materials. Detailed theoretical discussions of the inverse MCE have been provided by Ranke.[28-29] Generally, an inverse MCE can be observed for materials at temperatures below antiferromagnetic or ferromagnetic phase transitions. The Néel temperature, $T_N$, is 7 K for **$Fe_4$OBz** and is maximum in the $\chi_m$ vs. T plot (Figure 4.21). The value for $T_N$, which is unusually large for a molecular coordination complex,[30] indicates the temperature at which long range antiferromagnetic ordering occurs.

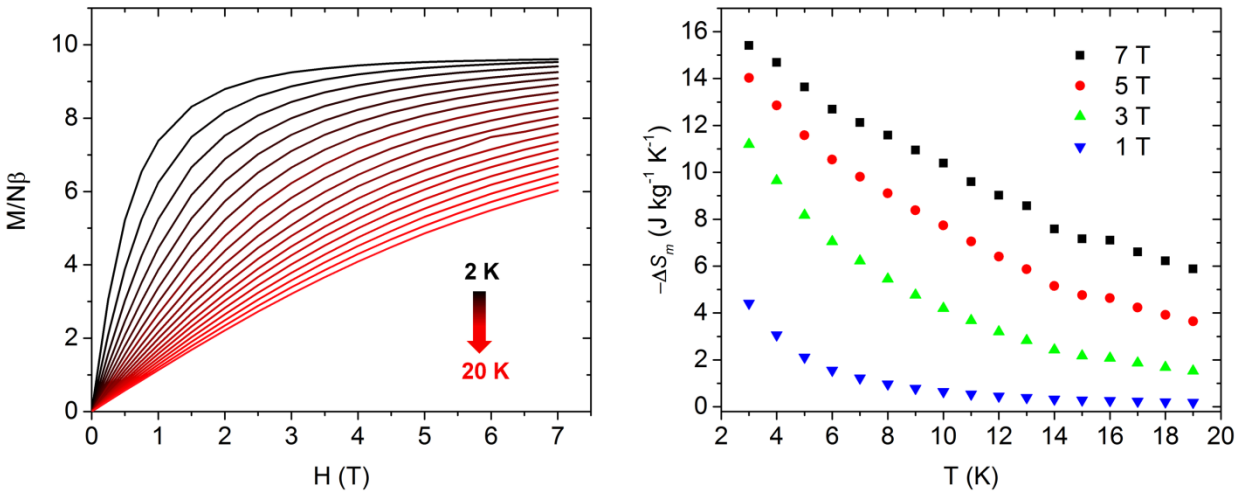


**Figure 4.19.** M/N$\mu_B$ vs. field at temperatures between 2 and 20 K (left) and the temperature-dependent magnetic entropy change for **$Fe_4$OAc**.

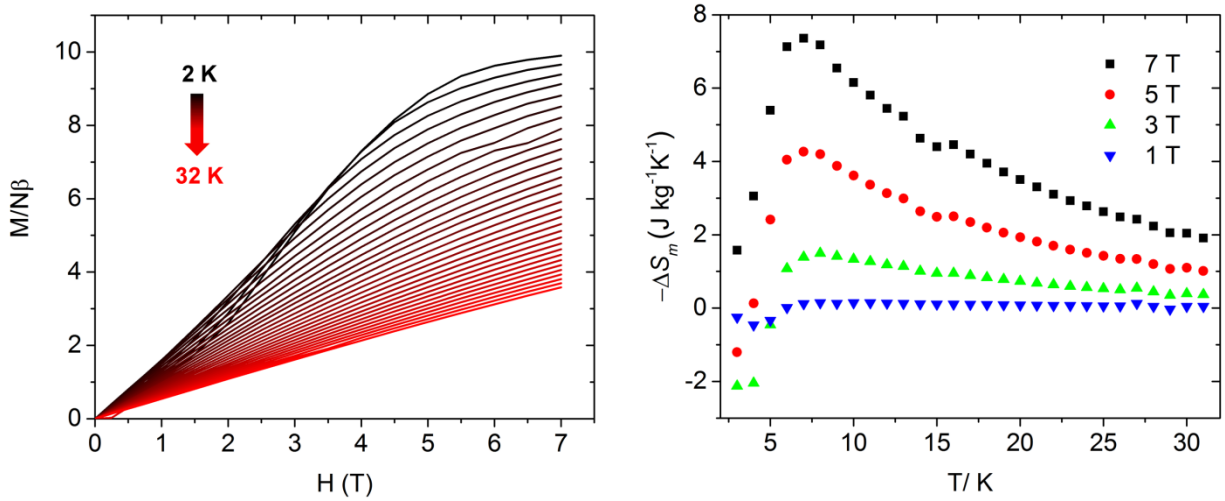


**Figure 4.20.** M/N$\mu_B$ vs. field at temperatures between 2 and 20 K (left) and the temperature-dependent magnetic entropy change for **$Fe_4$OBz**.

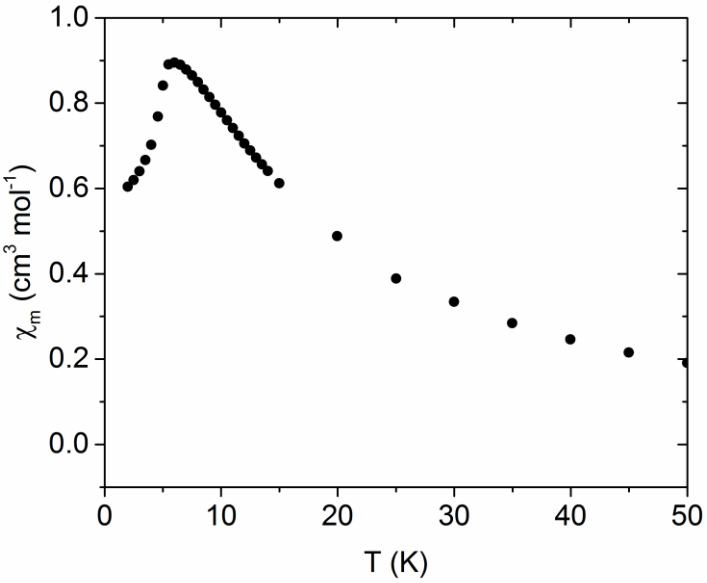


**Figure 4.21.** $\chi_m$ vs. T plot for **$Fe_4$OBz** at a temperature range of 2 to 50 K.

Characterization of the MCE for **$Fe_8$-A**, **$Fe_8$-B**, **$Fe_8$-C**, and **$Fe_8$-A-Dry**, can be seen in Figures 4.22, 4.23, 4.24 and 4.25, respectively. The most solvated sample, **$Fe_8$-A**, exhibits the largest MCE, with $-\Delta S_m$ = 9.9 J $kg^{-1}$ $K^{-1}$ at T = 5 K and $H$ = 7 T. Samples which contain less channel solvent display weaker MCE, as **$Fe_8$-B** and **$Fe_8$-C** have $-\Delta S_m$ = 9.1 J $kg^{-1}$ $K^{-1}$ (4 K and 7 T) and $-\Delta S_m$ = 7.4 J $kg^{-1}$ $K^{-1}$ (4 K and 7 T), respectively. The nearly completely desolvated sample, **$Fe_8$-A-Dry**, exhibits the smallest $-\Delta S_m$, with a value of -5.4 J $kg^{-1}$ $K^{-1}$. As is the case for **$Fe_4$OBz**, this trend may be explained by more prominent antiferromagnetic intermolecular interactions for the more desolvated **$Fe_8$** samples.

Since the magnetic interactions in the $Fe_4$ subunits are expected to be antiferromagnetic and similar to **$Fe_4$OAc** and **$Fe_4$OBz**, and the cluster-cluster interactions through the isopthalate bridges should not change with respect to the level of solvation, it can be reasoned that the loss of solvent leads to stronger antiferromagnetic intermolecular interactions. This may be due to the collapse of the channels and closer cluster to cluster contact. Furthermore, while we could not

ascertain the strength or sign of the exchange between $Fe_4$ subunits through the isopthalate bridges, it is likely non-negligible, since the susceptibility data for all **$Fe_8$** complexes begin to diverge at 200 K. It is not believed that this is due to intermolecular interactions, since they do not manifest in the **$Fe_4$OBz** until much lower temperatures (below 100 K).

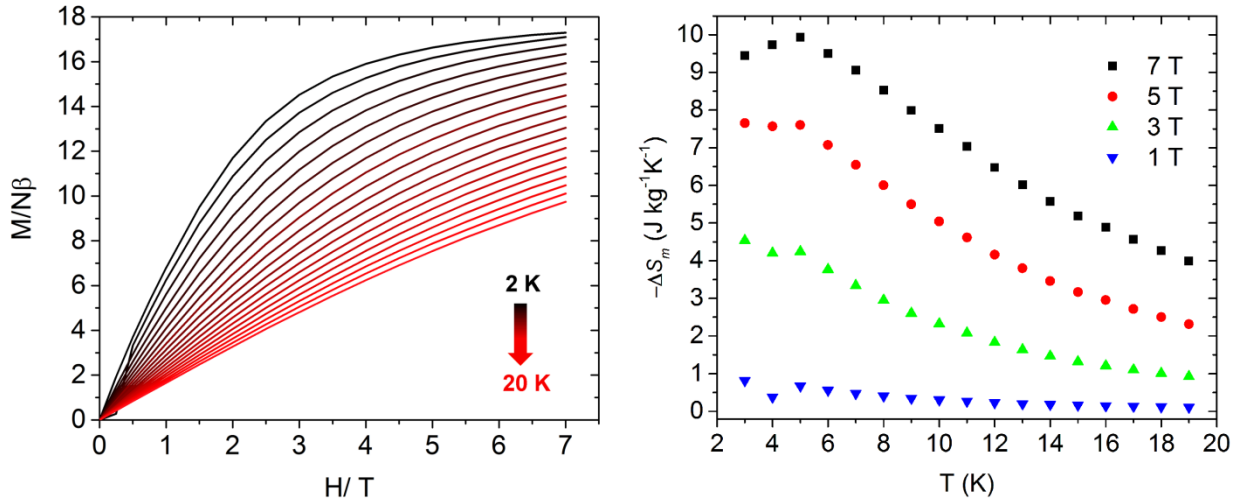


**Figure 4.22.** M/N$\mu_B$ vs. field at temperatures between 2 and 20 K (left) and the temperature-dependent magnetic entropy change for **$Fe_8$-A**.

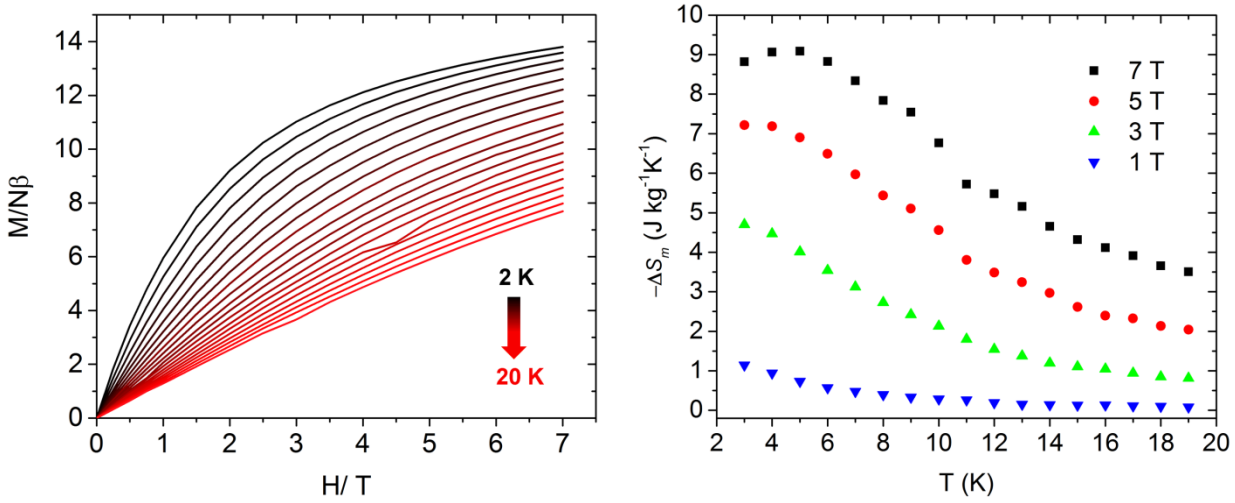


**Figure 4.23.** M/N$\mu_B$ vs. field at temperatures between 2 and 20 K (left) and the temperature-dependent magnetic entropy change for **$Fe_8$-B**.

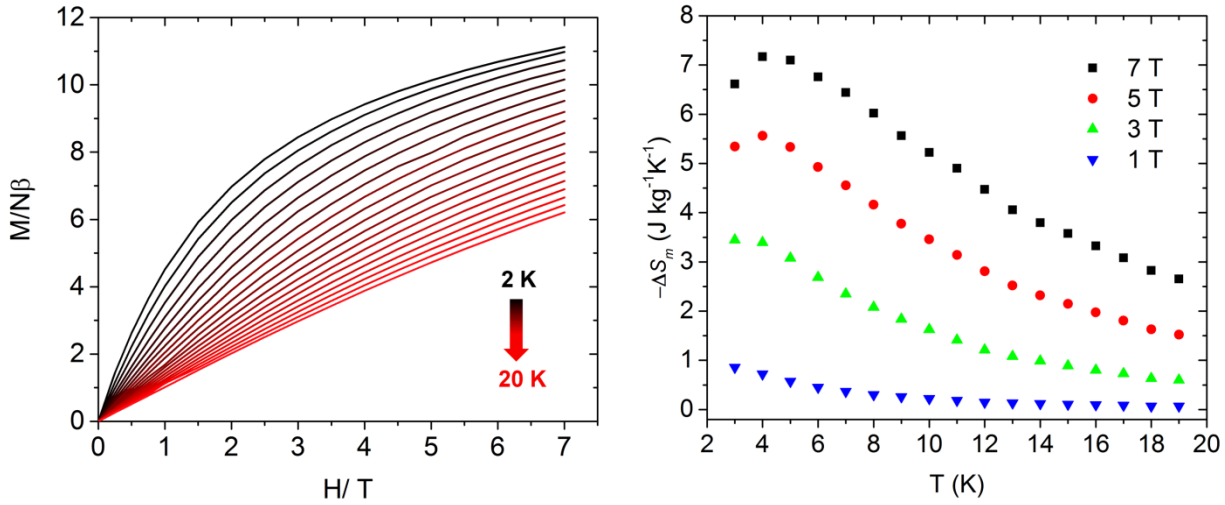


**Figure 4.24.** M/N$\mu_B$ vs. field at temperatures between 2 and 20 K (left) and the temperature-dependent magnetic entropy change for **Fe$_8$-C**.

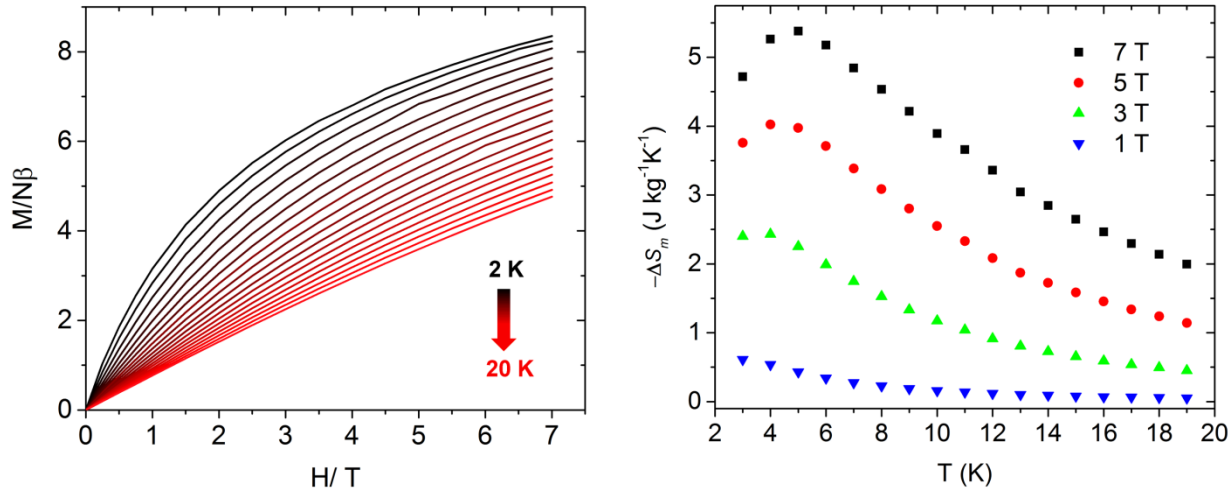


**Figure 4.25.** M/N$\mu_B$ vs. field at temperatures between 2 and 20 K (left) and the temperature-dependent magnetic entropy change for **Fe$_8$-A-Dry**.

Of the complexes studied in this chapter, the MCE for **Fe$_4$OAc** is the largest, because of the lack of long range intermolecular ordering. At 3 K and 7 T, it has a value of -$\Delta S_m$ = 2.1 *R*, approaching the theoretical limit of *R*ln(2*S* + 1) = 2.39 *R* (Equation 1.21) for an *S* = 5 system (Figure 4.26). On the other hand, **Fe$_4$OBz** has a smaller per mole $-\Delta S_m$ throughout the temperature range. **Fe$_8$-A** actually has the largest per mole -$\Delta S_m$ of the three compounds, although its gravimetric -$\Delta S_m$ is lower than **Fe$_4$OAc** due to higher molecular weight. In a per $Fe^{III}$

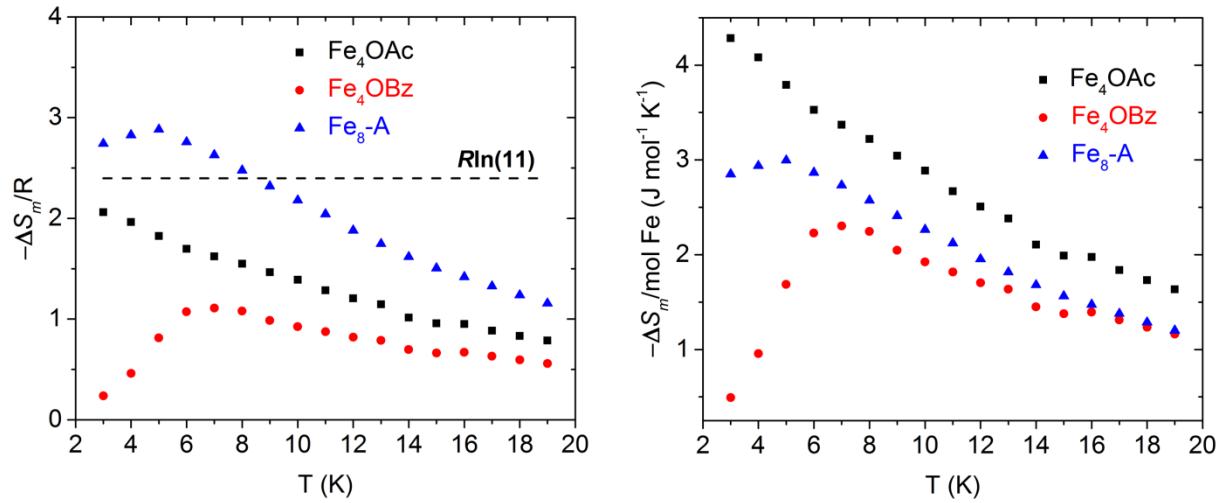


**Figure 4.26.** Temperature-dependence of the magnetic entropy change normalized to *R* (left) and normalized to the number of $Fe^{III}$ ions (right) for **$Fe_4$OAc**, **$Fe_4$OBz** and **$Fe_8$-A** at $H$ = 7 T.

ion basis, **$Fe_4$OAc** has the highest -$\Delta S_m$ for the entire temperature range of 2 to 20 K (Figure 4.26). Below 8 K, the per $Fe^{III}$ -$\Delta S_m$ of **$Fe_4$OBz** tracks with **$Fe_8$-A**, but then decreases towards zero.

In order to see how the $J_2/J_1$ ratio affects the -$\Delta S_m$ in an $Fe_4$ system with the same $J_2$ value (-5.95) and molecular weight (1111.55 g/mol) as **$Fe_4$OAc**, the program MAGPACK[31] was used to simulate the magnetization data for $Fe_4$ systems with $J_2/J_1$ ratios of 0.218, 0.333, 0.320 and 0.350. Figure 4.27 shows the calculated gravimetric -$\Delta S_m$ vs. temperature plots. For the simulated $J_2/J_1$ = 0.218, which matches **$Fe_4$OAc**, the maximum -$\Delta S_m$ (16.57 J $kg^{-1}$ $K^{-1}$) matches fairly well with the experimental value for **$Fe_4$OAc** (15.4 J $kg^{-1}$ K). The difference may be due to the small intermolecular interaction in **$Fe_4$OAc**, which was not included in the simulation. At the ideal $J_2/J_1$ ratio of 0.333, the maximum -$\Delta S_m$ is 22.38 J $kg^{-1}$ $K^{-1}$, a 35% increase over simulated data for $J_2/J_1$ = 0.218 (Figure 4.27, top right).

For $J_2/J_1$ ratios smaller or larger than the ideal value of 0.333, there is a decrease in the maximum simulated entropy change. For $J_2/J_1$ = 0.320, slightly smaller than the ideal value, the

simulated maximum -$\Delta S_m$ decreases to 20.10 J kg$^{-1}$ K$^{-1}$. When we increase the ratio past the ideal value to 0.35, the ground state becomes $S$ = 4 (Figure 4.15), and the -$\Delta S_m$ decreases to having a maximum value of 15.65 J kg$^{-1}$ K$^{-1}$ (Figure 4.27, bottom right). These simulations show that for a constant $J_2$, having the lowest $J_1$ value will not lead to a larger MCE. $J_1$ should be modulated so that the $J_2/J_1$ ratio is 0.333.

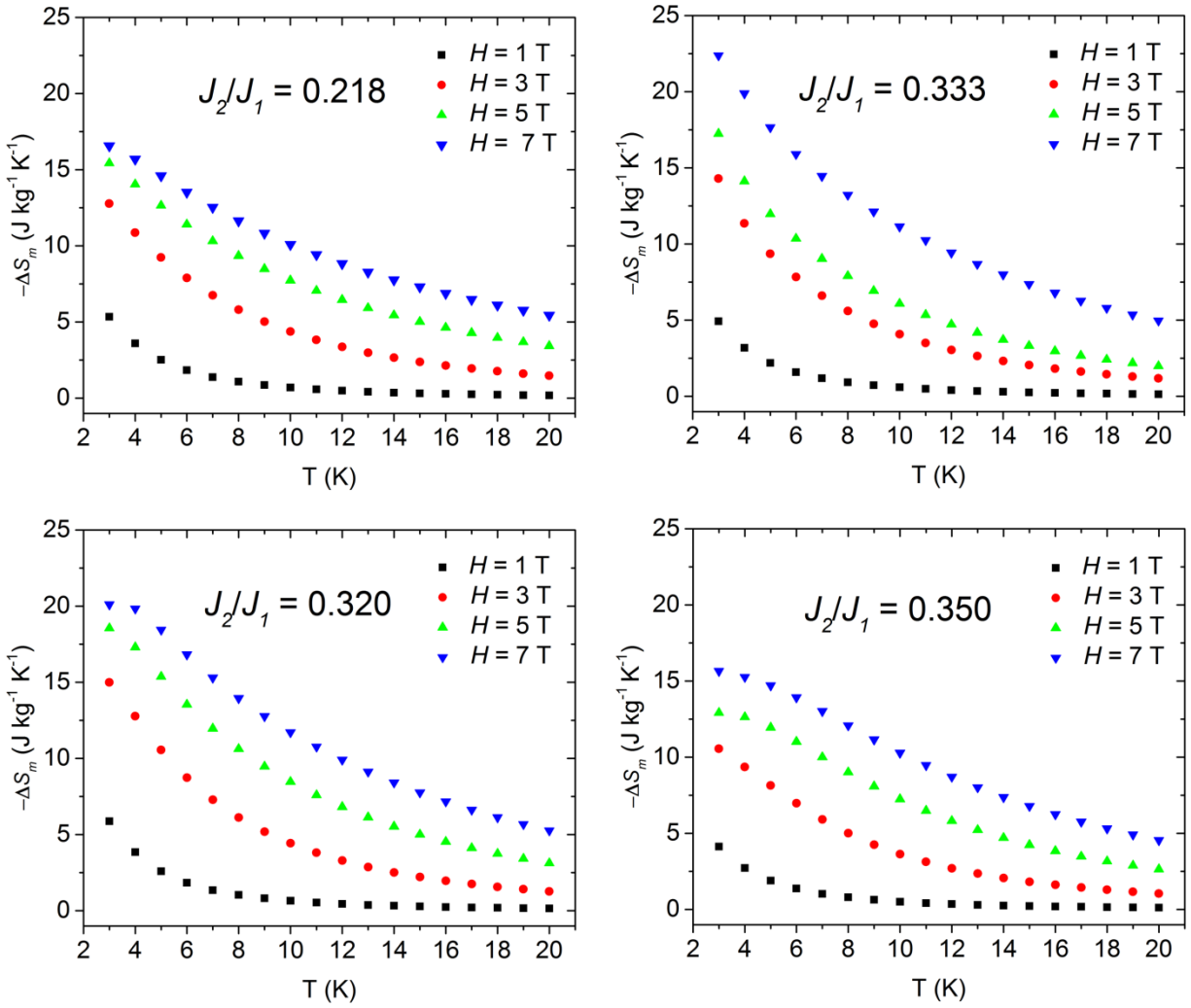


**Figure 4.27.** Simulated temperature dependent magnetic entropy change vs temperature for calculated **Fe$_4$** complexes with $J_2$ set to -5.95. $J_2/J_1$ values are 0.218 (top left), 0.333 (top right), 0.32 (bottom left) and 0.35 (bottom right).

## 4.4 Conclusions

Most of the reported transition metal based magnetic refrigerants involve large polynuclear clusters (more than eight metal ions). While this strategy often results in large ground spin states appropriate for MCE properties, it also makes it difficult to understand the fundamental magnetic interactions which lead to such behavior. The studies described in this chapter have shown that relatively large MCE can be achieved in smaller coordination complexes. More importantly, the underlying intra- and intermolecular interactions have been elucidated and have been used to explain the MCE phenomenon.

The estimated $-\Delta S_m$ = 15.4 $Jkg^{-1}K^{-1}$ for **$Fe_4$OAc** has been explained by a simple 2-*J* magnetic coupling model and offers the potential for modification to achieve even greater values for $-\Delta S_m$. Analysis of the high temperature susceptibility data of **$Fe_4$OBz** shows a shift closer to the ideal $J_2/J_1$ ratio of 0.333, but extensive antiferromagnetic intermolecular interactions have led to a decrease in the MCE. Similarly, these interactions have led to lower $-\Delta S_m$ values for the **$Fe_8$** dimer system. Future work may involve substituting the bridging ligand of the $Fe_4$ system to get closer to the ideal $J_2/J_1$ ratio. If the trend in the $pK_a$ of the bridging ligands of **$Fe_4$OAc** and **$Fe_4$OBz** correlates to the strength of $J_1$, then formate ($pK_a$ = 3.77) may be a reasonable option that could lower this value and also increase the metal to ligand weight ratio that is important for gravimetric values of $-\Delta S_m$. Additionally, the strength of $J_2$ may be decreased through modification of the $H_3$shi ligand. Ultimately, engineering weak ferromagnetic interactions is the key optimizing magnetic entropy change.

Lastly, it has been shown that aromatic ligands which mediate intermolecular π-π interactions can lead to strong antiferromagnetic interactions which quench the MCE. This suggests that using ligands that are more aliphatic in nature may be used to mitigate this and can

also reduce the molecular weight. However, ligands that are not bulky enough can also lead to strong intermolecular metal-metal exchange, as is the case for the $Mn^{II}$ based glycolate salts.[2] The factors which affect MCE, including selection of metal ligands, magnetic interactions and even crystal engineering, makes it difficult to design transition metal based materials. The work described in this chapter may offer some insight into overcoming the complexities involved.

## References


1. Liu, J.-L.; Chen, Y.-C.; Guo, F.-S.; Tong, M.-L. *Coord. Chem. Rev.* **2014**, *281*, 26-49.
2. Chen, Y.-C.; Guo, F.-S.; Liu, J.-L.; Leng, J.-D.; Vrábel, P.; Orendáč, M.; Prokleška, J.; Sechovský, V.; Tong, M.-L. *Chem. Eur. J.* **2014**, *20*, 3029-3035.
3. Bünzli, J.-C. G.; Piguet, C. *Chem. Rev.* **2002**, *102*, 1897-1928.
4. Delfs, C.; Gatteschi, D.; Pardi, L.; Sessoli, R.; Wieghardt, K.; Hanke, D. *Inorg. Chem.* **1993**, *32*, 3099-3103.
5. Sangregorio, C.; Ohm, T.; Paulsen, C.; Sessoli, R.; Gatteschi, D. *Phys. Rev. Lett.* **1997**, *78*, 4645-4648.
6. Zhang, X. X.; Hernandez, J. M.; Del Barco, E.; Tejada, J.; Roig, A.; Molins, E.; Wieghardt, K. *J. Appl. Phys.* **1999**, *85*, 5633-5635.
7. Barra, A. L.; Debrunner, P.; Gatteschi, D.; Schulz, C. E.; Sessoli, R. *Europhys. Lett.* **1996**, *35*, 133-138.
8. Zhang, X. X.; Wei, H. L.; Zhang, Z. Q.; Zhang, L. *Phys. Rev. Lett.* **2001**, *87*, 157203.
9. Rajaraman, G.; Cano, J.; Brechin, E. K.; Mcinnes, E. J. L. *Chem. Commun.* **2004**, 1476-1477.
10. Lah, M. S.; Kirk, M. L.; Hatfield, W.; Pecoraro, V. L. *J. Chem. Soc., Chem. Commun.* **1989**, 1606-1608.
11. Corporation, R. *Crystalclear 2.0*, Tokyo, Japan.
12. Sheldrick, G. M. *Acta. Cryst.* **2008**, *A64*, 112-122.
13. Hunter, C. A.; Sanders, J. K. M. *J. Am. Chem. Soc.* **1990**, *112*, 5525-5534.
14. Spek, A. L., Platon, A Multipurpose Crystallographic Tool. Utrecht University; Utrecht, The Netherlands, 2001.
15. Kambe, K. *J. Phys. Soc. Jpn.* **1936**, *5*, 48-51.
16. Kahn, O., *Molecular Magnetism*. VCH Publishers, Inc.: New York, 1993.
17. Sessoli, R. *Angew. Chem. Int. Ed.* **2012**, *51*, 43-45.
18. Huang, J.; Kertesz, M. *J. Am. Chem. Soc.* **2007**, *129*, 1634-1643.
19. Nguyen, T. N.; Abboud, K. A.; Christou, G. *Polyhedron* **2013**, *66*, 171-178.
20. Iasco, O.; Rivière, E.; Guillot, R.; Buron-Le Cointe, M.; Meunier, J.-F.; Bousseksou, A.; Boillot, M.-L. *Inorg. Chem.* **2015**.
21. Shaw, R.; Laye, R. H.; Jones, L. F.; Low, D. M.; Talbot-Eeckelaers, C.; Wei, Q.; Milios, C. J.; Teat, S.; Helliwell, M.; Raftery, J.; Evangelisti, M.; Affronte, M.; Collison, D.; Brechin, E. K.; Mcinnes, E. J. L. *Inorg. Chem.* **2007**, *46*, 4968-4978.
22. Evangelisti, M.; Candini, A.; Ghirri, A.; Affronte, M.; Piligkos, S.; Brechin, E. K.; Mcinnes, E. J. L. *Polyhedron* **2005**, *24*, 2573-2578.
23. Evangelisti, M.; Candini, A.; Ghirri, A.; Affronte, M.; Brechin, E. K.; Mcinnes, E. J. L. *Appl. Phys. Lett.* **2005**, *87*, -.
24. Anis, B.; Tapas, S.; Banerjee, S.; Das, I. *J. Phys. Condens. Mat.* **2009**, *21*, 506005.
25. Bourgault, D.; Tillier, J.; Courtois, P.; Maillard, D.; Chaud, X. *Appl. Phys. Lett.* **2010**, *96*, 132501.
26. Li, Z.; Zhang, Y.; Xu, K.; Yang, T.; Jing, C.; Zhang, H. L. *Solid State Commun.* **2015**, *203*, 81-84.
27. Krenke, T.; Duman, E.; Acet, M.; Wassermann, E. F.; Moya, X.; Manosa, L.; Planes, A. *Nat Mater* **2005**, *4*, 450-454.
28. Ranke, P. J. V.; Oliveira, N. a. D.; Alho, B. P.; Plaza, E. J. R.; Sousa, V. S. R. D.; Caron, L.; Reis, M. S. *J. Phys. Condens. Mat.* **2009**, *21*, 056004.
29. Alho, B. P.; Oliveira, N. a. D.; Sousa, V. S. R. D.; Plaza, E. J. R.; Carvalho, A. M. G.; Ranke, P. J. V. *J. Phys. Condens. Mat.* **2010**, *22*, 486008.
30. Evangelisti, M.; Luis, F.; De Jongh, L. J.; Affronte, M. *J. Mater. Chem.* **2006**, *16*, 2534-2549.

31. Borras-Almenar, J. J.; Clemente-Juan, J. M.; Coronado, E.; Tsukerblat, B. S. *J. Comput. Chem.* **2001**, *22*, 985-991.

# Chapter V

# Luminescent $Ga^{III}/Ln^{III}$ 12-MC-4 Complexes

## 5.1 Introduction

Lanthanide(III) metal ions have attractive luminescence properties for a broad range of applications due to their unique electronic properties. The sharp bandwidths, large energy gap between absorption and emission bands, and long luminescence lifetimes make $Ln^{III}$ luminescence attractive for practical application such as biological imaging,[1-3] solar energy conversion,[4-6] diode displays,[7] and telecommunications.[8-9] As noted in Chapter I, the sensitization through the "antenna effect" describes the excitation of an organic ligand ("antenna"), followed by the transfer of the corresponding energy to the accepting levels of the $Ln^{3+}$ generating the subsequent f-f emission with long luminescence lifetimes upon return of the system to the ground state. The energy difference ($\Delta E$) between the ligand's excited triplet state ($^3T_1$) and the accepting f-orbital electronic level of the lanthanide is one of the identified parameters that impact the global sensitization efficiency (Figure 1.37). Some systems have been identified as more efficient for the $Ln^{III}$ emitting in the visible ($Tb^{III}$, $Sm^{III}$, $Dy^{III}$, $Eu^{III}$)[10-11] while others are more suitable for those emitting in the NIR ($Nd^{III}$, $Er^{III}$, $Ho^{III}$, $Yb^{III}$, $Tm^{III}$).[12-13]

In the case of metallacrowns, the $LnZn_{16}L_{16}$ sandwich complexes have demonstrated remarkable NIR luminescence properties. The hydration number ($q$) for the $LnZn_{16}L_{16}$ derivatives is zero, indicating the absence of quenching solvent molecules directly bound to the

lanthanide cation. As a result, several of these compounds exhibit the highest luminescence quantum yield values reported to date for selected NIR emitting $Ln^{III}$ ($Yb^{3+}$, $Nd^{3+}$, $Er^{3+}$).[14-15] However, a drawback to this system is that visible emitting $Ln^{III}$ ions cannot be sensitized. To date, only a very limited selection of ligand systems has been demonstrated that sensitize $Ln^{III}$ across the entire spectrum.[16-17]

As a hypothesis for the creation of the ideal system, we can propose a good balance between two important parameters: the sensitization efficiency of the $Ln^{III}$ and the protection from the presence of sources of non-radiative deactivation due to the harmonic oscillation of –OH, –NH and –CH vibrations of solvent molecules and of the organic ligands of the complex. The closer the $Ln^{III}$ ion is to the organic chromophoric ligand environment, the larger the efficiency of the sensitization. On the other hand, non-radiative deactivation increases with decreasing distance between the $Ln^{III}$ ion and the vibrations of the chromophore. Consequently, the use of rigid systems to create new complexes is an attractive strategy, as it allows for the control of the distance between the antennae and the luminescent lanthanide(III) cations.

As the next step for the creation of novel lanthanide-based NIR reporters, we have chosen to design and synthesize MC compounds which incorporate $Ga^{3+}$ ions. In order to analyze the effects of the structure of MCs on their luminescence properties, we have to synthesize MCs based on $Ga^{III}$, an isoelectronic cation to $Zn^{II}$ and that cannot interfere (quench) with the excited states of the luminescent lanthanide. Therefore, we hypothesized that these novel $Ga^{III}$ MCs would possess many of the electronic features obtained for the $Zn^{II}$ system while allowing for the use of different chromophores (tri-anionic MC ligands to compensate for the charge of $Ga^{III}$). Moreover, the $Ga^{III}$ ring metals form the backbone of these MCs; various isotopes of gallium are used in several biomedical applications, providing the potential for these compounds to serve as

multipurpose therapeutic agents. The combination of luminescent $Ln^{III}$ and radioisotopes of $Ga^{III}$ allows for the prospect of the reported complexes being used as both bimodal imaging ($^{68}Ga$ is used in PET imaging[18]) and theranostic ($^{67}Ga$ is a potential therapeutic radionuclide[19-20]) agents.

This Chapter will focus on the photophysical properties of a series of **$Ga_4Ln$** MCs ($Ln^{III}$ = Sm, Eu, Gd, Tb, Dy, Ho, Er, Tm, Yb) isostructural to the $Dy^{III}(benzoate)_3[12\text{-}MC_{M^{III}N(shi)}\text{-}4](pyridinium^+)$ compounds reported in Chapter III. The framework ligand used in the above compounds, salicylhydroxamic acid ($H_3shi$), is structurally different from the picoline hydroxamic acid (picHA) ligand used in the first generation of $LnZn_{16}L_{16}$ complexes.[14] Furthermore, the central $Ln^{III}$ ions are encapsulated by bridging benzoate molecules, which may play a role in the sensitization of the lanthanide(III) ions. Lastly, the synthesis and luminescent properties of the $Gd^{III}$ and $Dy^{III}$ derivatives of a $Ln^{III}_2(isopthalate)_4[12\text{-}MC_{Ga^{III}N(shi)}\text{-}4]_2(NH_4^+)_2$ complex (**$Ga_8Ln_2$**) will be reported. Comparison of the photophysical properties of the **$Ga_4Ln$** and **$Ga_8Ln_2$** dimer compounds will be used to examine whether the identity of the bridging ligand (benzoate vs. isophthalate) affects lanthanide sensitization.

## 5.2 Experimental

All reagents and chemicals were purchased from commercial sources and used without further purification. CHN analysis was performed by Atlantic Microlabs Inc. All reactions were completed under aerobic conditions.

### *Synthetic Methods*

Preparation of **$Ga_4Ln$** Complexes. $H_3shi$ (153.1 mg, 1.0 mmol), $Ln(NO_3)_3{\cdot}xH_2O$ (0.25 mmol; 0.50 mmol for Ln = Sm and Eu), $Ga(NO_3)_3{\cdot}xH_2O$ (225.7 mg, 1.0 mmol) was dissolved in 40 mL methanol. Sodium benzoate (576.4 mg, 4.0 mmol) was added to the solution and stirred overnight. The solution was filtered, followed by addition of 2 mL pyridine. The solution was

stirred for 15 minutes and then filtered. Slow evaporation of half of the solution yielded crystalline compound after 2 weeks.

$[Ga_4Sm(shi^{3-})_4(C_6H_5CO_2)_4(C_5H_5N)(CH_3OH)] \cdot C_5H_6N \cdot C_5H_5N \cdot CH_3OH$ (**$Ga_4Sm$**). Yield: 104.9 mg (20.1%). ESI-MS, calc. for $[M]^-$, $C_{56}H_{36}N_4O_{20}SmGa_4$, 1513.8; found, 1514.2 Anal. Calcd for $SmGa_4C_{73}H_{60}N_7O_{22}$: C, 48.27; H, 3.33; N, 5.40. Found: C, 48.29; H, 3.16; N, 5.51.

$[Ga_4Eu(shi^{3-})_4(C_6H_5CO_2)_4(C_5H_5N)(CH_3OH)] \cdot C_5H_6N \cdot C_5H_5N \cdot CH_3OH$ (**$Ga_4Eu$**). Yield: 213.0 mg (20.1%). ESI-MS, calc. for $[M]^-$, $C_{56}H_{36}N_4O_{20}EuGa_4$, 1514.8; found, 1515.0. Anal. Calcd for $EuGa_4C_{73}H_{60}N_7O_{22}$: C, 48.224; H, 3.33; N, 5.39. Found: C, 48.35; H, 3.13; N, 5.58.

$[Ga_4Gd(shi^{3-})_4(C_6H_5CO_2)_4(C_5H_5N)(CH_3OH)] \cdot C_5H_6N \cdot C_5H_5N \cdot CH_3OH$ (**$Ga_4Gd$**). Yield: 91.8 mg (20.1%). ESI-MS, calc. for $[M]^-$, $C_{56}H_{36}N_4O_{20}GdGa_4$, 1519.8; found, 1519.8. Anal. Calcd for $GdGa_4C_{73}H_{60}N_7O_{22}$: C, 48.09; H, 3.32; N, 5.38. Found: C, 48.18; H, 3.07; N, 5.57.

$[Ga_4Tb(shi^{3-})_4(C_6H_5CO_2)_4(C_5H_5N)(CH_3OH)] \cdot C_5H_6N \cdot C_5H_5N \cdot CH_3OH$ (**$Ga_4Tb$**). Yield: 102.0 mg (22.4%). ESI-MS, calc. for $[M]^-$, $C_{56}H_{36}N_4O_{20}TbGa_4$, 1522.8; found, 1522.8. Anal. Calcd for $TbGa_4C_{73}H_{60}N_7O_{22}$: C, 48.04; H, 3.31; N, 5.37. Found: C, 48.33; H, 3.12; N, 5.54.

$[Ga_4Dy(shi^{3-})_4(C_6H_5CO_2)_4(C_5H_5N)(CH_3OH)] \cdot C_5H_6N \cdot C_5H_5N \cdot CH_3OH$ (**$Ga_4Dy$**). Yield: 106.6 mg (23.3%). ESI-MS, calc. for $[M]^-$, $C_{56}H_{36}N_4O_{20}DyGa_4$, 1525.8; found, 1525.8. Anal. Calcd for $DyGa_4C_{73}H_{60}N_7O_{22}$: C, 47.95; H, 3.31; N, 5.36. Found: C, 48.08; H, 3.10; N, 5.54.

$[HoGa_4(shi^{3-})_4(C_6H_5CO_2)_4(C_5H_5N)(CH_3OH)] \cdot C_5H_6N \cdot C_5H_5N \cdot CH_3OH$ (**$Ga_4Ho$**). Yield: 160.4 mg (35.0%). ESI-MS, calc. for $[M]^-$, $C_{56}H_{36}N_4O_{20}HoGa_4$, 1528.8; found, 1529.3. Anal. Calcd for $HoGa_4C_{73}H_{60}N_7O_{22}$: C, 47.88; H, 3.30; N, 5.35. Found: C, 48.01; H, 3.07; N, 5.50.

$[ErGa_4(shi^{3-})_4(C_6H_5CO_2)_4(C_5H_5N)(CH_3OH)] \cdot C_5H_6N \cdot C_5H_5N \cdot CH_3OH$ (**$Ga_4Er$**). Yield: 159.5 mg (34.8%). ESI-MS, calc. for $[M]^-$, $C_{56}H_{36}N_4O_{20}ErGa_4$, 1529.8; found, 1530.1. Anal. Calcd for $ErGa_4C_{73}H_{60}N_7O_{22}$: C, 47.82; H, 3.30; N, 5.35. Found: C, 47.29; H, 3.05; N, 5.53.

$[TmGa_4(shi^{3-})_4(C_6H_5CO_2)_4(C_5H_5N)(CH_3OH)] \cdot C_5H_6N \cdot C_5H_5N \cdot CH_3OH$ (**$Ga_4Tm$**). Yield: 148.4 mg (32.3%). ESI-MS, calc. for $[M]^-$, $C_{56}H_{36}N_4O_{20}TmGa_4$, 1532.8; found, 1532.8. Anal. Calcd for $TmGa_4C_{73}H_{60}N_7O_{22}$: C, 47.78; H, 3.30; N, 5.34. Found: C, 47.06; H, 2.95; N, 5.48.

$[YbGa_4(shi^{3-})_4(C_6H_5CO_2)_4(C_5H_5N)(CH_3OH)] \cdot C_5H_6N \cdot C_5H_5N \cdot CH_3OH$ (**$Ga_4Yb$**). Yield: 54.1 mg (11.8%). ESI-MS, calc. for $[M]^-$, $C_{56}H_{36}N_4O_{20}YbGa_4$, 1535.8; found, 1535.8. Anal. Calcd for $YbGa_4C_{73}H_{60}N_7O_{22}$: C, 47.67; H, 3.29; N, 5.33. Found: C, 47.69; H, 3.10; N, 5.49.

Preparation of **$Ga_8Ln_2$** Complexes. $H_3shi$ (306.3 mg, 2.0 mmol), $Ln(NO_3)_3 \cdot xH_2O$ (0.50 mmol), $Ga(NO_3)_3 \cdot xH_2O$ (511.5 mg, 2.0 mmol) and Isophthalic acid (166.1 mg, 1.0 mmol) was dissolved in 15 mL DMF. Ammonium bicarbonate (632.5 mg, 8.0 mmol) was added to the solution and stirred overnight. The solution was filtered. Slow evaporation of half of the solution yielded crystalline compound after 3 months.

$[Ga_8Dy_2(shi^{3-})_8(isophthalate^{2-})_4(DMF)_6] \cdot 8DMF \cdot 2H_2O$ (**$Ga_8Dy_2$**). Yield: 280.1 mg (34.6%). Anal. Calcd for $Dy_2Ga_8C_{130}H_{158}N_{24}O_{56}$: C, 40.71; H, 4.15; N, 8.76. Found: C, 40.75; H: 4.45; N: 8.87.

$[Ga_8Gd_2(shi^{3-})_8(isophthalate^{2-})_4(DMF)_6] \cdot 8DMF \cdot H_2O$ (**$Ga_8Gd_2$**). Yield: 321.0 mg (33.7%). Anal. Calcd for $Gd_2Ga_8C_{130}H_{156}N_{24}O_{55}$: C, 41.01; H, 4.13; N, 8.83. Found: C, 40.98; H: 4.28; N: 8.99.

***Physical Methods***

*X-Ray Crystallography*. Crystal data for compound **$DyGa_4$** were collected at 85(2) K on an AFC10K Saturn 944+ CCD-based X-ray diffractometer equipped with a Micromax007HF Cu-target microfocus rotating anode ($\lambda$ = 1.54187 Å), operated at 1200 W power (40 kV, 30 mA). The data were processed with CrystalClear 2.0[21] and corrected for absorption. The structure was solved and refined with the SHELXTL (version 6.12) software package[22] All non-hydrogen atoms were refined anisotropically. Hydrogen atoms placed in their idealized positions.

*Powder X-ray Diffraction (PXRD).* Powder X-ray diffraction data for air-dried samples of the **$Ga_4Ln$** complexes were collected at room temperature using a Bruker D8 Advance Diffractometer with Cu-K$\alpha$ raciation (1.5406 Å, 40 kV, 40 mA). Powder diffraction patterns were collected at room temperature from 3° to 50° (2$\theta$) using a step size of 0.05° and a scan time of 0.5 second/step.

*ESI-Mass Spectrometry*. ESI-MS spectra were collected with a Micromass LCT Time-of-Flight Electrospray Mass Spectometer in negative ion mode at cone voltages ranging from -40 to -70 V on samples dissolved in DMF. Samples were injected via syringe pump. Data were processed with the MassLynx 4.0 software.

*Solid State Diffuse Reflectance.* Solid state UV-Vis spectra were collected using an Agilent-Cary 5000 spectrophotometer equipped with a Praying Mantis diffuse reflectance accessory. Spectra were collected in reflectance mode, with $BaSO_4$ was used as a baseline. Samples (10% by

weight) were mulled in $BaSO_4$ (90% by weight). The spectra were converted into normalized absorbance by using the equation A = 1 – R.

*Solution Absorption Spectra.* UV-Vis spectra for the compounds dissolved in methanol were recorded on a Cary 100Bio UV-Vis Spectrophotometer. All spectra were collected in absorbance mode.

*Photophysical measurements***.** Luminescence data were collected on samples placed into 2.4 mm i.d. quartz capillaries or quartz Suprasil cells. Emission and excitation spectra were measured on a Horiba-Jobin-YvonFluorolog 3 spectrofluorimeter equipped with either a visible photomultiplier tube (PMT) (220-800 nm, R928P; Hamamatsu), a NIR solid-state InGaAs detector cooled to 77 K (800-1600 nm, DSS-IGA020L; Jobin-Yvon), or NIR PMTs (950-1450 nm, H10330-45; 950-1650 nm, H10330-75; Hamamatsu). All spectra were corrected for instrumental functions. Luminescence lifetimes were determined under excitation at 355 nm provided by a Nd:YAG laser (YG 980; Quantel), while the signal was detected in the NIR by the aforementioned PMT (H10330-75). The output signal from the detectors was then fed to a 500MHz bandpass digital oscilloscope (TDS 754C; Tektronix) and then transferred to a PC for treatment with Origin 8®. Luminescence lifetimes are averages of at least three independent measurements. Quantum yields in the NIR were determined with a Fluorolog 3 spectrofluorimeter according to an absolute method using an integration sphere (GMP SA). Each sample was measured several times under slightly different experimental conditions. Estimated experimental error for quantum yields determination is 10 %.

*Acknowledgements.* Svetlana Eliseeva (CNRS Orléans, France) and Evan Trivedi performed the photophysical measurements and data analysis for all samples.

**Table 5.1.** Crystallographic Details for **$Ga_8Dy_2$**.

| | **$Ga_8Dy_2$** |
|---|---|
| mol formula | $C_{96}H_{20}Dy_2Ga_8N_{12}O_{46}$ |
| fw (g/mol) | 2939.84 |
| cryst syst/ space group | Triclinic/ P-1 |
| *T* (K) | 85(2) |
| wavelength (Å) | 1.54178 |
| *a* (Å) | 14.1080(3) |
| *b* (Å) | 17.5806(3) |
| *c* (Å) | 19.2197(14) |
| α (deg) | 113.107(8) |
| β (deg) | 102.699(7) |
| γ (deg) | 98.218(7) |
| *V* (Å$^3$) | 4135.4(3) |
| *Z* | 1 |
| density, ρ (g/cm$^3$) | 1.180 |
| abs coeff, μ (mm$^{-1}$) | 6.713 |
| *F*(000) | 1408 |
| θ range for data collection (deg) | 2.62 to 68.24 |
| limiting indices | $-16 \le h \le 16$<br>$-20 \le k \le 21$<br>$-23 \le l \le 23$ |
| reflns collected/ unique | 111713 / 14938 |
| completeness to θ (%) | 98.6 |
| no. of data/ restraints/ params | 14938 / 0 / 815 |
| goodness of fit on $F^2$ | 1.929 |
| final *R* indices [$I > 2\sigma(I)$] | R1$^a$ = 0.1430<br>wR2$^b$ = 0.3897 |
| *R* indices (all data) | R1$^a$ = 0.1459<br>wR2$^b$ = 0.3981 |
| largest diff peak and hole (e$^-$ Å$^{-3}$) | 12.150 and -2.064 |

$^a$R1 = $\Sigma(||F_o| - |F_c||)/\Sigma|F_o|$. $^b$wR2 = $[\Sigma[w(F_o^2 - F_c^2)^2]/\Sigma[w(F^\circ)^2]]^{1/2}$; $w = 1/[\sigma^2(F_o^2) + (mp)^2 + np]$; p = $[\max(F_o^2,0) + 2F_c^2]/3$ (*m* and *n* are constants); $\sigma = [\Sigma[w(F_o^2 - F_c^2)^2]/(n-p)]^{1/2}$.

**Table 5.2.** Selected bond lengths for **$Ga_8Dy_2$**.

| **Bond** | **Length (Å)** |
|---|---|
| Dy(1)-O(5) | 2.301(10) |
| Dy(1)-O(2) | 2.326(8) |
| Dy(1)-O(112) | 2.328(9) |
| Dy(1)-O(111) | 2.343(8) |
| Dy(1)-O(101) | 2.347(7) |
| Dy(1)-O(103) | 2.353(8) |
| Dy(1)-O(8) | 2.391(9) |
| Dy(1)-O(11) | 2.396(7) |

## 5.3 Results and Discussion

**Synthesis and Characterization. (i) $Ga_4Ln$ Complexes.** The crystal structure and crystallographic parameters for the **$Ga_4Dy$** (Figure 5.1) compound are reported in Chapter III. In the $LnZn_{16}L_{16}$ structures described in Chapter I, the distance between the $Ln^{III}$ ion and the closest C-H oscillator was greater than 6 Å. For **$Ga_4Dy$**, and the other analogues of the series, the shortest Ln-CH distance was found to be 4.37 Å. Nevertheless, remarkable NIR photophysical properties have been observed for these complexes despite this relatively short distance. This is a qualitative indication that the effect of potential luminescence quenching is compensated by the chromophore to lanthanide energy transfer.

It should be noted that the centroid in the space in between the four benzoate groups is ~2.3 Å from the inner most hydrogen atoms. Although no electron density was observed in that region, this void space is large enough to be occupied by a water molecule, which would potentially have implications in the photophysical data for the **$Ga_4Ln$** complexes.

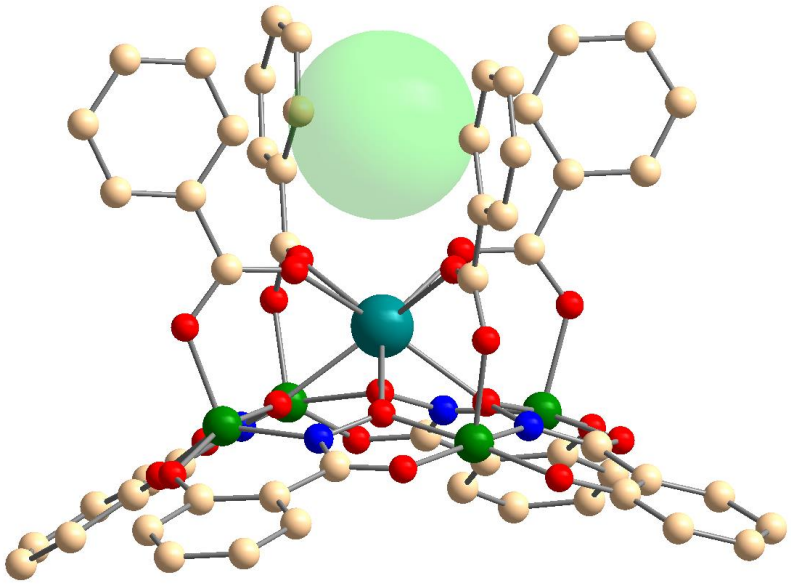

**Figure 5.1.** Crystal structure of **$Ga_4Dy$**.The blue dashed line represents the closest C-H oscillator to the $Dy^{III}$ ion. Teal = Dy; green = Ga; tan = C; red = O; blue = N. The transparent green sphere shows a void space where potential water molecules may reside.

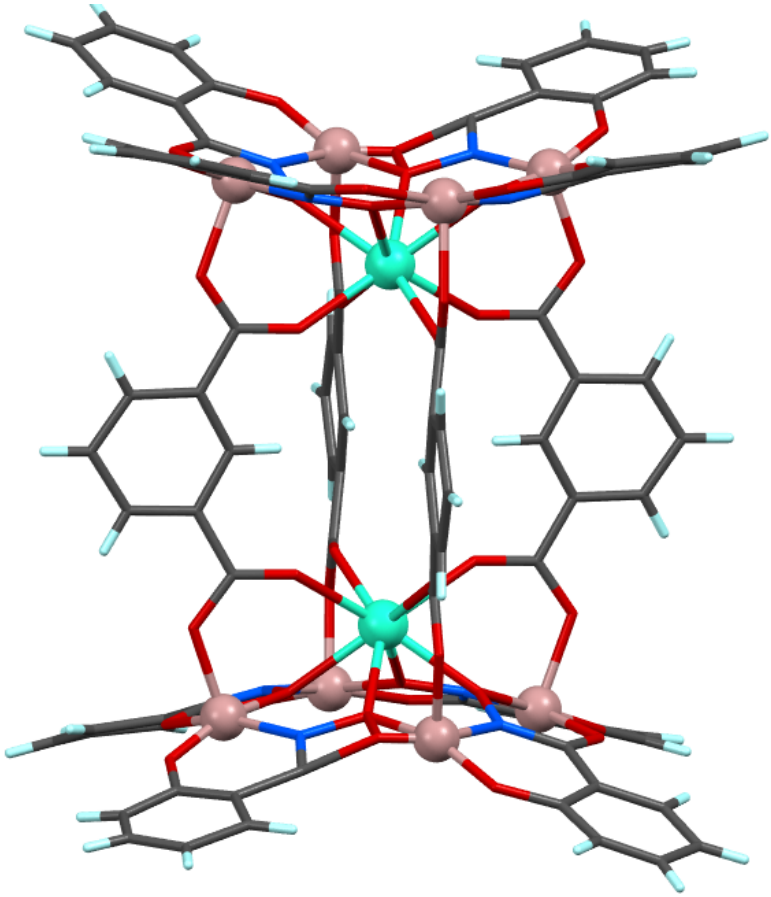

**Figure 5.2.** Crystal structure of **$Ga_8Dy_2$**. Coordinating solvent molecules are omitted for clarity.

**(ii) $Ga_8Ln_2$ Complexes.** Utilizing the same synthetic strategy as the **$Fe_8$** dimer complex in Chapter IV, two 12-MC-4 units of the **$Ga_4Ln$** complexes were linked together via isophthalate ligands. Using ammonium bicarbonate as a base, reaction of $H_3$shi, $Ln(NO_3)_3 \cdot xH_2O$, $Ga(NO_3)_3 \cdot xH_2O$ and Isophthalic acid in DMF forms the **$Ga_8Ln_2$** complex which can be described as two 12-MC-4 monomer subunits connected via four isophthalate groups (Figure 5.2). The molecular moiety has a net negative two charge. Since no metal atoms could be found in the electron density, the charge is likely balanced by two lattice $NH_4^+$ ions. However, these counter-ions could not be located due to weak scattering. Similarly, the diffuse electron density of the lattice solvent required the use of SQUEEZE routine of the PLATON suite of programs.[23]

Since the **$Ga_8Dy_2$** complex crystallizes in the space group P-1, the two $Dy^{III}$ ions are symmetry related by an inversion center and are situated 7.23 Å apart, such that any through-space interactions are likely negligible. As with **$Ga_4Ln$**, the closest C-H oscillator resides on the inner most carbon of a bridging benzoate and is 4.51 Å from the nearest $Dy^{III}$ ion (Figure 5.2). This distance is longer than the 4.37 Å for **$Ga_4Dy$**.

**Photophysical Properties. (i) $Ga_4Ln$ Complexes.** All synthesized complexes (excluding **$Ga_4Gd$**) of the series showed the ability to emit visible (**$Ga_4Tm$**, **$Ga_4Dy$**, **$Ga_4Tb$**, **$Ga_4Sm$**, **$Ga_4Eu$**) and/or near-infrared luminescence (**$Ga_4Dy$**, **$Ga_4Yb$**, **$Ga_4Ho$**, **$Ga_4Er$**, **$Ga_4Sm$** ). For each of these MCs, the bands observed in both solution (Figure 5.3) and solid state (Figure 5.4) absorption spectra match well with those observed in the excitation spectra (Appendix C, Figures C1-C11) of the different **$Ga_4Ln$** complexes. This indicates that the excitation light is absorbed by the $\pi \rightarrow \pi^*$ transition located on the chromophoric $shi^{3-}$ ligands and that the corresponding energy is being transferred to the luminescent lanthanides. Thus, this MC design is able to provide an antenna effect for these different lanthanide cations emitting in the visible and in the NIR.

The $Gd^{III}$ derivative in this series is a useful probe to assess the electronic structure of these MCs, since this cation is not expected to exhibit $Ln^{III}$ luminescence under UV excitation as the energy of the triplet state of the $shi^{3-}$ ligand is hypothesized to be too low due to transfer to the accepting $Gd^{III}$ level. The absorption spectrum of **$Ga_4Gd$** exhibits two major features attributed to ligand based $\pi \rightarrow \pi^*$ transitions on the basis of their high values of molar extinction coefficients with the lower energy absorption band located at 310 nm (corresponding to an energy of ca. 32,250 $cm^{-1}$, Figure 5.5**;** black). This band is likely due to $\pi \rightarrow \pi^*$ transitions on the ligand $H_3shi$, which has an absorption at 299 nm; sodium benzoate does not show an absorption

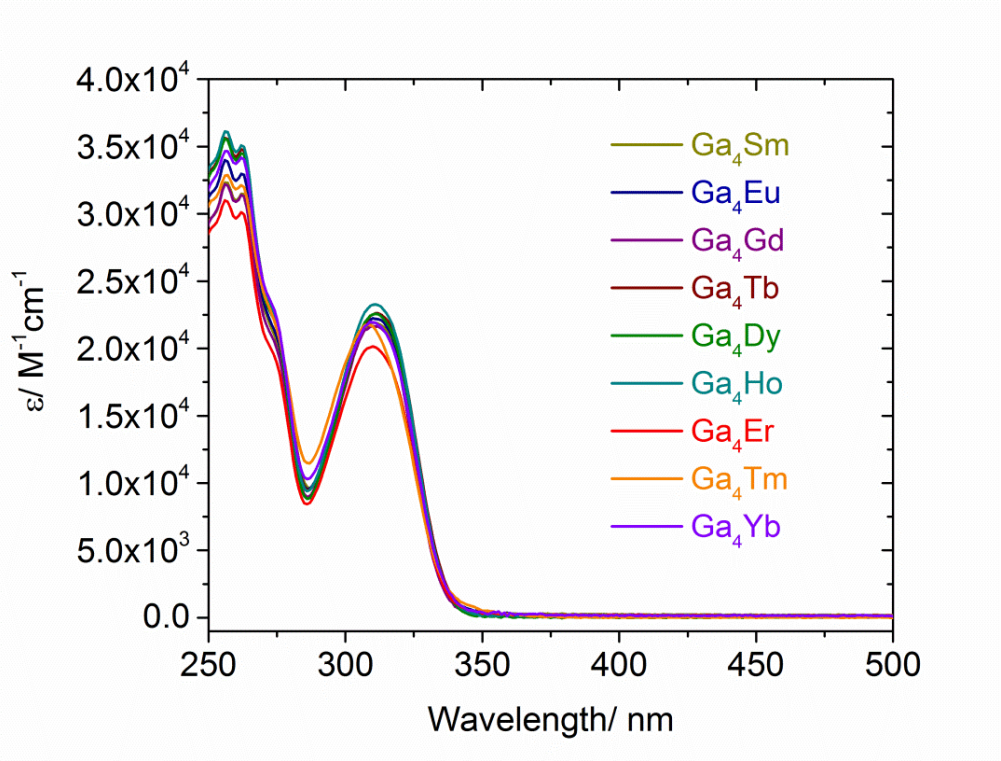


**Figure 5.3.** UV-Vis absorption spectra for the **$Ga_4Ln$** complexes in methanol at 298 K.

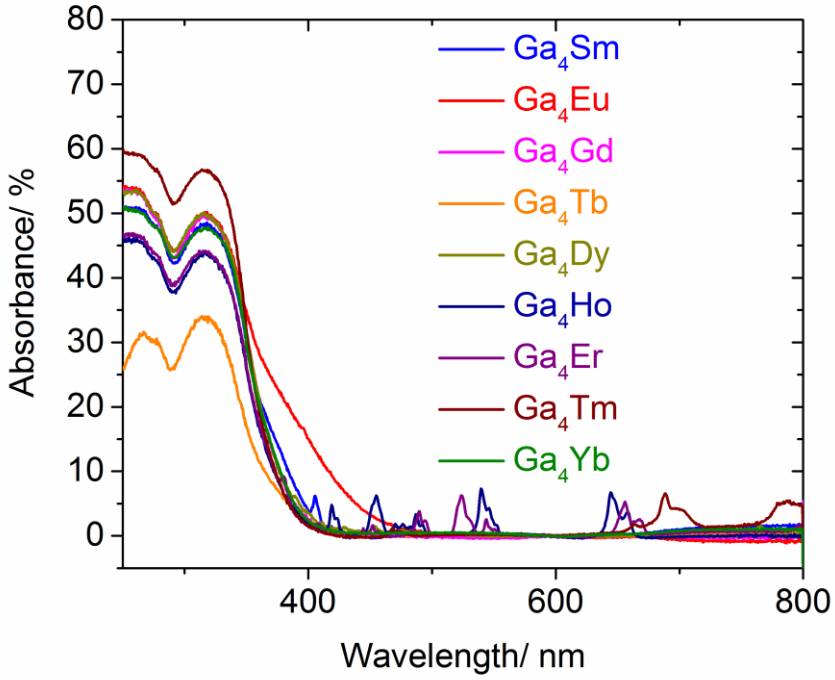


**Figure 5.4.** Solid state absorption spectra for the **$Ga_4Ln$** complexes.

until below ca. 285 nm (Figure 5.6). In the solution state absorption spectra, no bands that could be assigned to metal or ligand-based charge transfer were identified at lower energies.

Aside from **$Ga_4Eu$**, all of the synthesized **$Ga_4Ln$** complexes exhibit similar absorption spectra indicating that the nature of the lanthanide ion does not affect the electronic properties of the resulting complex (Figure 5.3 and Figure 5.4). In the case of **$Ga_4Eu$**, ligand-to-metal charge transfer (LMCT) can be observed in the solid state absorption spectra as an extension of the band to longer wavelengths (Figure 5.4). The LMCT cannot be observed in the solution UV-Vis spectra due to its low absorption coefficient. However, it is visible in the solid state reflectance experiments due to the yellow color of the **$Ga_4Eu$** sample.[24]

Under excitation at 325 nm in solution ($CD_3OD$) at room temperature, **$Ga_4Gd$** exhibits fluorescence arising from its chromophoric moieties at 367 nm (ca. 27,250 $cm^{-1}$, Figure 5.5; red). Phosphorescence can be observed by recording the signal emitted from **$Ga_4Gd$** in the time-resolved mode in the solid state at 77K upon excitation at 350 nm and using a 200µs delay after the excitation flash (Figure 5.5; blue). The 0-0 component of this band represents the energy level of the ligand's triplet state ($T_1$) which is attributed to the energy level responsible for the main contribution of the energy transfer to the $Ln^{3+}$. The deconvolution of the phosphorescence spectrum (Figure 5.7) shows that the $T_1$ level is located at 451 nm or (ca. 22,170 $cm^{-1}$) which is sufficiently high in energy to populate the excited states of a wide range of visible and NIR-emitting $Ln^{3+}$.[25] However, the energy difference ($\Delta E$) between the donating triplet state of the reported MCs and the accepting main emitting levels of $Tm^{III}$ ($^1G_4$, 21 350 $cm^{-1}$), $Tb^{III}$ ($^5D_4$, 20 400 $cm^{-1}$) and $Dy^{III}$ ($^4F_{9/2}$, 21 100 $cm^{-1}$) is relatively small (<2 300 $cm^{-1}$), suggesting that a back energy transfer processes from the luminescent lanthanide to the chromophoric ligand is possible as discussed below.

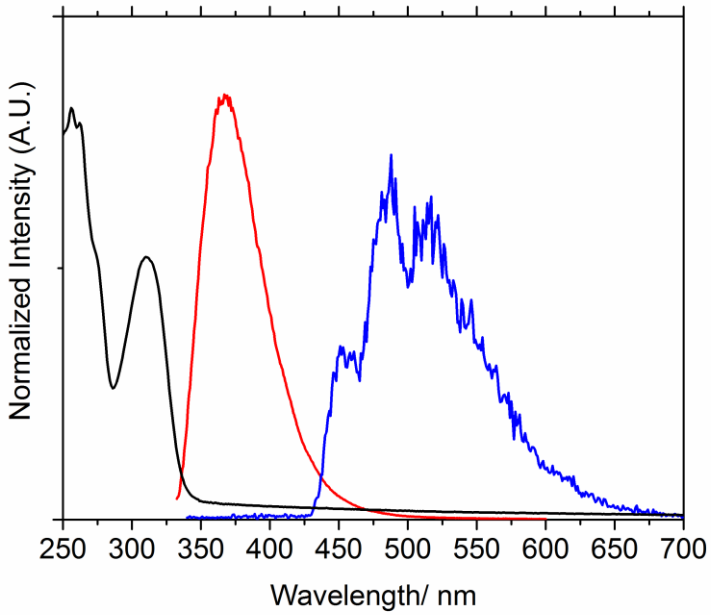


**Figure 5.5.** Ligand based photophysical properties of **$Ga_4Gd$** including the absorption spectrum (black), fluorescence (red; $CD_3OD$, $\lambda_{ex}$ = 325 nm, 298 K, 0 µs delay), and phosphorescence (blue; solid, $\lambda_{ex}$ = 350 nm, 77 K, 200 µs delay).

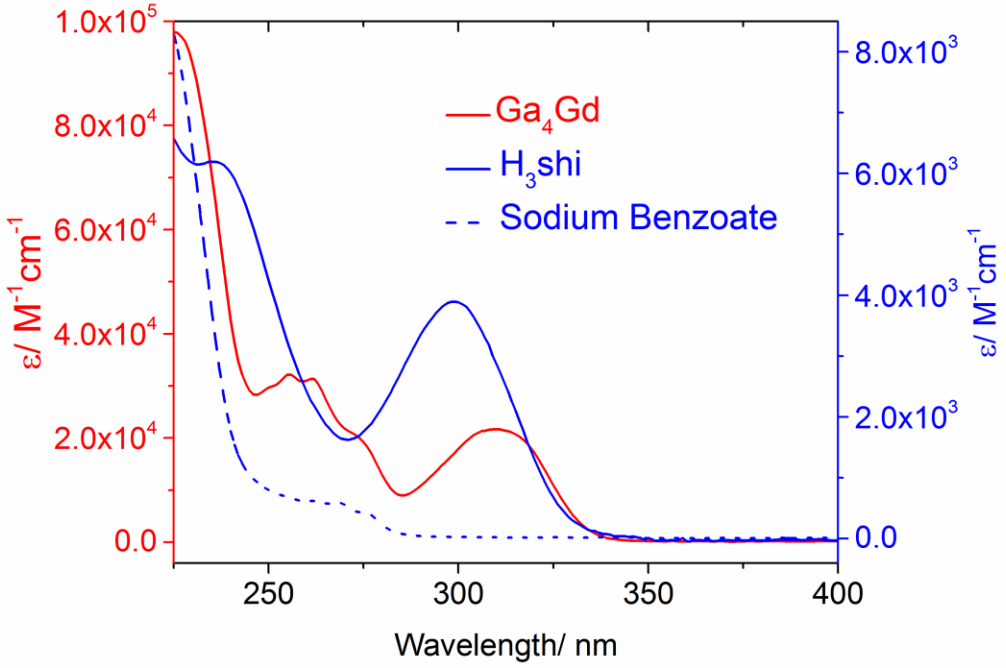


**Figure 5.6.** Solution state absorption spectra of **$Ga_4Gd$** (red), $H_3$shi (blue) and sodium benzoate (blue dashed) in methanol at 298 K.

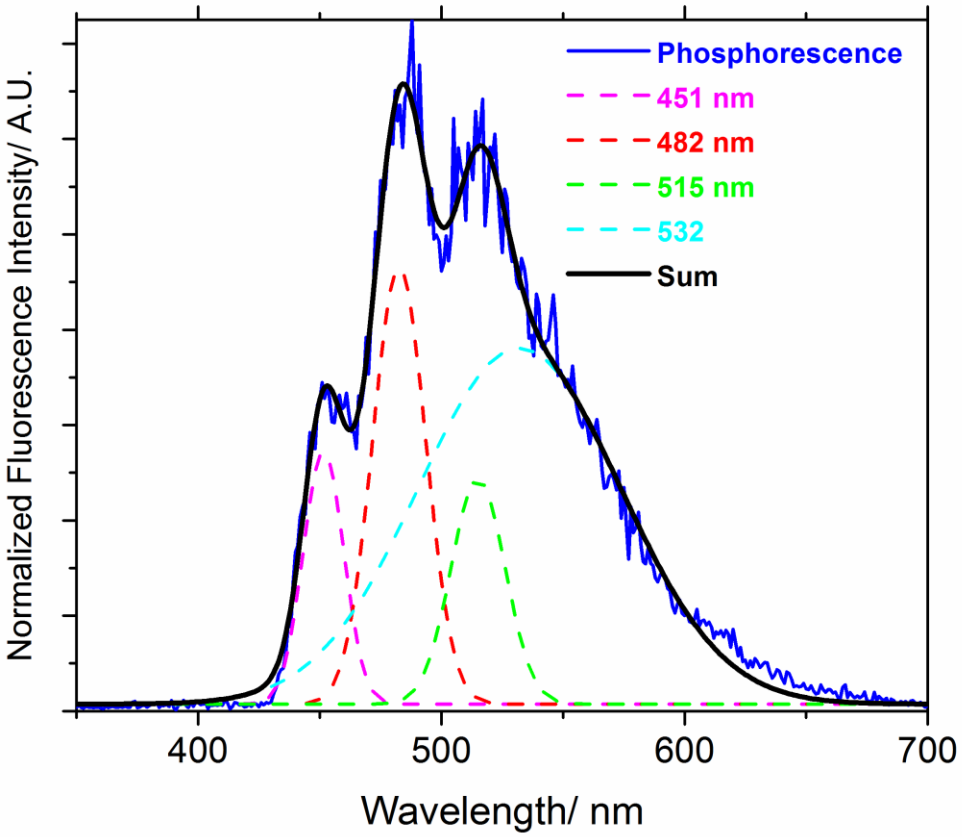


**Figure 5.7.** Deconvolution of the **$Ga_4Gd$** phosphorescence signal for the location of the $T_1$ energy level (451 nm). Phosphorescence (blue), peaks obtained from deconvolution (dashed) and the sum (black).

Emission spectra of **$Ga_4Sm$**, **$Ga_4Eu$**, **$Ga_4Dy$**, **$Ga_4Tb$**, **$Ga_4Ho$**, **$Ga_4Yb$**, and **$Ga_4Er$** were collected in solid state samples (Figure 5.8), and in MeOH or MeOD solutions when possible (Appendix C, Figures C12 to C17). The results of this photophysical study are summarized in Table 5.3. Excitation spectra recorded on solid samples (Appendix C, Figures C1 to C7) and on solutions (Appendix C, Figures C8 to C11) are dominated by broad-bands due to ligand-based $\pi \rightarrow \pi^*$ transitions and have two apparent maxima located at ca. 350 nm and at ca. 325 nm. In addition, fine structure that can be assigned to f-f transitions were observed for the **$Ga_4Dy$**, **$Ga_4Ho$**, and **$Ga_4Er$** samples recorded in the solid state, though they are less pronounced for the

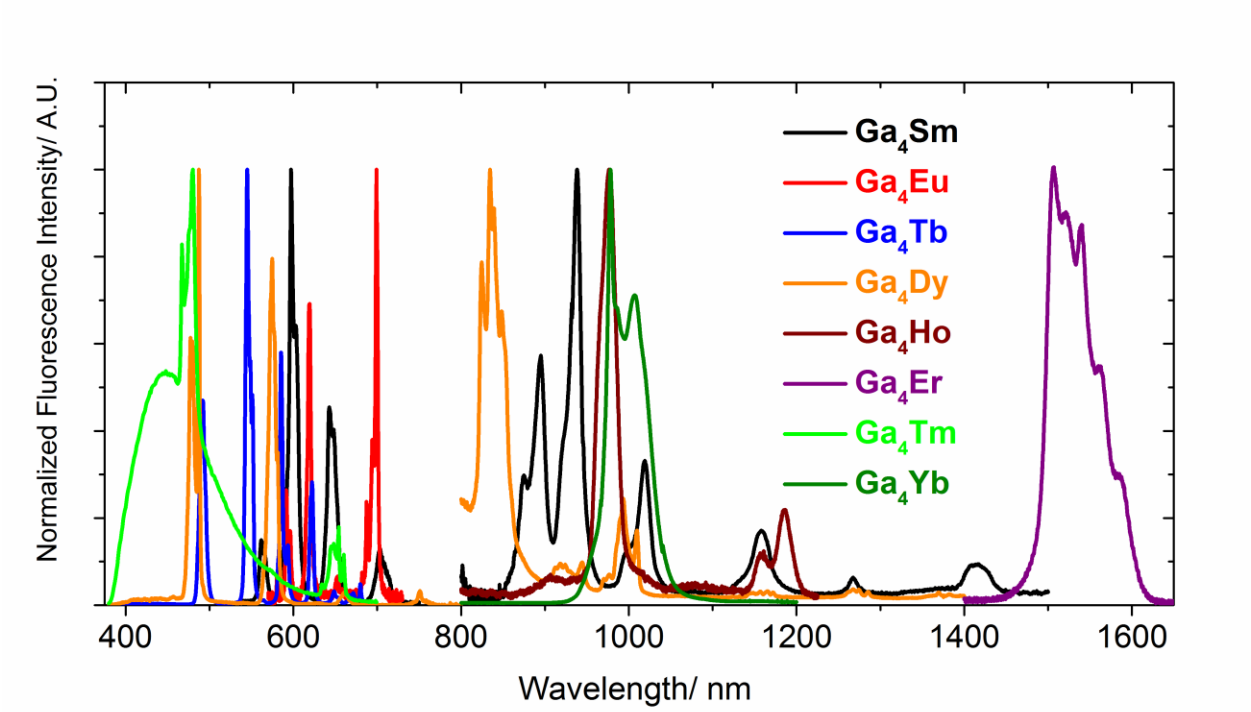


**Figure 5.8.** Solid state emission spectra of the **$Ga_4Ln$** complexes collected at 298 K.

**$Ga_4Tb$**, which has a lower relative fluorescence intensity. These f-f transitions were not observed in solution.

An important parameter that can be obtained from the recording of luminescence lifetimes is the hydration number *q*.[26-27] Reliable estimations have been developed by comparing lifetimes in deuterated and protic solvents for $Tb^{III}$ and $Yb^{III}$ and are summarized in Table 5.3. The hydration number was calculated to be between ca. 0.7 and 1.2 for the range of compounds, indicating that the $Ln^{III}$ is coordinated to one molecule of solvent; such non-zero *q* values are detrimental for the intensity of the luminescence (and to the corresponding quantum yield values) as an indication that the overtone of a vibrations located in molecule of solvent create a route for non-radiative deactivation. As described previously, it is possible that the void space between bridging benzoate molecules may be occupied by a water molecule (Figure 5.1).

**Table 5.3.** Photophysical data for MC complexes. [a] $\Delta E(T–E^{Ln})$ is the energy gap between the ligand triplet state and $Ln^{3+}$ emissive state: $E^{Tm}(^1G_4)$ = 21 350 $cm^{-1}$, $E^{Tb}$ ($^5D_4$) = 20 400 $cm^{-1}$, $E^{Dy}$ ($^4F_{9/2}$) = 21 100 $cm^{-1}$, $E^{Yb}(^2F_{5/2})$ = 10 300 $cm^{-1}$, $E^{Ho}(^5F_5)$ = 15 500 $cm^{-1}$, $E^{Er}(^4I_{13/2})$ = 6 700 $cm^{-1}$. [b] quantum yield reflects the subtraction of the organic based signal; for organic and $Tm^{III}$ emission, $Q$ = 0.12(1). [c] $q_{Tb} = 8.2 * (k_{CH_3OH} - k_{CD_3OD})$ in ms. [d] $q_{Tb} = 10.0 * (k_{CH_3OH} - k_{CD_3OD} - 0.06)$ in ms. [e] $q_{Yb} = 2 * (k_{CH_3OH} - k_{CD_3OD} - 0.1)$ in µs.

| $Ln^{3+}$ complex | State/Solvent | ΔE ($cm^{-1}$)[a] | $\tau_{obs}$ (µs) | $q$ | $Q^L_{Ln}$ (%) (visible) | $Q^L_{Ln}$ (%) (NIR) |
|---|---|---|---|---|---|---|
| **$Ga_4Tm$** | Solid | 820 | 1.47(1) | | 0.02(1)[b] | |
| | $CD_3OD$ | | --- | | | |
| | $CH_3OH$ | | --- | | | |
| **$Ga_4Dy$** | Solid | 1 070 | 21.2(2) | | 2.10(1) | 0.21(1) |
| | $CD_3OD$ | | 25.5(7) | | 0.78(1) | $6.0(1)\cdot10^{-2}$ |
| | $CH_3OH$ | | 12.0(1) | | 0.38(1) | $2.4(1)\cdot10^{-2}$ |
| **$Ga_4Tb$** | Solid | 1 770 | $1.08(1)\cdot10^{3}$ | 1.2[c] | 34.7(1) | --- |
| | $CD_3OD$ | | $1.96(1)\cdot10^{3}$ | 0.9[d] | 28.6(1) | --- |
| | $CH_3OH$ | | $1.51(1)\cdot10^{3}$ | | 23.7(3) | --- |
| **$Ga_4Yb$** | Solid | 11 870 | 55.7(3) | | --- | 5.88(2) |
| | $CD_3OD$ | | 36.6(1) | 0.72[e] | --- | 4.29(1) |
| | $CH_3OH$ | | 2.06(4) | | --- | 0.26(1) |
| **$Ga_4Ho$** | Solid | 6 670 | --- | | --- | $2.0(2)\cdot10^{-3}$ |
| | $CD_3OD$ | | --- | | --- | --- |
| | $CH_3OH$ | | --- | | --- | --- |
| **$Ga_4Er$** | Solid | 15 470 | 6.75(3) | | --- | $4.4(1)\cdot10^{-2}$ |
| | $CD_3OD$ | | 1.74(1) | | --- | $4.5(3)\cdot10^{-2}$ |
| | $CH_3OH$ | | --- | | --- | --- |
| **$Ga_4Sm$** | Solid | 4320 | 148(1) | | 2.46(8) | $4.50(4)\cdot10^{-1}$ |
| | $CD_3OD$ | | 255(1) | | 2.33(5) | $2.98(1)\cdot10^{-1}$ |
| | $CH_3OH$ | | 26.7(1) | | $2.52(2)\cdot10^{-1}$ | $2.65(6)\cdot10^{-2}$ |
| **$Ga_4Eu$** | Solid | 4930 | 242(7): 79%<br>43(2): 21% | | $1.59(4)\cdot10^{-2}$ | --- |
| **$Ga_8Dy_2$** | Solid | 878 | 15.0(1) | | 0.85(1) | 0.01(1) |

The **$Ga_4Eu$** complex exhibited transitions between the $^5D_0$ emitting state to $^7F_{0\text{-}4}$ states between 525 nm and 725 nm (Figure 5.8) in the solid state, which are typical for $Eu^{III}$ compounds.[24] The relatively small quantum yield and luminescent life time observed (Table 5.3) are likely due to the LMCT described previously. The main emitting state for $Sm^{III}$ ions ($^4G_{5/2}$) is only slightly higher in energy than the $^5D_0$ state for $Eu^{III}$. In both the solid state and in solution, the visible emission spectrum for **$Ga_4Sm$** displays $^4G_{5/2} \rightarrow {}^6H_J$ ($J$ = 5/2, 7/2, 9/2 and 11/2) transitions between 550 nm and 750 nm (Figure 5.8; Appendix C, Figure C12). The quantum yields for the visible emission in solution (2.33% in $CD_3OD$) and in the solid state (2.46%) are modest; quantum yields up to 11% have been reported.[28] However, the lifetime in $CD_3OD$ (255 μs) is quite high.[29] Furthermore, the NIR emission corresponding to the $^4G_{5/2} \rightarrow {}^4F_J$ ($J$ = 5/2, 7/2, 9/2 and 11/2) transitions (Figure 5.8; Appendix C, Figure C13) are intense enough to obtain quantum yields in both the solid state and in solution (Table 1), which is rare.

The observation of an emission signal arising from $Tm^{III}$ in molecular complexes that are formed with organic ligands is extremely rare. The emission spectrum obtained for **$Ga_4Tm$** (Figure 5.8) recorded on solid state samples shows two visible characteristic bands originating from the $^1G_4$ energy level and terminating on the $^3H_6$ and $^3F_4$ ground state levels, the signal of this last transition overlaps with a broad organic emission arising from the chromophoric ligand as the result of a not complete ligand to lanthanide energy transfer. The NIR bands of $Tm^{III}$ could not be observed. We could not observe any visible or NIR emission from samples in solution, which could be explained by the presence of quenching processes that bring the emission signal below the limit of detection of our instrument.

The emission spectrum of **$Ga_4Dy$** recorded on solids-sate samples (Figure 5.8) exhibits a number of sharp bands across the visible and NIR regions, originating from electronic transitions

between the excited $^4F_{9/2}$ energy level and the $^6H_J$ (J = 15/2 – 5/2) and $^6F_J$ (J = 11/2 – 1/2) ground state levels. In solution, a residual emission signal from the organic ligands is also observed, indicating an incomplete energy transfer to $Dy^{III}$. Quantum yields recorded for **$Ga_4$Dy** in the visible and the NIR are reported separately in Table 5.3. This result is remarkable as, to the best of our knowledge, this result is the first quantitative report of NIR emission arising from $Dy^{III}$. Relatively strong emission bands resulting from transitions between the $^5D_4$ level and terminating at the $^7F_J$ (J = 6 – 0) ground states are observed for **$Ga_4$Tb** with a quantum yield of 34.7% in the solid state.

The desirable NIR emission from $Ho^{III}$ is extremely rare in systems that contain organic lanthanide sensitizers, with fewer than five reports in the literature.[13, 17, 30-31] Such NIR emission arising from **$Ga_4$Ho** was observed at 965 – 990 nm and is due to the $^5F_5 \rightarrow {}^5I_7$ transition and at 1160 – 1190 nm originating from the $^5I_6 \rightarrow {}^5I_8$ transition. The quantum yield for **$Ga_4$Ho** in the solid-state ($2.0(2)\cdot10^{-3}$ %) is the first quantitative value ever reported and could be obtained as a results of the higher emission intensity. This value is two orders of magnitude larger than other reported quantum yields for complexes in solution. Emission signals in the visible were not observed, nor was it possible to collect an emission spectrum in solution.

An $Yb^{III}$ emission signal was observed with an apparent maximum at 960 nm for **Yb-1** and is attributed to the $^2F_{5/2} \rightarrow {}^2F_{7/2}$ transition. The relatively shorter distance between the $Ln^{III}$ and C-H oscillators in comparison to MCs that we have studied previously[14-15] is expected to result in additional deactivation by quenching through these oscillators. In addition, we have identified an additional source of quenching through the coordination of a solvent molecule due to the insufficient protection of $Ln^{III}$. Surprisingly, the value quantum yield value that we have measured for **$Ga_4$Yb** in the solid state (5.88(2) %) is over 1.5 fold higher than any other

comparable reported quantum yields for $Yb^{III}$ complexes with organic ligands containing C-H bonds. However, in solution, quantum yields are in average values and are significantly lower than those measured in the solid state. These results can be partially explained by the non-zero value of *q* where the deactivation from the solvent will gain importance. From these observations, we can conclude that the intrinsic sensitization efficiency is relatively high for this system, as demonstrated by the relatively high quantum yields in the solid state.

For the $Er^{III}$ complex **Er-1**, the typical long wavelength emission is observed at ca. 1500 – 1600 nm originating from the $^4I_{13/2} \rightarrow {}^4I_{15/2}$ transition. The quantum efficiency of this transition in the solid state is equal or slightly higher than the value observed for previously reported MC complexes, $4.4(1)\cdot10^{-2}$ % versus $4.2(1)\cdot10^{-2}$ %.[14-15] This difference increases when the measurements are performed in deuterated solvent with respective values of $4.5(3)\cdot10^{-2}$ % and $3.60(6)\cdot10^{-2}$ %. *It is important to notice that these values are the highest ever reported in the literature*.

**(ii) $Ga_8Ln_2$ Complexes.** Since the **$Ga_8Ln_2$** dimer compounds are quite insoluble in all solvents, only the solid state photophysical data were collected. As with the **$Ga_4Gd$** compound, the **$Ga_8Gd_2$** complex may be used to examine the ligand based photophysical properties. At room temperature in the solid state and under 350 nm excitation, **$Ga_8Gd_2$** exhibits ligand fluorescence at 393 nm (25445 $cm^{-1}$, Figure 5.9, black). The solid state ligand phosphorescence was obtained at 77 K using an excitation wavelength of 350 nm and a 100 μs delay (Figure 5.9, red). The profile of the phosphorescence is similar to that of **$Ga_4Gd$** (Figure 5.7), which is expected, since both compounds are sensitized by the framework ligand, $H_3$shi. Deconvolution of the phosphorescence spectrum shows that the $^3T_1$ level is located at 455 nm, or 21978 $cm^{-1}$ (Figure 5.10). This triplet state energy is slightly lower than that of the **$Ga_4Gd$** compound

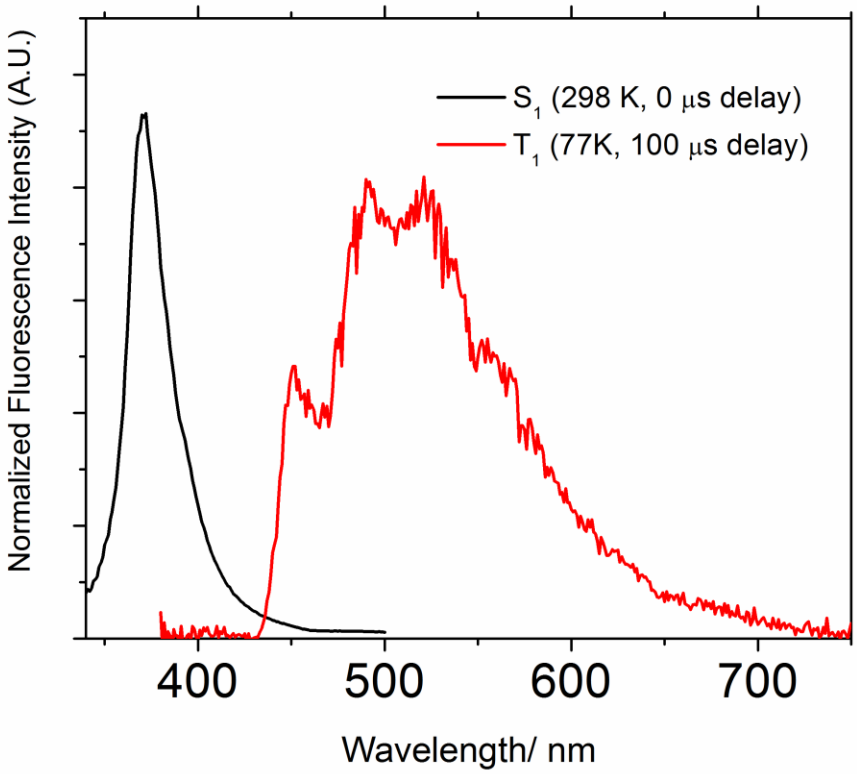


**Figure 5.9.** Ligand based photophysical properties of **$Ga_8Gd_2$** including the ligand fluorescence (black, $\lambda_{ex}$ = 320 nm, 298 K, 0 μs delay), and phosphorescence (red; solid, $\lambda_{ex}$ = 350 nm, 77 K, 100 μs delay).

(22,170 $cm^{-1}$), but still is sufficiently high enough in energy to sensitize the emitting $^4F_{9/2}$ state of $Dy^{III}$ ($\Delta E$ = 878 $cm^{-1}$).

The excitation spectrum for **$Ga_8Dy_2$** ($\lambda_{em}$ = 808 nm) exhibits a profile similar to that of the **$Ga_4Dy$** complex (Appendix C, Figure C4) and has a maximum intensity at 340 nm (Figure 5.11). Using an excitation wavelength of 350 nm, both visible (Figure 5.12) and NIR (Figure 5.13) emission can be observed. The quantum yields for visible and NIR emission were determined to be 0.85(1)% and 0.01%, respectively, with the luminescence lifetime measured at 15.0 μs. These values are smaller than those found for **$Ga_4Dy$** (Table 5.3). This can be explained by an enhanced lanthanide to ligand back energy transfer in **$Ga_8Dy_2$** due to the smaller $\Delta E$.

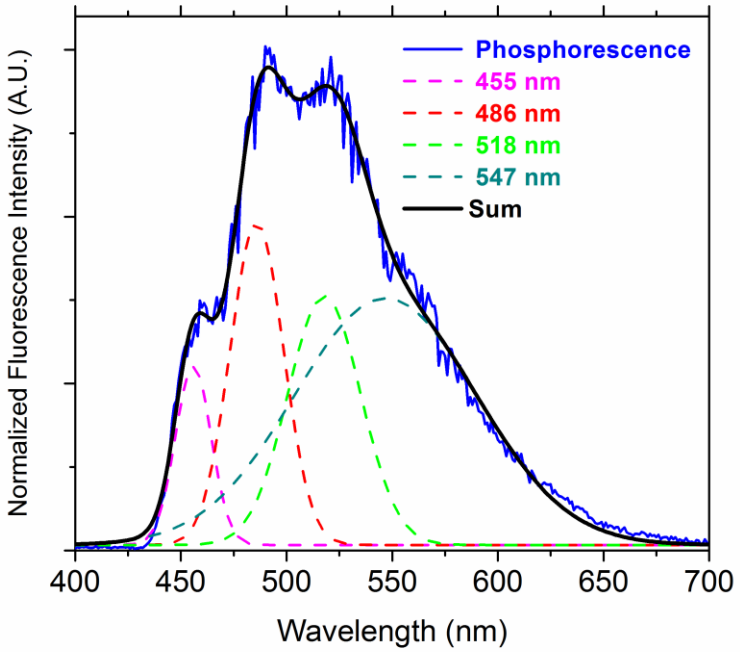


**Figure 5.10.** Deconvolution of the $Ga_8Gd_2$ phosphorescence signal for the location of the $T_1$ energy level (451 nm). Phosphorescence (blue), peaks obtained from deconvolution (dashed) and the sum (black).

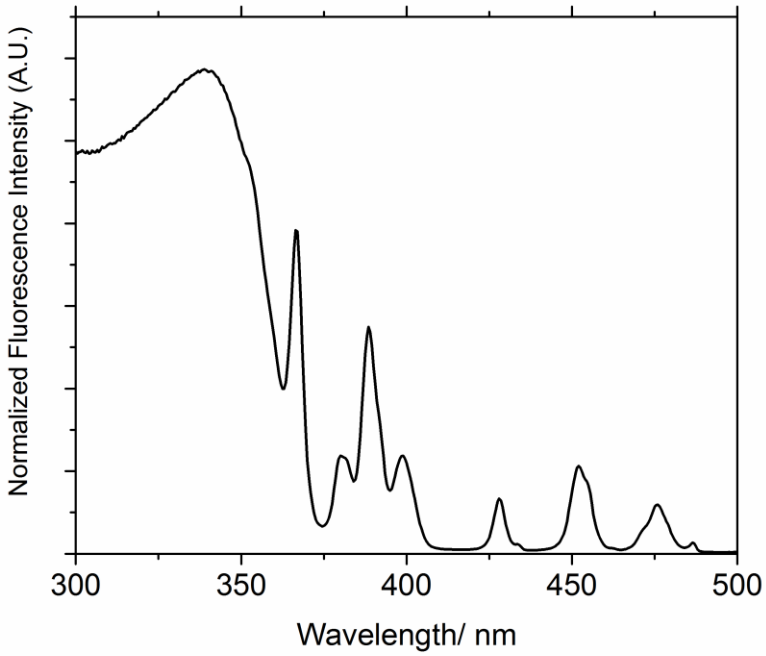


**Figure 5.11.** Excitation spectrum for $Ga_8Dy_2$ at 298 K. $\lambda_{em}$ = 808 nm

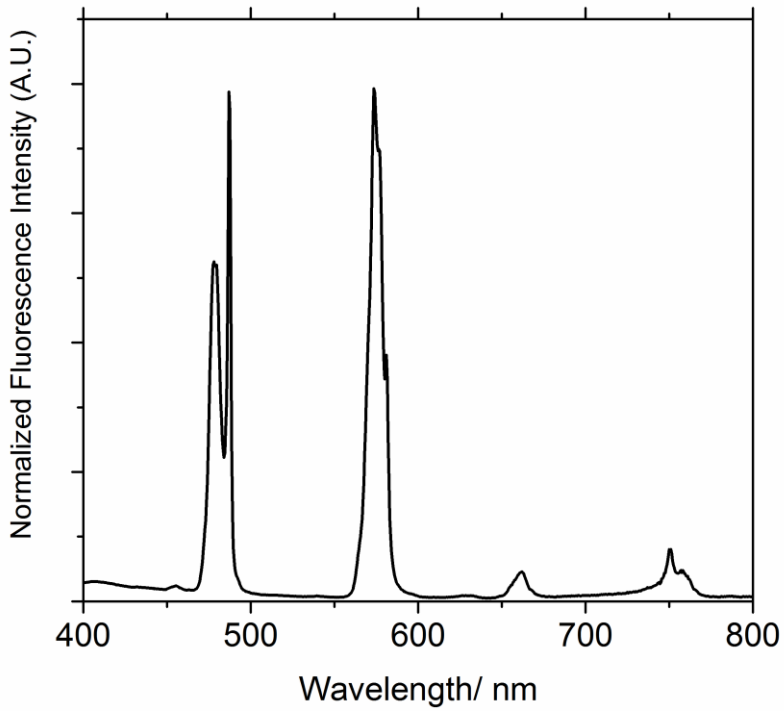


**Figure 5.12.** Visible emission spectrum for **$Ga_8Dy_2$** at 298 K**.** $\lambda_{ex}$ = 350 nm

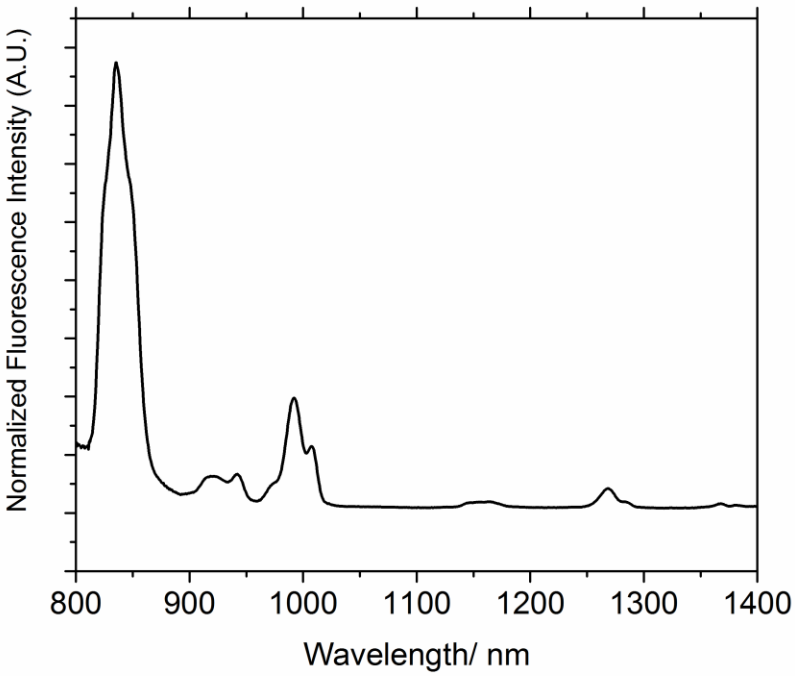


**Figure 5.13.** NIR emission spectrum for **$Ga_8Dy_2$** at 298 K**.** $\lambda_{ex}$ = 350 nm

## 5.4 Conclusions

The work in this Chapter presents a modular metallacrown platform highly efficient for the sensitization of visible and near-infrared lanthanide metal ions. By following basic principles from the metallacrown synthetic strategy, highly luminescent **$Ga_4Ln$** coordination compounds can be obtained by a simple four-component self-assembly synthetic process. The size of the lanthanide has an impact on the formation of the complex as the assembly for $Ln^{III}$ ions larger than $Sm^{III}$ could not be obtained. The electronic structure of the metallacrowns is remarkable in its ability to sensitize several lanthanide cations emitting in the visible ($Eu^{III}$, $Tb^{III}$) and in the near-infrared ($Ho^{III}$, $Er^{III}$, $Tm^{III}$, $Yb^{III}$) or in both ($Sm^{III}$ and $Dy^{III}$). The sensitization of additional NIR emitting lanthanide cations opens new possibilities for multiplex bioanalytical experiments.

Unlike the $LnZn_{16}L_{16}$ sandwich complexes, the protection of the lanthanide cation against non-radiative deactivation is not optimized as indicated by the non-zero hydration number which indicates that the design of the MC could be optimized. The design of these structures localizes the lanthanide cations at the center of the assembly, with the goal of precluding luminescence quenching solvent molecules. However, a pocket between the bridging carboxylates may provide space for a water molecule, as the calculated the *q* value was 1 for the $Tb^{III}$ and $Yb^{III}$ analogues. Nevertheless, the efficient sensitization from the $H_3$shi chromophore to the $Ln^{III}$ leads to highly luminescent visible and NIR emitters. In particular, we have recorded the highest quantum yield values for $Yb^{III}$ and $Er^{III}$ for complexes containing organic ligands. Such results are indicative of a high sensitization efficiency from the chromophoric parts of ligands to the accepting levels of lanthanides which is in line with the observation that quantum yields and luminescence lifetimes are all higher in the solid state than they are in the solution phase. Therefore, there is room for

improvement of the luminescence properties through a modification of this MC providing a better protection to the lanthanide cations.

The **$Ga_8Dy_2$** dimer compound exhibited lower quantum yields and luminescent lifetimes than the **$Ga_4Ln$** monomer complex. This is possibly due to the smaller energy gap between the excited $T_1$ state of the ligand and the emitting $^4F_{9/2}$ state $Dy^{III}$ (878 $cm^{-1}$ and 1070 $cm^{-1}$ for **$Ga_8Dy_2$** and **$Ga_4Dy$**, respectively. This also suggests that the carboxylate bridging ligand may have an effect on the triplet state energy of the $shi^{3-}$ antenna. The work presented in this Chapter provides model systems which efficiently sensitizes a wide range of $Ln^{III}$. The simplicity and synthetic reliability of the 12-MC-4 system provides ample opportunity to modulate structural features such as the framework and bridging ligands, in order to tune both the photophysical parameters and physical properties such as solution integrity and solubility.

## References


1. Verwilst, P.; Eliseeva, S. V.; Vander Elst, L.; Burtea, C.; Laurent, S.; Petoud, S.; Muller, R. N.; Parac-Vogt, T. N.; De Borggraeve, W. M. *Inorg. Chem.* **2012**, *51*, 6405-6411.
2. Bonnet, C. S.; Buron, F.; Caille, F.; Shade, C. M.; Drahos, B.; Pellegatti, L.; Zhang, J.; Villette, S.; Helm, L.; Pichon, C.; Suzenet, F.; Petoud, S.; Toth, E. *Chem. Eur. J.* **2012**, *18*, 1419-1431.
3. Foucault-Collet, A.; Gogick, K. A.; White, K. A.; Villette, S.; Pallier, A.; Collet, G.; Kieda, C.; Li, T.; Geib, S. J.; Rosi, N. L.; Petoud, S. *Proc. Natl. Acad. Sci. U. S. A.* **2013**, *110*, 17199-17204.
4. Suffren, Y.; Zare, D.; Eliseeva, S. V.; Guenee, L.; Nozary, H.; Lathion, T.; Aboshyan-Sorgho, L.; Petoud, S.; Hauser, A.; Piguet, C. *J. Phys. Chem. C* **2013**, *117*, 26957-26963.
5. Zhang, Q. Y.; Huang, X. Y. *Prog. Mater. Sci.* **2010**, *55*, 353-427.
6. Van Der Ende, B. M.; Aarts, L.; Meijerink, A. *PCCP* **2009**, *11*, 11081-11095.
7. Suzuki, H. *J. Photochem. Photobiol., A* **2004**, *166*, 155-161.
8. Bunzli, J. C. G.; Eliseeva, S. V. *J. Rare Earth* **2010**, *28*, 824-842.
9. Bunzli, J. C. G.; Comby, S.; Chauvin, A. S.; Vandevyver, C. D. B. *J. Rare Earth* **2007**, *25*, 257-274.
10. Biju, S.; Gopakumar, N.; Bunzli, J. C. G.; Scopelliti, R.; Kim, H. K.; Reddy, M. L. P. *Inorg. Chem.* **2013**, *52*, 8750-8758.
11. Petoud, S.; Muller, G.; Moore, E. G.; Xu, J. D.; Sokolnicki, J.; Riehl, J. P.; Le, U. N.; Cohen, S. M.; Raymond, K. N. *J. Am. Chem. Soc.* **2007**, *129*, 77-83.
12. Caille, F.; Bonnet, C. S.; Buron, F.; Villette, S.; Helm, L.; Petoud, S.; Suzenet, F.; Toth, E. *Inorg. Chem.* **2012**, *51*, 2522-2532.
13. Zhang, J.; Badger, P. D.; Geib, S. J.; Petoud, S. *Angew. Chem. Int. Ed.* **2005**, *44*, 2508-2512.
14. Jankolovits, J.; Andolina, C. M.; Kampf, J. W.; Raymond, K. N.; Pecoraro, V. L. *Angew. Chem., Int. Ed.* **2011**, *50*, 9660-9664.
15. Trivedi, E. R.; Eliseeva, S. V.; Jankolovits, J.; Olmstead, M. M.; Petoud, S.; Pecoraro, V. L. *J. Am. Chem. Soc.* **2014**, *136*, 1526-1534.
16. Biju, S.; Eom, Y. K.; Bunzli, J. C. G.; Kim, H. K. *J. Mater. Chem. C* **2013**, *1*, 3454-3466.
17. Law, G. L.; Pham, T. A.; Xu, J. D.; Raymond, K. N. *Angew. Chem. Int. Ed.* **2012**, *51*, 2371-2374.
18. Al-Nahhas, A.; Win, Z.; Szyszko, T.; Singh, A.; Nanni, C.; Fanti, S.; Rubello, D. *Anticancer Res.* **2007**, *27*, 4087-4094.
19. Jonkhoff, A. R. P., M. A.; Ossenkoppele, G. J.; Teule, G. J.; Huijgens P. C. *Br. J. Cancer* **1995**, *72*, 1541-1546.
20. Mariani, G. B., L.; Adelstein, S. J.; Kassis, A. I. *J. Nuc. Med.* **2000**, *41*, 1519-1521.
21. Corporation, R. *Crystalclear 2.0*, Tokyo, Japan.
22. Sheldrick, G. M. *Acta. Cryst.* **2008**, *A64*, 112-122.
23. Spek, A. L., Platon, A Multipurpose Crystallographic Tool. Utrecht University; Utrecht, The Netherlands, 2001.
24. Pasatoiu, T. D.; Madalan, A. M.; Kumke, M. U.; Tiseanu, C.; Andruh, M. *Inorg. Chem.* **2010**, *49*, 2310-2315.
25. Bunzli, J.-C. G.; Piguet, C. *Chem. Soc. Rev.* **2005**, *34*, 1048-1077.
26. Beeby, A.; M. Clarkson, I.; S. Dickins, R.; Faulkner, S.; Parker, D.; Royle, L.; S. De Sousa, A.; A. G. Williams, J.; Woods, M. *J. Chem. Soc., Perkin Trans. 2* **1999**, 493-504.
27. Faulkner, S.; Beeby, A.; Carrié, M.-C.; Dadabhoy, A.; Kenwright, A. M.; Sammes, P. G. *Inorg. Chem. Commun.* **2001**, *4*, 187-190.
28. Regulacio, M. D.; Pablico, M. H.; Vasquez, J. A.; Myers, P. N.; Gentry, S.; Prushan, M.; Tam-Chang, S.-W.; Stoll, S. L. *Inorg. Chem.* **2008**, *47*, 1512-1523.
29. Law, G.-L.; Pham, T. A.; Xu, J.; Raymond, K. N. *Angew. Chem. Int. Ed.* **2012**, *51*, 2371-2374.

30. Moore, E. G.; Szigethy, G.; Xu, J.; Palsson, L.-O.; Beeby, A.; Raymond, K. N. *Angew. Chem. Int. Ed.* **2008**, *47*, 9500-9503.
31. Quici, S.; Cavazzini, M.; Marzanni, G.; Accorsi, G.; Armaroli, N.; Ventura, B.; Barigelletti, F. *Inorg. Chem.* **2005**, *44*, 529-537.

# Chapter VI

# Conclusions and Future Directions

Supramolecular assembly can be considered the Wild West of chemical research. A search on the Cambridge Crystallographic Database reveals that there are 14 different crystal structures (including several unreported by Boron[1]) containing the ligand $H_3$shi and a metal ion.[2] These structures, along with the $H_3$shi-based compounds reported in this thesis exemplify the structural promiscuity of the metallacrown type ligands. Certainly, predictable structure types such as the 9-MC-3 (with $Fe^{III}$) and 12-MC-4 (with $Ga^{III}$ and $Mn^{III}$) can be reliably formed under the appropriate crystallization conditions. Nonetheless, serendipity reveals itself in the $\mathbf{M_4Ln_2}$ compounds described in Chapters II and III and also $\mathbf{Mn_6Ln_2(shi^{3-})_7(H_2shi^{-})_2}$ (Figure 6.1) and $\mathbf{Ga_4Ln(shi^{3-})_4(H_2shi^{-})_2}$ (Figure 6.2) compounds that have been synthesized over the course of this thesis, but have not been reported in the previous chapters. Though, even in the apparent randomness of the structures, there are still elements of metallacrown design in these complexes; 12-MC-4 fragments are present in the structures in Figures 6.1 and 6.2. However, with so much uncertainty involved, is it truly possible to 'design' a coordination complex for a specific application? The underlying goals of this thesis are not simply the synthesis of novel complexes, but to also explore different avenues of study for existing materials.

In recent literature, the two most common approaches to designing SMMs are to (i) control the ligand field around the metal ion(s) to maximize molecular anisotropy and (ii) link the metals in such a way that optimizes magnetic interactions. While the metallacrown

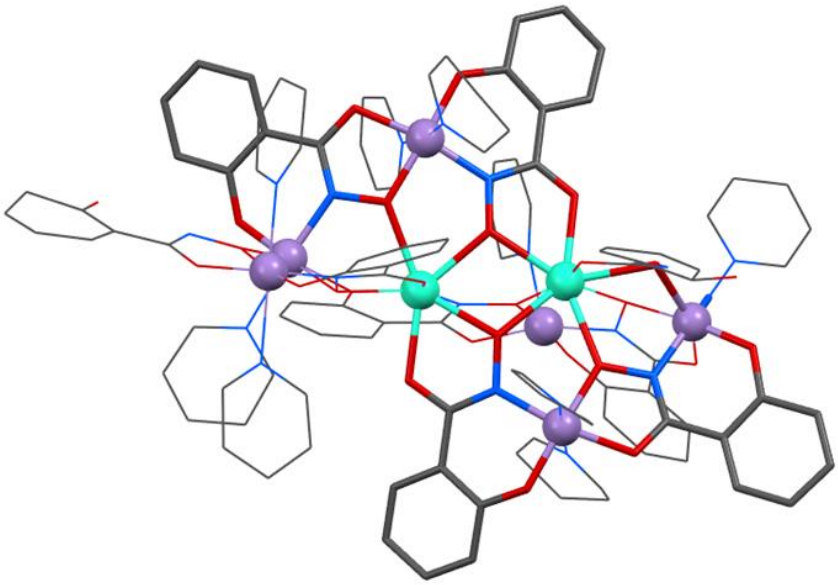

**Figure 6.1.** Crystal structure of **$Mn_6Dy_2(shi^{3-})_7(H_2shi^{-})_2$**. Teal spheres - $Dy^{III}$; purple spheres – $Mn^{III}$; gray – C; red – O; blue – N. Hydrogens and lattice solvent were removed for clarity. In bold are two 12-MC-4 fragments which have merged to form the molecular plane.

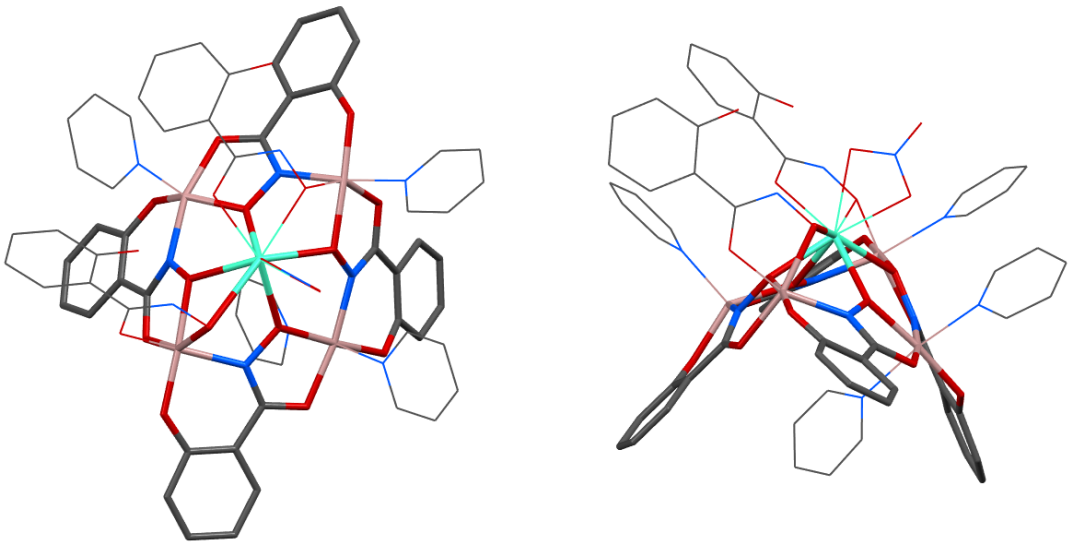

**Figure 6.2.** Crystal structure of **$Ga_4Ln(shi^{3-})_4(H_2shi^{-})_2$**. Teal - $Dy^{III}$; tan – $Ga^{III}$; gray – C; red – O; blue – N. Hydrogens and lattice solvent were removed for clarity. In bold is a bent 12-MC-4 core structure.

strategy offers a measure of control over ligand field geometry,[3] there has to fore not been a definitive description of how metallacrowns can optimize magnetic interactions. Thus, the focus of this thesis is the evaluation of how metal-metal interactions can affect slow magnetic relaxation in lanthanide metallacrown complexes. It has been proposed that strong magnetic exchange can aide in the suppression of quantum tunneling,[4] and much of the current research has involved strengthening this interaction in polynuclear lanthanide complexes.[5-7]

The **$Ga_4Ln_2$** complexes described in Chapter II were good candidates to study the effects of $Ln^{III}$-$Ln^{III}$ magnetic exchange. The short $Ln^{III}$-$Ln^{III}$ distances (~3.8 Å) and coupling through hydroximate oxygens allowed for potential dipolar and superexchange pathways. The **$Ga_4Dy_2$** analogue exhibited relaxation behavior originating from the decoupled $Dy^{III}$ ions (26 K) and from the *excited ferromagnetic state* (18 K). This finding was remarkable, as to our knowledge, there have not been any reports of multiple relaxation processes in polynuclear $Ln^{III}$ complexes containing symmetrically equivalent $Ln^{III}$ ions. A combination of computation micro-SQUID studies and magnetic dilution experiments corroborated the above results. In Chapter III, the study of mixed *3d*/*4f* metallacrown complexes showed that antiferromagnetic *3d-4f* coupling effectively quenched SMM behavior due to the creation of low-lying excited states.

Considering these findings, what does it mean for the future of SMM research? Simply put, there is still much work to be done. The results presented in this thesis have shown that both *4f-4f* and *3d-4f antiferromagnetic* coupling has an adverse effect on slow magnetic relaxation. However, the Powell group has garnered evidence that *ferromagnetic 3d-4f* interactions in a $Dy^{III}Fe^{II}_2$ SMM is crucial to increasing the anisotropic barrier height.[8] Practically speaking, however, inducing ferromagnetic interactions in coordination compounds will be very difficult, especially for $Ln^{III}$ based complexes. The major limitation of lanthanide-based SMMs is the

prevalence of nuclear spin driven quantum tunneling.[9-10] To mitigate this effect, strategies such as modifying the first-coordination sphere of the $Ln^{III}$ ions[11-12] and coupling $Ln^{III}$ ions through radicals[7] have been employed, though only a few lanthanide SMMs display high temperature, high coercive field magnetic hysteresis. Transition metal SMMs have been shown to exhibit hysteresis with large coercive fields,[13-14] though these materials are limited by low energy barriers. A current trend in the literature is the use of $Co^{II}$ ions, due to their potential for large magnetoanisotropy.[15-17] It is quite apparent that the SMM field is still at a nascent stage of development, and all potential possibilities should be pursued. For instance, mixed $Ln^{III}$ complexes have not been extensive studied, due to difficulties in synthesis. A $\mathbf{Ga_4Er_{1.8}Dy_{0.2}}$ complex may be of interest to see how oblate-prolate lanthanide interactions may affect slow relaxation. This compound could also potentially lead to ferromagnetic exchange interaction, as is the case in the pure $Er^{III}$ derivative.

Often a by-product of SMM research, ideal MCE materials have weak ferromagnetic interactions leading to a high ground *S* state and low molecular anisotropy.[18] Similar to SMMs, the control of magnetic interactions is necessary to achieve high performance materials. A drawback of the metallacrown motif is that the -N-O- linking unit generally leads to antiferromagnetic interactions, which was problematic in the mixed *3d*/*4f* SMM complexes described in Chapter III. Although it is difficult to design ferromagnetic coupling in molecular materials, careful consideration of both the number and spatial arrangement of the metal ions may lead to high spin *ferrimagnetic* materials which display significant MCE. As described in Chapter IV, the **$Fe_4$OAc** complex displayed a significant MCE at 3 K, with $-\Delta S_m$ = 15.4 J $kg^{-1}$ $K^{-1}$ and $-\Delta S_m$ = 11.2 J $kg^{-1}$ $K^{-1}$ at $\Delta H$ = 7 T and $\Delta H$ = 3 T, respectively. These values are comparable to those of much higher nuclearity iron(III) clusters.[19] This suggests that, although

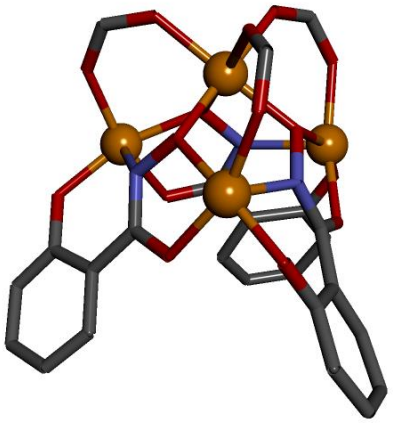

**Figure 6.3.** Structure of the proposed $Fe^{III}$(formate)$_3$[9-$MC_{Fe^{III}N(shi)}$-3] complex.

antiferromagnetic interactions are dominant in metallacrown complexes, careful molecular design can lead to ferrimagnetic complexes with significant MCE.

A formate-bridged $Fe_4$ compound (Figure 6.3) may potentially be a good candidate to improve the MCE of the $Fe_4$ system. In Chapter VI, the bridging ligand with the lower $pK_a$, benzoate, also had the larger $J_2/J_1$ ratio (closer to the ideal value of 0.333). If this trend continues, then formate, which has a lower $pK_a$ than both acetate or benzoate, should have the largest $J_2/J_1$ ratio and be closest to the ideal value. It should be stated that coupling is highly dependent on bond lengths and angles,[20] though these parameters are quite difficult to control. Formate would also be an advantageous ligand because its lower molecular weight would increase the metal : ligand weight ratio, and the lack of aryl moieties may preclude strong intermolecular interactions. Development of materials with large MCE properties may ultimately require inducing ferromagnetic interactions. In a recent report, a ferromagnetically coupled $Fe_{42}$ cyanide-bridged complex was found to have a ground spin state $S$ = 45.[21] Thus, linking metallacrown clusters through cyanide groups may be a potential route towards higher spin complexes.

In SMM and MCE research, emphasis is placed on controlling the first-coordination sphere and spatial arrangement of metal centers, in order to induce favorable magnetic

anisotropy and coupling. Ligand-based electronic properties have been found to have only a small effect in the $Mn_{12}$ derivatives[14] and has largely been ignored in the SMM literature. On the other hand, for research in luminescent lanthanide complexes, the reverse is true; the electronic properties of the antenna ligands are crucial to lanthanide sensitization and eliminating vibrational quenching from solvent molecules is necessary for efficient energy transfer. In this regard, metallacrowns are perhaps better suited for applications in luminescence rather than as molecular nanomagnets. The aryl hydroxamate ligands have excited triplet states which are a good energy match for the emitting states of $Ln^{III}$ ions and MC complexes have a tendency to encapsulate the $Ln^{III}$ ions.[3, 22-24] Moreover, MCs are also quite amenable to ligand substitution, which allows for the tuning of both physical and photophysical properties.

As an extension to the work of Jankolovits[23] and Trivedi[24], the **$Ga_4Ln$** 12-MC-4 complexes were synthesized and have shown the ability to sensitize both visible and NIR lanthanides (ranging from $Sm^{III}$ to $Yb^{III}$) with notable efficiency. The efficiency of the energy transfer from the ligand $T_1$ state to the $Ln^{III}$ emitting states was high enough such that these complexes exhibit some of the highest luminescence quantum yields and lifetimes reported in the literature. Examination of the **$Ga_8Ln_2$** dimer complexes have shown that even though the $T_1$ state is based on the $shi^{3-}$ ligands, the identity of the bridging carboxylate can affect luminescent properties. These results show that the 12-MC-4 motif presents an effective, modular platform on which to design highly luminescent lanthanide complexes.

In the evolution of the luminescent $LnZn_{16}Ln_{16}$ complexes, ligand substitutions were employed to both redshift the absorption profile and enhance the water solubility, in order to make them useful for practical bio-imaging applications.[23-24,25] Similar modifications could potentially be made the above mentioned 12-MC-4 systems; the ability to sensitize both visible

and NIR lanthanides make for a particularly attractive target. More fundamentally, metallacrown based complexes may give insight into how the 3-dimensional arrangement of the antenna ligands around the $Ln^{III}$ will affect sensitization. For instance, how would the photophysical properties of other compounds formed with $H_3$shi (such as in Figure 6.2) compare with the more planar **$Ga_4Ln$** complexes?

To borrow a phrase from biology, the central dogma of metallacrown research is the innate capacity for the systematic substitution of ligands, metals and counter-ions in MC complexes, while still retaining the core structure. In Chapters II and III, the metallacrown ring metals were substituted with diamagnetic ($Ga^{III}$) and paramagnetic ($Mn^{III}$, $Fe^{III}$) to better understand *3d-4f* interactions. In the studies of the MCE and luminescent materials, ligand substitution was employed to modulate magnetic and photophysical parameters. The compounds described in this thesis are simple, yet highly modular in nature. Based on the previous studies and the work presented in this thesis, it is clear that metallacrowns offer great potential in both fundamental and applied research.

## References


1. Boron, T. T. Control of Single-Molecule Magnetic Properties Using Metallacrowns. University of Michigan, Ann Arbor, 2012.
2. Accessed March 30, 2015.
3. Mezei, G.; Zaleski, C. M.; Pecoraro, V. L. *Chem. Rev.* **2007**, *107*, 4933-5003.
4. Wernsdorfer, W.; Aliaga-Alcalde, N.; Hendrickson, D. N.; Christou, G. *Nature* **2002**, *416*, 406-409.
5. Rinehart, J. D.; Fang, M.; Evans, W. J.; Long, J. R. *J. Am. Chem. Soc.* **2011**, *133*, 14236-14239.
6. Rinehart, J. D.; Fang, M.; Evans, W. J.; Long, J. R. *Nat. Chem.* **2011**, *3*, 538-542.
7. Demir, S.; Jeon, I.-R.; Long, J. R.; Harris, T. D. *Coord. Chem. Rev.* **2015**, *289–290*, 149-176.
8. Liu, J.-L.; Wu, J.-Y.; Chen, Y.-C.; Mereacre, V.; Powell, A. K.; Ungur, L.; Chibotaru, L. F.; Chen, X.-M.; Tong, M.-L. *Angew. Chem. Int. Ed.* **2014**, n/a-n/a.
9. Ishikawa, N.; Sugita, M.; Wernsdorfer, W. *J. Am. Chem. Soc.* **2005**, *127*, 3650-3651.
10. Ishikawa, N.; Sugita, M.; Wernsdorfer, W. *Angew. Chem. Int. Ed.* **2005**, *44*, 2931-2935.
11. Wang, H.; Wang, K.; Tao, J.; Jiang, J. *Chem. Commun.* **2012**, *48*, 2973-2975.
12. Aldamen, M. A.; Clemente-Juan, J. M.; Coronado, E.; Martí-Gastaldo, C.; Gaita-Ariño, A. *J. Am. Chem. Soc.* **2008**, *130*, 8874-8875.
13. Milios, C. J.; Inglis, R.; Bagai, R.; Wernsdorfer, W.; Collins, A.; Moggach, S.; Parsons, S.; Perlepes, S. P.; Christou, G.; Brechin, E. K. *Chem. Commun.* **2007**, 3476-3478.
14. Bagai, R.; Christou, G. *Chem. Soc. Rev.* **2009**, *38*, 1011-1026.
15. Ruamps, R.; Batchelor, L. J.; Guillot, R.; Zakhia, G.; Barra, A.-L.; Wernsdorfer, W.; Guihery, N.; Mallah, T. *Chem. Sci.* **2014**, *5*, 3418-3424.
16. Murrie, M. *Chem. Soc. Rev.* **2010**, *39*, 1986-1995.
17. Zadrozny, J. M.; Long, J. R. *J. Am. Chem. Soc.* **2011**, *133*, 20732-20734.
18. Sessoli, R. *Angew. Chem. Int. Ed.* **2012**, *51*, 43-45.
19. Liu, J.-L.; Chen, Y.-C.; Guo, F.-S.; Tong, M.-L. *Coord. Chem. Rev.* **2014**, *281*, 26-49.
20. Kahn, O., *Molecular Magnetism*. VCH Publishers, Inc.: New York, 1993.
21. Kang, S.; Zheng, H.; Liu, T.; Hamachi, K.; Kanegawa, S.; Sugimoto, K.; Shiota, Y.; Hayami, S.; Mito, M.; Nakamura, T.; Nakano, M.; Baker, M. L.; Nojiri, H.; Yoshizawa, K.; Duan, C.; Sato, O. *Nat Commun* **2015**, *6*.
22. Azar, M. R.; Boron, T. T.; Lutter, J. C.; Daly, C. I.; Zegalia, K. A.; Nimthong, R.; Ferrence, G. M.; Zeller, M.; Kampf, J. W.; Pecoraro, V. L.; Zaleski, C. M. *Inorg. Chem.* **2014**, *53*, 1729-1742.
23. Jankolovits, J.; Andolina, C. M.; Kampf, J. W.; Raymond, K. N.; Pecoraro, V. L. *Angew. Chem., Int. Ed.* **2011**, *50*, 9660-9664.
24. Trivedi, E. R.; Eliseeva, S. V.; Jankolovits, J.; Olmstead, M. M.; Petoud, S.; Pecoraro, V. L. *J. Am. Chem. Soc.* **2014**, *136*, 1526-1534.
25. Unpublished work by Dr. Tu Nguyen

# Appendices

# Appendix A

# Computational Details

**Table A1.** SHAPE analysis of compound **$Ga_4Dy_2$**.

| OP ($D_{8h}$) | HPY ($C_{7v}$) | HPBY ($D_{6h}$) | CU ($O_h$) | SAPR ($D_{4d}$) | TDD ($D_{2d}$) | JGBF ($D_{2d}$) | JETBPY ($D_{3h}$) | JBTP ($C_{2v}$) | BTPR ($C_{2v}$) | JSD ($D_{2d}$) | TT ($T_d$) | TBPY ($D_{3h}$) |
|---|---|---|---|---|---|---|---|---|---|---|---|---|
| 31.549 | 24.076 | 15.088 | 13.16 | 3.463 | **1.131** | 11.071 | 27.127 | 3.008 | 2.61 | 2.365 | 13.686 | 24.070 |

Abbreviations: OP – Octagon, HPY – Heptagonal pyramid, HBPY – Hexagonal bipyramid, CU – Cube, SAPR – Square antiprism, TDD – Triangular dodecahedron, JGBF – Johnson – Gyrobifastigium, JETBPY – Johnson Elongated triangular bipyramid, JBTP – Johnson Biaugmented trigonal prism, BTPR – Biaugmented trigonal prism, JSD – Snub disphenoid, TT – Triakis tetrahedron, ETBPY – Elongated trigonal pyramid

**Table A2:** Energy gaps and g factors of the lowest states of $GdLuGa_4$.

| Kramers Doublet | $\Delta E$ ($cm^{-1}$) | $g_i$ |
|---|---|---|
| 1 | 0 | 13.92 ; 0.03 ; 0.02 |
| 2 | 1.0 | 9.64 ; 1.15 ; 0.98 |
| 3 | 1.6 | 6.07 ; 5.39 ; 4.45 |
| 4 | 2.1 | 13.10 ; 1.40 ; 0.75 |
| 5 | 40600 | |

**Table A3:** Energy in $cm^{-1}$ of the states of **$Ga_4Gd_2$** issued from the ground spin octuplet of the monomers**.** The first line with J=0 considers only dipolar interaction.

| | |
|---|---|
| E with J=0 | -0.72;-0.72;-0.62;-0.62;-0.53;-0.46;-0.46;-0.41;-0.41;-0.41;-0.41;-0.37;-0.37;-0.34;-0.34;-0.34<br>-0.31;-0.31;-0.22;-0.22;-0.16;-0.16;-0.15;-0.15;-0.12;-0.12;-0.09;-0.09;-0.08;-0.04; ; -0.04;<br>0.04;0.04;0.08;0.08;0.09;0.09;0.12;0.12;0.13;0.13;0.19;0.19;0.25;0.25;0.27;0.27;0.29;<br>0.29;0.30;0.40;0.40;0.40;0.40;0.43;0.43;0.45;0.50;0.57;0.57;0.58;0.58;0.75;0.75 |
| E with J=-0.16 $cm^{-1}$ | -2.67;-2.58;-2.58;-2.33;-2.33;-2.08;-1.92;-1.92;-1.92;-1.92;-1.62;-1.56;-1.56;-1.35;-1.35;<br>-1.29;-1.29;-1.15;-1.02;-1.02;-0.77;-0.77;-0.64;-0.64;-0.60;-0.60;-0.53;-0.33;-0.33;-0.07;-0.07;<br>0.11;0.11;0.21;0.21;0.22;0.22;0.26;0.52;0.52;0.77;0.77;0.97;0.97;1.12;1.12;1.21;1.21;1.21;1.21;<br>1.24;1.52;1.52;1.78;1.78;2.00;2.00;2.17;2.17;2.29;2.29;2.36;2.36;2.38 |

**Table A4.** Energy gaps and g factors of the lowest Kramer Doublets of $DyLuGa_4$.

| Kramer Doublets | $\Delta E$ ($cm^{-1}$) | $g_i$ |
|---|---|---|
| 1 | 0 | 19.47 ; 0.08 ; 0.04 |
| 2 | 153 | 15.75 ; 0.35 ; 0.66 |
| 3 | 241 | 14.09 ;1.09 ; 1.39 |
| 4 | 272 | 12.05 ; 6.15 ; 2.52 |
| 5 | 329 | 8.86 ; 4.01 ; 1.04 |
| 6 | 341 | 10.34 ; 5.68 ; 1.33 |

**Table A5:** Energy in $cm^{-1}$ of the states of $\mathbf{Ga_4Dy_2}$ issued from the ground Kramer's doublet of the monomers. The first column with J = 0 considers only dipolar interaction.

| states | E with J = 0 | E with $J_{exc}$ = –0.29 $cm^{-1}$ |
|---|---|---|
| $\vert + + \rangle \vert - - \rangle$ | -0.63 | -2.36 |
| $\vert + - \rangle \vert - + \rangle$ | 0.63 | 2.36 |

**Table A6.** Energy gaps and g factors of the lowest doublets of $TbLuGa_4$.

| Non Kramer doublets | $\Delta E$ ($cm^{-1}$) | $g_i$ |
|---|---|---|
| 1-2 | 0 ; 0.2 | 17.85 ; 0.00 ; 0.00 |
| 3-4 | 83 ; 85 | 16.82 ; 0.00 ; 0.00 |
| 5-6 | 148 ; 160 | 12.47 ; 0.00 ; 0.00 |
| 7-8 | 228 ; 240 | 8.80 ; 0.00 ; 0.00 |
| 9 | 278 | |
| 10-11 | 334 ; 344 | 16.44 ; 0.00 ; 0.00 |
| 12-13 | 432 ; 433 | 16.86 ; 0.00 ; 0.00 |
| 14-15 | 1828 ; 1832 | |

**Table A7:** Energy in $cm^{-1}$ of the states of $\mathbf{Ga_4Tb_2}$ issued from the ground doublet of the monomers**.** The first column with J=0 considers only dipolar interaction. The gap between the $|++\rangle$ and the $|--\rangle$ states is due to the small splitting in the non Kramer's doublet of the monomer of 0.2 $cm^{-1}$ (see Table A6, second line).

| states | E with J=0 | E with J=-0.12 $cm^{-1}$ |
|---|---|---|
| $\|++\rangle \|--\rangle$ | -0.63 | -1.40 |
| $\|++\rangle$ | 0.54 | 1.60 |
| $\|--\rangle$ | 0.94 | 2.00 |

**Table A8.** Energy gaps and g factors of the lowest Kramer Doublets of $ErLuGa_4$.

| Kramer Doublets | $\Delta E$ ($cm^{-1}$) | $\Delta E*1.8$ ($cm^{-1}$) (1.8 is the reduction factor applied on the energy spectrum in order to be able to fit the magnetization data) | $g_i$ |
|---|---|---|---|
| 1 | 0 | 0 | 9.94 ; 5.14 ; 0.25 |
| 2 | 19 | 34 | 7.81 ; 5.51 ; 2.13 |
| 3 | 50 | 89 | 12.20 ; 2.14 ; 0.40 |
| 4 | 77 | 138 | 8.53 ; 5.46 ; 2.43 |
| 5 | 139 | 251 | 8.93 ; 5.25 ; 1.94 |
| 6 | 192 | 345 | 11.13 ; 3.57 ; 0.84 |
| 7 | 235 | 422 | 9.49 ; 5.21 ; 2.84 |
| 8 | 278 | 501 | 15.74 ; 1.23 ; 0.58 |
| 9 | 6117 | 11010 | |

**Table A9:** Energy in $cm^{-1}$ of the states of $\mathbf{Ga_4Er_2}$ issued from the ground Kramer's doublet of the monomers**.** The first column with J=0 considers only dipolar interaction.

| states | E with J=0 | E with J=2.4 $cm^{-1}$ |
|---|---|---|
| $\|T0\rangle = 1/\sqrt{2}\,(\|+-\rangle + \|-+\rangle)$ | -0.20 | -2.31 |
| $\|T+\rangle = 1/\sqrt{2}\,(\|++\rangle + \|--\rangle)$ | -0.33 | -1.47 |
| $\|T-\rangle = 1/\sqrt{2}\,(\|++\rangle - \|--\rangle)$ | 0.33 | 1.47 |
| $\|S\rangle = 1/\sqrt{2}\,(\|+-\rangle - \|-+\rangle)$ | 0.20 | 2.31 |

**Table A10:** Orbital and spin contributions to the g factors of the ground doublets. The ratio of the orbital and spin contributions is the same as in the free ion term. For gadolinium, the magnetic moment is the one of a pure spin. As in the free ion, the spin and orbital contributions are additive since the open shell is more than half filled and from Tb to Er, the orbital contribution increases while the spin one diminishes.

| | Gd | Tb | Dy | Er |
|---|---|---|---|---|
| **$g_1$** | **13.92** | **17.85** | **19.47** | **9.94** |
| $g_1^L$ | 0.05 | 5.92 | 9.70 | 6.60 |
| $g_1^S$ | 13.87 | 11.93 | 9.77 | 3.34 |
| **$g_2$** | **0.03** | **0.00** | **0.08** | **5.14** |
| $g_2^L$ | 0.00 | 0.00 | 0.04 | 3.42 |
| $g_2^S$ | 0.03 | 0.00 | 0.04 | 1.72 |
| **$g_3$** | **0.02** | **0.00** | **0.04** | **0.25** |
| $g_3^L$ | 0.00 | 0.00 | 0.02 | 0.18 |
| $g_3^S$ | 0.02 | 0.00 | 0.02 | 0.07 |

**Table A11.** Overlap integral between the different NSO for the **$Ga_4Dy_2$** complex along the direction of easy magnetization

| overlap integral | NSO1 | NSO2 | NSO3 | NSO4 | NSO5 | NSO6 | NSO7 |
|---|---|---|---|---|---|---|---|
| NSO1 | -1,08E-004 | -2,77E-005 | -4,02E-005 | -5,32E-005 | -1,69E-005 | 1,03E-004 | -9,39E-005 |
| NSO2 | -2,77E-005 | -5,31E-004 | 6,79E-004 | -6,66E-005 | 3,40E-004 | -1,58E-004 | -1,50E-004 |
| NSO3 | -4,02E-005 | 6,79E-004 | **-1,11E-003** | -1,67E-004 | 1,67E-004 | 3,05E-004 | 1,14E-004 |
| NSO4 | -5,32E-005 | -6,66E-005 | -1,67E-004 | 4,85E-004 | -2,37E-004 | -2,96E-005 | 7,01E-005 |
| NSO5 | -1,69E-005 | 3,40E-004 | 1,67E-004 | -2,37E-004 | -2,40E-004 | -1,38E-004 | 7,64E-005 |
| NSO6 | 1,03E-004 | -1,58E-004 | 3,05E-004 | -2,96E-005 | -1,38E-004 | 3,26E-004 | -7,73E-005 |
| NSO7 | -9,39E-005 | -1,50E-004 | 1,14E-004 | 7,01E-005 | 7,64E-005 | -7,73E-005 | 2,01E-004 |

**Table A12.** Overlap integral between the different NSO for the **$Ga_4Tb_2$** complex along the direction of easy magnetization

| overlap integral | NSO1 | NSO2 | NSO3 | NSO4 | NSO5 | NSO6 | NSO7 |
|---|---|---|---|---|---|---|---|
| NSO1 | -1,14E-004 | 1,59E-005 | 1,40E-005 | -2,35E-005 | 3,57E-004 | 1,26E-004 | -8,28E-005 |
| NSO2 | 1,59E-005 | -3,80E-004 | -5,75E-005 | -1,41E-004 | 8,10E-004 | -1,83E-004 | -3,21E-006 |
| NSO3 | 1,40E-005 | -5,75E-005 | 2,37E-004 | -1,86E-004 | 5,37E-005 | 9,34E-005 | -8,05E-005 |
| NSO4 | -2,35E-005 | -1,41E-004 | -1,86E-004 | -8,81E-005 | -2,97E-004 | -2,08E-004 | 3,21E-004 |
| NSO5 | 3,57E-004 | 8,10E-004 | 5,37E-005 | -2,97E-004 | **-1,04E-003** | -3,11E-004 | 6,99E-005 |
| NSO6 | 1,26E-004 | -1,83E-004 | 9,34E-005 | -2,08E-004 | -3,11E-004 | 2,82E-005 | 2,12E-005 |
| NSO7 | -8,28E-005 | -3,21E-006 | -8,05E-005 | 3,21E-004 | 6,99E-005 | 2,12E-005 | 3,87E-004 |

**Table A13.** Overlap integral between the different NSO for the **$Ga_4Er_2$** complex along the two directions of the plane of magnetization: direction 1 (top), direction 2 (bottom)

| overlap integral | NSO1 | NSO2 | NSO3 | NSO4 | NSO5 | NSO6 | NSO7 |
|---|---|---|---|---|---|---|---|
| NSO1 | -5,03E-004 | -1,18E-005 | -1,90E-004 | -5,12E-004 | 3,67E-004 | 9,36E-005 | -1,87E-004 |
| NSO2 | -1,18E-005 | 7,82E-005 | 1,48E-004 | 9,92E-005 | 8,86E-005 | 9,85E-005 | 1,78E-004 |
| NSO3 | -1,90E-004 | 1,48E-004 | -3,10E-004 | 2,39E-004 | -2,26E-004 | 3,42E-004 | 3,65E-004 |
| NSO4 | -5,12E-004 | 9,92E-005 | 2,39E-004 | -2,44E-004 | 6,22E-004 | 9,79E-006 | -2,62E-004 |
| NSO5 | 3,67E-004 | 8,86E-005 | -2,26E-004 | 6,22E-004 | -2,72E-004 | -1,75E-004 | -8,01E-005 |
| NSO6 | 9,36E-005 | 9,85E-005 | 3,42E-004 | 9,79E-006 | -1,75E-004 | 3,19E-004 | 1,38E-004 |
| NSO7 | -1,87E-004 | 1,78E-004 | 3,65E-004 | -2,62E-004 | -8,01E-005 | 1,38E-004 | 3,42E-004 |

| overlap integral | NSO1 | NSO2 | NSO3 | NSO4 | NSO5 | NSO6 | NSO7 |
|---|---|---|---|---|---|---|---|
| NSO1 | -3,75E-004 | 2,98E-004 | -1,23E-005 | -5,43E-006 | -2,94E-004 | 1,90E-005 | -7,75E-005 |
| NSO2 | 2,98E-004 | -1,87E-004 | 8,49E-005 | -2,44E-004 | 3,63E-003 | 5,82E-005 | 4,92E-007 |
| NSO3 | -1,23E-005 | 8,49E-005 | 6,14E-006 | -3,86E-004 | 2,82E-004 | 1,18E-004 | -3,56E-004 |
| NSO4 | -5,43E-006 | -2,44E-004 | -3,86E-004 | -8,87E-004 | 5,39E-004 | 2,61E-004 | 3,68E-005 |
| NSO5 | -2,94E-004 | 3,63E-003 | 2,82E-004 | 5,39E-004 | 4,54E-004 | -3,46E-005 | -1,43E-004 |
| NSO6 | 1,90E-005 | 5,82E-005 | 1,18E-004 | 2,61E-004 | -3,46E-005 | 1,94E-004 | 7,06E-005 |
| NSO7 | -7,75E-005 | 4,92E-007 | -3,56E-004 | 3,68E-005 | -1,43E-004 | 7,06E-005 | 2,06E-004 |

## Calculation of NSOs

A local modification of MOLCAS was used to generate natural spin orbitals (NSOs) from SO-CASSCF calculations. Within the frame of the principal magnetic axes of the doublet ground state $X$, $Y$ and $Z$, to generate the NSOs $\phi_p^u$ in direction $u = X, Y, Z$, one considers linear combinations of the ground state doublet components $|\Psi_0^u\rangle$ and $|\Psi_0'^u\rangle$ diagonalizing the magnetic moment operator $\widehat{M}_U$ and the NSOs $\phi_i^u$ are the eigen-functions of the one-particle spin-magnetization density matrices. It results that when the external magnetic field is applied along direction u, the spin density is $\rho^u(\boldsymbol{r}) = \sum_{i=1}^{7} n_i \phi_i(\boldsymbol{r})^2$ where $\phi_i$ is NSOi with occupation $n_i$. The spin magnetization in this direction is $\sum_{i=1}^{7} n_i = 2\langle \Psi_0^u | \hat{S}_u | \Psi_0^u \rangle = g_i^S/2$

## Calculation of the states of the dimers

Properties of the dimers are deduced from the properties of the monomers. Let us define the zero field state of the monomer A(B) as $|I\rangle^{A(B)}$ with the corresponding energies $E_I$. All matrix elements $\langle I|L_u|J\rangle$, $\langle I|S_u|J\rangle$ and $\langle I|M_u|J\rangle$ ($u = x, y, z$) are calculated within this basis set where $\vec{L}$, $\vec{S}$ and $\vec{M} = -\mu_B(\vec{L} + g_e \vec{S})$ are the orbital, the spin angular momenta and the total magnetic momentum. $g_e$ is the

g-factor of the free electron and $\mu_B$ is the Bohr magneton. The basis set for the dimer is built as the tensor product of SO states of the monomers $|\, I\, J\rangle = \; |\, I\rangle^A \otimes \; |\, J\rangle^B$ . The dipolar magnetic interaction can be written as

$$\hat{H}^{dip} = \frac{\mu_0}{4\pi R^3}\left\{\hat{\vec{M}}^A.\hat{\vec{M}}^B - 3\hat{M}_z^A\,\hat{M}_z^B\right\} \qquad (A1)$$

where $R$ is the intermetallic distance, $z$ the intermetallic direction and $\mu_0$ the magnetic constant. Matrix elements for the dimers are deduced from those of the monomer as

$$\langle I\, J\,|\,\hat{H}^{dip}\,|\,I'J'\rangle = \frac{\mu_0}{4\pi R^3}\{\langle I\mid \hat{M}_x^A \mid I'\rangle\langle J\mid \hat{M}_x^B \mid J'\rangle + \langle I\mid \hat{M}_y^A \mid I'\rangle\langle J\mid \hat{M}_y^B \mid J'\rangle - 2\,\langle I\mid \hat{M}_z^A \mid I'\rangle\langle J\mid \hat{M}_z^B \mid J'\rangle\}$$

The exchange interactions are carried by the spin densities and are described by a Heisenberg-Dirac-Van Vleck (HDVV) Hamiltonian

$$\hat{H}^{Heis} = -J\,\hat{\vec{S}}^A \cdot \hat{\vec{S}}^B \qquad (A2)$$

Matrix elements of this operator are

$$\langle I\, J|\hat{H}^{heis}|I'J'\rangle = -J\{\langle I|\hat{S}_x^A|I'\rangle\langle J|\hat{S}_x^B|J'\rangle + \langle I|\hat{S}_y^A|I'\rangle\langle J|\hat{S}_y^B|J'\rangle + \langle I\mid \hat{S}_z^A \mid I'\rangle\langle J\mid \hat{S}_z^B \mid J'\rangle\}.$$

Finally, the Zeeman interaction in the dimer is described by the following Hamiltonian

$$\hat{H}^{Zee} = -\mu_B\,\vec{B}\cdot\left(\hat{\vec{M}}^A + \hat{\vec{M}}^B\right) \qquad (A3)$$

where $\mu_B$ is the Bohr magneton and $\vec{B}$ is the external magnetic field with components $B_x$, $B_y$ and $B_z$. The matrix elements of this Hamiltonian are

$$\langle I\, J|\hat{H}^{Zee}|I'J'\rangle = -\mu_B\{B_x(\langle I|\hat{M}_x^A|I'\rangle\delta_{J\,J'} + \langle J|\hat{M}_x^B|J'\rangle\delta_{I\,I'}) + B_y(\langle I|\hat{M}_y^A|I'\rangle\delta_{J\,J'} + \langle J|\hat{M}_y^B|J'\rangle\delta_{I\,I'}) + B_z(\langle I|\hat{M}_z^A|I'\rangle\delta_{J\,J'} + \langle J|\hat{M}_z^B|J'\rangle\delta_{I\,I'})\}$$

where $\delta$ denotes the Kronecker symbol. Finally, the full matrix diagonalization of the total Hamiltonian $\hat{H} = \hat{H}^A + \hat{H}^B + \hat{H}^{dip} + \hat{H}^{Heis} + \hat{H}^{Zee}$ provides all energy eigenvalues and eigenvectors. This allows the calculation of the magnetization of the dimer using a Boltzmann statistics. All terms are first principles except the exchange coupling parameter $J$.

## Magnetic dipole interaction between two magnetic planes

The magnetic plane is denoted xy and the intermetallic axis is $\vec{u} = \alpha\overrightarrow{e_x} + \beta\overrightarrow{e_y} + \gamma\overrightarrow{e_z}$. We note $\kappa = \frac{\mu_0}{4\pi R^3}$. We restrict the discussion to the lowest doublet where $|+\rangle$ and $|-\rangle$ are the local states on one monomer. The matrices for the magnetization on one center are

| $\widehat{M}_x$ | $\lvert+\rangle$ | $\lvert-\rangle$ |
|---|---|---|
| $\langle+\rvert$ | $0$ | $m$ |
| $\langle-\rvert$ | $m$ | $0$ |

| $\widehat{M}_y$ | $\lvert+\rangle$ | $\lvert-\rangle$ |
|---|---|---|
| $\langle+\rvert$ | $0$ | $-i\,m$ |
| $\langle-\rvert$ | $i\,m$ | $0$ |

The states for the dimer are obtained as a tensor product of the states of the monomer $\lvert++\rangle$, $\lvert+-\rangle$, $\lvert-+\rangle$ and $\lvert--\rangle$. The matrix of operator $\widehat{H}^{dip}$ defined in Eq. A1 is

| $\widehat{H}^{dip}$ | $\lvert++\rangle$ | $\lvert+-\rangle$ | $\lvert-+\rangle$ | $\lvert--\rangle$ |
|---|---|---|---|---|
| $\langle++\rvert$ | $0$ | $0$ | $0$ | $-3\kappa m^2(\alpha-i\beta)^2$ |
| $\langle+-\rvert$ | $0$ | $0$ | $\kappa m^2(2-3(\alpha^2+\beta^2))$ | $0$ |
| $\langle-+\rvert$ | $0$ | $\kappa m^2(2-3(\alpha^2+\beta^2))$ | $0$ | $0$ |
| $\langle--\rvert$ | $-3\kappa m^2(\alpha-i\beta)^2$ | $0$ | $0$ | $0$ |

In the case where **the magnetic plane is perpendicular to the intermetallic axis**, $\gamma=1$ and $\alpha=\beta=0$. Introducing a new basis set, $\lvert T+\rangle=1/\sqrt{2}\left(\lvert++\rangle+\lvert--\rangle\right)$, $\lvert T-\rangle=1/\sqrt{2}\left(\lvert++\rangle-\lvert--\rangle\right)$, $\lvert T0\rangle=1/\sqrt{2}\left(\lvert+-\rangle+\lvert-+\rangle\right)$, $\lvert S\rangle=1/\sqrt{2}\left(\lvert+-\rangle-\lvert-+\rangle\right)$ the previous matrix becomes

| $\widehat{H}^{dip}$ | $\lvert T+\rangle$ | $\lvert T0\rangle$ | $\lvert T-\rangle$ | $\lvert S\rangle$ |
|---|---|---|---|---|
| $\langle T+\rvert$ | $0$ | $0$ | $0$ | $0$ |
| $\langle T0\rvert$ | $0$ | $2\kappa m^2$ | $0$ | $0$ |
| $\langle T-\rvert$ | $0$ | $0$ | $0$ | $0$ |
| $\langle S\rvert$ | $0$ | $0$ | $0$ | $-2\kappa m^2$ |

The ground state is the $\lvert S\rangle$ state.

In the case were **the magnetic plane includes the intermetallic axis**, $\alpha=1$ and $\beta=\gamma=0$ and the matrix becomes

| $\widehat{H}^{dip}$ | $\lvert T+\rangle$ | $\lvert T0\rangle$ | $\lvert T-\rangle$ | $\lvert S\rangle$ |
|---|---|---|---|---|
| $\langle T+\rvert$ | $-3\kappa m^2$ | $0$ | $0$ | $0$ |
| $\langle T0\rvert$ | $0$ | $-\kappa m^2$ | $0$ | $0$ |
| $\langle T-\rvert$ | $0$ | $0$ | $3\kappa m^2$ | $0$ |
| $\langle S\rvert$ | $0$ | $0$ | $0$ | $\kappa m^2$ |

The ground state is $\lvert T+\rangle$ as it is the case for $Er_2Ga_4$ without exchange interaction.

## Exchange interaction between two magnetic planes

We develop the case where there is an asymmetry in the magnetic plane and for an isotropic Heisenberg Hamiltonian $J$. The matrices for the magnetization on one center are

| $\widehat{M}_x$ | $\lvert+\rangle$ | $\lvert-\rangle$ |
|---|---|---|
| $\langle+\rvert$ | $0$ | $m_x$ |
| $\langle-\rvert$ | $m_x$ | $0$ |

| $\widehat{M}_y$ | $\lvert+\rangle$ | $\lvert-\rangle$ |
|---|---|---|
| $\langle+\rvert$ | $0$ | $-i\,m_y$ |
| $\langle-\rvert$ | $i\,m_y$ | $0$ |

The matrix of operator $\widehat{H}^{Heis}$ defined in Eq. A2 is

| $\widehat{H}^{Heis}$ | $\lvert++\rangle$ | $\lvert+-\rangle$ | $\lvert-+\rangle$ | $\lvert--\rangle$ |
|---|---|---|---|---|
| $\langle++\rvert$ | $0$ | $0$ | $0$ | $-J\left(m_x^2-m_y^2\right)$ |
| $\langle+-\rvert$ | $0$ | $0$ | $-J\left(m_x^2+m_y^2\right)$ | $0$ |
| $\langle-+\rvert$ | $0$ | $-J\left(m_x^2+m_y^2\right)$ | $0$ | $0$ |
| $\langle--\rvert$ | $-J\left(m_x^2-m_y^2\right)$ | $0$ | $0$ | $0$ |

or in the other basis set

| $\widehat{H}^{Heis}$ | $\lvert T+\rangle$ | $\lvert T0\rangle$ | $\lvert T-\rangle$ | $\lvert S\rangle$ |
|---|---|---|---|---|
| $\langle T+\rvert$ | $J\left(-m_x^2+m_y^2\right)$ | $0$ | $0$ | $0$ |
| $\langle T0\rvert$ | $0$ | $J\left(-m_x^2-m_y^2\right)$ | $0$ | $0$ |
| $\langle T-\rvert$ | $0$ | $0$ | $J\left(m_x^2-m_y^2\right)$ | $0$ |
| $\langle S\rvert$ | $0$ | $0$ | $0$ | $J\left(m_x^2+m_y^2\right)$ |

With a ferromagnetic coupling $J>0$, the ground state is $\lvert T0\rangle$. The asymmetry in the x and y directions leads to an energy gap between $\lvert T+\rangle$ and $\lvert T-\rangle$ states.

The Zeeman Hamiltonian of Eq. A3 couples $\lvert T0\rangle$ with $\lvert T+\rangle$ ( $\lvert T-\rangle$) when the magnetic field is applied along x (y).

# Appendix B

## Estimation of the Molecular Weight of **$Fe_4$OAc**, **$Fe_4$OBz**, **$Fe_8$-A**, **$Fe_8$-B**, **$Fe_8$-C** and **$Fe_8$-A-Dry**

A combination of TGA, elemental analysis and PXRD was used to determine the molecular weights of the $Fe^{III}$ complexes described in chapter 4. Each compound was analyzed by TGA; the thermolysis of each compound gave a reddish-brown powder that was determined by PXRD (Figure A1) to be α-$Fe_2O_3$ (Hematite). The molecular weight can be determined by TGA through back calculation using the equation:

$$MW = \frac{\text{Mass of sample at start}}{\left(\frac{\text{mass of sample at end}}{\text{MW of } Fe_2O_3}\right) \div (\text{mol } Fe_2O_3 \text{ generated per mol of compound})}$$

A possible formula was also determined through elemental analysis results. The average MW from the TGA and elemental analysis was used for treating the magnetic data.

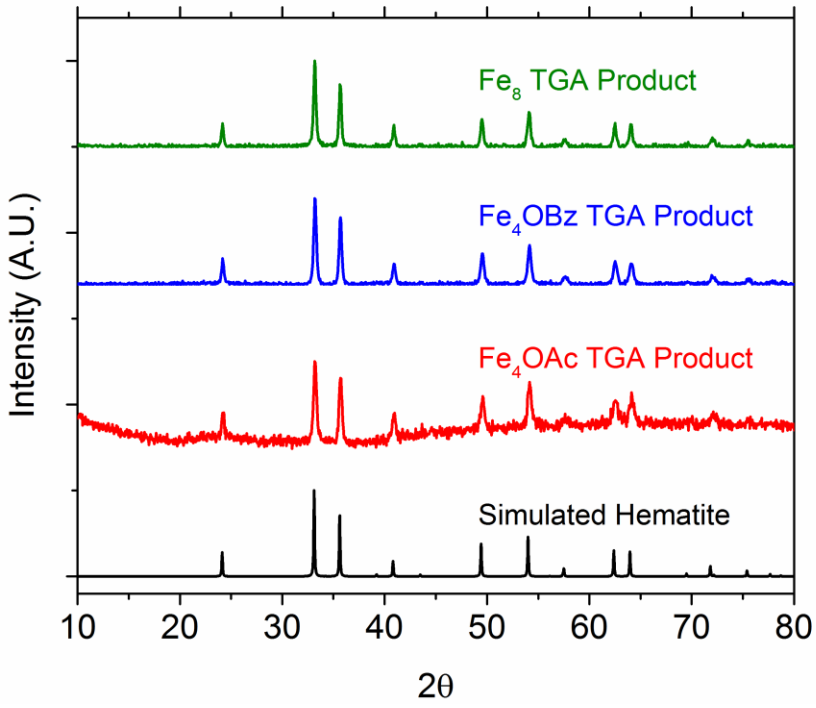


**Figure B1.** PXRD patterns for the resultant TGA product of **$Fe_4$OAc** (red), **$Fe_4$OBz** (blue) and **$Fe_8$** (green) and hematite (simulated, black).

**$Fe_4OAc$**

Elemental analysis results were: C, 33.47; H, 4.60; N, 3.78.

A potential formula derived from the CHN analysis is $[Fe_8(shi^{3-})_6(isopthalate^{-})_3(H_2O)_6]\cdot H_2O$ ($Fe_8C_{66}H_{50}N_6O_{37}$), which gives a MW of **1105.13 g/mol**

MW back calculated from the TGA (Figure A2) is: **1117.97 g/mol**

The average MW determined is: **1111.52 g/mol**

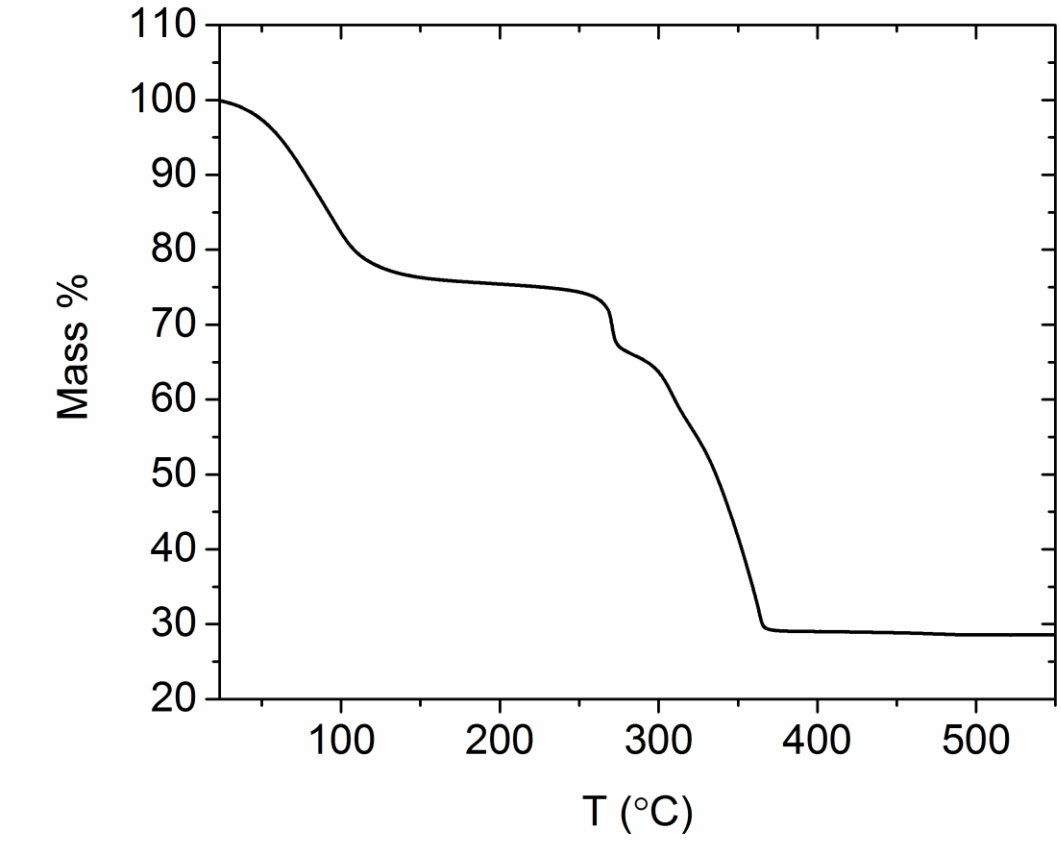


**Figure B2.** TGA trace of **$Fe_4OAc$**.

**$Fe_4$OBz**

Elemental analysis results were: C, 44.86; H, 4.12; N, 3.40.

A potential formula derived from the CHN analysis is $[Fe_4(shi^{3-})_3(benzoate^-)_3(MeOH)_3]\cdot MeOH\cdot 4H_2O$ ($Fe_4C_{46}H_{51}N_3O_{23}$), which gives a MW of **1237.29 g/mol**

MW back calculated from the TGA (Figure A3) is: **1264.55 g/mol**

The average MW determined is: **1250.92 g/mol**

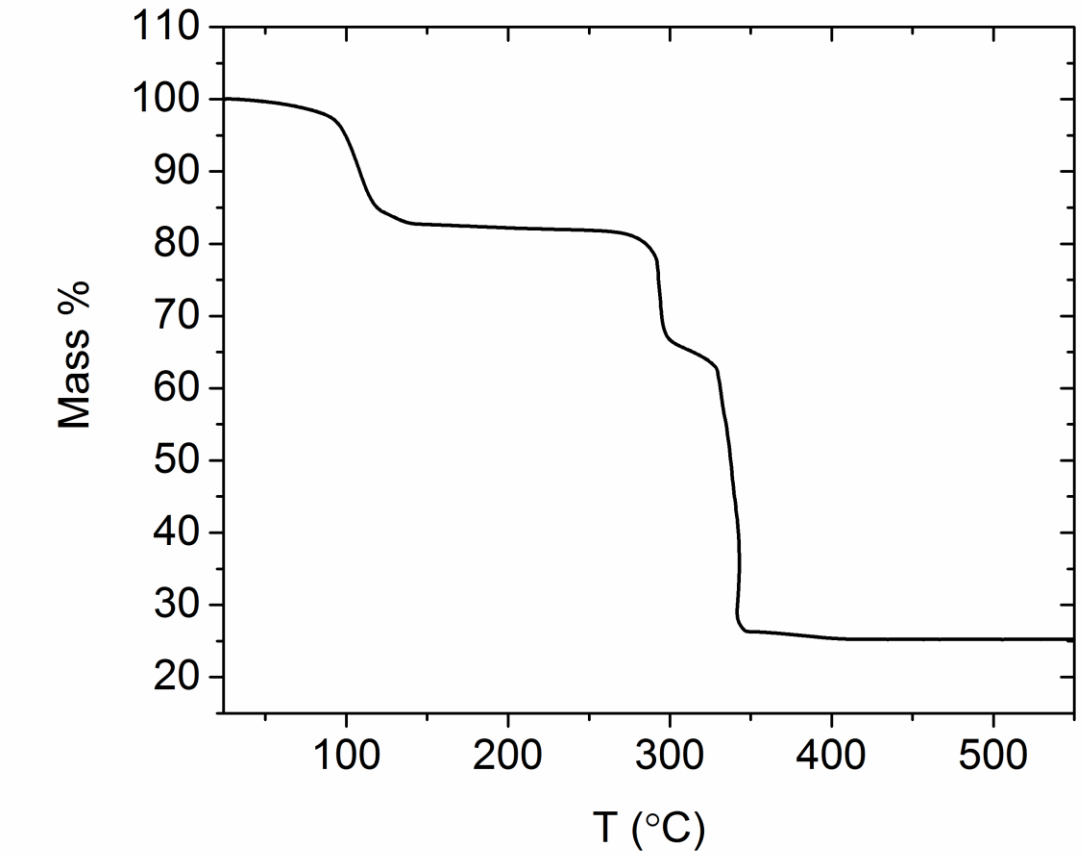


**Figure B3.** TGA trace of **$Fe_4$OBz**.

**$Fe_8$-A**

Elemental analysis results were: C, 33.47; H, 4.60; N, 3.78.

A potential formula derived from the CHN analysis is $[Fe_8(shi^{3-})_6(isopthalate^{-})_3(H_2O)_6]\cdot 24H_2O$ ($Fe_8C_{66}H_{96}N_6O_{60}$), which gives a MW of **2380.25 g/mol**

MW back calculated from the TGA (Figure A4) is: **2447.51 g/mol**

The average MW determined is: **2413.88 g/mol**

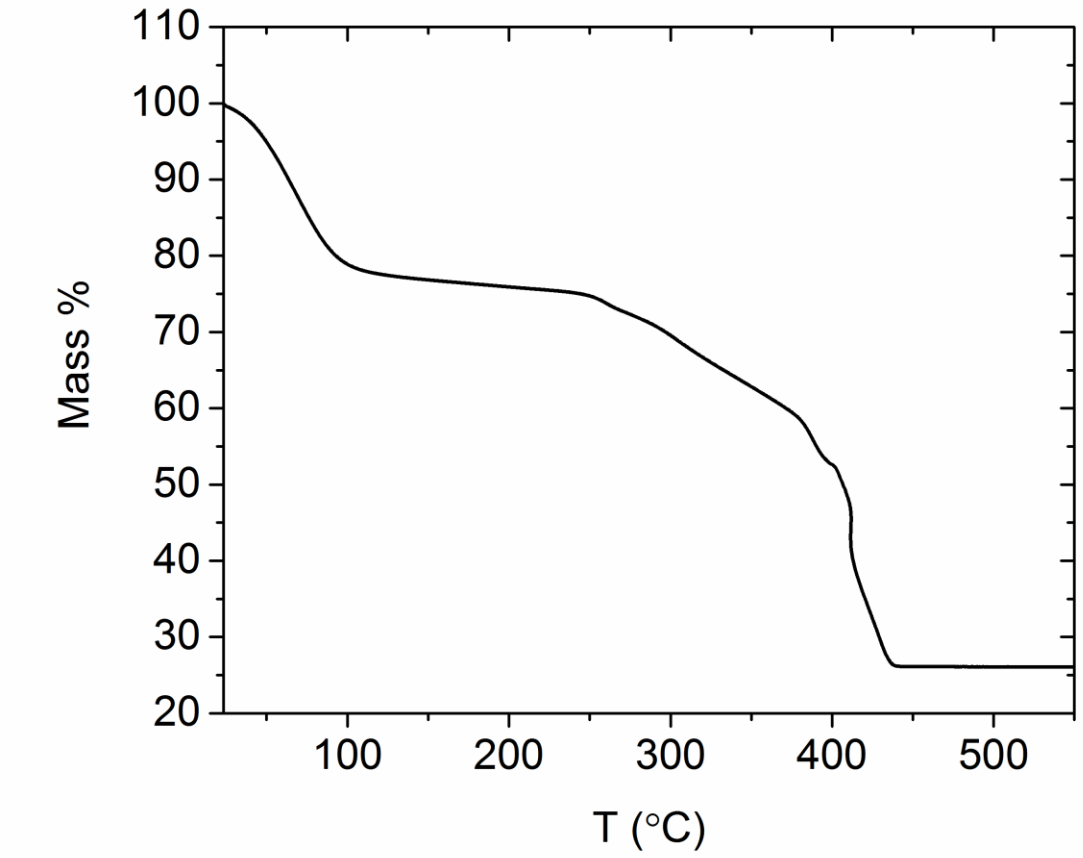


**Figure B4.** TGA trace of **$Fe_8$-A**.

**$Fe_8$-B**

Elemental analysis results were: C, 39.47; H, 3.25; N, 3.91

A potential formula derived from the CHN analysis is $[Fe_8(shi^{3-})_6(isopthalate^{-})_3(H_2O)_6]\cdot 4H_2O\cdot 2EtOH$ ($Fe_8C_{70}H_{70}N_6O_{42}$), which gives a MW of **2114.07 g/mol**

MW back calculated from the TGA (Figure A5) is: **2138.66 g/mol**

The average MW determined is: **2126.37 g/mol**

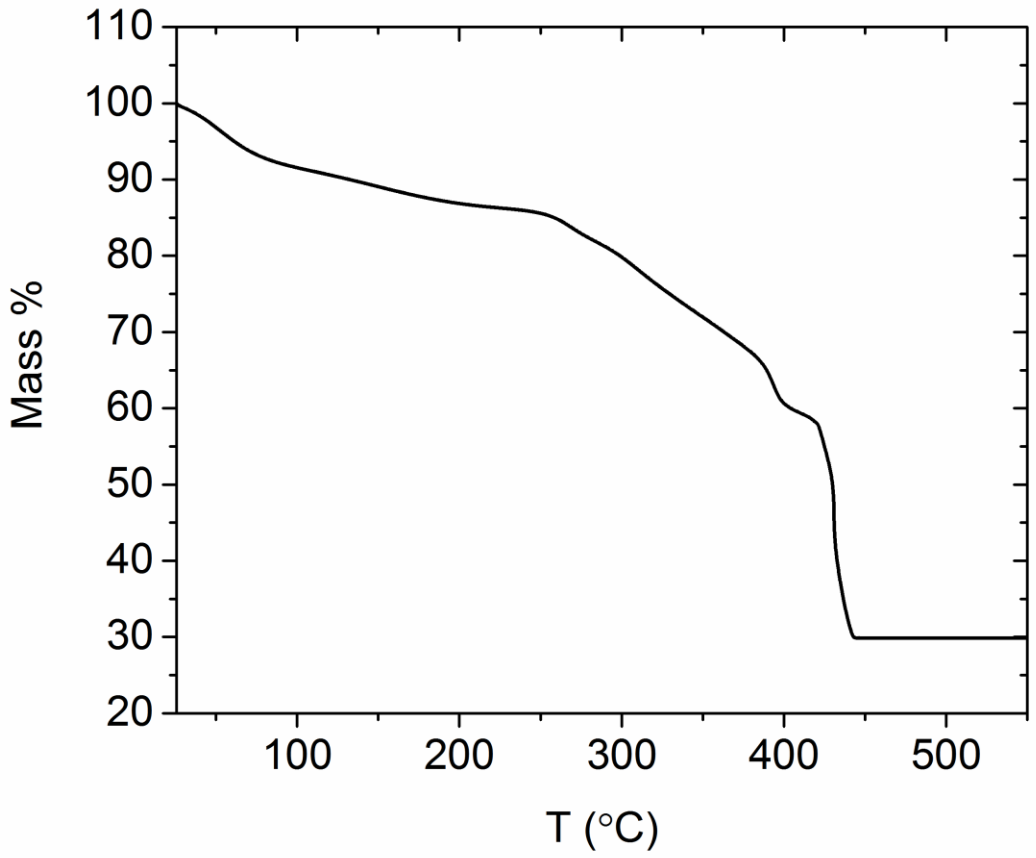


**Figure B5.** TGA trace of **$Fe_8$-B**.

**$Fe_8$-C**

Elemental analysis results were: C, 33.47; H, 4.60; N, 3.78.

A potential formula derived from the CHN analysis is $[Fe_8(shi^{3-})_6(isopthalate^{-})_3(H_2O)_6]\cdot 4H_2O\cdot EtOH$ ($Fe_8C_{68}H_{62}N_6O_{41}$), which gives a MW of **2066.01 g/mol**

MW back calculated from the TGA (Figure A6) is: **2112.63 g/mol**

The average MW determined is: **2089.32 g/mol**

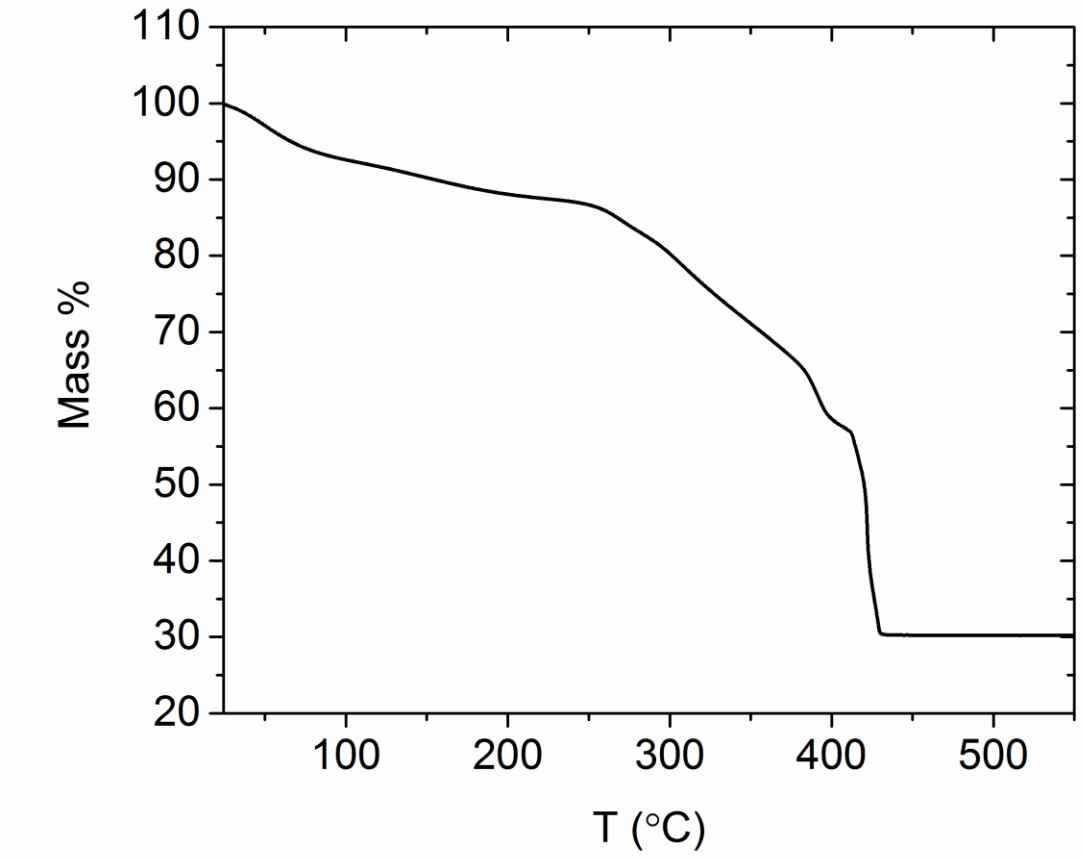


**Figure B6.** TGA trace of **$Fe_8$-C**.

**$Fe_8$-A-Dry**

Elemental analysis results were: C, 33.47; H, 4.60; N, 3.78.

A potential formula derived from the CHN analysis $[Fe_8(shi^{3-})_6(isopthalate^{-})_3(H_2O)_6]\cdot H_2O$ ($Fe_8C_{66}H_{50}N_6O_{37}$), which gives a MW of **1965.89 g/mol**

MW back calculated from the TGA (Figure A7) is: **1963.61 g/mol**

The average MW determined is: **1964.75 g/mol**

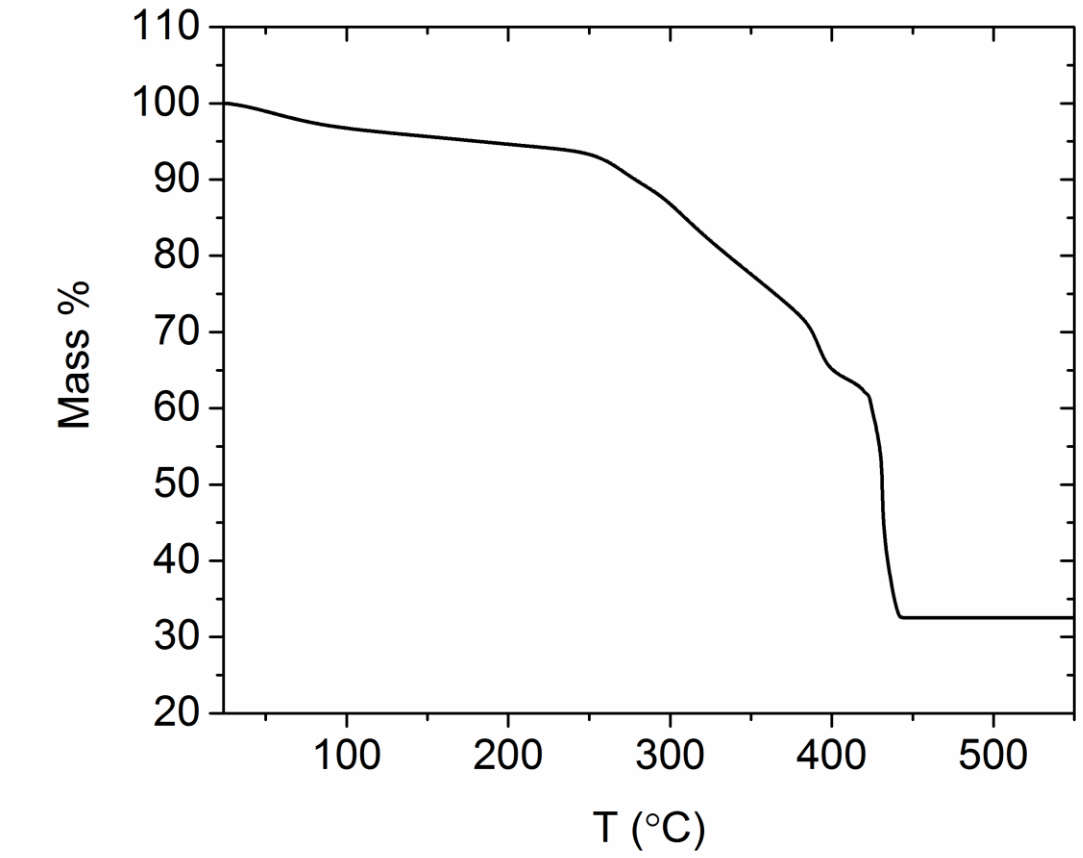


**Figure B7.** TGA trace of **$Fe_8$-A-Dry**.

# Appendix C

## Additional Photophysical Spectra of **$Ga_4Ln$** Complexes

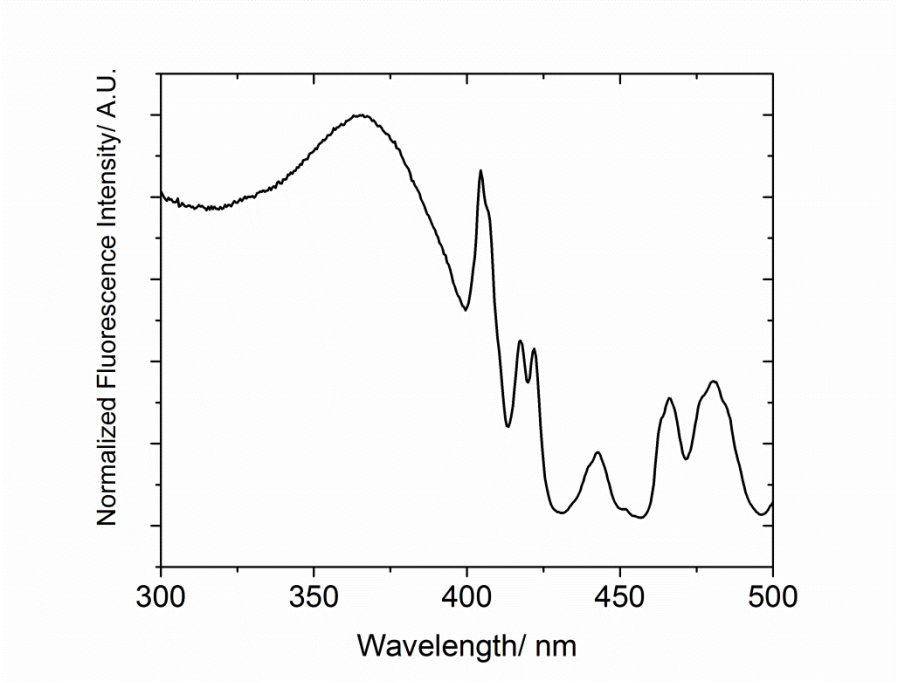


**Figure C1.** Solid state excitation spectrum in for **$Ga_4Sm$** recorded at 298 K with $\lambda_{em}$ = 600 nm.

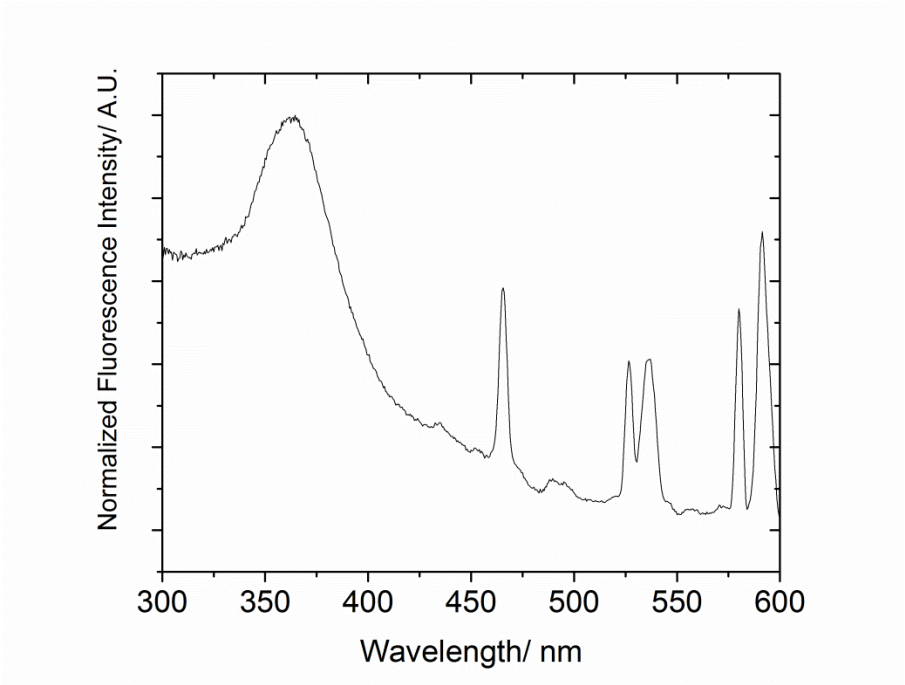


**Figure C2.** Solid state excitation spectrum in for **$Ga_4Eu$** recorded at 298 K with $\lambda_{em}$ = 615 nm.

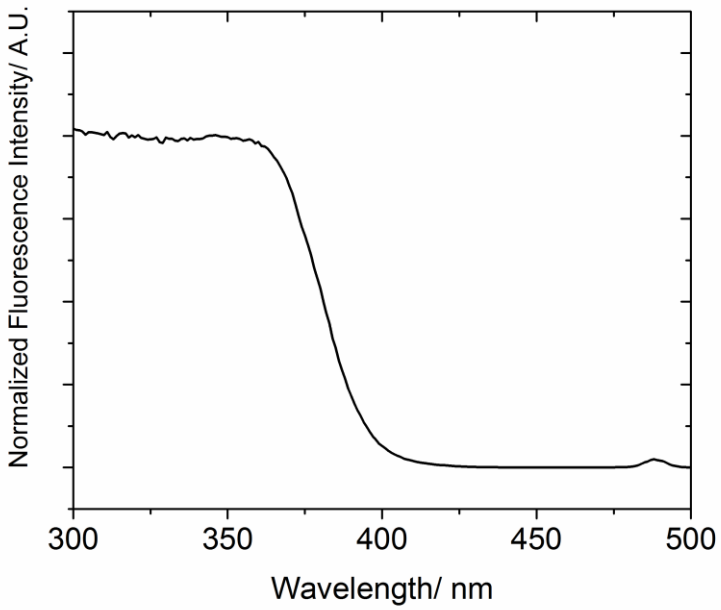


**Figure C3.** Solid state excitation spectrum in for **$Ga_4Tb$** recorded at 298 K with $\lambda_{em}$ = 545 nm.

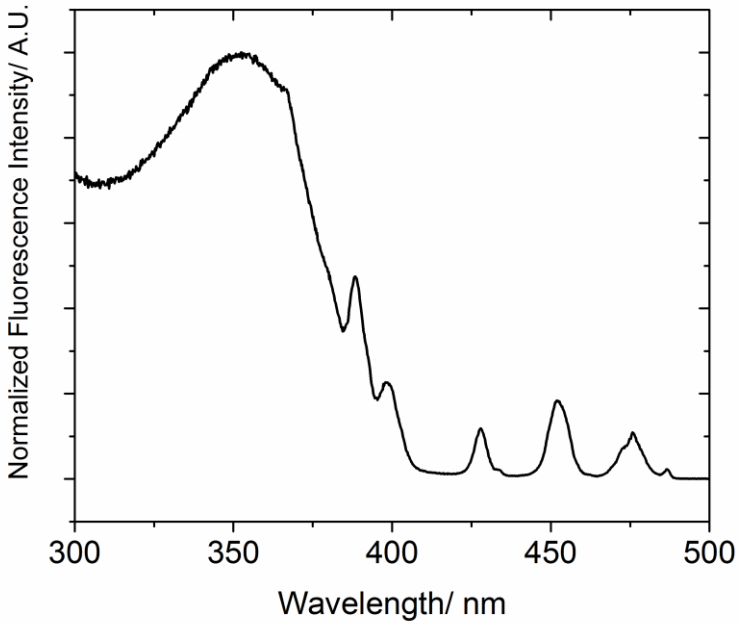


**Figure C4.** Solid state excitation spectrum in for **$Ga_4Dy$** recorded at 298 K with $\lambda_{em}$ = 575 nm.

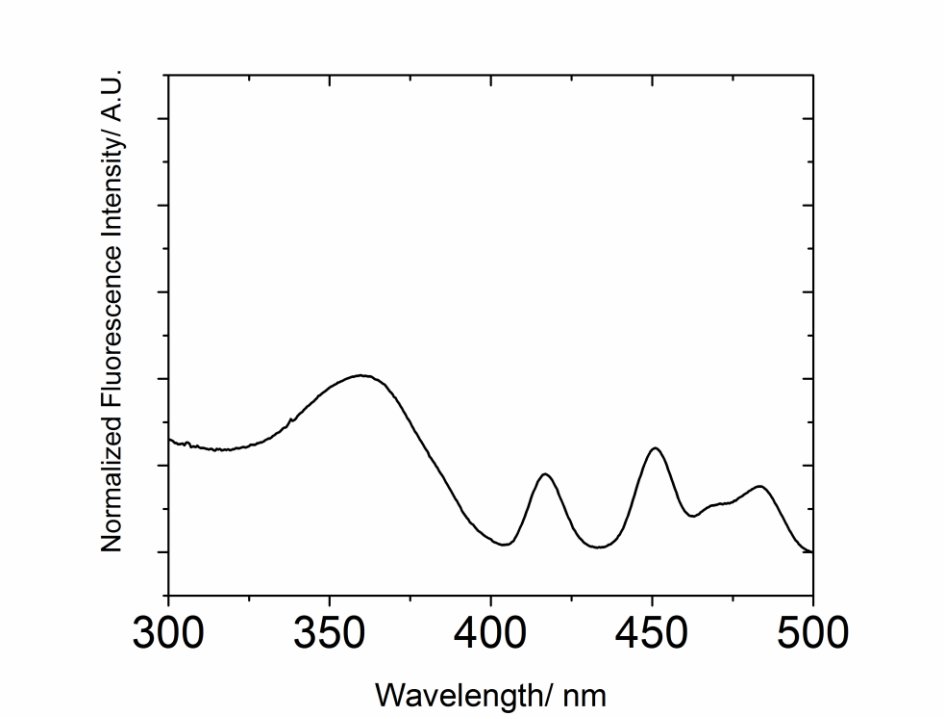


**Figure C5.** Solid state excitation spectrum in for **$Ga_4Ho$** recorded at 298 K with $\lambda_{em}$ = 985 nm.

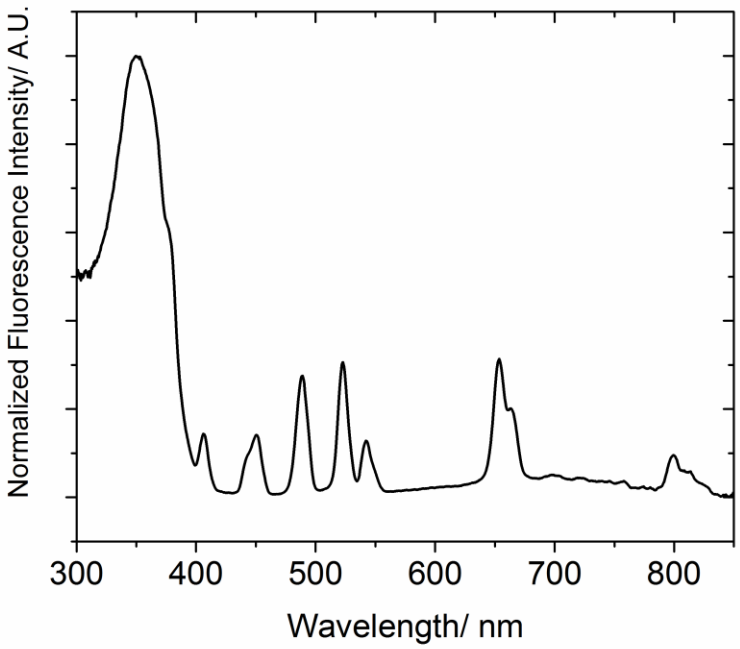


**Figure C6.** Solid state excitation spectrum in for **$Ga_4Er$** recorded at 298 K with $\lambda_{em}$ = 1510 nm.

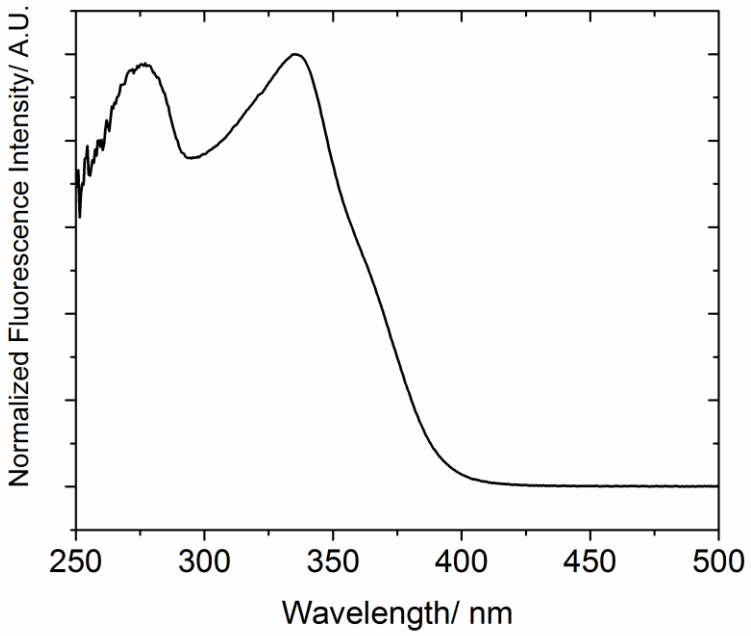


**Figure C7.** Solid state excitation spectrum in for **$Ga_4Yb$** recorded at 298 K with $\lambda_{em}$ = 965 nm.

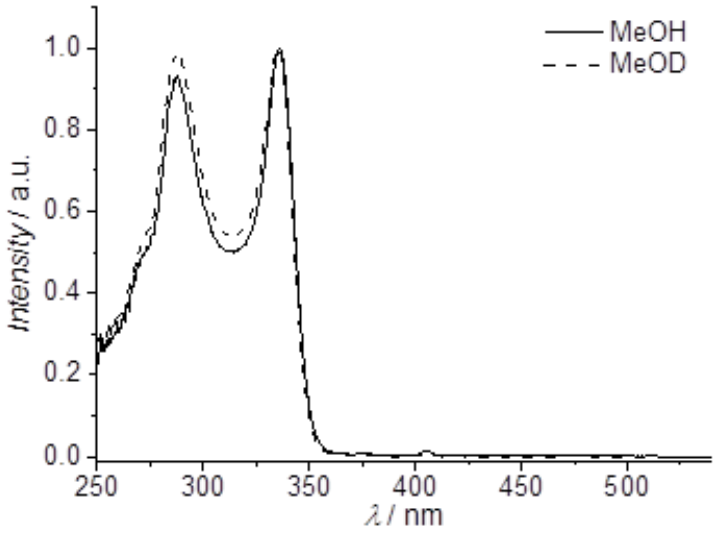


**Figure C8.** Excitation spectrum in for **$Ga_4Sm$** recorded at 298 K with $\lambda_{em}$ = 600 nm in $CH_3OH$ (solid line) and $CD_3OD$ (dashed line).

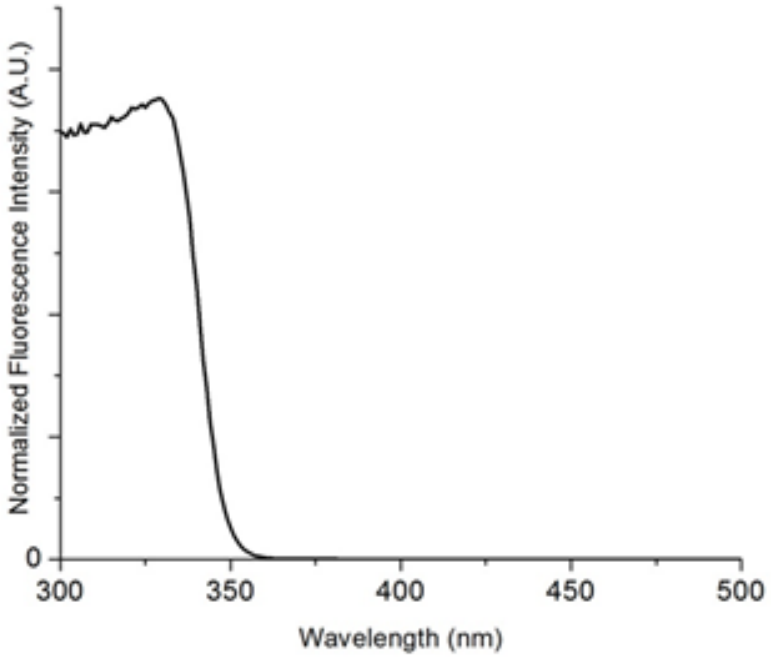


**Figure C9.** Excitation spectrum in for **$Ga_4Tb$** recorded at 298 K with $\lambda_{em}$ = 545 nm in $CD_3OD$.

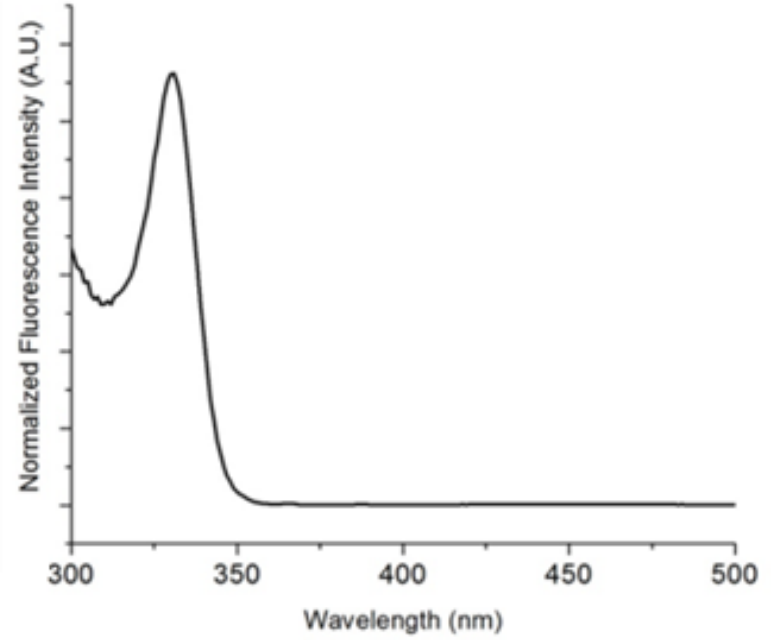


**Figure C10.** Excitation spectrum in for **$Ga_4Dy$** recorded at 298 K with $\lambda_{em}$ = 575 nm in $CD_3OD$.

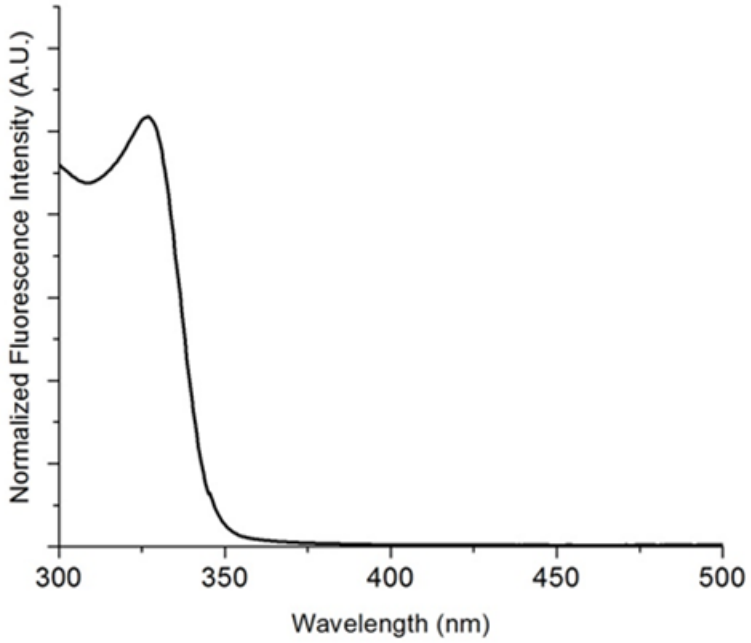


**Figure C11.** Excitation spectrum in for **$Ga_4Yb$** recorded at 298 K with $\lambda_{em}$ = 960 nm in $CD_3OD$.

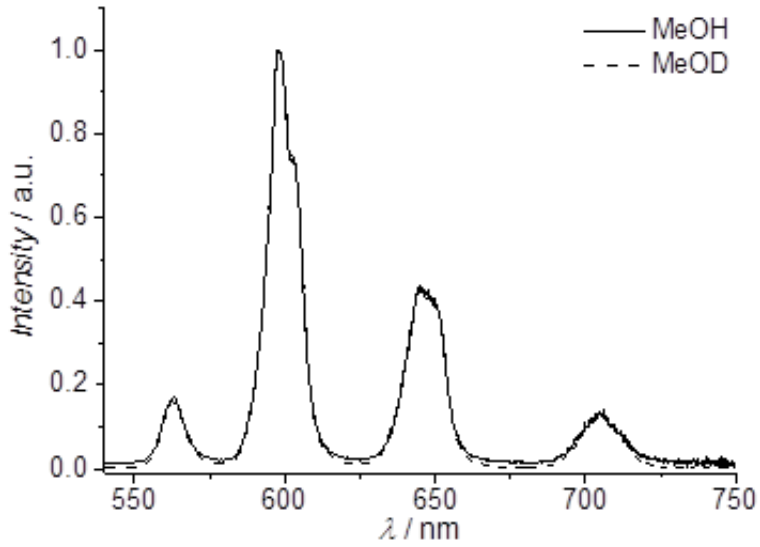


**Figure C12.** Visible emission spectrum in for **$Ga_4Sm$** recorded at 298 K with $\lambda_{ex}$ = 325 nm in $CH_3OH$ (solid line) and $CD_3OD$ (dashed line).

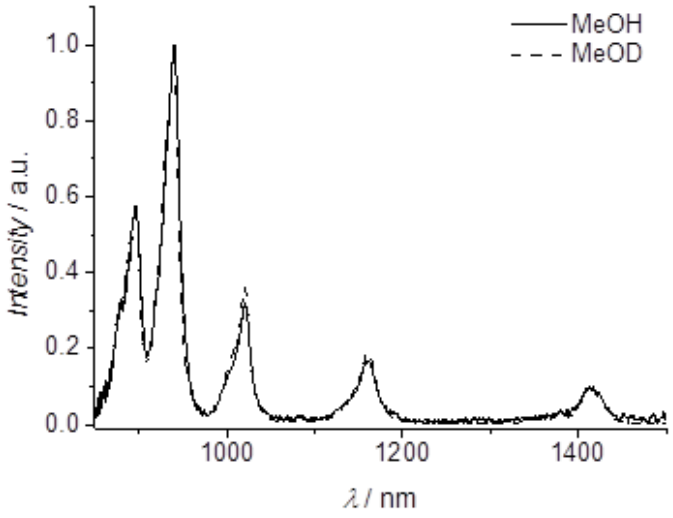


**Figure C13.** NIR emission spectrum in for **$Ga_4Sm$** recorded at 298 K with $\lambda_{ex}$ = 325 nm in $CH_3OH$ (solid line) and $CD_3OD$ (dashed line).

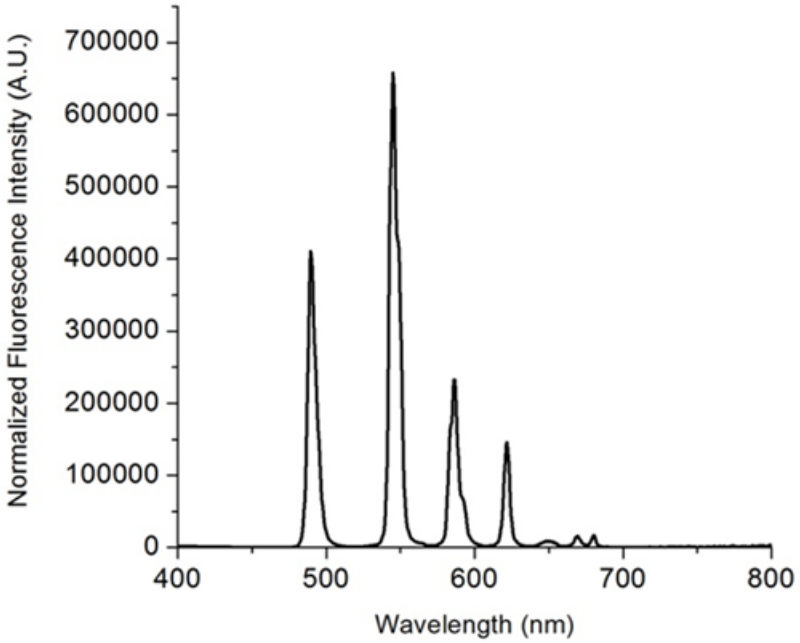


**Figure C14.** Visible emission spectrum in for **$Ga_4Tb$** recorded at 298 K with $\lambda_{ex}$ = 325 nm in $CD_3OD$.

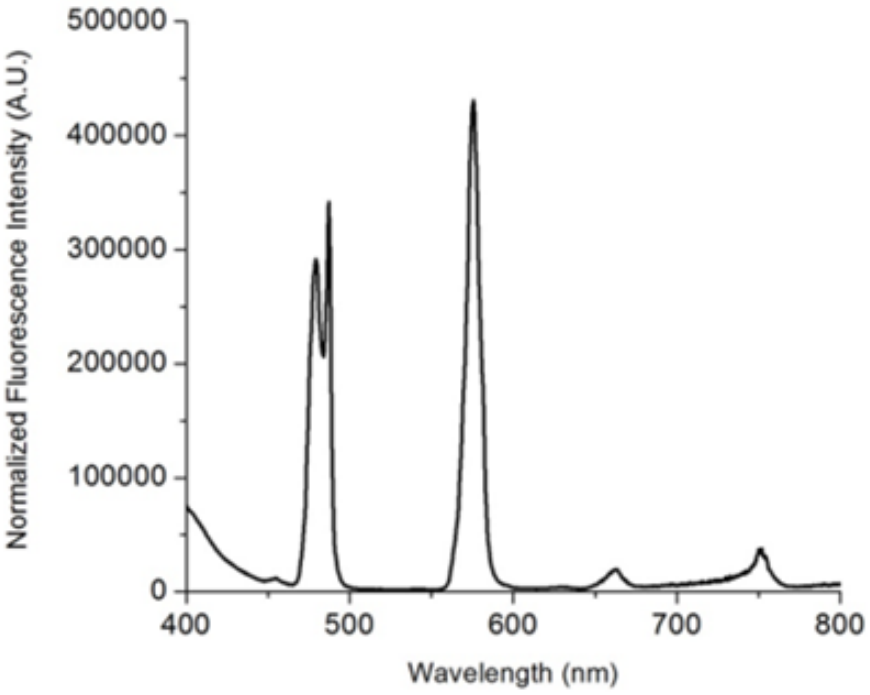


**Figure C15.** Visible emission spectrum in for **$Ga_4Dy$** recorded at 298 K with $\lambda_{ex}$ = 325 nm in $CD_3OD$.

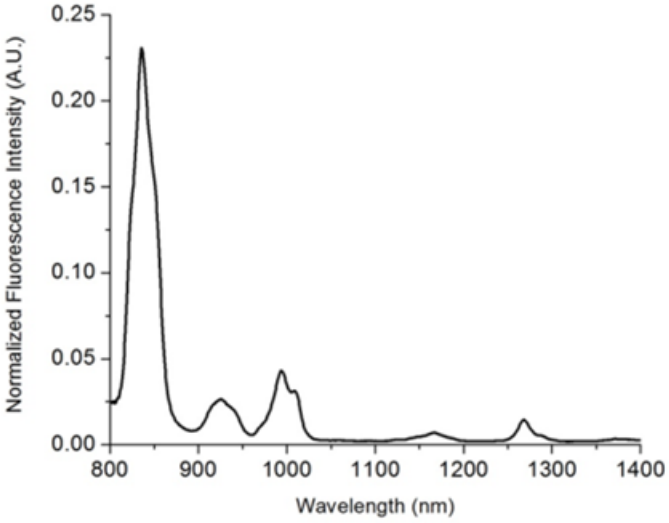


**Figure C16.** NIR emission spectrum in for **$Ga_4Dy$** recorded at 298 K with $\lambda_{ex}$ = 325 nm in $CD_3OD$.

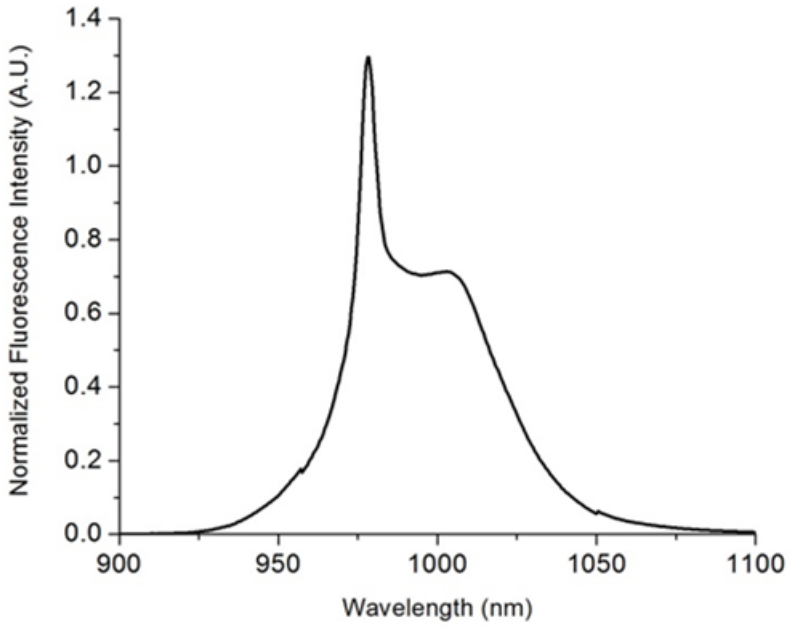


**Figure C17.** NIR emission spectrum in for **$Ga_4Yb$** recorded at 298 K with $\lambda_{ex}$ = 325 nm in $CD_3OD$.